Analysis of a solid desiccant cooling system with indirect evaporative cooling

Bellemo, Lorenzo

Publication date:
2017

Document Version
Publisher's PDF, also known as Version of record

Analysis of a solid desiccant cooling system with indirect evaporative cooling

PhD Thesis

$$(EIv'')'' = q - \rho A \ddot{v}$$

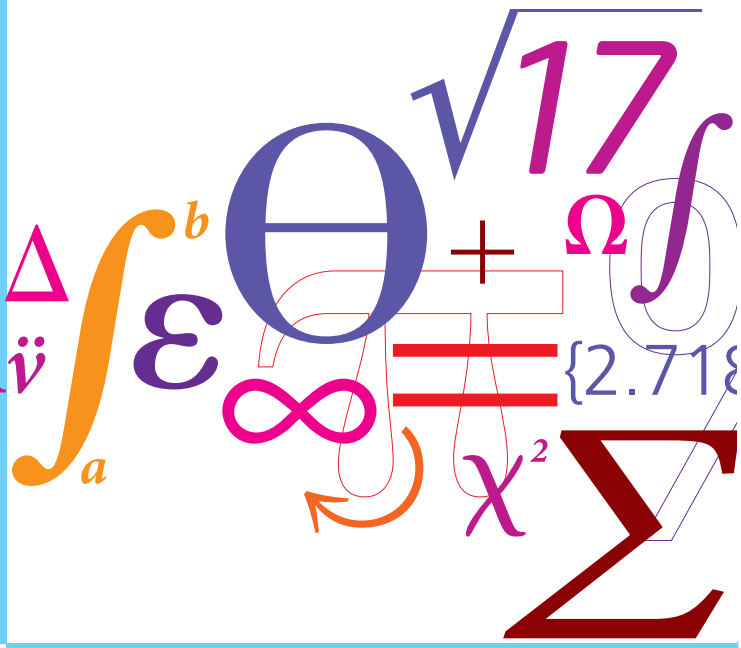

Lorenzo Bellemo
DCAMM Special Report No. S232
June 2016

DTU Mechanical Engineering
Department of Mechanical Engineering

Analysis of a solid desiccant cooling system with indirect evaporative cooling

PhD Thesis
TECHNICAL UNIVERSITY OF DENMARK

for the degree of Doctor of Philosophy

by
Lorenzo Bellemo

under suggestion of:
Brian Elmegaard (DTU), Head of Section and Associate Professor (DTU), main supervisor
Wiebke Brix Markussen, Associate Professor (DTU), co-supervisor
Martin Ryhl Kærn, Senior Researcher (DTU), co-supervisor
Lars Ove Reinholdt, Engineer (DTI) , co-supervisor

Analysis of a solid desiccant cooling system with indirect evaporative cooling

PhD Thesis
Printed by Rosendahls – Schultz Grafisk A/S
Font: Utopia typeset with LaTeX 2ε

DTU Mechanical Engineering
Section of Thermal Energy
Technical University of Denmark

Nils Koppels Allé, Bld. 403
DK-2800 Kongens Lyngby
Denmark
Phone: (+45) 4525 4131
Fax: (+45) 4525 4325
www.mek.dtu.dk

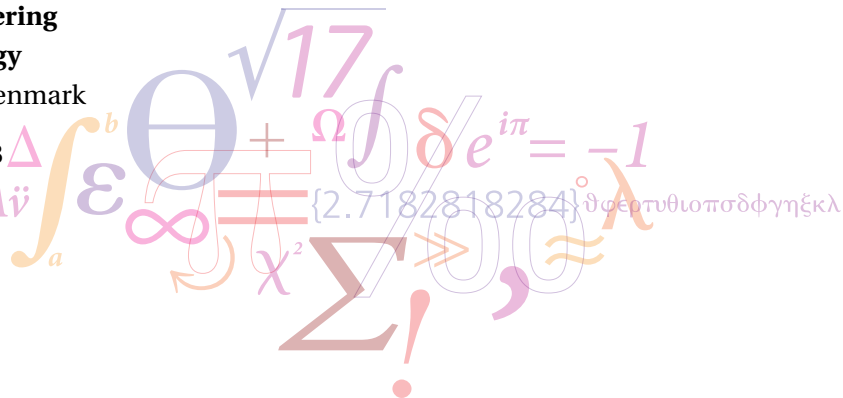

There is nothing noble in being superior to your fellow man;
true nobility is being superior to your former self.

Ernest Hemingway

Preface

The present thesis was prepared at the Section of Thermal Energy, Department of Mechanical Engineering, Technical University of Denmark (DTU). It is submitted in partial fulfilment of the requirements for acquiring the Ph.D degree and it is written as a monograph.

The work was carried out from September 2012 to June 2016, under supervision of Associate Professor Brian Elmegaard (DTU) and co-supervision of Associate Professor Wiebke Markussen (DTU), Senior Researcher Martin Kærn (DTU), and Engineer Lars Reinholdt (Danish Technological Institute, DTI).

The Ph.D project was funded by the Danish Energy Research and Development program ELFORSK, to support a parallel industrial development project in close collaboration with DTI and the Danish company COTES.

An external research stay was carried out at the Energy Centre of the Commonwealth Scientific and Industrial Research Organisation (CSIRO) in Newcastle (Australia), under guidance of Ph.D Subbu Sethuvenkatraman and Ph.D Mark Goldsworthy, from November 2013 to April 2014. The external research project focused on the development of a solar air collector thermodynamic model, within the Australian project RP1008 "Industry Support Mechanisms for Renewable Heating and Cooling", which served to improve the Australian Interim Standard AS5389 "Solar heating and cooling systems – Calculation of energy consumption". The work performed during the external research stay is not reported in the present thesis.

An additional Research Assistant project, funded by ELFORSK, was carried out from May 2015 to October 2015, under supervision of Associate Professor Brian Elmegaard (DTU). The work, focusing on the modelling of desiccant wheels regenerated with superheated steam, supported the development of an efficient technology for industrial drying processes in collaboration with COTES, DryingMate and DTI. The industrial project won the ELFORSK price 2016. The work performed during this project is not reported in the present thesis.

Lyngby, 15th June 2016 Lorenzo Bellemo

Acknowledgements

The completion of this Ph.D project has not only been a professional challenge, but also an important personal growth, enriched by the people I have met and worked with.

I deeply thank my supervisor Brian Elmegaard for the trust he has put in my capabilities and for the guidance throughout these years. I thank my co-supervisor Wiebke Markussen for her support. Special thanks go to my co-supervisor Martin Kærn, who has spent many precious hours to assist me. His help has been fundamental to the completion of this work. My sincere gratitude goes also to my co-supervisor Lars Reinholdt, from whom this project has originated.

I am sincerely grateful to Thomas Rønnow and Rasmus Toftegaard from COTES, and Ebbe Nørgaard from DryingMate. Collaborating with them has been a precious experience, that made me appreciate their strong open mindedness and sense for innovation.

My time at DTU and in Denmark would not have been the same without my office mates Erasmus and Torben, my Italian friends Andrea, Danilo, Leonardo, Angelo, Adriano, Roberta, Simone, Davide, Andrea Meroni, Enrico, Valentina, Paride, Alberto, as well as Tuong-Van, Jorrit, Jonas, Jesper and Jonatan. It is important to me to express my most profound gratitude to Andrea for all the good laughs we have had, for his support and compassion, and for all the experiences we have shared. His friendship is invaluable to me.

I also want to thank Mark Goldsworthy, who has assisted me during my external stay at CSIRO in Australia, and has given me important tools for completing this work. My external stay in Australia has been an amazing experience, and I always remember with great affection the people I met. I am very happy to share so many nice memories with Sergio, Stefano, Magda, Simona and Annette.

At last, my most special thanks go to my mother Lorella, my father Luciano, and my brother Edoardo for the love, support and encouragement they have always given me. My achievements would not have been possible without them.

Abstract

The demand for air conditioning has been consistently increasing worldwide in recent years, concomitantly to the introduction of ambitious energy and environmental targets. As a result, high efficiency air conditioners running on low polluting energy sources need to be developed. This thesis investigates the performance of a solid desiccant cooling system implementing indirect evaporative cooling processes. The aim is to quantify the system thermal and electrical performance for varying component dimensions and operating conditions, and to identify its range of applicability. This information serves to support the industrial development of the system. Ultimately, the aim is to understand if and to which extent the system is more efficient than electrically and thermally driven chiller-based systems.

The core system components are a silica gel desiccant wheel and a counter-flow indirect evaporative cooler. Detailed steady state numerical models are developed and implemented in MATLAB. The models need to be accurate and require low computational effort, for analysing the internal heat and mass transfer processes, as well as carrying out repetitive design and optimization simulations and seasonal simulations.

The desiccant wheel model is based on the parabolic moisture concentration profile assumption, which enables to consider the resistance to moisture diffusion in the desiccant pores while keeping a low computational effort. The comparison with a validated transient model indicates the parabolic profile assumption is very accurate for wheel rotational speeds up to 20 rph, considering silica gel properties and typical desiccant layer thickness.

The indirect evaporative cooler model is tuned to predict the performance of coolers manufactured by StatiqCooling, according to the manufacturer selection software. Different compositions of the secondary air stream are considered, including partial recirculation of the cooled primary air stream, i.e. dew point cooling, and use of air from a separate ambient.

The desiccant cooling system combines the two components, including a compact air-to-air heat exchanger for enhancing cooling capacity and thermal performance. The system performance is investigated considering regeneration temperatures between 50°C and 90°C, which enable low temperature heat sources, such as solar energy or waste heat, to be used. The effects of several geometrical and operational parameters on the system thermal and electrical performance, supply conditions, and water consumption are investigated. The use of exhaust air from the conditioned space for indirect evaporative cooling provides the most promising results, with thermal COP above 1 and electrical COP above 20. These results indicate the system has a great potential for saving energy in respect to electrically and thermally driven chiller-based system.

An exergy analysis is carried out to identify the most important sources of irreversibility in the system, including the conversion of primary energy sources into heat and electricity. Results indicate that solar energy is utilized more efficiently than fossil fuels for supplying low regeneration temperatures.
In the end, a novel technical solution aiming to make desiccant cooling systems independent of external water sources is introduced. Water desorbed from the desiccant dehumidifier is condensed in a closed regeneration circuit and used to run evaporative coolers. This solution enables the system to run regardless of water availability, and avoids the use of water demineralization equipment, which consumes additional water and increases operational costs and maintenance. These benefits are achieved at the expense of higher electricity consumption, regeneration temperatures, space requirements and investment costs. The solution is analysed for the desiccant cooling system operating with dew point cooling. Mediterranean climatic conditions are considered for seasonal system simulations, with the possibility to store water recovered in excess for operating the system with open regeneration circuit in case of high loads. The system is found independent of external water sources.

Resumé

Behovet for luftkonditionering har været støt stigende i de seneste år, sideløbende med at der er blevet indført ambitiøse energi- og klimamål. Som et resultat af dette er der opstået et behov for udviklingen af energieffektive luftkonditioneringsanlæg, der drives af energikilder med ene lav miljøpåvirkning. I denne afhandling analyseres et tørrende køleanlæg, der benytter indirekte fordampningskøling. Formålet er at kvantificere systemets termiske og elektriske ydeevne for varierende dimensioner og driftsforhold samt at identificere mulige anvendelsesområder. Resultaterne skal understøtte den industrielle udvikling af denne type anlæg. Endelig er formålet at undersøge om og til hvilken grad systemet er mere energieffektiv end elektricitets- og varmedrevne chiller-løsninger. Hovedkomponenterne i systemet er et silica gel tørrehjul og en indirekte modstrømsfordampningskøler. Der er blevet udviklet detaljerede steady-state modeller af disse komponenter, som er blevet implementeret i Matlab. Det var et krav til modellerne, at de er nøjagtige, men samtidig kræver korte beregningstider for at kunne analysere de interne varme- og massetransportprocesser, gennemføre gentagne simuleringer til designoptimering og køre simuleringer i forhold til årsvariationer. Modellen af tørrehjulet er baseret på en antagelse om parabolsk fugtkoncentration i det tørrende materiale, hvilket betyder at der tages hensyn til modstanden mod diffusion af fugten samtidig med at beregningstiderne holdes korte. En sammenligning af modellen med en valideret transient model viser at antagelsen om det parabolske profil er meget god for rotationshastigheder op til 20 rpm for typiske tykkelser af det tørrende materiale og ved brug af silica gel som det tørrende materiale. Modellen for den indirekte fordampningskøler er blevet tilpasset således at den forudsiger ydelsen af fordampningskølere af fabrikatet StaticCooling i overensstemmelse med producentens udvælgelsessoftware. Forskellige sammensætninger af den sekundære luftstrøm er blevet undersøgt. Disse inkluderer delvis recirkulering af den kølede primære luftstrøm, dvs. dugpunktskøling, samt brugen af luft fra andre omgivelser. I det samlede tørrende køleanlæg kombineres de to komponenter sammen med en kompakt luft-luft varmeveksler for at øge systemets kølekapacitet og effektivitet. Systemets ydeevne analyseres for genvindingstemperaturer i tørrehjulet på mellem 50°C og 90°C, hvilket muliggør brugen af lavtemperatur varmekilder som solvarme eller overskudsvarme. Effekten af variationen af forskellige parametre for geometri og driftsbetingelser på anlæggets termiske og elektriske ydeevne er blevet undersøgt. Brugen af afkastluften fra det konditionerede rum til den indirekte fordampningskøling viste de mest lovende resultater med en termisk COP over 1 og en elektrisk COP på over 20. Disse resultater indikerer at systemet har et stort potentiale for energibesparelser i forhold til konventionelle elektricitets- og varmedrevne chiller-løsninger. En exergianalyse af systemet

er blevet lavet for at identificere de vigtigste irreversibiliteter. Konverteringen af primær energi til varme og elektricitet indgår i denne analyse. Resultaterne viser at solenergi bruges mere effektivt end fossile brændstoffer, når der skal bruges lave genvindingstemperaturer. Endeligt introduceres en ny teknisk løsning, der stiler efter at gøre tørrende køleanlæg uafhængig af eksterne vandkilder. Vandet, som er desorberet fra tørrehjulet, kondenseres i et lukket kredsløb og anvendes i fordampningskøleren. Denne løsning gør det muligt for systemet at operere, uden at vand ellers er tilgængeligt fra anden kilde. Samtidig er det med denne konfiguration ikke nødvendigt at anvende vandbehandlingsudstyr for at demineralisere vandet, en process, der har et yderligere vandforbrug og øger omkostningerne til drift og vedligehold. Fordelene opnås på bekostning af et højere elforbrug, en højere genvindingstemperatur i tørrehjulet, øget pladsbehov og højere investeringsomkostninger. Årssimuleringer er lavet for Middelhavs-klima for et system med mulighed for at lagre overskydende vand fra regenerering og med mulighed for at køre systemet med åben regenereringskreds ved høje belastninger. Resultaterne viser at systemet kan køres uafhængigt af vand fra eksterne kilder.

List of publications

Journal papers

[1] Bellemo, L., Elmegaard, B., Markussen, W.B., Reinholdt, L.O., 2015. Formulation and validation of a two-dimensional steady-state model of desiccant wheels. Science and Technology for the Built Environment 21 (3), pp. 300-311.

Conference papers

[2] Bellemo, L., Elmegaard, B., Markussen, W.B., Reinholdt, L.O., Jakobsen, A., 2013. Modelling and analysis of a desiccant cooling system using the regenerative indirect evaporative cooling process. Proceedings of ECOS 2013 - the 26th International Conference on Efficiency, Cost, Optimization, Simulation and Environmental Impact of Energy Systems. Guilin, China.

[3] Bellemo, L., Elmegaard, B., Markussen, W.B., Reinholdt, L.O., 2013. Modelling of a regenerative indirect evaporative cooler for a desiccant cooling system. Proceedings of TPTPR 2013 - the 4th IIR Conference on Thermophysical Properties and Transfer Processes of Refrigerants. Delft, The Netherlands.

[4] Bellemo, L., Elmegaard, B., Markussen, W.B., Reinholdt, L.O., 2014. Steady state modeling of desiccant wheels. Proceedings of ISHPC 2014 - the 14th International Sorption Heat Pump Conference. Washington, USA.

[5] Bellemo, L., Elmegaard, B., Markussen, W.B., Reinholdt, L.O., 2015. Desiccant dew-point cooling system independent of external water sources. Proceedings of ICR 2015 - the 24th IIR International Congress of Refrigeration. Yokohama, Japan.

[6] Bellemo, L., Elmegaard, B., Markussen, W.B., Reinholdt, L.O., 2015. Applicability of a desiccant dew-point cooling system independent of external water sources. Proceedings of SAC 2015 - the 6th International Conference on Solar Air-Conditioning. Rome, Italy.

Others

[7] Bellemo, L., 2014. Review and modelling of solar air collectors for solar air-conditioning. CSIRO Energy Centre Internal Technical Report, pp. 88. Newcastle, Australia.

Contents

Preface **5**

Acknowledgements **7**

Abstract (English/Dansk) **9**

Papers and Presentations **13**

Contents **16**

Nomenclature **22**

1 Introduction **1**
1.1 Background 1
1.2 Motivation 3
1.3 Literature review 4
1.4 Statement 6
1.5 Methods 7

2 Desiccant wheel model **11**
2.1 Introduction 11
2.2 Model formulation 15
2.3 Results and discussion 24
2.4 Conclusions 41

3 Indirect evaporative cooler model **43**
3.1 Introduction 43
3.2 Model formulation 48
3.3 Results and discussion 55
3.4 Conclusions 72

4 System design and operation **73**
4.1 System design 73
4.2 System model formulation 74
4.3 Results 77
4.4 Discussion 99

4.5 Conclusions 100

5 Exergy Analysis **103**
5.1 Introduction 103
5.2 Methods 104
5.3 Results and discussion 108
5.4 Conclusions 113

6 Independence of external water sources **115**
6.1 Introduction 115
6.2 DDC-DWR system analysis 119
6.3 Case study - applicability in the Mediterranean climate 133
6.4 Conclusions 143

7 Concluding remarks **147**
7.1 Discussion 147
7.2 Conclusions 149
7.3 Recommendations for future work 150

Bibliography **151**

A Desiccant wheel model numerical implementation **159**

B Silica gel properties **165**

C Indirect evaporative cooler model numerical implementation **169**

Nomenclature

Abbreviations

BF	by-pass factor
CAC	condensation air cooler
COP	coefficient of performance
CV	control volume
DDC	desiccant dew-point cooling
DEC	direct evaporative cooler
DIEC	desiccant indirect evaporative cooling
DPC	dew point cooler
DW	desiccant wheel
DWR	desorbed water recovery
GSR	gas side resistance
GSSR	gas ans solid side resistance
HEX	heat exchanger
HHV	higher heating value
HIEC	hybrid indirect evaporative cooler
HR	heat recovery
IEC	indirect evaporative cooler
IHRU	internal heat recovery unit
LHV	lower heating value
M-cycle	Maisotsenko cycle

MRC	moisture removal capacity
MSEC	minimum specific electricity consumption
MSWC	minimum specific water consumption
NTU	number of transfer units
PCP	parabolic concentration profile
PGS	pseudo gas side resistance
RD	regular density
RH	regeneration heater
RHSI	regeneration specific heat input
SHR	sensible heat ratio
SSR	solid side resistance

Greek letters

α	convective heat transfer coefficient [W m^{-2} K^{-1}]
Δ	absolute variation [-]
ϵ	effectiveness [-]
η	efficiency [-]
ρ	density [kg m^{-3}]
σ	convective mass transfer coefficient [kg s^{-1}]
θ	circumferential coordinate [m]
φ	relative humidity [-]
ζ	pore tortuosity [-]

Roman letters

$\dot{C}$	heat capacity rate [W K^{-1}]
$\dot{E}$	exergy flow [W]
$\dot{m}$	mass flow rate [kg s^{-1}]
$\dot{Q}$	heat flow [m]
$\dot{V}$	volume flow rate [m^3 s^{-1}]

$\dot{W}$	power [W]
Le	Lewis number [-]
Nu	Nusselt number [-]
Re	Reynolds number [-]
th	thickness [m]
A	area [m^2]
a	sinusoidal channel height [m]
b	sinusoidal channel width [m]
C_1	first parabolic concentration profile geometrical parameter [-]
C_2	second parabolic concentration profile geometrical parameter [-]
c_p	specific heat capacity [J kg^{-1} K^{-1})]
c	solid layer thickness [m]
D_{eff}	effective diffusivity [m^2 s^{-1}]
D_h	hydraulic diameter [m]
D_K	Knudsen diffusivity [m^2 s^{-1}]
D_O	ordinary diffusivity [m^2 s^{-1}]
D_s	surface diffusivity [m^2 s^{-1}]
D	diameter [m]
e	specific exergy [J kg^{-1}]
f_f	friction factor [-]
f_{des}	desiccant fraction [-]
f_{ext}	external fraction [-]
f_{rec}	recirculation fraction [-]
f_{reg}	regeneration fraction [-]
f_{sec}	secondary fraction [-]
f_{wr}	water recovery fraction [-]
f_h	enthalpy fraction [-]

Nomenclature

h_{ads}	heat of adsorption [J kg^{-1}]
h_{fg}	latent heat of vaporization [J kg^{-1}]
H	height [m]
h	specific enthalpy [J kg^{-1}]
k	thermal conductivity [W m^{-1} K^{-1}]
L	length [m]
N_p	number of plates [-]
N_θ	number of control volumes along the circumferential direction [-]
N_z	number of control volumes along the axial direction [-]
N	rotational speed [rph]
P	perimeter [m]
p	pressure [Pa]
R	specific gas constant [J kg^{-1} K^{-1}]
S	desiccant wheel process to total face area ratio [-]
s	entropy [J kg^{-1} K^{-1}]
T	temperature [K] or [°C]
U	overall heat transfer coefficient [W m^{-2} K^{-1}]
u	velocity [m s^{-1}]
W	desiccant specific water content [kg$_w$ kg$_d^{-1}$]
x	humidity ratio [kg$_v$ kg$_a^{-1}$]
z	axial coordinate [m]

Subscripts

chan	channel
coll	collector
cool	cooling or coolant
des	destruction
dp	dew point

el	electrical
eq	equilibrium or equivalent
ext	external
ex	exergy
ha	humid air
ht	heat transfer
lat	latent
mt	mass transfer
nom	nominal
rec	recirculation
ref	reference
sat	saturation
sec	secondary
sens	sensible
sup	supply
surf	surface
th	thermal
tot	total
wb	wet bulb
wp	primary side wall
ws	secondary side wall
a	air
d	desiccant
i	inlet
m	material
o	outlet
p	process or primary

r or reg	regeneration
s	secondary
s	solid
v	water vapour
w	liquid water

1 Introduction

1.1 Background

Climate change, energy security, population growth and improvement of life standards are key factors driving today's energy policies.
By 2020, the European Union is aiming to reduce greenhouse gas emissions by 20% in respect to 1990 levels, decrease the total energy consumption by 20% in respect to a reference projection, and increase the share of energy production from renewable sources to cover 20% of the total final energy demand. In the longer run, by 2050, the European Union aims to reduce greenhouse gas emissions by at least 80% in respect to 1990 levels.
Substantial changes in the production, storage and utilization of energy are needed, improving existing technologies and developing more efficient and cleaner technologies.
European 2010 energy statistics indicate that heating and cooling for the residential, commercial and industrial sectors were responsible for half of the primary energy utilization [1]. On a global scale, energy consumption in buildings accounts for more than 40% of primary energy use and 24% of greenhouse gas emissions [2]. In residential and commercial buildings, space heating and air conditioning are responsible for most of the energy consumption.
In the last decades, the air conditioning market has been constantly increasing worldwide. In Europe, the number of installed air conditioning units in 2010 has been estimated around 60 millions, approximately 24 times more than in 1990, with a steady increase rate of approximately 2 million units/year from 2005 to 2010 [1]. This tremendous increase is mainly caused by the increase of room air conditioning units, particularly in the residential sector, rather than the increase of centralized air conditioning units. However, while room units account for more than 90% of all installed units, centralized units account for more than 50% of the total installed capacity, as their average installed capacity is 104 kW/unit instead of 6 kW/unit for room units [1]. The corresponding European total electricity consumption from air conditioners in 2010 has been estimated around 150 TWh, approximately 600% higher than in 1990 [1].
Today's air conditioning market is still dominated by the mechanical vapour compression cycle, characterized by stable performance and relatively low investment costs. Conventional

air conditioning systems, based on this technology, consume electricity primarily for vapour compression, and secondarily for heat rejection and mechanical air circulation. Alternative absorption and adsorption cycles have gained attention in the last decades, as they are heat-driven technologies with no vapour compression.
All of the above mentioned cycles are closed, and so they are cooling-based dehumidification technologies, i.e. they cool air below its dew point to remove moisture. Consequently, in order to cover latent loads, these technologies cool the air more than needed for covering sensible loads, requiring an additional re-heating process.
In common practise, the stong coupling between sensible and latent loads leads to operate cooling-based dehumification systems with indoor temperature control only, with no direct indoor humidity control [3].
Indoor humidity control is important for maintaining human comfort and productivity, avoiding mould and condensate formation, and minimizing the growth of biological contaminants. Brandemuehl [3] highlighted some key factors that, over the last decades, have increased the problem of inadequate humidity control by means of cooling-based dehumidification systems:

- Increasing ventilation requirements by indoor air quality standards have increased the load on air conditioning systems, resulting in bulkier systems and higher energy consumptions. Particularly, increasing ventilation requirements increase latent loads on the system more than sensible loads, which is critical for cooling-based dehumidification systems that handle these loads simultaneously.
- The use of better insulated buildings and more efficient lighting systems have reduced indoor sensible loads, increasing the influence of latent loads for determining the size and energy consumption of air conditioning systems.

Desiccant cooling systems are an alternative heat-driven technology to cooling-based dehumidification systems. There are several reasons making desiccant cooling systems an attractive solution [4–8]:

- Latent and sensible loads are handled separately, allowing to achieve an accurate humidity control. Latent loads are handled by desiccant dehumidifiers, which require heat for regeneration, while sensible loads are handled by evaporative coolers.
- Regeneration of desiccant materials can be achieved by means of low temperature thermal energy, such as waste heat or renewable energy sources, with particular interest for solar energy.
- Evaporative coolers use water as refrigerant, which is not harmful nor polluting.
- Desiccant materials are effective and economical for dehumidification.
- Air can be dehumidified to extremely low dew points, as low as -40°C, with no freezing problems.

- Desiccant materials have an air cleaning potential, which can improve indoor air quality. Alternatively, desiccant cooling systems could recirculate more air from the conditioned space than conventional systems, resulting into lower sensible and latent loads on the system, for reaching the same indoor air quality in terms of ventilation requirements.

Solid desiccant materials are often preferred to liquid desiccants as they require lower levels of maintenance, particularly because of no corrosion problems.
Desiccant cooling systems are of particular interest in commercial applications, such as office buildings, supermarkets, museums, libraries, hotels, art galleries, pharmaceutical clean-rooms, electronics manufacturing facilities, indoor swimming pools, etc., where centralized units providing high ventilation rates are generally employed [5].
The interest in the use of solar energy for heat-driven air conditioning systems is continuously growing, with fundamental contributions from the IEA Solar Heating and Cooling Program, which aims to help reaching the target of 50% coverage of low temperature heating and cooling demand by solar thermal energy by 2050 [2].
The fact that solar energy can reduce the use of polluting and limited sources, does not directly imply that desiccant cooling systems can lead to energy savings only in regions with high availability of solar energy. In Europe, high energy savings can as well be achieved in the Nordic countries [9], which are characterized by lower solar energy availability but also lower latent loads.

1.2 Motivation

Even though the potential advantages of solid desiccant cooling systems are clear, the lack of knowledge on optimal system design and operation is one of the biggest limitations to their deployment [6]. Research, development and demonstration activities are therefore essential to make desiccant cooling systems truly competitive.

The coupling of desiccant dehumidifiers and indirect evaporative coolers have gained attention in the last decade, particularly because of recent developments in indirect evaporative cooling technology. The author carried out a master's thesis on a novel desiccant cooling system implementing the regenerative indirect evaporative cooling process [10], also termed dew point cooling, confirming the potential for reducing electricity consumption and emissions in respect to conventional air conditioning systems.

In 2012, on the basis of these promising results, the Danish R&D program ELFORSK decided to fund the present PhD research project for improving the technology and supporting the industrial development of an efficient solid desiccant cooling system in collaboration with the Danish Technological Institute (DTI), the Danish supplier of desiccant-based drying systems COTES, the Danish consultant company OBH-Group, and a Danish installer of ventilation

systems.

1.3 Literature review

The first solid desiccant cooling cycle was introduced by Pennington in the 1950s [11], contemporarily to the development of the first desiccant wheels. This first cycle was meant to dry and cool a stream of fresh air, and therefore it is often referred to as ventilation cycle in the literature [5]. It consists of a Desiccant Wheel (DW), a Regeneration Heater (RH), a Thermal Wheel (TW), and two Direct Evaporative Coolers (DEC). The cycle schematics and typical operation are illustrated in Figure 1.1.

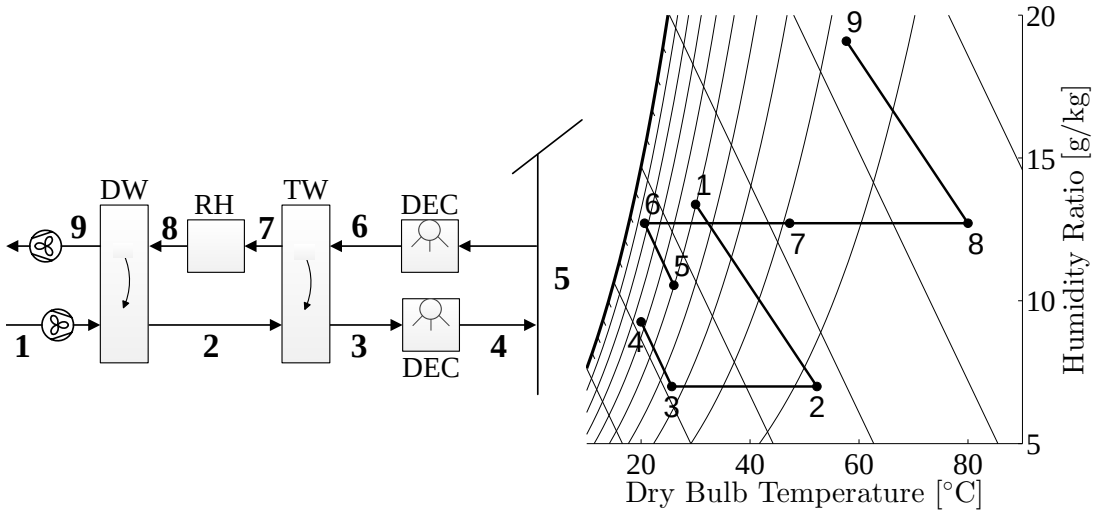

Figure 1.1: Pennington cycle schematics and psychrometric processes.

Fresh process air is dried and heated in the DW (1-2), pre-cooled cooled in the TW (2-3), and adiabatically cooled in the DEC (3-4). Exhaust indoor air is adiabatically cooled in another DEC (5-6), pre-heated in the TW (6-7), and successively heated in the RH by a selected heat source (7-8) for regenerating the DW (8-9).
The Pennington cycle has some distinguishing characteristics:

- The system dehumidification capacity needs to be high in order to supply cool and dry air, due to the use of direct evaporative cooling.
- Humidity control is limited because of the trade-off between supply temperature and supply humidity content, again due to the use of direct evaporative cooling.
- The thermal wheel is necessary for the system operation, and its effectiveness is critical to the system performance.

Extensive research has been carried out on this system configuration. Experimental studies

[12–14] reported system thermal COP varying between 0.28 and 0.78, with an important dependence on outdoor conditions, regeneration temperature, and component effectiveness. A thermal COP of 0.8 has been obtained with numerical simulations for varying component effectiveness [15]. The recirculation of exhaust air from the conditioned space to obtain the process air stream, while using outdoor air to obtain the regeneration air stream, provides analogous performance to the ventilation cycle [16].

Maclaine-Cross [17] proposed an advanced cycle, the SENS cycle, by adding an additional thermal wheel and a cooling coil fed by a cooling tower for replacing direct evaporative cooling. Partial recirculation of exhaust air from the conditioned space was also adopted for lowering the load on the system, still supplying enough fresh air. Numerical simulations of the SENS cycle estimated a thermal COP above 2, and a thermal COP of 2.45 was obtained experimentally under standard conditions [16]. However, the complexity of the cycle discouraged its use.

Similar but less complex systems were proposed by removing one of the two thermal wheels, resulting in the SENC and REVERS cycles [17], which differ because of the regeneration air source. Experimental investigations of the SENC cycle [18] resulted in a thermal COP between 0.6 and 2 with regeneration temperatures between 50°C and 90°C.

The combination of direct and indirect evaporative cooling was used in the DINC cycle proposed by Waugaman [19], further reducing the system complexity in comparison to the SENC and REVERS cycles. The DINC cycle modifies the original ventilation cycle by adding an indirect evaporative cooler in front of the process direct evaporative cooler, with secondary air coming from the conditioned space exhaust, and regeneration air taken from the outdoor ambient with no direct evaporative cooling. Investigations of the system performance indicated a thermal COP between 0.6 and 2.16.

More recently, Goldsworthy and White [20] have investigated numerically the potential of a simple configuration constituted by a desiccant wheel and a regenerative indirect evaporative cooler. The resulting thermal COP was below 1 and the electrical COP above 20, with 70°C regeneration temperature. The electrical COP was identified as the critical economic and environmental justification for installing a desiccant cooling system, driven by solar energy or other cheap and clean sources, instead of conventional electrically driven air conditioners.

The use of efficient regenerative indirect evaporative coolers based on the Maisotsenko cycle has been considered to further improve desiccant cooling system performance [21]. A potential operational cost reduction of approximately 60% in comparison to conventional air conditioners was estimated [22].

Another solution for improving the thermal performance of desiccant cooling systems is the isothermal dehumidification process [23], which constists in dividing the dehumidification process into multiple stages with inter-cooling. As a result, the regeneration temperature requirements are reduced and the system dehumidification capacity is increased, which is of particular interest in humid climates. Ge et al. [24, 25] introduced and investigated two different types of two-stage dehumidification systems, either with two desiccant wheels, TSDC system, or with a single wheel divided into quadrants, OTSDC system. Both systems can achieve thermal COP above 1 at low regeneration temperatures, around 16% more than with a single wheel providing a single dehumidification stage. The TSDC system was found capable

of reducing significantly the regeneration temperature for achieving the same level of dehumidification, e.g. a reduction from 100°C to 70°C was reported for removing 6 g/kg of moisture under standard summer conditions. On the other hand, the OTSDC system is characterized by smaller space requirements.
The coupling of desiccant cooling and traditional vapour compression or absorption machines into hybrid systems has also been investigated in several studies [26–31]. The use of desiccants for covering latent loads increases the efficiency of cooling-based dehumdification technologies as they handle sensible loads only. The integration of desiccant and vapour compression machines have shown reductions of the required evaporator cooling capacity between 35 and 50% [29, 31], as well as reductions of compressor power consumption between 50 and 70% [27], increasing the vapour compression cycle COP of approximately 40% [28, 30].
Another solution of interest is ceiling radiant cooling, which has potential for reducing energy consumption and improving thermal comfort and indoor condition control in comparison to conventional air conditioners [5]. Radiant cooling systems cover the majority of the indoor sensible load by means of chilled water circulating into radiant panels installed in the ceiling. A separate ventilation system is required for supplying fresh air. Low indoor humidity contents are essential for covering indoor latent loads as well as avoiding condensation on the cold ceiling, making desiccant cooling systems an attractive solution. Niu et al. [32] have estimated energy savings up to 44% by using a desiccant-assisted radiant cooling system instead of a conventional air conditioning system.

1.4 Statement

The focus of the present PhD research project is to analyse the performance a solid desiccant cooling system implementing indirect evaporative cooling processes. Results will serve to support a parallel industrial development project, and the successive system demonstration.

The fundamental question that this thesis seeks to answer is "*How can the thermal and electrical system performance be enhanced in order to maximize the competitiveness over cooling-based dehumidification technologies?*".

For answering this question, the objectives of this thesis are:

- Development and validation of a detailed desiccant wheel model for design, optimization and simulation of operation.
- Development and validation of a detailed indirect evaporative cooler model for design, optimization and simulation of operation.
- Identification of key performance indicators at component and system levels.
- Understanding the effects of geometrical and operational parameters at component and system levels.

- Identification of optimal system design and operation.
- Identification of limits of operation depending on climatic conditions and supply requirements.
- Proposal of solutions for improving the applicability and performance of the system.

1.5 Methods

The present work is based on the numerical modelling of the core components constituting the considered desiccant cooling system, namely a silica gel desiccant wheel and a counter-flow indirect evaporative cooler. The development of these models constitute a significant part of the work. System of equations are formulated for describing the heat and mass transfer processes in both components, and solved by means of finite difference methods. The models compute the component steady state operations, providing meaningful results in terms of system performance and capability, but not being suitable for simulating intermittent system operation, which exceeds the scope of this thesis. The models are built and implemented to obtain low computational effort and high accuracy, resulting into powerful tools for repetitive design simulations, optimizations, and simulations across long periods of time on an hourly basis. A limited amount of experimental work has been carried out during this project. Hence, the models are verified and proved accurate by means of validated models and manufacturer data. A validated desiccant wheel model has been provided by Mark Goldsworthy from the Australian CSIRO Energy Centre, while indirect evaporative cooler performance data have been obtained from the manufacturer StatiqCooling simulation software that is built based on test results. All models are implemented in MATLAB, which is used to carry out both component and system simulations. Engineering Equation Solver (EES) is also used for preliminary investigations by means of simplified models. Details on the numerical models and other methods used for the energy and exergy analyses are reported in the following chapters and appendices.

1.5.1 Outline

The present thesis is constituted of 7 chapters, following the structure illustrated in Figure 1.2.

Chapter 1 introduces the project, along with motivation, literature review, statement and outline.

Chapter 2 includes an introduction to desiccant wheel dehumidifiers, reports the formulation, tuning and validation of a 2D steady state numerical model, and ultimately presents a study on the effects of varying geometrical parameters and operating conditions on the wheel performance.

Chapter 3 includes an introduction to indirect evaporative coolers, reports the formulation,

tuning and validation of a 1D steady state numerical model, and ultimately presents a study on the effects of varying geometrical parameters and operating conditions on the indirect evaporative cooler performance considering different modes of operation.

Chapter 4 introduces the complete solid desiccant cooling system, and presents a comprehensive analysis by comparing different system configurations on the basis of attainable supply conditions, thermal performance, electrical performance and water consumption.

Chapter 5 presents an exergy analysis of the desiccant cooling systems considering different system configurations, influence of regeneration temperature, and comparison with electric chillers in the terms of primary energy consumption including the use of solar energy.

Chapter 6 introduces a novel technical solution for making desiccant cooling systems independent of external water sources, and investigates its characteristics when applied to the desiccant cooling system with dew point cooling, ultimately presenting the results of seasonal simulations in the Mediterranean climate to prove water independence.

Chapter 7 concludes the work, including a discussion of main results, fundamental conclusions, and suggestions for future work.

The thesis contains also 3 appendices:

Appendix A reports the numerical finite difference method adopted to solve the desiccant wheel model and its implementation in MATLAB.

Appendix B reports the silica gel properties considered in the analysis.

Appendix C reports the numerical finite difference method adopted to solve the indirect evaporative cooler model and its implementation in MATLAB.

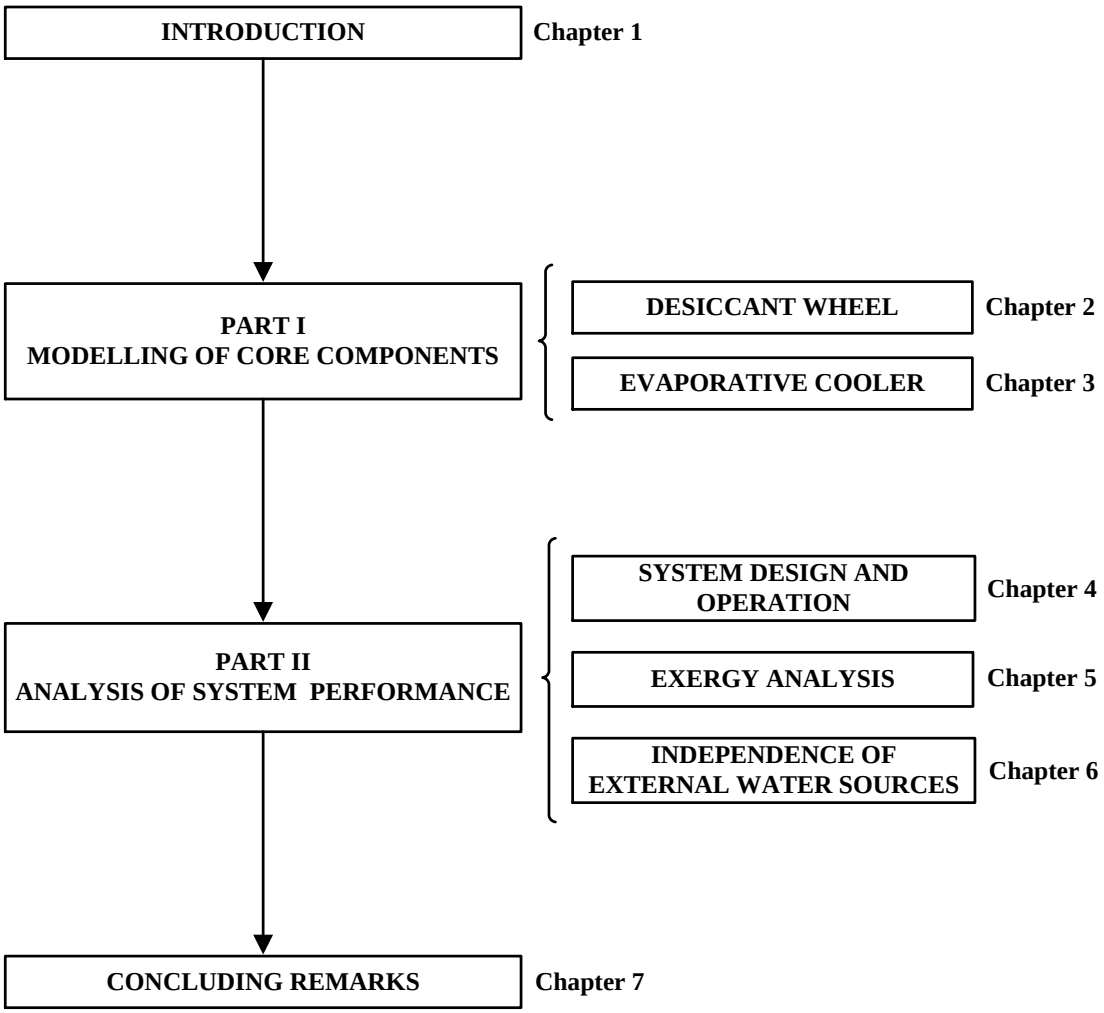

Figure 1.2: Thesis structure.

2 Desiccant wheel model

2.1 Introduction

Desiccant wheels are dehumidifiers employed in various applications, such as air conditioning and drying processes.
A schematic representation of the principle of operation for a generic desiccant wheel is reported in Figure 2.1.

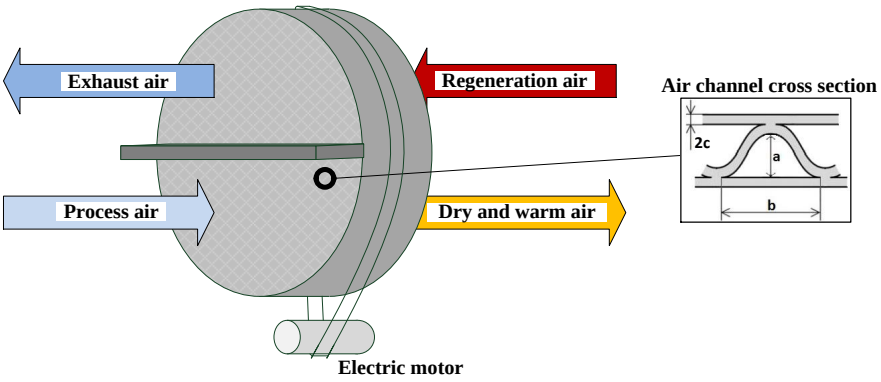

Figure 2.1: Schematics of a desiccant wheel.

The wheel is constituted by a large amount of small channels (hydraulic diameter ~2 mm) aligned lengthwise. Details of the cross section of a typical sinusoidal shaped air channel are also shown in Figure 2.1. The channels are delimited by solid walls that contain a desiccant material impregnated onto a support structure. The wheel is mounted on a shaft and rotated by an electric motor and belt drive system.
The process air stream is dehumidified flowing across a part of the wheel, termed process section, while the regeneration air stream flows typically from the opposite direction across the remaining part of the wheel, termed regeneration section. Typically, the ratio of process to total wheel face area is in the range 50-75%. The air streams flow across the channels with velocities in the range 1-5 m/s, resulting in laminar flows.

Dehumidification takes place by means of adsorption of water vapour molecules onto the desiccant surface and subsequent diffusion into the desiccant pores. The driving potential for adsorption and desorption is the water vapour partial pressure difference between the air in the stream bulk and the air in contact with the desiccant surface. The specific desiccant sorption characteristics determine the water vapour partial pressure at the surface. Heat of adsorption is released at the desiccant surface as water vapour molecules get bound onto it. Subsequently the process air stream is simultaneously dried and heated. The potential for adsorption decreases as more water is bound on the desiccant surface. The desiccant is regenerated, i.e. water vapour molecules are desorbed from the desiccant surface, by the regeneration air stream that carries moisture away. Regeneration air enters the wheel at temperatures in the range 50-140°C, leaving colder and humidified. Continuous dehumidification of the process air stream is permitted by the wheel rotation, which continuously moves the desiccant material from the process to the regeneration section. Rotational speeds are relatively low, typically in the range 5-30 rph, allowing water vapour to diffuse into and out of the desiccant pores. Steady state operation can be reached under constant air inlet conditions and constant rotational speed.
Alternative wheel designs have been considered to improve the wheel performance [33], e.g. use of additional purge air streams, internal cooling during dehumidification, split of regeneration into multiple stages with different regeneration temperatures, and multiple dehumidification and regeneration stages.

The first desiccant wheels were developed by Pennington in the 1950s [11], employing highly adsorptive packed beds of lithium chloride (LiCl), which resulted in unstable and unsafe operation due to liquefation of LiCl at high moisture contents.
Jurinak [34] evaluated numerically the use of desiccant wheels in complete desiccant cooling systems, concluding that the added heat capacity due to adsorbed moisture reduces the system cooling capacity and that the heat of adsorption should be minimized. As an example, up to 50% of a silica gel wheel thermal capacity can be due to the adsorbed water under saturated conditions [33].
Collier et al. [35–37] studied the influence of desiccant properties on the cooling performance of desiccant cooling systems. Results highlighted a trade-off of these parameters to optimize the performance of the dehumidification and regeneration processes, and the importance of minimizing the wheel thermal capacity to improve the dehumidification performance.
A number of alternative desiccant materials has been investigated and developed in the past decades [7], with particular focus on increasing the equilibrium moisture capacity of new desiccants, such as composite desiccants (e.g. silica gel-LiCl [38] or hydratable salts like silica gel-$CaCl_2$ [39]), polymeric desiccants [40–42] and nano-porous inorganic desiccants. However the combination of thermal effects due to exothermic adsorption and carry over of heat from regeneration to process air are still key factors to improve the dehumidification performance, requiring minimization of the enthalpy of adsorption and wheel thermal capacity, which would otherwise overcome the benefits provided by increased equilibrium adsorption capaci-

ties [43].
As a result, silica gel still dominates the market of commercially available desiccant wheels for air conditioning due to its good dehumidification performance over a wide range of conditions and the need of more data about new materials. There exist a variety of types of silica gel, differentiated by their pore structure (pore size, specific surface and density) resulting into different dehumidification performance. Regular Density (RD) silica gel is typically employed, being characterized by a microporous structure with average pore radius of 11$\mathring{A}$. Pesaran [44, 45] investigated the influence of different diffusion mechanisms in silica gel particles, concluding that the importance of surface diffusion versus Knudsen diffusion vary significantly for different types of silica gel, due to different pore sizes. Surface diffusion is the dominant moisture diffusion mechanism in the pores of RD silica gel. The properties of RD silica gel, which is the desiccant material considered throughout this thesis, are reported in Appendix B.

The development of modelling approaches for simulating desiccant wheels is essential to investigate their integration in complete desiccant cooling systems as well as the effects of different desiccant materials. A comprehensive review of desiccant wheel models has been presented by Ge et al. [46], including both physical and empirical models. Apart from empirical models, which adopt fitted correlations of experimental results, physical models can be classified on the basis of the heat and mass transfer phenomena implemented.

- Gas-Side Resistance (GSR) models
- Gas and Solid-Side Resistance (GSSR) models
  - Pseudo Gas-Side (PGS) models
  - Solid-Side Resistance (SSR) models
  - Parabolic Concentration Profile (PCP) models

GSR models implement only the resistances to convective heat and mass transfer in the air stream, while GSSR models take into consideration also the resistances to mass diffusion and heat conduction in the desiccant layer. For this reason GSR models are characterized by lower computational effort but also lower accuracy.
PGS models maintain the low computational effort of GSR models with improved accuracy, as the resistances to mass diffusion and heat conduction are taken into account by modifying the convective heat and mass transfer resistances. Still PGS models do not allow to reproduce the operation of desiccant wheels with high accuracy as the nature of convective and diffusive transfer phenomena is different.
SSR models improve accuracy to a great extent by modelling the heat conduction and mass diffusion on the solid side. These models represent an essential tool for studying the heat and mass transfer phenomena inside desiccant wheels in detail [43], but are not well suited for repetitive simulations, due to the high computational effort.

PCP models simplify the computation of heat conduction and mass diffusion in the desiccant by imposing parabolic distribution profiles within the desiccant layer. The validity of the parabolic moisture concentration profile within desiccant particles has been investigated in previous studies [47, 48], showing it enables to capture the effects of moisture diffusion with good accuracy and limited computational effort. In the case of desiccant wheels, the assumption of parabolic moisture concentration profile within the desiccant was found in good agreement with experimental data at low and medium rotational speeds [48]. Therefore PCP models are particularly suitable for seasonal simulations and repetitive design/dimensioning simulations, also when the influence of different desiccant material properties has to be taken into account. More generally, different shaped profiles can be considered, but parabolic profiles represent a good trade-off between accuracy and complexity. The use of the higher order quartic moisture concentration profile was found to improve the agreement with experimental data [47, 48] particularly at high wheel rotational speeds at the expense of increased model complexity.

The complexity and non-linear nature of the coupled heat and mass diffusion equations require the use of numerical methods for solving the corresponding system of differential equations. Most of the existing models employ finite difference methods, while less employ finite volume and analogy methods [46].

Both transient and steady state models have been developed by several authors [46].
Transient models typically compute the variation of air and desiccant conditions along a single channel following its rotation, i.e. a control mass of solid (desiccant and support material) and a control volume of air flowing in the channel with varying inlet conditions according to the circumferential position in the wheel. The resulting system of partial differential equations describing heat and mass transfer between the air stream and the desiccant wall is discretized in space and integrated over time, reaching a steady state solution after some complete spins of the wheel.
Steady state models neglect the time-dependent terms in the system of partial differential equations and employ a full control volume approach by spatial discretization of the wheel, allowing for a faster computation of the steady state operation.

A two-dimensional GSR steady state model was formulated and validated at the early stages of the present research project [49]. Validation was carried out considering experimental data from the literature [50], also considering the influence of air entrance effects on the heat and mass transfer resistances. It was shown that the use of course discretizations allows to obtain convergence with computational times in the order of seconds. In comparison to experimental data from the literature, the model reproduces the correct variations of the process air outlet conditions for varying parameters, such as regeneration temperature, air velocity, channel length and rotational speed. However the model did not provide accurate process air outlet

conditions, presumably because of no resistance to moisture diffusion within the desiccant layer.
A measure of the relative magnitude of the gas-side convective resistances in comparison to the solid-side diffusive resistances is given by the dimensionless heat and mass transfer Biot numbers. Low Biot numbers indicate the gas-side resistance dominates over the solid-side resistance, and vice versa. Typical desiccant wheels are characterized by heat transfer Biot numbers much lower than 1, i.e. the solid-side resistance to heat conduction is negligible, and mass transfer Biot numbers in the order of 10, i.e. both solid-side and gas-side resistances are potentially important to moisture transfer [33].
The clear importance of including the resistance to moisture diffusion in the desiccant has motivated the development of an improved desiccant wheel model using the GSR model presented in [49] as a basis. The improved model is a two-dimensional steady state PCP model aiming to achieve better accuracy while keeping the computational effort low. The model is presented and analysed in the following. The benchmark for validation is a detailed SSR transient model developed and validated against experimental data by Mark Goldsworthy at the Energy Centre of the Australian Commonwealth Scientific and Industrial Research Organisation (CSIRO). The detailed SSR model was utilizied by Goldsworthy and White for relevant analyses on desiccant wheels as well as on complete systems [20, 33, 43].

2.2 Model formulation

2.2.1 Modelling approach

The two-dimensional control volume approach along the axial and circumferential directions is presented in Figure 2.2. The streams of humid air and solid matrix (that includes desiccant, support material and adsorbed water) crossing a generic control volume are also indicated. The conditions of these streams are constant during steady state operation.

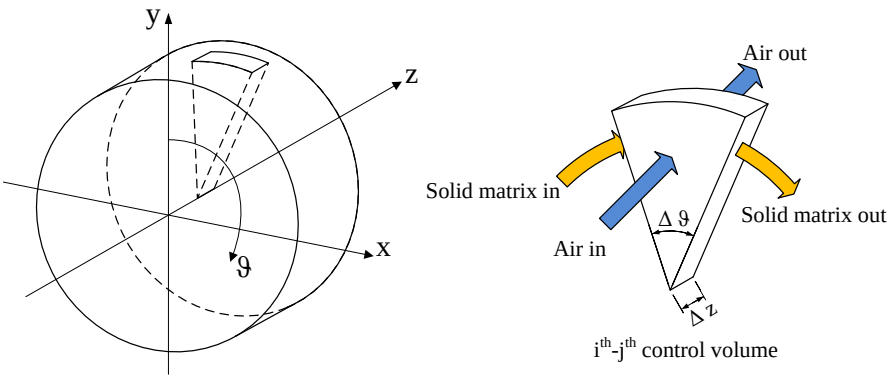

Figure 2.2: Schematics of the control volume approach.

The considered heat and mass transfer phenomena between the streams of humid air and solid are schematically represented in Figure 2.3 for the case of adsorption in a generic control

volume (the heat and moisture flows change direction during desorption). The scheme is simplified by representing the air and solid streams in counter-current arrangement, instead of cross-flow arrangement. The depth of the control volume represented in Figure 2.3 is such that the resulting transfer area is equivalent to the sum of the transfer areas of all air channels in the considered control volume. However, the geometry and airflow characteristics determining the heat and mass transfer processes refer to a single channel.

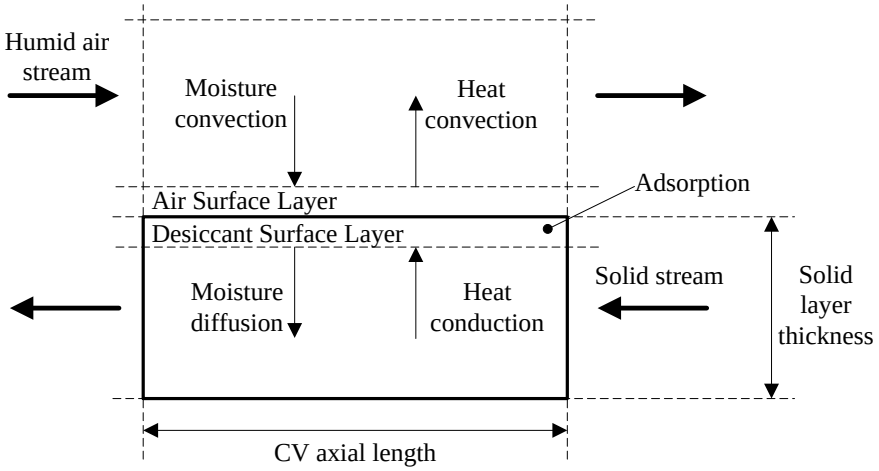

Figure 2.3: Schematics of the interaction between humid air and solid.

The resulting two-dimensional computational grid is shown in Figure 2.4 for a wheel with equal split between process and regeneration sections and an arbitrary number of control volumes in the axial direction N_z and circumferential direction N_θ. To simplify the representation, the circumferential length of the computational grid corresponds to the circumference with diameter equal to the wheel radius.

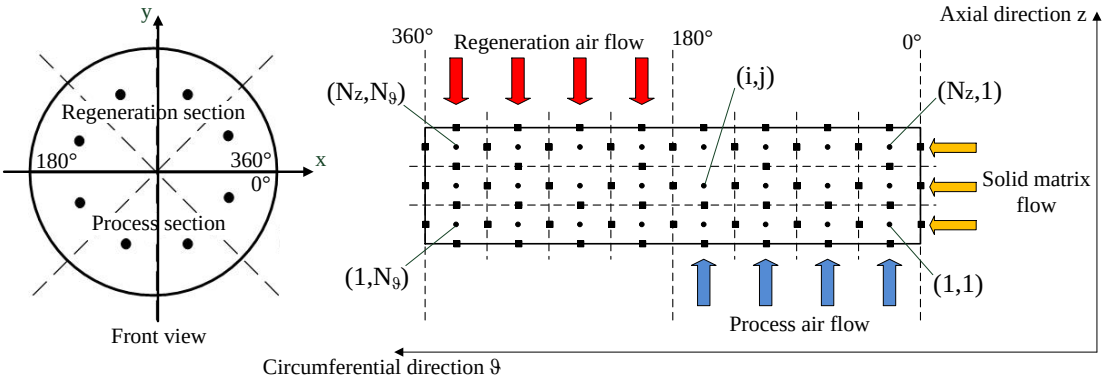

Figure 2.4: Two-dimensional computational grid.

2.2.2 Assumptions

The model is based on the following assumptions:

- The wheel does not exchange heat with the surroundings.
- Air infiltrations in the air streams are negligible.
- Air enters and exits the same CV, as the air velocity is much higher than the wheel rotational speed.
- All channels are identical and airflows are homogeneously distributed among channels.
- Heat and mass are not exchanged between adjacent channels.
- Air entrance effects are neglected.
- The desiccant material is uniformly distributed within the solid structure.
- The support material is not hygroscopic and does not interfere with moisture diffusion.
- Air and desiccant are in equilibrium at the desiccant surface.
- Thermal resistance to heat conduction in the solid layer is negligible.
- The heat of adsorption generated at the surface is entirely transferred to the solid.
- The moisture concentration profile across the solid layer is parabolic.
- Heat conduction and mass diffusion in the air stream are neglected along all directions.
- Heat conduction and mass diffusion in the solid are neglected along the axial direction.
- Temperatures and humidity contents among channels placed along the wheel radial direction are constant.
- Possible condensation of water vapour in the regeneration section is not considered.

The validity of neglecting the abovementioned heat and mass transfer phenomena was confirmed in previous studies by Goldsworthy and White [33, 43].

Under these assumptions, the inputs required by the model are:

- Geometrical characteristics including wheel diameter (D), air channel length (L), process to total face area ratio (S), active face area fraction (accounting for shaft, sealing, etc.), channel cross sectional dimensions (as shown in Figure 2.1), positioning and dimensions of eventual additional sections (e.g. purge sections).

- Wheel rotational speed (N).
- Solid (desiccant and support material) characteristics including desiccant bulk density (ρ), desiccant fraction, specific heat capacity (c_p), desiccant adsorption isotherm, desiccant heat of adsorption (h_{ads}).
- Air streams inlet conditions including air temperature (T_a), air humidity ratio (x_a), and air mass flow rate ($\dot{m}_a$).
- Heat and mass transfer parameters including the Nusselt number (Nu) for fully developed laminar flow in the channels, the Lewis number (Le), the effective moisture diffusivity in the desiccant pores (D_{eff}).
- Number of control volumes along the axial (N_z) and circumferential (N_θ) directions.

2.2.3 Governing equations

The governing equations describe the heat and mass transfer phenomena taking place between the streams of air and solid, ensuring energy and mass conservation.
In the following the governing equations are introduced for a generic infinitesimal control volume with axial length dz and circumferential length $d\theta$.

The conservation of energy in the air stream is written as:

$$\dot{m}_a \frac{\partial h_a}{\partial z} = \alpha P_i \left(T_d - T_a\right) + \sigma P_i \left(x_d - x_a\right) h_v \tag{2.1}$$

The term on the LHS accounts for the rate of energy variation in the air stream along the axial direction. The first term on the RHS expresses the convective sensible heat transfer rate between the air bulk and the solid surface. The driving potential for convective heat transfer during adsorption and desorption is the temperature difference between the air bulk and the layer of air in equilibrium with the desiccant surface. The second term on the RHS expresses the latent heat transfer between the air bulk and the solid surface related to convective moisture transfer. The driving potential for convective moisture transfer during adsorption and desorption is the water vapour partial pressure difference between the air bulk and the layer of air in equilibrium with the desiccant surface, which can be approximated by the corresponding difference in humidity ratio.
P_i is the wet perimeter perpendicular to the airflow direction z, equivalent to the sum of the wet perimeters of all channels in the considered control volume.
The convective heat transfer coefficient (α) is obtained from the Nusselt number definition:

$$Nu = \frac{\alpha D_h}{k_{ha}} \tag{2.2}$$

The convective mass transfer coefficient (σ) is obtained from the heat and mass transfer

analogy [51]. The Lewis number (*Le*), defined as the ratio of thermal to moisture diffusivity or equivalently the ratio of Schmidt and Prandtl numbers, relates the convective mass transfer coefficient to the convective heat transfer coefficient:

$$\sigma = \frac{\alpha}{c_{p,ha} Le^{(1-n)}} \tag{2.3}$$

where n can be reasonably assumed equal to 0.33 for laminar flow conditions [33]. For air at standard temperature and pressure, Le is approximately 0.88 [52], indicating enhanced mass transfer relatively to heat transfer.

The enthalpy definitions for humid air and water vapour are written as:

$$h_a = (c_{p,a} + x_a c_{p,v})(T_a - T_{ref}) + h_{fg,T_{ref}} x_a = c_{p,ha}(T_a - T_{ref}) + h_{fg,T_{ref}} x_a \tag{2.4}$$

$$h_v = c_{p,v}(T_v - T_{ref}) + h_{fg,T_{ref}} \tag{2.5}$$

with reference temperature (T_{ref}) set to 0°C. The Simplification $h_v \approx h_{fg,T_{ref}}$ is assumed.

The conservation of moisture in the air stream is written as:

$$\dot{m}_a \frac{\partial x_a}{\partial z} = \sigma P_i (x_d - x_a) \tag{2.6}$$

The term on the LHS accounts for the rate of humidity content variation in the air stream along the axial direction. The term on the RHS expresses the convective moisture transfer rate between the air bulk and the solid surface.

The conservation of energy in the air stream can be re-written substituting Equations 2.4, 2.5 and 2.6 into Equation 2.1:

$$\dot{m}_a \frac{\partial c_{p,ha} T_a}{\partial z} = \alpha P_i (T_d - T_a) \tag{2.7}$$

The conservation of energy in the solid is written as:

$$\dot{m}_s \frac{\partial h_s}{\partial \theta} = -\alpha P_j (T_d - T_a) - h_{ads} \sigma P_j (x_d - x_a) \tag{2.8}$$

The term on the LHS accounts for the rate of energy variation in the solid (desiccant and support structure) stream along the circumferential direction. The first term on the RHS expresses the sensible heat transfer rate between the air and the solid as in Equation 2.1. The second term on the RHS expresses the amount of heat of adsorption generated at the desiccant surface related to the amount of water vapour adsorbed/desorbed.
P_j is the wet perimeter perpendicular to the solid flow direction θ.

The enthalpy of the solid is defined as:

$$h_s = \left(c_{p,s} + f_{des} W_d c_{p,w}\right)(T_d - T_{ref}) \tag{2.9}$$

where the thermal capacity of the water adsorbed in the desiccant is set equal to the thermal capacity of liquid water [33]. The reference temperature is the same as for humid air.

The conservation of moisture in the solid is derived from the assumption of parabolic concentration moisture profile across the solid layer. The conservation equations under the parabolic moisture concentration profile assumption are derived in accordance to the study by Chant and Jeter [48].
The conservation of average water content in the desiccant layer is expressed as:

$$f_{des}\dot{m}_d \frac{\partial W_d}{\partial \theta} = -C_1 \sigma P_j (x_d - x_a) \tag{2.10}$$

The term on the LHS accounts for the rate of average water content variation in the desiccant stream (as the support structure is inert to mass diffusion) along the circumferential direction. The term on the RHS expresses the moisture diffusion rate at the desiccant surface. C_1 is an additional parameter characterizing the geometry of the desiccant layer.
The expression for the corresponding desiccant water content at the surface, needed for computing the equilibrium air conditions, is written as:

$$W_{surf} = -\frac{\sigma c}{C_2 f_{des} \rho_s D_{eff}} (x_d - x_a) + W_d \tag{2.11}$$

C_2 is a second parameter characterizing the desiccant layer geometry.
The coefficients C_1 and C_2 are respectively 1 and 3 for a desiccant plane wall, or 3 and 5 for a desiccant sphere.
The effective diffusivity (D_{eff}) of water vapour into the desiccant pores takes into account different types of diffusion phenomena, namely surface and pore diffusion. Surface diffusion regards the movement of adsorbed moisture along the pore walls, driven by the adsorbed moisture content gradient and proportional to the surface diffusivity (D_s). Pore diffusion regards the combined effect of ordinary and Knudsen diffusion that account for the movement of moisture in the air contained in the pores, driven by the air humidity gradient and proportional to the combined ordinary (D_O) and Knudsen (D_K) diffusivity. The resulting effective diffusivity is expressed as:

$$D_{eff} = \frac{1}{\zeta}\left[D_s + \frac{\rho_{ha}}{f_{des}\rho_s}\phi\left(\frac{1}{D_O} + \frac{1}{D_K}\right)^{-1}\frac{\partial x_a}{\partial W_d}\right] \tag{2.12}$$

where ζ is the pore tortuosity factor and ϕ is the porosity of the solid. For RD silica gel, the first term on the RHS is dominant [44, 45].

The air pressure drop along a channel is computed assuming an overall average friction factor (f_f) for fully developed laminar flow, and an additional loss factor of 1.5 [33] to account for entrance and exit effects:

$$\Delta p_a = 0.5 \rho_a u_a^2 \left(\frac{f_f L}{Re D_h} + 1.5 \right) \tag{2.13}$$

The discretization of the governing equations and the solution strategy implemented in Matlab are described in Appendix A.

2.2.4 Theoretical limits of operation of desiccant wheels

The theoretical limits of operation of desiccant wheels are identified in order to introduce a meaningful reference for defining their performance.

Desiccant materials can adsorb and desorb moisture until they reach equilibrium with the surrounding air, i.e. desiccant and air are at the same temperature and there is no water vapour partial pressure difference between the air bulk and the air at the desiccant surface. Equilibrium sorption isotherms express the equilibrium desiccant water content as a function of the air relative humidity at constant temperature. In a desiccant wheel, the desiccant material tends to equilibrium with the process and regeneration air streams as it rotates across the process and regeneration sections. Therefore, the best desiccant wheels can do is to bring the process air stream to the inlet relative humidity of the regeneration air stream [43].
It follows that the process air outlet relative humidity cannot be lower than the regeneration air inlet relative humidity, as well as the regeneration air outlet relative humidity cannot be higher than the process air inlet relative humidity.
These limits are applicable to the average air stream outlet conditions. In practise, depending on the operating conditions, desorption and adsorption phenomena can take place in the process and regeneration sections respectively. These phenomena are detrimental for the wheel performance and can lead to local outlet conditions exceeding the limits imposed by the inlet air relative humidities.

The definition of a physical limit on the air enthalpy change is also needed, as each air stream could reach its limiting relative humidity at different enthalpies, i.e. temperatures and humidity ratios. The air enthalpy change along the adsorption and desorption processes is caused by the generated heat of adsorption as well as by the carry-over of heat between process and regeneration sections.
Typically, the heat of adsorption of water vapour on desiccants is equal or greater than the enthalpy of condensation/evaporation of water. Close and Banks [53] stated that the Clausius-Clapeyron equation can be used to express the heat of adsorption in terms of the vapour

partial pressure at specified adsorbed water contents:

$$\left(\frac{\partial \ln p_v}{\partial \ln p_{v,sat}}\right)_{W_d} = \frac{h_{ads}}{h_{fg}} \tag{2.14}$$

This relationship is valid if the sorbent has no hysteresis (i.e. the adsorption process is thermodynamically reversible) and the vapour can be considered a perfect gas with negligible liquid phase volume in comparison to the gas phase. This is the case of the silica gel-water vapour pair, as well as of the majority of desiccant-water vapour pairs.
Equation 2.14 indicates the heat of adsorption decreases as the amount of adsorbed water increases, tending to the latent heat of condensation of water at saturated conditions. When the desiccant is saturated, multi-layer condensation can still take place.
Consequently, in the limit of no carry-over of heat between process and regeneration sections and heat of adsorption equal to latent heat of condensation, the adsorption process would be isenthalpic, as also argued by Eicker et al. [54].

The resulting theoretical limits of operation of desiccant wheels are given by iso-relative humidity curves and iso-enthalpy curves related to process and regeneration air stream inlet conditions, as shown on the psychrometric chart in Figure 2.5 for arbitrary air inlet conditions.

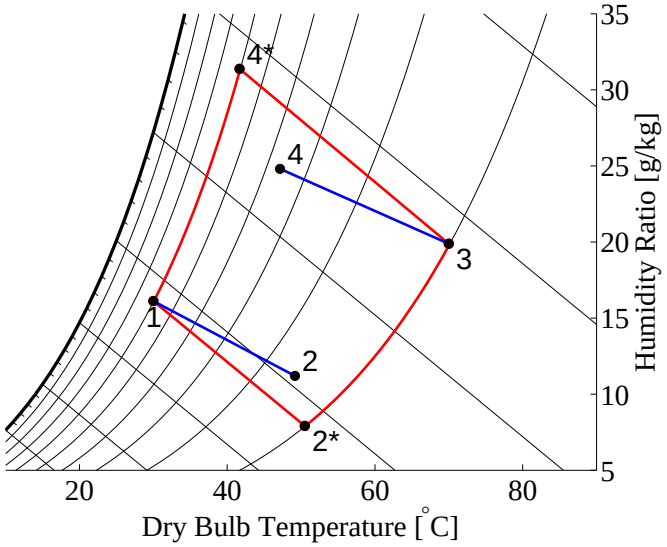

Figure 2.5: Theoretical operating limits of a desiccant wheel. (1) process air inlet, (2*) limit process air outlet, (2) realistic process air outlet, (3) regeneration air inlet, (4*) limit regeneration air outlet, (4) realistic regeneration air outlet.

2.2.5 Performance indicators

The following indicators are selected for describing the performance of desiccant wheels:

- Process air dehumidification

$$\Delta x_{a,p} = x_{a,p,i} - x_{a,p,o} \tag{2.15}$$

The process air dehumidification expresses the extent to which the process air moisture content is decreased under specified operating conditions.

- Moisture Removal Capacity

$$MRC = \dot{m}_{a,p} \Delta x_{a,p} \tag{2.16}$$

The MRC expresses the amount of water removed from the process air stream per unit of time, as defined by the ANSI/ASHRAE 139-2007 Standard [55]. It is important to distinguish between MRC and process air dehumidification, as smaller capacities are likely to correspond to higher degrees of dehumidification, for example by decreasing the air mass flow rate across the wheel.
A useful indication of the airflow rate magnitude relatively to the wheel dimensions is the air face velocity that, for the process air stream, is defined as:

$$u_{face,p} = \frac{\dot{V}_{a,p,i}}{A_{face,p}} = \frac{\dot{m}_{a,p}}{S\pi(D/2)^2 \rho_{ha,p,i}} \tag{2.17}$$

The regeneration air face velocity is defined analogously.
Additionally, it is useful to introduce the regeneration fraction, defined as the ratio of process and regeneration air volume flow rates:

$$f_{reg} = \frac{\dot{V}_{a,r,i}}{\dot{V}_{a,p,i}} \tag{2.18}$$

In the case of equal split between process and regeneration sections, i.e. S=0.5, the regeneration fraction corresponds to the ratio of the air face velocities.

- Regeneration Specific Heat Input

$$RSHI = \frac{\dot{m}_{a,r}(h_{a,r,i} - h_{a,r,source})}{MRC} \tag{2.19}$$

The RSHI indicates the minimum amount of heat that a thermal source has to generate to increase the regeneration air temperature from specified initial conditions to the required regeneration temperature. Generally, the regeneration air humidity content does not change during the heating process. The amount of regeneration heat consumed depends on the required regeneration temperature as well as on the regeneration air source conditions ($h_{a,r,source}$). Therefore the definition of the source conditions can affect the amount of regeneration heat consumed to a great extent. Considering no integration with other components, the regeneration air source conditions are set equal to the process air inlet conditions.

- Dehumidification effectiveness

$$\varepsilon_{dehum} = \frac{\Delta x_{a,p}}{\Delta x_{a,p,max}} = \frac{\Delta x_{a,p}}{x_{a,p,i} - x_{a,p,o,min}} \tag{2.20}$$

  The dehumidification effectiveness expresses how much of the theoretical dehumidification potential a wheel, operating at specific conditions, is able to attain, or alternatively how close the process air stream can get to the minimum theoretical humidity content. At best the dehumidification effectiveness is 1, meaning the process air stream leaves the wheel with no enthalpy change at the regeneration air inlet relative humidity, as indicated in Figure 2.5.

- Process air enthalpy ratio

$$f_{h,p} = \frac{h_{a,p,o}}{h_{a,p,i}} \tag{2.21}$$

  The ratio of enthalpies at the process outlet and inlet is used to quantify the process air enthalpy increase during the dehumidification process, which is unknown by the dehumidification effectiveness alone. The process is isenthalpic in the limit of enthalpy ratio equal to 1.

2.3 Results and discussion

At first, the formulated model is compared against the validated SSR model, for tuning the geometrical parameters C_1 and C_2. The tuned model is then validated against the SSR model for varying parameters.
Details of the desiccant wheel operation are reported by investigating the variations of temperatures and humidity contents across the two-dimensional computational grid.
The influence of operating and geometrical parameters on the wheel performance is presented.
RD silica gel is considered for all simulations, whose properties are reported in Appendix B.

2.3.1 Model tuning

The formulated PCP steady state model, hereafter termed DW model, is compared against the validated SSR transient model, hereafter termed reference model, in terms of the process air dehumidification and temperature increase.
The errors committed by the models in conserving energy and moisture between the two air streams are not reported, as they are always below 1%.
The number of control volumes in the DW model is set to 40 along the circumferential direction and 5 along the axial direction (200 control volumes in total), as the variation of the process air outlet conditions is negligible for higher grid refinements and the required computational time (always below 2 seconds) does not decrease significantly for courser computational grids.

In the reference model, moisture diffusion and heat conduction phenomena are considered both along and across the solid layer.

The reference wheel geometry and operating conditions for the model comparison are reported in Table 2.1.

Table 2.1: Reference scenario for model comparison.

Wheel geometry	Air inlet conditions
D = 365 mm	$T_{a,p,i}$ = 30°C
L = 200 mm	$T_{a,r,i}$ = 80°C
S = 0.5	$x_{a,p,i}$ = 13 g/kg
a = 3.8 mm	$x_{a,r,i}$ = 13 g/kg
b = 1.9 mm	$u_{face,p}$ = 2 m/s (i.e. $\dot{V}_{a,p,i}$ = 755 m^3/h)
c = 0.2 mm	f_{reg} = 1

The influence of the geometrical parameters C_1 and C_2 on the agreement between the models is investigated by discrete variations between the cases of plane wall and sphere particle, i.e. C_1 between 1 and 3 and C_2 between 3 and 5 respectively. Results are reported in Figure 2.6.

The geometrical parameter C_1 varies in each graph in Figure 2.6, while C_2 is varied among the graphs. It is noticeable that the agreement between the models depends on the assumed geometry, i.e. C_1 and C_2, as well as on the operating conditions, particularly the wheel rotational speed. A good agreement is found for C_1 equal to 1 and C_2 equal to 4 (Figures 2.6c and 2.6d) at low and medium rotational speeds (5-20 rph), as the models compute similar process outlet conditions and similar optimal rotational speed, i.e. the rotational speed maximizing the process air dehumidification. At higher rotational speeds, the agreement improves for increasing C_2, while C_1 has a nearly negligible influence. It is also noticed that the agreement in terms of process air outlet temperature improves for C_2 equal to 5, but the corresponding increased dehumidification difference makes C_2 equal to 4 preferable.
In the following, C_1 is set to 1 and C_2 to 4, as the wheel optimal rotational speed is generally below 20 rph.

Chant and Jeter [48] concluded that the parabolic moisture concentration profile assumption agreed best with experimental data for mass transfer Fourier numbers across the desiccant thickness above 0.3. Goldsworthy and White [33] reported that the same Fourier number for conventional desiccant wheels is in the order of 1, as the optimal rotational speed is typically low. For the results in Figure 2.6, the mass transfer Fourier number is equal to 0.3 at 30 rph, and 0.45 at 20 rph, which is here suggested as lower limit for considering the parabolic moisture concentration profile assumption valid. This indication applies to RD silica gel and the considered geometry. The use of different desiccants and geometries can influence the range of validity, e.g. because of different moisture diffusion mechanisms in the desiccant

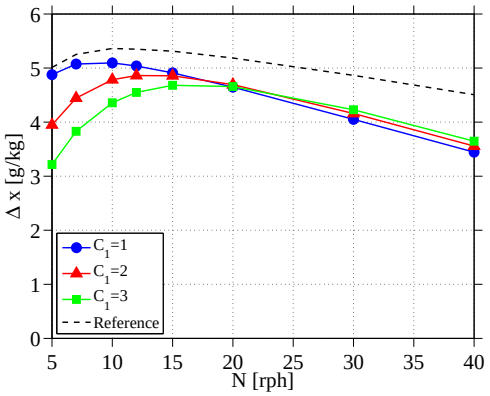

(a) Process air dehumidification with C_2=3.

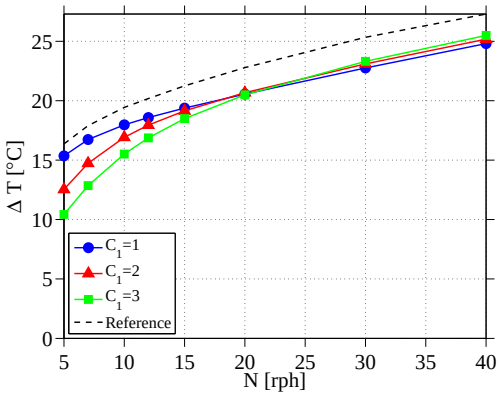

(b) Process air temperature increase with C_2=3.

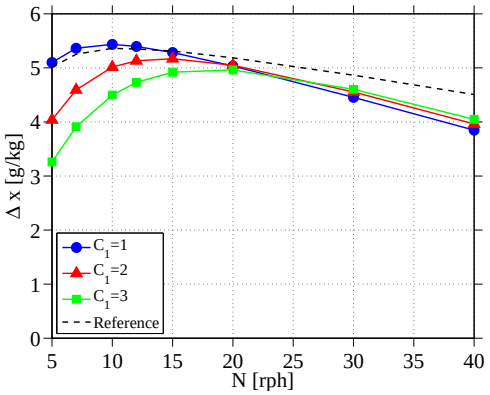

(c) Process air dehumidification with C_2=4.

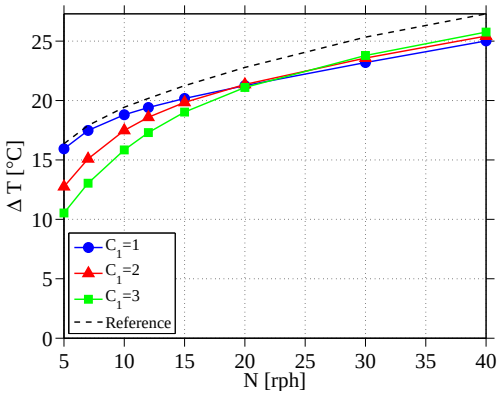

(d) Process air temperature increase with C_2=4.

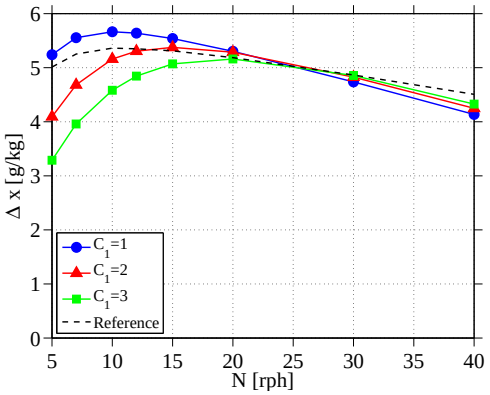

(e) Process air dehumidification with C_2=5.

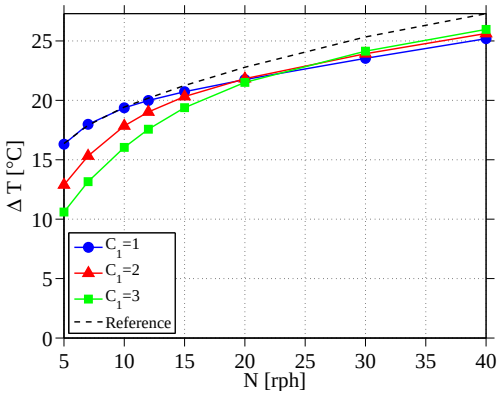

(f) Process air temperature increase with C_2=5.

Figure 2.6: Effects of varying geometrical parameters C_1 and C_2.

pores, different desiccant layer thickness, etc.
Therefore the values of C_1 and C_2 providing the best fitting at low rotational speeds are

considered to describe the physical geometry of the solid layer, while the values providing the best fitting at high rotational speeds are considered to alter the diffusion process characteristics to account for non-parabolic moisture concentration profile, as moisture does not penetrate in the desiccant pores as much as at low rotational speeds. This hypothesis is reinforced by noticing that C_2, which directly multiplies the effective diffusivity as shown in Equation 2.11, has the strongest influence on the model agreement at high rotational speeds.
Expressing C_2 as function of parameters affecting the moisture concentration profile (e.g. rotational speed, solid layer thickness, etc.) allows to extend the applicability of the model. Alternatively, higher order moisture concentration profiles could be used.

2.3.2 Model validation

A brief comparison between the tuned DW model, the reference model, and the GSR model initially developed during the research project [49] is presented in Figure 2.7, to highlight the importance of accounting for the moisture diffusion resistance in the desiccant. The reference scenario described in Table 2.1 is considered.

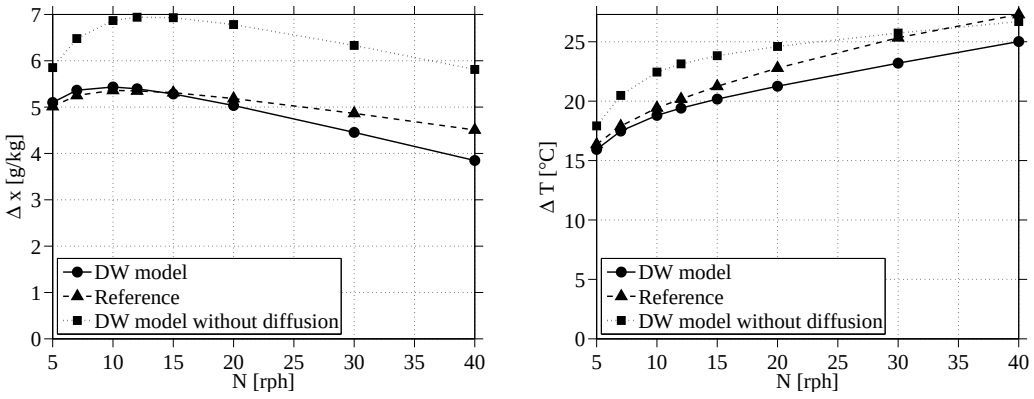

(a) Process air dehumidification.

(b) Process air temperature increase.

Figure 2.7: Model comparison including the GSR model.

Figure 2.7 shows that the GSR model largely overestimates the process air dehumidification due to the absence of any resistance to moisture diffusion in the desiccant pores. Consequently the GSR model computes also higher process air temperature increases. At higher rotational speeds, the GSR and reference models compute similar process air outlet temperatures, still with different degrees of dehumidification, suggesting that they estimate different wheel thermal capacities and so different carry-overs of heat between the sections.
The computational time required to solve the GSR and PCP models is nearly the same, confirming the PCP model increases the accuracy of the solution without increasing the computational effort.

A more comprehensive comparison between the DW and reference models is carried out for variations of the regeneration temperature (Figure 2.8), air face velocity (Figure 2.9), and wheel length (Figure 2.10), in respect to the reference scenario in Table 2.1. The wheel rotational speed is varied between 5 and 30 rph.

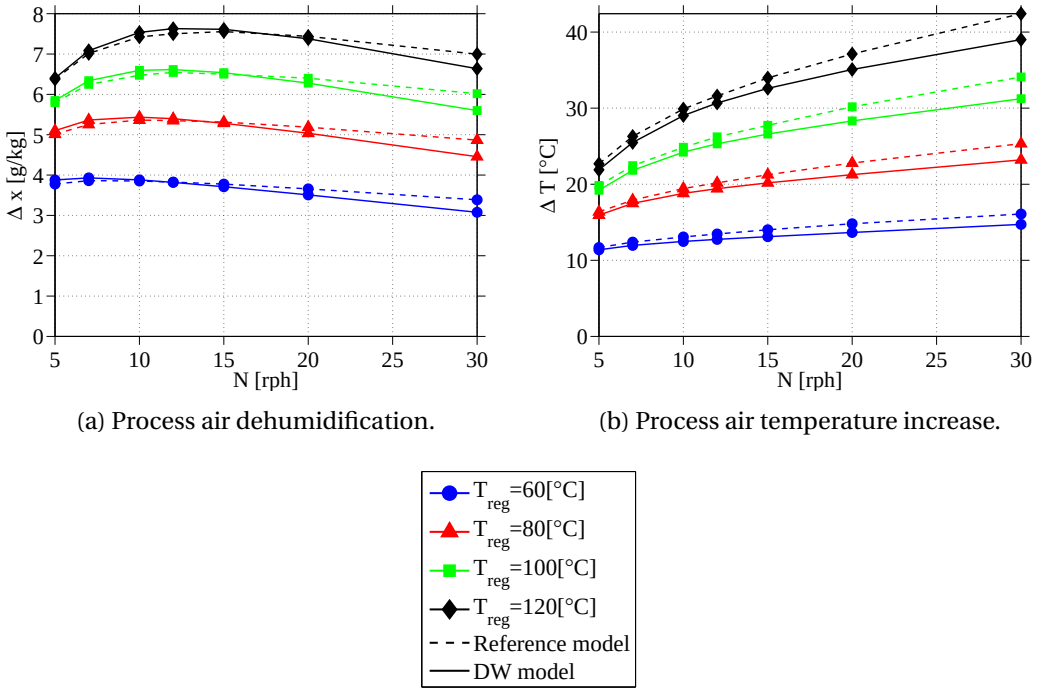

(a) Process air dehumidification.

(b) Process air temperature increase.

Figure 2.8: Model comparison for varying regeneration temperature and rotational speed.

Figure 2.8 shows a good agreement between the models for all the considered regeneration temperatures. The process air dehumidification is nearly doubled increasing the regeneration temperature from 60°C to 120°C at the optimal rotational speed, which is found to increase for increasing regeneration temperatures. The process air temperature increase is very sensitive to the regeneration temperature because of the carry-over of heat between process and regeneration sections, which results into steeper increases with rotational speed as the regeneration temperature increases.

Figure 2.9 shows that the models agree well for rotational speeds up to 20 rph, particularly in terms of process air dehumidification, while the agreement gets worse at higher rotational speeds. Process air temperature increase and optimal rotational speed increase for decreasing air face velocities. For high air face velocities, the reference model computes nearly constant dehumidification after certain rotational speeds, with high optimal values, while the DW model always computes a decreasing dehumidification for corresponding rotational speeds. This trend reflects the influence of the parabolic moisture concentration profile.
Process air dehumidification increases for decreasing air face velocities at low and medium

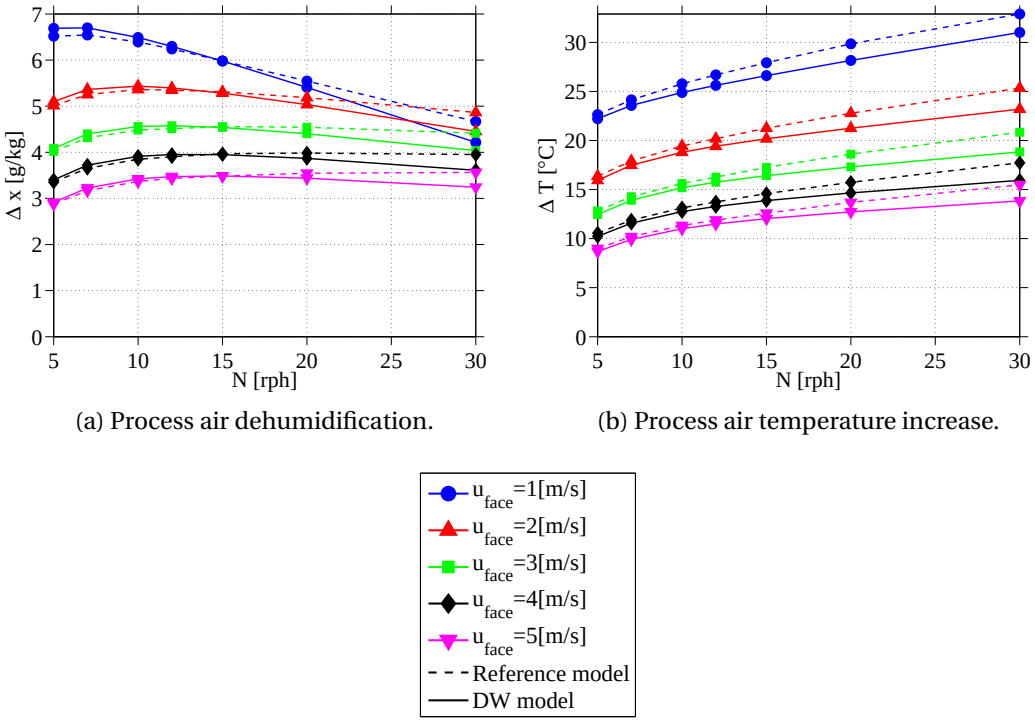

(a) Process air dehumidification.

(b) Process air temperature increase.

Figure 2.9: Model comparison for varying air face velocity and rotational speed.

rotational speeds, but low air face velocities does not lead to the highest process air dehumidification at higher rotational speeds.

Figure 2.10 shows again a good agreement between the models for rotational speeds up to 20 rph. Process air temperature increase and optimal rotational speed always increase for decreasing wheel lengths. Differently, process air dehumidification increases for increasing wheel lengths at low and medium rotational speeds, but longer wheels do not provide the highest process air dehumidification at high rotational speeds.
These trends suggest that the effect of wheel length is opposite to the effect of air face velocity.

The trends observed in Figures 2.8, 2.9, and 2.10 indicate that the process air dehumidification has a complex dependence on the wheel parameters. In fact, optimal rotational speeds are found to change for different parameter combinations, while long wheels and low air flow velocities lead to higher dehumidifications only at low and medium rotational speeds. The interdependence among these parameters can be explicated by the concept of contact time between the air streams and the desiccant in the process and regeneration sections. Goldsworthy and White [33] have introduced the dimensionless contact time number for describing the relative time that the desiccant spends in the process or regeneration section in comparison to the time that the process or regeneration air stream takes to flow across the channels. Consequently the time of contact is directly proportional to the air face velocity and

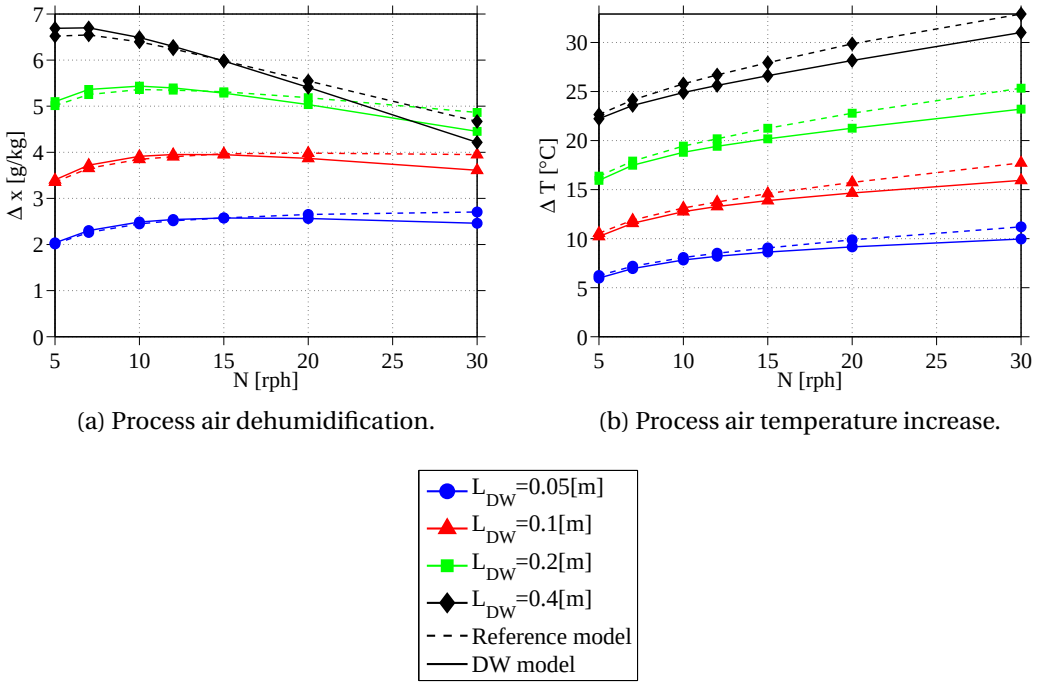

(a) Process air dehumidification.

(b) Process air temperature increase.

Figure 2.10: Model comparison for varying wheel length and rotational speed.

inversely proportional to the wheel rotational speed and length. Short times of contact result in the desiccant rotating with still an important potential for adsorbing or desorbing moisture at the end of the sections. Long times of contact make the desiccant approach equilibrium with the air streams before moving from one section to the other, resulting into a partially inactive wheel. Optimally, the time of contact should lead to complete loading and unloading of the desiccant with successive immediate switch between the sections.
This also explains the increasing optimal rotational speed for increasing air face velocities and decreasing wheel length.

The process air dehumidification does not vary significantly within a certain range of rotational speeds around the optimal value. This suggests to choose the lowest rotational speed in the range of nearly optimal values in order to minimize the process air temperature increase, unless the wheel is used for applications that benefit from higher supply temperatures, e.g. drying processes at medium to high temperatures.

For all reported simulations, the DW model computational time is less than 2 seconds on a laptop equipped with Intel Core i7-3720 CPU and 8 GB RAM. Differently, the computational time of the reference model is between 15 and 50 times longer for reaching comparable accuracies in the steady state solution, i.e. energy and mass conservation between the air streams, depending on the simulated conditions. Even though the reference model could be

optimized for reducing its computational time, the advantage of using the developed PCP model for repetitive system simulations is evident.

2.3.3 Analysis of desiccant wheel operation

The DW model provides information on the air and desiccant condition profiles along the axial and circumferential directions in the wheel. These information are reported in the following, considering the reference scenario reported in Table 2.1 and wheel rotational speed set to 10 rph. The number of control volumes is set to 200 along the circumferential direction and 10 along the axial direction (2000 control volumes in total) in order to visualize detailed property variations.

The air temperature and humidity ratio profiles as well as the desiccant temperature and average water content profiles are reported in Figure 2.11 on the two-dimensional computational grid introduced in Figure 2.4. The axial position is reported relatively to the wheel length from 0 (process air inlet face) to 1 (regeneration air inlet face). The process section is located circumferentially between 0° and 180°, while the regeneration section between 180° and 360°.

Figures 2.11a and 2.11c show the air and desiccant temperature profiles have similar distributions. The desiccant is warmer than the air at coincident locations in the process section, and colder in the regeneration section, as it can be noticed by comparing the reported temperature scales.
The temperature of the regeneration air leaving the wheel at 360° circumferential position provides an indication of the degree of regeneration reached along the axial direction. In the limit of equal outlet and inlet air temperatures, the desiccant is in equilibrium with the air stream along the whole axial length. The more the desiccant is regenerated, the more potential for adsorption there is in the process section. However, if outlet and inlet temperatures get close before 360° circumferential position, a part of the regeneration section is inactive in respect to desorption. In this case heat consumption can be reduced by, e.g., reducing the regeneration air face velocity, which reduces the time of contact between regeneration air and desiccant, and the air pressure drop. In practise, the use of one or more temperature sensors monitoring the regeneration air outlet temperature at the end of the regeneration section would allow to implement such control strategies.
Additionally, the temperature of the process air leaving the wheel at 180° circumferential position can be used to indicate of how close the desiccant and process air stream get to equilibrium, i.e. if there is still potential for adsorption. In this case, varying the process airflow rate might not be possible, e.g. constant ventilation rates might be required in air conditioning applications. Alternatively the wheel rotational speed can be varied.
The simultaneous control of rotational speed and regeneration air face velocity by monitoring the air temperature at the above mentioned locations would allow to maximize the process air dehumidification, tending to the optimal time of contact between desiccant and air streams.

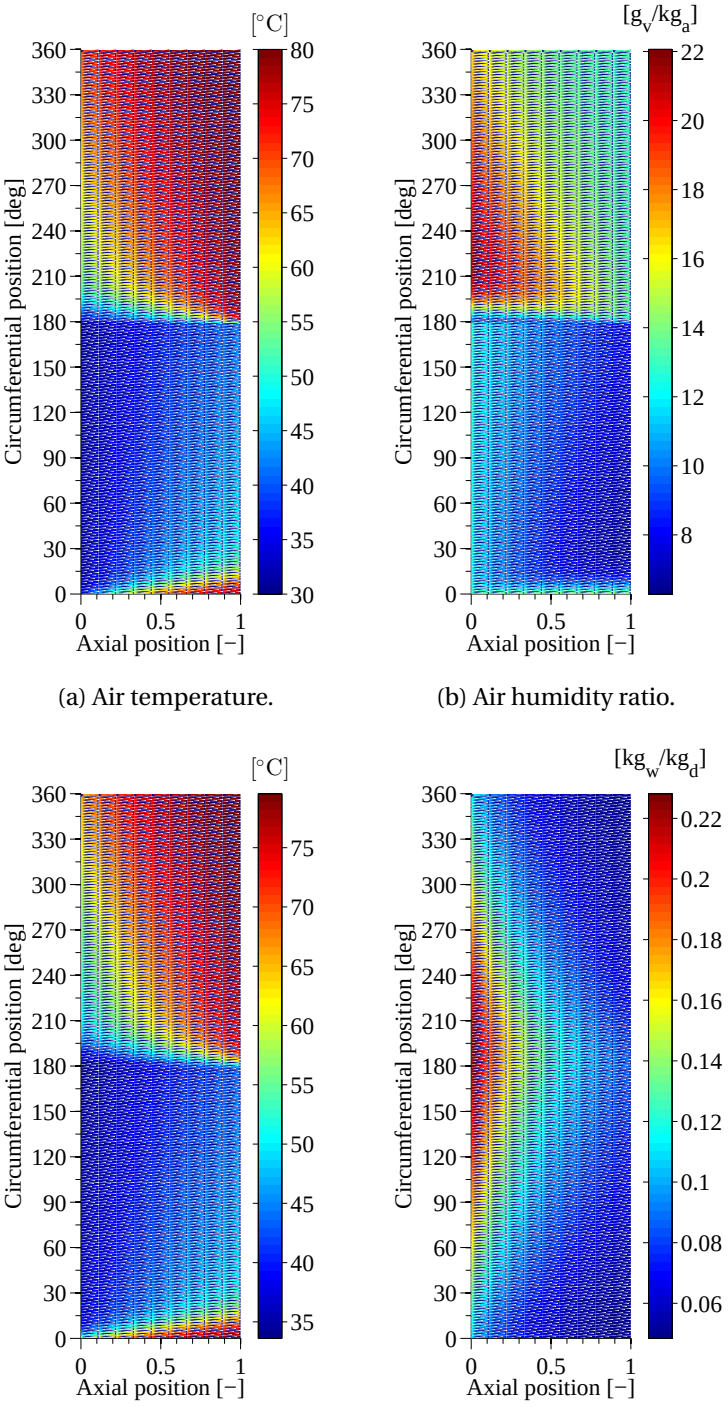

(a) Air temperature.

(b) Air humidity ratio.

(c) Desiccant temperature.

(d) Average desiccant water content.

Figure 2.11: Temperature and water content profiles.

Generally, monitoring the process and regeneration air outlet temperatures at the end of the respective sections provides useful information for controlling the wheel operation. The best control strategy has to take into account other limits of operation, such as required ventilation rates, regeneration temperature range, maximum allowable pressure drop, etc.

Figure 2.11b shows that the process air humidity ratio does not immediately decrease at the beginning of the process section, where an initial desorption process takes place. This effect, detrimental for the wheel dehumidification performance, is due to the fact that the desiccant is warm when entering the process section. For this reason, purge sections are used to cool the desiccant before it enters in contact with the process air stream.
Analogous observations can be made for the desiccant entering the regeneration section, as the regeneration air stream is initially subjected to an adsorption process while heating the desiccant.

Figure 2.11d shows the desiccant moisture content has the highest axial gradient at the end of the process section, indicating there is still potential for adsorption. The small axial gradient at the end of the regeneration section indicates the desiccant is almost completely regenerated. These information cannot be directly extracted from the air and desiccant temperature gradients at the end of the process and regeneration sections. In fact, while the temperature gradients at these locations look quite similar and small, the desiccant water content gradients are different.

The air conditions from Figures 2.11a and 2.11b are reported on psychrometric diagrams in Figure 2.12, indicating also the physical limits of operation. In Figure 2.12a, the average process air outlet conditions are limited by the process air inlet enthalpy and regeneration air inlet relative humidity (solid red lines), and vice versa in Figure 2.12b for the regeneration air outlet conditions.

The small desorption and adsorption phenomena taking place respectively at the beginning of process and regeneration sections can also be identified in Figure 2.12. The process air stream increases both its temperature and humidity ratio along the axial direction at the first considered circumferential positions, while the regeneration air decreases both its temperature and humidity ratio. However these phenomena are not strong enough for causing local air outlet conditions to exceed the physical limits of operation. In both air streams, the air conditions get closer to each other for increasing circumferential positions, while the change of conditions tend to be isenthalpic along the axial direction.

Details on the moisture diffusion potential in the desiccant pores are provided in Figure 2.13, where the surface and average desiccant water contents are reported at different axial and circumferential positions in the wheel. The potential for diffusion is indicated by the difference

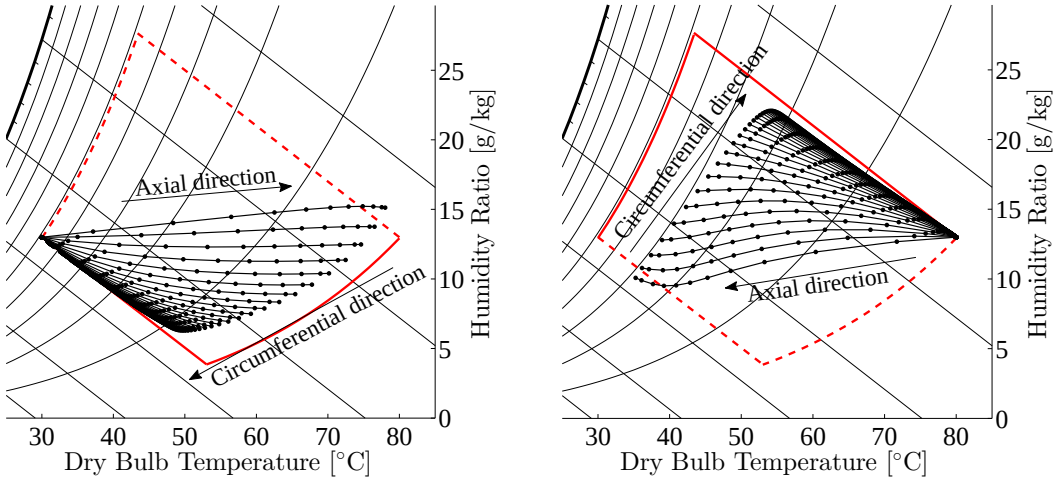

(a) Process air.

(b) Regeneration air.

Figure 2.12: Air conditions across the wheel.

between the surface and average desiccant moisture contents. Adsorption takes place when the surface moisture content is higher than the average value, and vice versa.

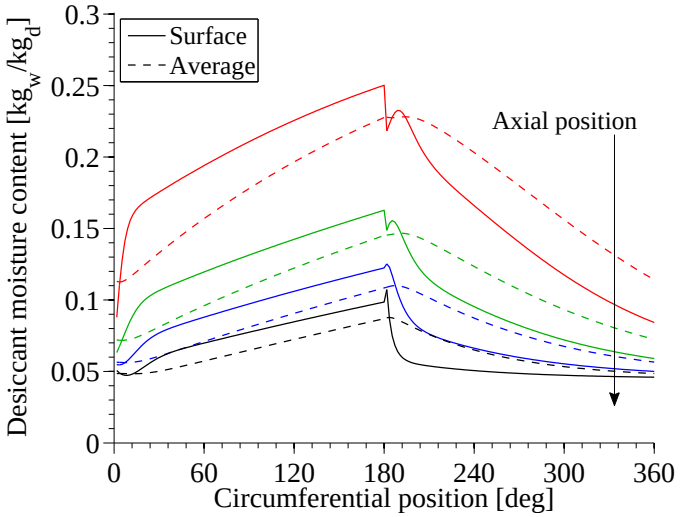

Figure 2.13: Potential for moisture diffusion across the wheel.

The highest potentials for diffusion are found at the process air inlet face and regeneration air outlet face, not considering the initial circumferential regions at the beginning of each section, where the desiccant water content exhibits steep changes. At the beginning of the regeneration section, a sudden adsorption is noticeable at the regeneration air inlet face. Moving further along the regeneration air flow direction, the initial adsorption peak decreases until desorption

takes place, where adsorption takes place with a little delay in the circumferential direction. Analogous observations can be made for the process air stream along its flow direction at the beginning of the process section.

2.3.4 Influence of operating conditions and wheel geometry

The influence of operating conditions and geometrical parameters on the selected performance indicators is investigated. The baseline for all variations is the reference scenario reported in Table 2.1 and wheel rotational speed of 10 rph.
The influence of different wheel lengths are not investigated further as already reported in Figure 2.10.

Air inlet conditions

The process air inlet conditions are varied in the temperature range 15-45°C and humidity ratio range 10-30 g/kg.
The regeneration air inlet humidity ratio is set equal to the process air inlet humidity ratio, considering the regeneration air stream is taken from the same ambient as the process air stream, with no intermediate humidification or dehumidification processes.
The effects on the process air dehumidification, RSHI, dehumidification effectiveness, and process air enthalpy ratio are reported in Figure 2.14. The MRC is not reported as it varies analogously to the process air dehumidification because of the constant process airflow rate, with minor differences caused by varying air density. Results are presented on psychrometric charts, such that each point corresponds to simulated process air inlet conditions, while the performance indicator values are reported by means of iso-value curves.

Figure 2.14a shows that the process air dehumidification increases for increasing inlet humidity ratios and decreasing inlet temperatures. Generally, fixing either the temperature or the humidity ratio, the process air dehumidification increases as the air gets closer to saturation.
Figure 2.14b shows that the RSHI decreases for increasing inlet humidity ratios and decreasing inlet temperatures. The RSHI exhibits a weaker dependence on the inlet temperature than the process air dehumidification. This is due to the fact that the regeneration heat is importantly affected by the regeneration air inlet temperature, with a smaller dependence on the inlet humidity ratio.
Figure 2.14c shows that the dehumidification effectiveness ranges from approximately 52% to 70% in the considered range of conditions. Its variation does not follow the process air dehumidification, as the potential for adsorption varies with the air inlet conditions.
At last Figure 2.14d shows that the process air enthalpy ratio is nearly constant along iso-enthalpy lines, increasing for decreasing temperatures and humidity ratios as the process air stream gets closer to the limit conditions.

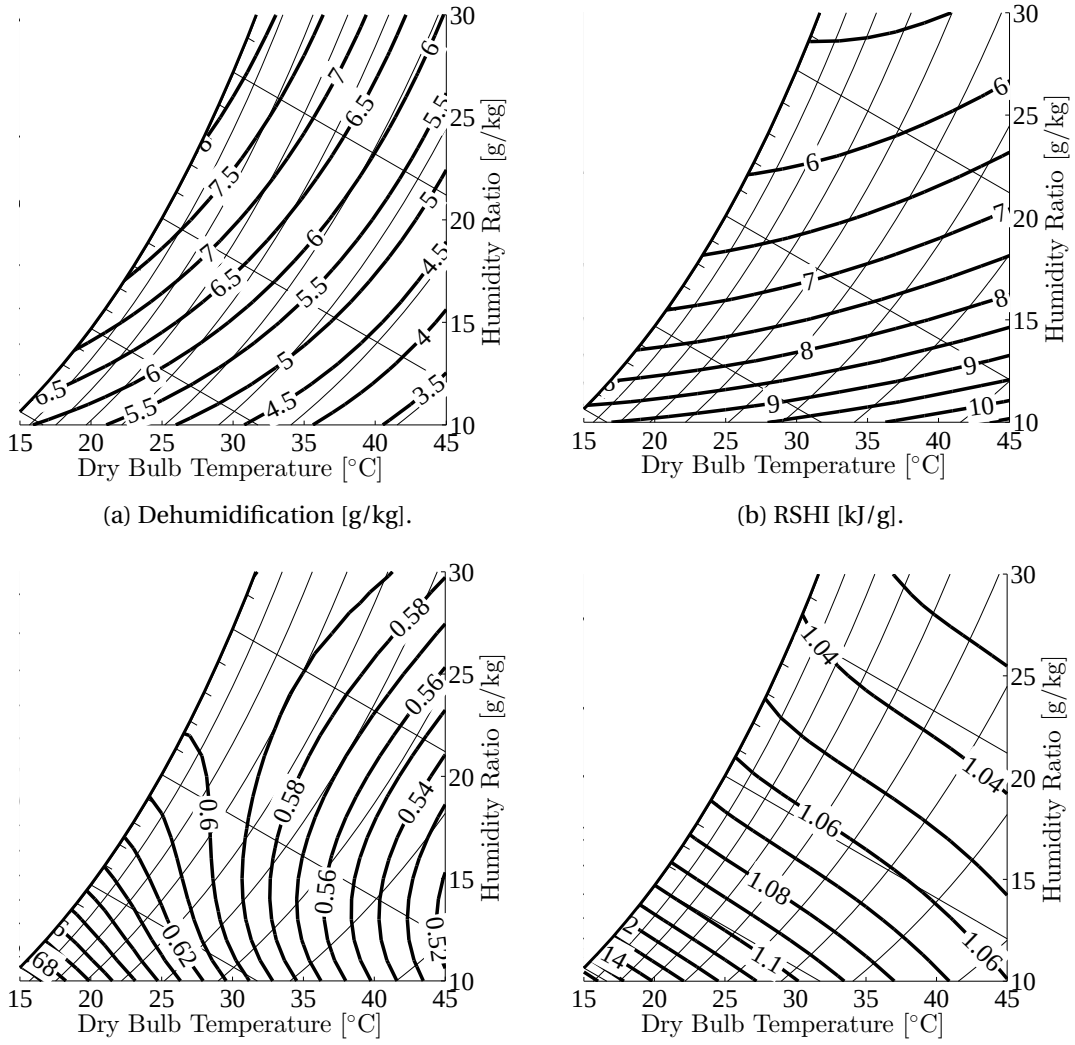

(a) Dehumidification [g/kg].

(b) RSHI [kJ/g].

(c) Dehumidification effectiveness [-].

(d) Process air enthalpy ratio [-].

Figure 2.14: Influence of process air inlet conditions.

Regeneration conditions

The regeneration temperature and regeneration fraction are varied in ranges 50-120°C and 0.5-1 respectively. The effects on the process air dehumidification, RSHI, dehumidification effectiveness, and process air enthalpy ratio are reported in Figure 2.15. Also in this case the MRC is not reported as it varies analogously to the process air dehumidification, due to the constant process airflow rate.

Figure 2.15a shows that the regeneration temperature has a bigger influence on the process air dehumidification than the regeneration fraction, with almost constant dehumidification for regeneration fraction above 0.7. However, the dehumidification effectiveness varies signifi-

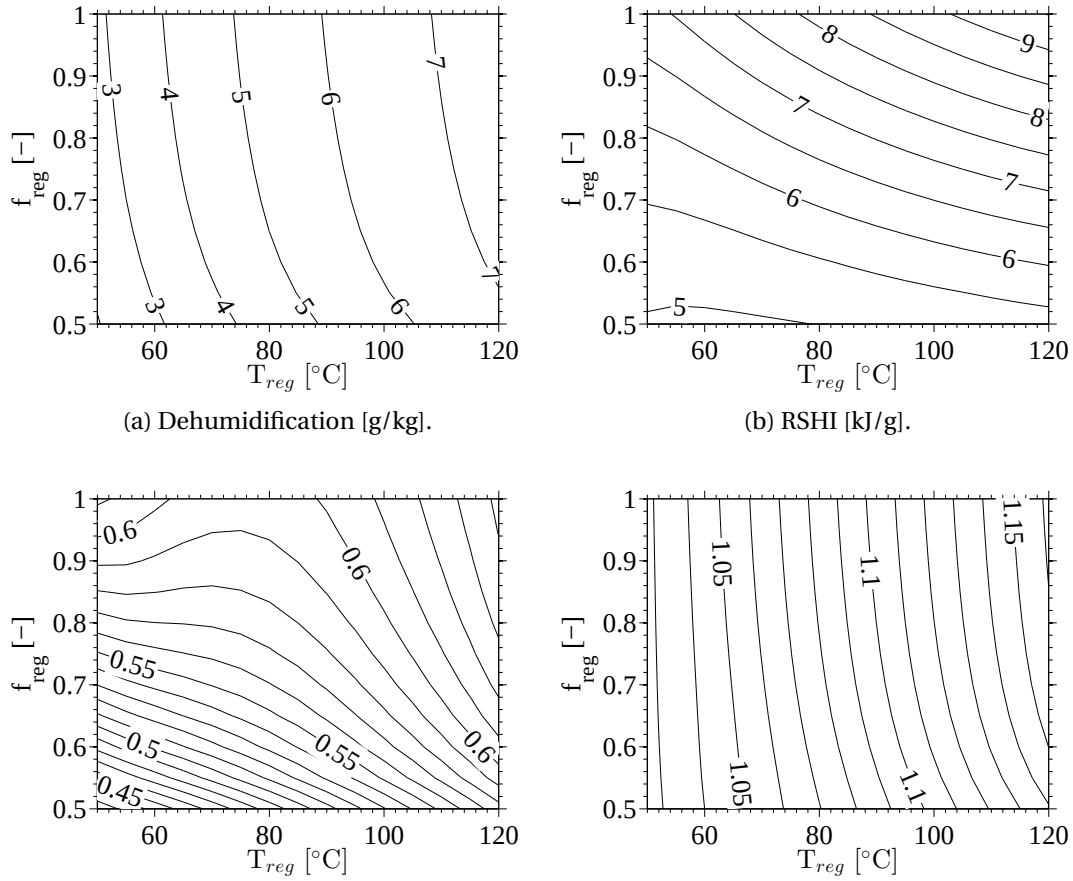

(a) Dehumidification [g/kg].

(b) RSHI [kJ/g].

(c) Dehumidification effectiveness [-].

(d) Process air enthalpy ratio [-].

Figure 2.15: Influence of regeneration temperature and regeneration air fraction.

cantly with the regeneration fraction as shown in Figure 2.15c, particularly at low regeneration temperatures at which the dehumidification potential is smaller.
The regeneration fraction has a strong influence on the RSHI as shown in Figure 2.15b, which decreases as the regeneration fraction decreases. At low regeneration fractions, e.g. 0.5, the RSHI is nearly independent of the regeneration temperature. Similarly, the air pressure drop across the regeneration section decreases for decreasing regeneration fractions.
Figure 2.15d shows that the process air enthalpy ratio varies similarly to the process air dehumidification, increasing for increasing regeneration temperatures, because of higher generations of adsorption heat with increasing dehumidifications, and higher amounts of heat carried over from the regeneration to the process side by increased wheel thermal capacities, i.e. increased temperatures and moisture contents.

Airflow rates

The airflow rates of both process and regeneration air streams are varied by means of the process air face velocity in the range 1-5 m/s, and regeneration fraction, in the range 0.5-1. The effects on the process air dehumidification, MRC, RSHI, and process air enthalpy ratio are reported in Figure 2.15. In this case the dehumidification effectiveness varies similarly to the process air dehumidification, due to the constant process and regeneration air inlet temperatures and humidity ratios, i.e. dehumidification potential.
Varying the process air face velocity with constant regeneration fraction makes also the regeneration air face velocity vary. The effect of varying process air velocities at constant regeneration air face velocity is indicated in Figure 2.15 by means of dashed lines, which refer to constant regeneration air face velocity of 2 m/s.

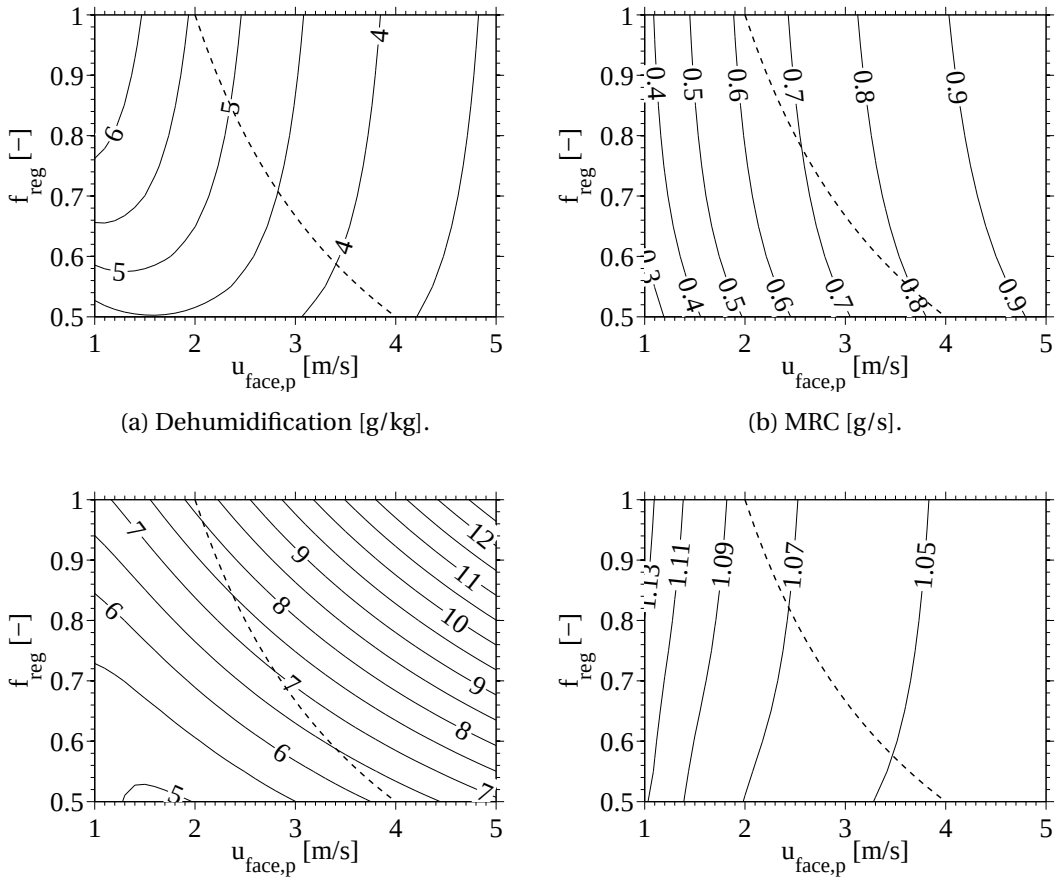

(a) Dehumidification [g/kg].

(b) MRC [g/s].

(c) RSHI [kJ/g].

(d) Process air enthalpy ratio [-].

Figure 2.16: Influence of process air velocity and regeneration air fraction. The dashed lines indicate constant regeneration air face velocity of 2 m/s.

The comparison of Figures 2.16a and 2.16b shows that increasing process air flow rates, i.e. face velocities for a fixed geometry, decrease the process air dehumidification while increasing

the MRC. This result is quite important depending on the application for which a desiccant wheel is used. If the aim is to rapidly remove moisture from a space/drying chamber with recirculation of air, higher face velocities are advantageous. On the other hand if the supply air humidity content has to be low and/or no recirculation can be used (causing the moisture load on the wheel to be decoupled from the moisture load in the space/drying chamber), lower air velocities are preferable.
Figure 2.16a shows also that, at low regeneration fractions and low process air face velocities, the process air dehumidification initially decreases for increasing process air velocities, indicating the existence of optimal process air face velocity for given regeneration fractions.
Figure 2.16c shows that the RSHI generally increases for higher regeneration fractions and process air face velocities, as the heat consumption rate increases more than the MRC. In case of constant regeneration air face velocity (2 m/s along the dashed line), the RSHI decreases for increasing process air face velocities, as the amount of regeneration heat consumed is constant while the MRC increases.
Figure 2.16d indicates that the process air enthalpy ratio is higher at low process air face velocities, mainly because of higher dehumidification. Its variation at higher process air face velocities diminishes significantly.

Wheel face area split

The process to total face area ratio (S) is used to identify the relative sizes of process and regeneration sections. Its effect on both process air dehumidification and MRC at regeneration temperatures of 50°C and 80°C respectively and varying rotational speed are investigated by varying it in the range 0.25-0.75. Results are reported in Figure 2.17, indicating with dashed lines the optimal rotational speeds that maximize the process air dehumidification.

Figure 2.17 shows that the optimal rotational speed increases for increasing regeneration temperatures and peaks at intermediate values of S. Figures 2.17c and 2.17d show that the MRC is maximized by the same rotational speeds. However, while the MRC peaks at specific values of S, the process air dehumidification keeps increasing as S decreases. The MRC is found to peak at S equal to approximately 0.53 for 50°C regeneration temperature, and 0.59 for 80°C regeneration temperature. This is due to the fact that the process air face velocity is kept constant, resulting into lower process airflow rates as S decreases. These values are in accordance with the results reported by Chung and Lee [56] that investigated the combined influence of S, desiccant adsorption isotherm shape, wheel rotational speed and regeneration temperature on the wheel dehumidification performance. They concluded that values of S maximizing the MRC at optimal rotational speeds increase as the regeneration temperature increases. For isotherm shapes analogous to RD silica gel, they found optimum values of S of 0.55 at 50°C regeneration temperature and 0.6 at 80°C regeneration temperature.

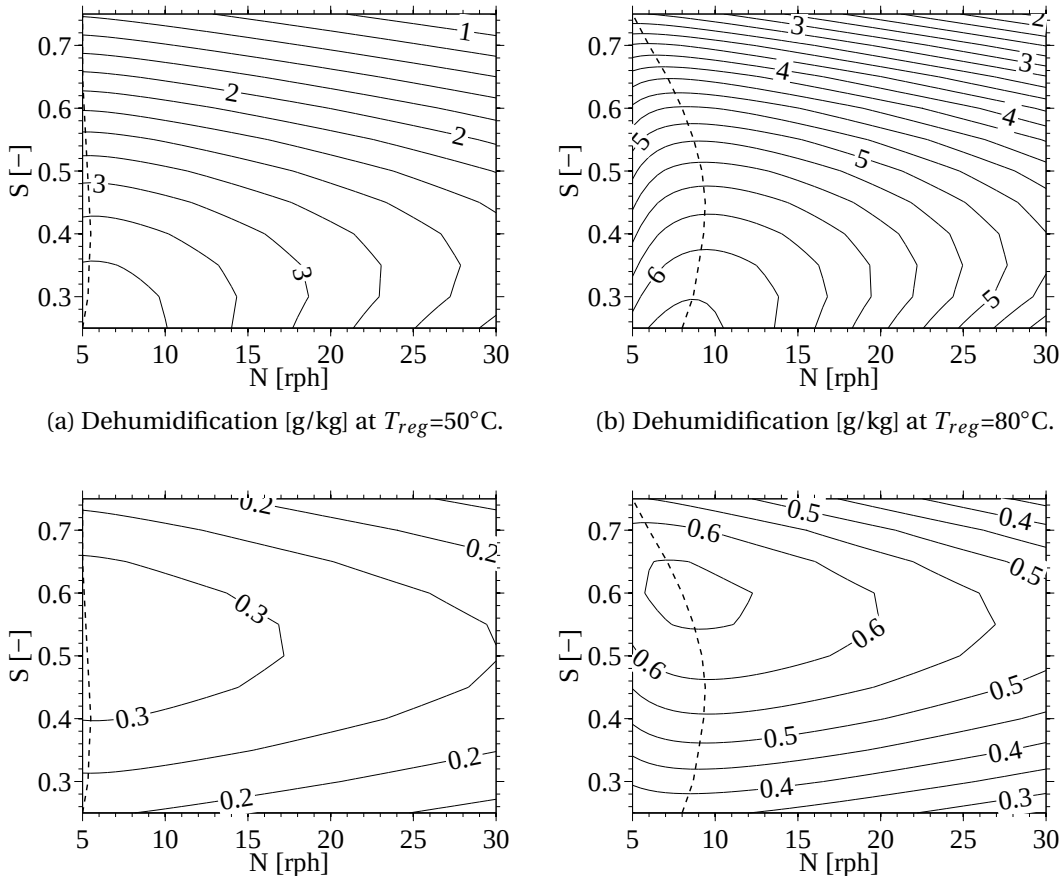

(a) Dehumidification [g/kg] at T_{reg}=50°C.

(b) Dehumidification [g/kg] at T_{reg}=80°C.

(c) MRC [g/s] at T_{reg}=50°C.

(d) MRC [g/s] at T_{reg}=80°C.

Figure 2.17: Influence of process to total face area ratio at different regeneration temperatures. The dashed lines indicate optimal rotational speeds maximizing dehumidification.

Solid layer thickness

The desiccant layer thickness impacts both the diffusion of moisture in the desiccant pores (see Equation 2.11) and the wheel thermal capacity, as it determines the mass of desiccant and support material. The desiccant layer thickness is varied in the range 0.05-0.4 mm and its influences on the process air dehumidification and process air enthalpy ratio are reported in Figure 2.18, for varying rotational speeds.

Figure 2.18a shows that the influence of the layer thickness on the process air dehumidification is strongly influenced by the rotational speed. Optimal rotational speeds for different layer thickness are indicated by the dashed line, indicating the optimal rotational speed increases as the layer thickness decreases. This is explained by the fact that thicker layers require longer times of contact between desiccant and air, i.e. lower rotational speeds, to allow moisture to penetrate across the whole layer. For a fixed layer thickness, rotational speeds higher than

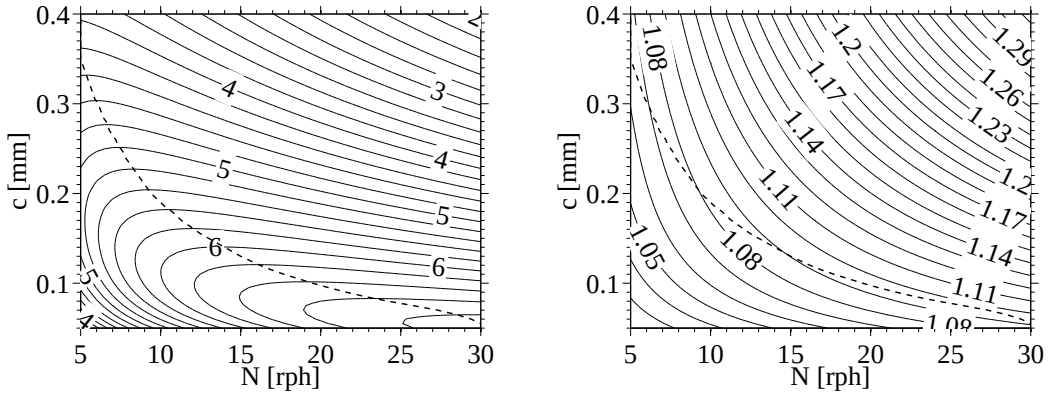

(a) Dehumidification [g/kg].

(b) Process air enthalpy ratio [-].

Figure 2.18: Influence of solid layer thickness and wheel rotational speed. The dashed lines indicate optimal rotational speeds maximizing dehumidification.

the optimal value lead to reduced moisture penetrations across the layer, as well as increased carry-overs of heat from regeneration to process section. On the other hand, rotational speeds lower than the optimal value lead the desiccant to reach equilibrium with the air streams while rotating along the corresponding sections. The reason for the process air dehumidification to increase with thinner layers of solid is mainly the resulting lower wheel thermal capacity, which allows to reduce the carry-over of heat from process to regeneration section.
Figure 2.18b shows that the increase of both layer thickness and rotational speed result in increased process air enthalpy ratios. The use of optimal rotational speeds for different layer thickness leads to small variations of the process air enthalpy ratio.
Ultimately, Figure 2.18 indicates that the desiccant layer should be as thin as possibly permitted by technological limitations for maximizing the wheel dehumidification performance.
The parabolic moisture concentration profile assumption is still expected to the suitable for thinner desiccant layers and higher rotational speeds, as they have opposite effects on the mass transfer Fourier number, used as a validity index for the parabolic profile assumption.

2.4 Conclusions

A two-dimensional steady state desiccant wheel model has been developed for performing fast and accurate simulations, allowing to consider different wheel geometries and operating conditions, as well as different desiccant materials.
From the comparison with other models, it can be concluded that:

- The resistance to moisture diffusion in the desiccant has to be considered for obtaining accurate results.

- The assumption of parabolic moisture concentration profile implemented in the model makes possible to account for the resistance to moisture diffusion with low computational effort. This solution is very convenient for repetitive component and system simulations, instead of more detailed models.
- The assumption of parabolic moisture concentration profile provides accurate results for low and medium rotational speeds, depending on the selected desiccant material and solid layer thickness. Silica gel desiccant wheels can be simulated with good accuracy, as usually operated at low rotational speeds.
- Accuracy at high rotational speeds can be achieved by tuning identified model parameters. Alternatively, higher order moisture concentration profiles could be implemented.

From model simulations considering silica gel desiccant wheels, it is concluded that:

- The optimal wheel rotational speeds leading to the highest levels of dehumidification are low, typically below 20 rph. Process air dehumidification does not vary significantly within a range of rotational speeds around the optimal value, while process air outlet temperature always increases for increasing rotational speeds. Therefore the rotational speed should be set depending on the specific application.
- The process and regeneration air outlet temperatures at the end of the respective sections provide useful information on the wheel operation. Improved wheel control systems can be built by monitoring these temperatures.
- For a specified wheel geometry, the process air dehumidification improves for colder and more humid process air inlet conditions, increasing regeneration temperatures, and decreasing process air flow rates. Increasing regeneration air flow rates also improve the process air dehumidification, with little influence above approximately 0.7, while increasing regeneration heat consumption and air pressure drop. Therefore the regeneration fraction should be selected considering a trade-off between improved dehumidification and increased energy consumption.
- Varying the process air flow rate has opposite effects on the process air dehumidification and moisture removal capacity. The optimal process air flow rate for a given wheel geometry is therefore dependent on the specific application.
- The wheel face area split should be set depending on the operative range of regeneration temperatures. A bigger portion of the wheel should be allocated to the process section for increasing regeneration temperatures. An equal split between process and regeneration sections is favourable in case of regeneration temperatures between 50°C and 90°C.
- The desiccant layer should be as thin as possibly permitted by technological limitations for enhancing the dehumidification capacity, adopting increased optimal wheel rotational speeds.

3 Indirect evaporative cooler model

3.1 Introduction

Evaporative coolers exploit the latent heat of vaporization of water for cooling air, replacing energy intensive compressors, cooling towers, and avoiding the use of artifical refrigerants. Evaporative coolers can reach electric COPs as high as 20 [57], since only fan power is consumed for air circulation. As the cooling performance of evaporative coolers depends strongly on the ambient conditions, their applicability is generally limited to warm and dry climates, but the coupling with desiccant dehumidifiers allows to employ them in more humid conditions [4, 57].
Evaporative coolers can be classified as reported in Figure 3.1.

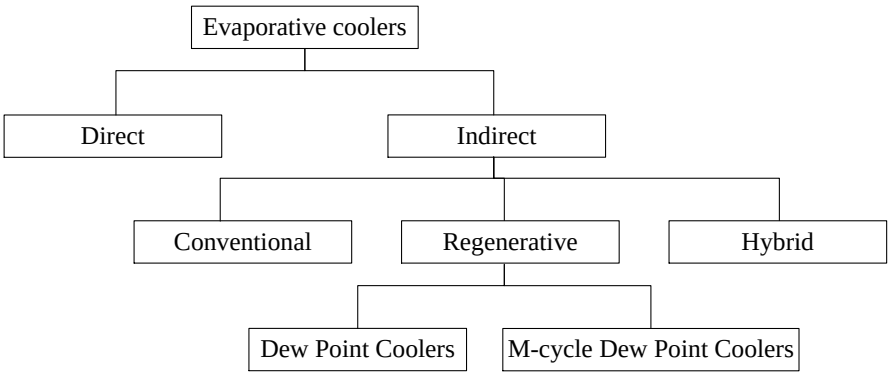

Figure 3.1: Classification of evaporative coolers.

Direct Evaporative Coolers (DECs) cool air adiabatically, i.e. air is cooled and simultaneously humidified at approximately constant enthalpy by direct evaporation of water. This is typically achieved by making the air stream flow across wetted surfaces, e.g. membranes or pads. The minimum theoretical supply temperature DECs can provide is the air wet bulb temperature.

Indirect Evaporative Coolers (IECs) cool a primary air stream by evaporating water into a secondary air stream, without adding moisture to the primary stream. IECs are generally air-to-air heat exchangers, with more complex structures than DECs. Approximately 80 % of the existing IEC designs adopt a flat-plate-stack construction [58], with primary air flowing in dry channels and secondary air flowing in adjacent wet channels. The minimum theoretical supply temperature IECs can provide is the secondary air wet bulb temperature at the inlet of the wet secondary channels.
As IECs do not add any moisture to the primary air stream, their use in desiccant cooling systems does not increase the required dehumidification capacity, allowing to reduce energy consumption in respect to systems employing DECs.
IECs can be further classified on the basis of the composition of the secondary air stream.

Conventional IECs use a secondary air stream taken either at the same conditions of the primary air stream or at different conditions. An example of the resulting flow configuration with a counter-flow arrangement is shown in Figure 3.2a. In the following, conventional IECs are simply referred to as IECs.

Regenerative IECs cool also the secondary air stream before recirculating it into the secondary wet channels. Consequently the minimum theoretical supply temperature they can provide is the inlet secondary air dew point. Typically the primary and secondary air streams enter at the same conditions, hence the minimum theoretical supply temperature is the primary air dew point. For this reason regenerative IECs are also termed Dew Point Coolers (DPCs).
The first DPC was introduced in 1976 by Maisotsenko. The working principle consisted of recirculating part of the cooled primary air stream into wet secondary channels. An example of the resulting flow configuration with a counter-flow arrangement is shown in Figure 3.2b. In the following, this type of coolers are referred to as DPCs.
More recently, Maisotsenko et al. [21, 59] introduced a modified working principle, wherein the secondary air stream is kept separated from the primary air stream. The secondary air stream is first cooled into dry secondary channels before being recirculated into wet secondary channels. An example of the resulting flow configuration with a counter-flow arrangement is shown in Figure 3.2c, where the wall between the secondary dry and wet channels is perforated, allowing for a gradual recirculation. The resulting dew point cooling process has also been termed Maisotsenko cycle (M-cycle) in the literature [60, 61]. In the following, this type of coolers are referred to as M-cycle DPCs.

Hybrid IECs (HIECs) use a mix of recirculated cooled primary air and external air (intended as external to the cooler) for obtaining the secondary air stream. The minimum theoretical supply temperature they can provide is the wet bulb temperature of the secondary air stream entering the wet channels. The aim of HIECs is to combine the advantages of DPCs and IECs by controlling the secondary air composition. In fact, DPCs typically supply lower temperatures

than IECs at the expense of lower cooling capacities because of lower supply flow rates due to secondary air recirculation. An example of the resulting flow configuration with a counter-flow arrangement is shown in Figure 3.2d, combining the IEC and DPC configurations shown in Figures 3.2a and 3.2b.

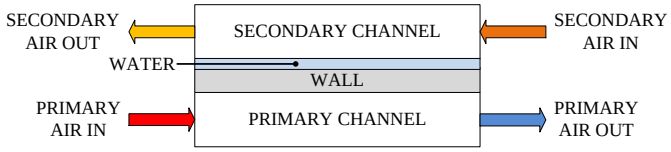

(a) Counter-flow conventional IEC configuration.

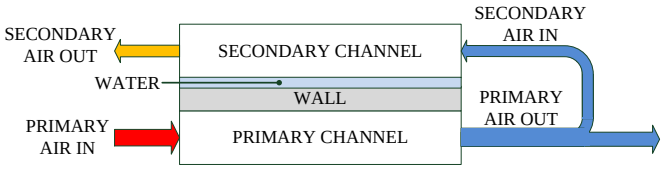

(b) Counter-flow DPC configuration.

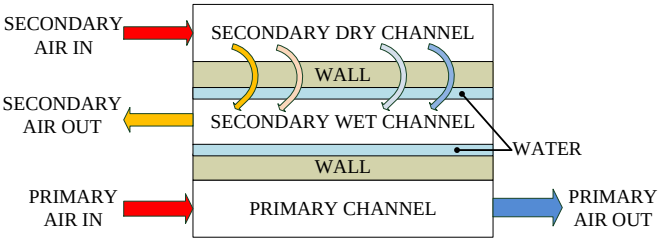

(c) Counter-flow M-cycle DPC configuration.

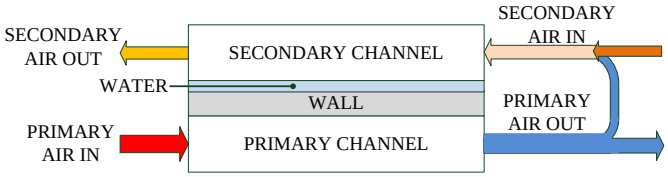

(d) Counter-flow Hybrid IEC configuration.

Figure 3.2: Examples of different IEC configurations.

Hsu et al. [62] compared IECs with parallel and counter-flow configurations with a counter-flow DPC, obtaining upper limits for their wet bulb effectiveness of 80%, 100% and 130% respectively.

Riangvilaikul and Kumar modelled and tested a vertical counter-flow DPC [63, 64], obtaining wet bulb effectiveness in the range 92-114% and dew point effectiveness in the range 58-84% for various air inlet conditions.

Janssen and Uges [65] presented a parametric analysis on the performance of a counter-flow DPC by means of a numerical model, comparing the results with experimental data. The

model and experimental data agreed well by reducing the active transfer area in the model to approximately 60% of the total geometrical area, suggesting the real DPC does not operate as described by the ideal modelling assumptions. In particular the real DPC does not work with a perfect counter-flow arrangement.
The same counter-flow DPC design was modelled and analysed by the author [10, 66] for investigating its use in desiccant cooling systems.
Zhao et al. [67–69] studied and compared cross-flow and counter-flow M-cycle DPCs by means of validated numerical models. Results showed the counter-flow configuration provides approximately 15% higher dew point effectiveness and 23% higher wet bulb effectiveness than the cross-flow configuration, as well as higher air pressure drops.
Hasan [70, 71] presented an analytical model based on a modified ε-NTU method and used it for modelling both IECs and DPCs, with good agreement with alternative numerical models and experimental data.
Anisimov et al. [72–76] and Pandelidis et al. [77–79] also adopted an analytical model based on the modified ε-NTU method and used it for investigating and comparing the performance of different DPC and M-cycle DPC configurations.
Anisimov et al. [74] studied the cross-flow M-cycle DPC configuration, reporting wet bulb effectiveness between 85 and 115 %, and dew point effectiveness between 15 and 78 % over a wide range of air inlet conditions, temperatures between 20°C and 44°C and humidity ratios between 9 and 26 g/kg. Primary air temperature drops as high as 20°C were obtained for the warmest and driest considered air inlet conditions.
Anisimov et al. [72] also simulated different DPC and M-cycle DPC configurations, concluding that counter-flow DPCs can provide lower primary air temperatures than cross-flow M-cycle DPCs.
Pandelidis et al. [80] modelled and compared two different counter-flow DPC configurations, also considering perforated walls between the dry primary channels and wet secondary channels. Perforations were found to improve the cooler temperature effectiveness for secondary to primary airflow ratios above 0.45, due improved distributions of the secondary airflow in the wet channels. However the highest cooling capacity relatively to the cooler size was found for secondary to primary airflow ratios in the range 0.3-0.45, suggesting better performances can be achieved without perforated walls.
Recently Lin et al. [81] presented a validated numerical model of the counter-flow DPC configuration, and analysed the internal heat and mass transfer processes as well as the influence of operating conditions on the cooler performance.
Pandelidis et al. [82] have also recently investigated the HIEC concept, concluding it provides supply temperatures closer to DPCs at cooling capacities closer to IECs.

3.1.1 Description of considered indirect evaporative cooler design

The counter-flow DPC design modelled and analysed in previous studies by the author [10, 66] is reported in Figure 3.3a, and termed Design 1. This DPC design reproduces the design of a commercial cooler manufactured by StatiqCooling [83].

An alternative cooler design is considered, again referring to a commercial cooler from the same manufacturer. This design is reported in Figure 3.3b, and termed Design 2.

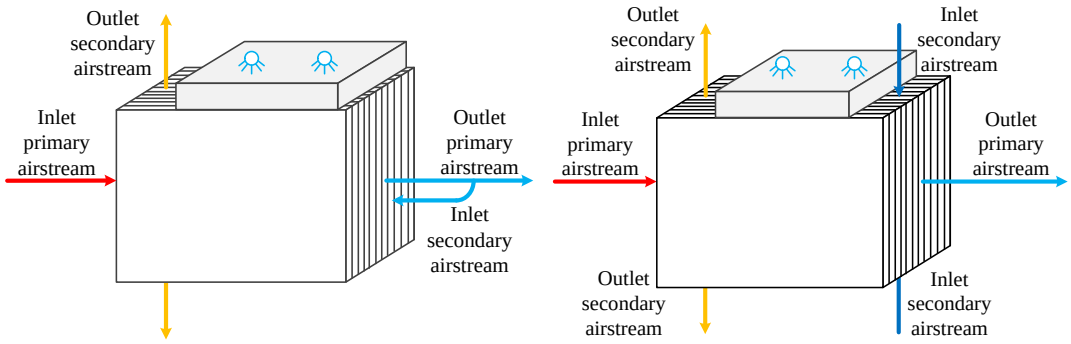

(a) Design 1. (b) Design 2.

Figure 3.3: Considered cooler designs.

Design 1 in Figure 3.3a is characterized by the placement of the secondary air inlet on the same face as the primary air outlet. Therefore it can only operate as DPC, by recirculating part of the outlet primary air stream back into the secondary wet channels. The secondary air stream flows across the cooler and it is exhausted at the top and bottom.
Design 2 in Figure 3.3b is characterized by a different positioning of the secondary air inlet, which allows to use the cooler as IEC, DPC or Hybrid IEC, depending on the composition of the secondary air stream as indicated in Figure 3.4, as well as sensible heat recovery unit. The latter option allows to use the component in air conditioning systems also during the heating season. The secondary air stream exits the cooler again from top and bottom.

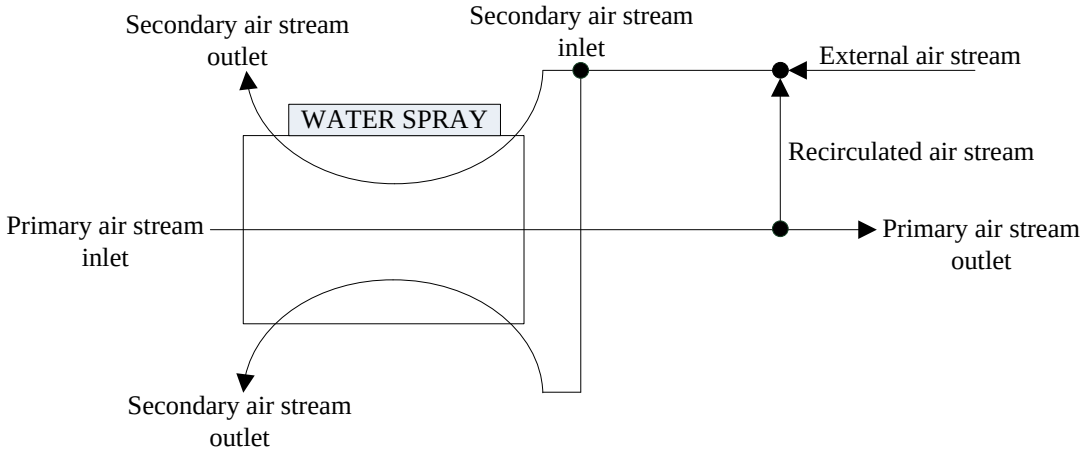

Figure 3.4: Schematics of considered flow configuration.

Considering fixed component dimensions, design 1 is expected to provide lower supply tem-

peratures as the secondary air enters the secondary channels in a counter-current arrangement with the primary air stream. However design 2 is preferable because of operational flexibility.

Independently of the design, the considered cooler is made of polypropylene structures, constituted by two plates kept separated with a series of parallel strips aligned longitudinally, resulting into a series of rectangular air channels. The polypropylene structures are covered with hygroscopic foils. Primary air is circulated inside the rectangular channels, while secondary air is circulated between adjacent structures, in direct contact with the hygroscopic foils. The resulting air flow regimes are typically laminar. A cross section of the corresponding internal structure is shown in Figure 3.5.

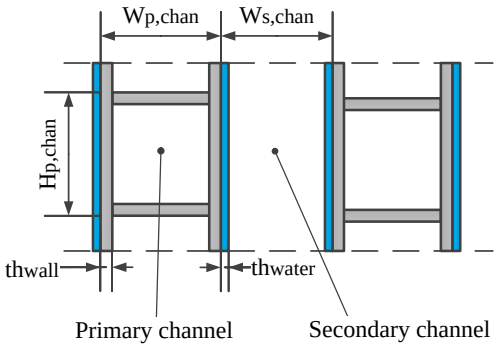

Figure 3.5: Schematics of the cooler internal structure.

A water distribution system is placed on top of the cooler to spray water onto the hygroscopic foils. The secondary channels are closed on top, hence the hygroscopic layers get wet by water diffusion due to capillary forces and gravity.
Water requires filtration and eventually softening, to avoid formation of lime scale deposits that would clog the hygroscopic layers.

The model developed for computing the steady state cooler operation is introduced in the following.

3.2 Model formulation

3.2.1 Modelling approach

A schematic representation of the modelled geometry including relevant geometrical parameters is reported Figure 3.6. The remaining geometrical parameters needed to characterize the channel dimensions and so the component width are reported in Figure 3.5.

The geometry is discretized into control volumes along the component length. Each control

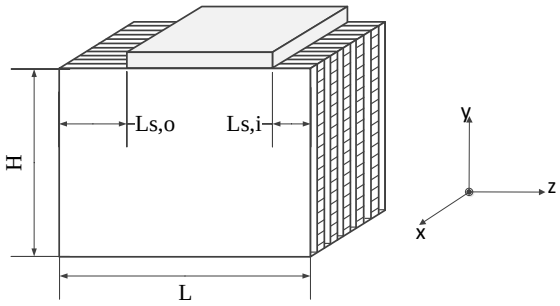

Figure 3.6: Schematics of the modelled cooler geometry.

volume includes half width of a primary channel and half width of the adjacent secondary channel, including the wall and hygroscopic layer in between. The control volume height coincides with the height of a primary air channel. The corresponding discretization is shown in Figure 3.7.

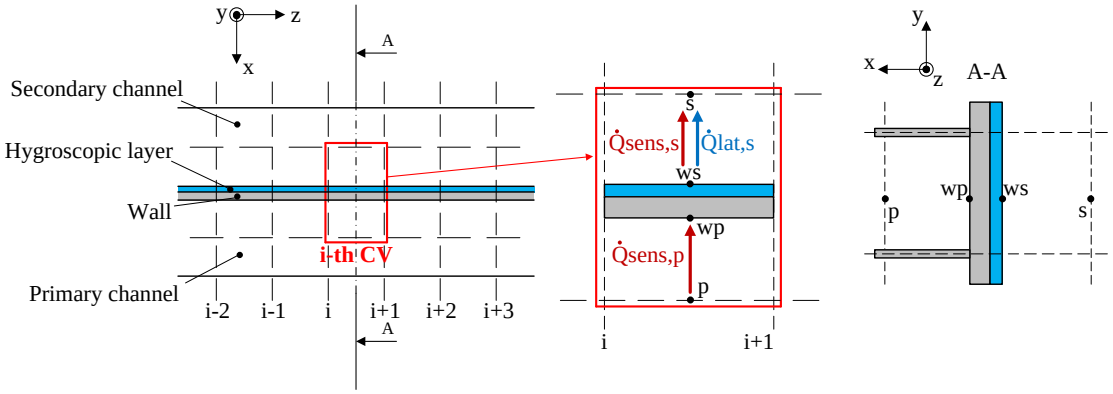

Figure 3.7: Control volume discretization approach.

Sensible heat is transferred from the primary air stream to the wall ($\dot{Q}_{sens,p}$), subsequently flowing into the secondary air stream in the form of sensible ($\dot{Q}_{sens,s}$) and latent ($\dot{Q}_{lat,s}$) heat.

3.2.2 Assumptions

The model is based on the following assumptions:

1. The cooler does not exchange heat with the surroundings.
2. The air streams are evenly distributed among the channels.
3. The primary and secondary air streams are in counter-flow arrangement along the whole cooler length.
4. Heat conduction in the airflows is neglected.

5. Heat transfer along the vertical component direction is neglected.
6. The hygroscopic foils are treated as layers of water.
7. The secondary air adjacent to the water layer is at saturated conditions.
8. The air specific thermal capacity is independent of temperature.

Under these assumptions, the inputs to the model are:

- Geometrical characteristics as indicated in Figures 3.5 and 3.6.
- Primary air stream inlet conditions including inlet temperature $T_{a,p,i}$, humidity ratio $x_{a,p,i}$ and mass flow rate $\dot{m}_{a,p,i}$.
- External air conditions eventually used for obtaining the secondary air stream including temperature $T_{a,ext}$ and humidity ratio $x_{a,ext}$.
- Secondary airflow rate and composition.
- Supply water temperature $T_{w,i}$.
- Wall material thermal conductivity k_m.
- Number of control volumes along the axial direction N_z.

3.2.3 Governing Equations

The governing equations describe the heat and mass transfer phenomena taking place between the air streams, ensuring energy and mass are conserved.
In the following the governing equations are introduced for a generic infinitesimal control volume with axial length dz.

The conservation of thermal energy in the primary air stream is written as:

$$\dot{m}_{a,p} c_{p,a,p} \frac{\partial T_{a,p}}{\partial z} = \alpha_p P_{p,eff} \left(T_{wp} - T_{a,p} \right) \tag{3.1}$$

The term on the LHS accounts for the rate of thermal energy variation in the air stream. The term on the RHS expresses the convective sensible heat transfer rate between the primary air bulk and the wall, driven by the temperature difference between these points.
$P_{p,eff}$ is the effective wall perimeter at the primary side, which considers the channel top and bottom walls as fins. The effective fin perimeter, accounting for the fin efficiency, is computed and added to the side wall perimeter (P_p).

As no mass transfer takes place in the primary channel, the conservation of moisture in the primary air stream results into:

$$\frac{\partial x_{a,p}}{\partial z} = 0 \tag{3.2}$$

The conservation of energy in the secondary air stream is written as:

$$\dot{m}_{a,s}\frac{\partial h_{a,s}}{\partial z} = \alpha_s P_s \left(T_{ws} - T_{a,s}\right) + h_{fg,T_{ref}}\sigma_s P_s \left(x_{ws} - x_{a,s}\right) \tag{3.3}$$

The term on the LHS accounts for the rate of energy variation in the secondary air stream. The first term on the RHS expresses the convective sensible heat transfer rate between the secondary air bulk and the water layer surface. The second term on the RHS expresses the convective latent heat transfer between the secondary air bulk and the water layer surface, driven by the water vapour partial pressure difference between these two points, which is reasonably approximated by the corresponding difference in humidity ratio.
P_s is the wall perimeter at the secondary side for simultaneous heat and mass transfer.
Note that $\dot{m}_{a,s}$ is a negative quantity as the secondary air stream flows oppositely to the positive axial direction.

The conservation of moisture in the secondary air stream is expressed as:

$$\dot{m}_{a,s}\frac{\partial x_{a,s}}{\partial z} = \sigma_s P_s \left(x_{ws} - x_{a,s}\right) \tag{3.4}$$

The conservation of energy in the secondary air stream is re-written introducing the enthalpy definitions from Equations 2.4 and 2.5, and Equation 3.3:

$$\dot{m}_{a,s}\frac{\partial c_{p,a,s}T_{a,s}}{\partial z} = \alpha_s P_s \left(T_{ws} - T_{a,s}\right) \tag{3.5}$$

The convective heat transfer coefficients α_p and α_s are computed for fully developed laminar flow conditions, considering average Nusselt numbers (see Equation 2.2) between constant wall heat flux and constant wall temperature. The Nusselt number for nearly squared channels (primary channels) corresponds to 3.5, while for narrow channels (secondary channels) corresponds to 7.9 [84].
The convective mass transfer coefficient σ_s is obtained from the heat and mass transfer analogy as described in Equation 2.3.

The thermal resistances of the wall and the water layer are taken into account to compute the

wall temperature difference between the two sides:

$$T_{ws} - T_{wp} = \alpha_p P_{p,eff} \left(T_{wp} - T_{a,p}\right) \left(\frac{th_{wall}}{P_p k_m} + \frac{th_{water}}{P_p k_w}\right) \tag{3.6}$$

The model is expected to overestimate the cooling performance in respect to a real component, in particular because of practical imperfect counter-flow arrangement as well as inhomogeneous air and water distributions in the channels. In this regard, two tuning parameters are introduced in the model for taking into account the discrepancies between ideal assumptions and practical operation. The two parameters are used to make parts of the heat and mass transfer areas inactive, while the active parts work under the ideal assumptions considered:

- Heat transfer area effectiveness (ε_{ht}).
  This parameter accounts for the effects that decrease the sensible heat transfer between the primary and secondary channels, e.g. imperfect counter-flow arrangement, inhomogeneous airflow distributions, etc.

- Mass transfer area effectiveness (ε_{mt}).
  This parameter accounts for the effects that decrease the evaporation of water in the secondary channels, e.g. imperfect counter-flow arrangement, inhomogeneous wetting of the hygroscopic layers, inhomogeneous airflow distributions, etc.

The tuning parameters are included in the energy and mass conservation Equations 3.1, 3.5 and 3.4:

$$\dot{m}_{a,p} c_{p,a,p} \frac{\partial T_{a,p}}{\partial z} = \varepsilon_{ht} \alpha_p P_{p,eff} \left(T_{wp} - T_{a,p}\right) \tag{3.7}$$

$$\dot{m}_{a,s} \frac{\partial c_{p,a,s} T_{a,s}}{\partial z} = \varepsilon_{ht} \alpha_s P_s \left(T_{ws} - T_{a,s}\right) \tag{3.8}$$

$$\dot{m}_{a,s} \frac{\partial x_{a,s}}{\partial z} = \varepsilon_{mt} \sigma_s P_s \left(x_{ws} - x_{a,s}\right) \tag{3.9}$$

The use of distinct parameters to modify the effective heat and mass transfer areas allows to simulate the cooler with dry secondary channels, i.e. by setting ε_{mt}=0.
Moreover the parameters could be set to different values along the component length, e.g. to account for the positioning of the secondary air inlet and outlet.

The air pressure drop in the primary channels is mainly constituted by core losses due to internal friction, as for conventional compact heat exchangers. The contributions due to initial flow contraction and final flow expansion are neglected. The core losses are computed

as [84]:

$$\Delta P_p = f_{f,p} \frac{1}{2} \overline{\rho}_{a,p} \overline{u}^2_{a,p} \frac{L}{D_h} + (\rho_{a,p,o} u^2_{a,p,o} - \rho_{a,p,i} u^2_{a,p,i}) \tag{3.10}$$

The first term on the RHS accounts for the frictional losses, while the second term accounts for the losses due to flow acceleration or deceleration along the cooler. The friction factor $f_{f,p}$ for fully developed laminar flow across nearly squared channels is inversely proportional to the Reynolds number and correspondent to $57/Re_p$ [84].

The air pressure drop in the secondary channels has a more complex nature due to the curvature of the air stream entering and leaving the component. The correspondent pressure drop is computed analogously to the primary air stream with the addition of a correction factor ($f_{\Delta P_s}$) accounting for the flow deviations:

$$\Delta P_s = \left[f_{f,s} \frac{1}{2} \overline{\rho}_{a,s} \overline{u}^2_{a,s} \frac{L}{D_h} + (\rho_{a,s,o} u^2_{a,s,o} - \rho_{a,s,i} u^2_{a,s,i}) \right] f_{\Delta P_s} \tag{3.11}$$

The friction factor $f_{f,s}$ for fully developed laminar flow across narrow channels corresponds to $96/Re_s$ [84].
The correction factor $f_{\Delta P_s}$ has to be tuned to fit experimental data.

The discretization of the governing equations and the solution strategy implemented in Matlab are described in Appendix C.

3.2.4 Performance indicators

The following indicators are chosen to describe the component performance:

- Primary air temperature drop

  $$\Delta T_p = T_{a,p,i} - T_{a,p,o} \tag{3.12}$$

  The primary air temperature drop expresses the extent to which the primary air temperature can be decreased under specified operating conditions.

- Total cooling capacity

  $$\dot{Q}_{cool,tot} = \dot{m}_{a,p} c_{p,a,p} \Delta T_p \tag{3.13}$$

  The total cooling capacity corresponds to the heat transfer rate between the primary

and secondary channels.

- Net cooling capacity

$$\dot{Q}_{cool,net} = \dot{m}_{a,p}\left(1 - f_{rec}\right) c_{p,a,p} \Delta T_p \tag{3.14}$$

The net cooling capacity corresponds to the useful cooling rate provided by the cooler, which does not correspond to the total cooling capacity if part of the primary air stream is recirculated to obtain the secondary air stream. The ratio of recirculated air stream and primary air stream is termed recirculation fraction:

$$f_{rec} = \frac{\dot{m}_{a,s,rec}}{\dot{m}_{a,p}} \tag{3.15}$$

Analogously the ratio of secondary air stream taken from an external environment and primary air stream is termed external fraction:

$$f_{ext} = \frac{\dot{m}_{a,s,ext}}{\dot{m}_{a,p}} \tag{3.16}$$

A general relationship between the secondary and primary airflow rates independent of the secondary air flow composition is introduced from the previous two definitions, termed secondary fraction:

$$f_{sec} = \frac{\dot{m}_{a,s}}{\dot{m}_{a,p}} = f_{rec} + f_{ext} \tag{3.17}$$

- Wet bulb effectiveness

$$\varepsilon_{wb} = \frac{\Delta T_p}{T_{a,p,i} - T_{a,p,i,wb}} \tag{3.18}$$

where $T_{a,p,i,wb}$ is the primary air inlet wet bulb temperature, which is the lowest theoretical temperature that can be provided by a DEC or by an IEC with equal primary and secondary air inlet wet bulb temperature.

- Dew point effectiveness

$$\varepsilon_{dp} = \frac{\Delta T_p}{T_{a,p,i} - T_{a,p,dp}} \tag{3.19}$$

where $T_{a,p,dp}$ is the primary air dew point, which is the lowest theoretical temperature that can be provided by a DPC.

- Minimum Specific Water Consumption (MSWC)

$$MSWC = \frac{\dot{m}_{w,evap}}{\dot{Q}_{cool,net}} = \frac{\dot{m}_{a,s}\left(x_{a,s,o} - x_{a,s,i}\right)}{\dot{Q}_{cool,net}} = \frac{f_{sec}\left(x_{a,s,o} - x_{a,s,i}\right)}{\left(1 - f_{rec}\right) c_{p,a,p} \Delta T_p} \tag{3.20}$$

The amount of water evaporated in the cooler represents the minimum amount of water consumed. In practise, more water is consumed by water filtration and demineralization processes, and by incomplete or absent recirculation of eventual water dripping from the cooler.

- Minimum Specific Electricity Consumption (MSEC)

$$MSEC = \frac{\dot{V}_{a,p}\Delta P_{a,p} + \dot{V}_{a,s}\Delta P_{a,s}}{\dot{Q}_{cool,net}} = \frac{\rho_{a,p}\Delta P_{a,p} + \rho_{a,s} f_{sec}\Delta P_{a,s}}{\left(1 - f_{rec}\right) c_{p,a,p}\Delta T_p} \tag{3.21}$$

The considered electricity consumption is the minimum amount required for circulating the air streams across the cooler. In practise, more electricity is consumed due to the conversion of electricity into mechanical energy in the fans as well as additional pressure drops in the ventilation system for circulating and regulating the airflows.

The above mentioned performance indicators are applicable to characterize the following modes of operation:

- IEC mode (f_{rec}=0, f_{ext}>0). Secondary air is taken from an external ambient, e.g. outdoor, indoor, treated or exhaust air from other processes.
- DPC mode (f_{rec}>0, f_{ext}=0). Secondary air is obtained by recirculating part of the cooled primary air stream.
- HIEC mode (f_{rec}>0, f_{ext}>0). Secondary air is a mix of recirculated primary air and air from an external ambient.
- Heat Recovery (HR) mode (f_{rec}=0, f_{ext}>0). No water is sprayed onto the cooler, keeping the secondary channels dry, allowing only sensible heat to be transferred between the two air streams. The use of conventional heat exchanger effectiveness definition is preferable to quantify the component performance operating in HR mode. For air conditioning applications, this mode of operation can be used during the heating season to warm up cold outdoor air with exhaust air from the indoor space.

3.3 Results and discussion

At first, results from the model are compared against manufacturer data for tuning the heat and mass transfer area effectiveness ε_{ht} and ε_{mt}, as well as the secondary air pressure drop correction factor $f_{\Delta P_s}$.
Successively the cooler operation is analysed in more details, looking at the variations of primary and secondary air stream conditions along the cooler length.
The influence of operating and geometrical parameters on the cooler performance is also presented and discussed.

3.3.1 Model validation

The heat and mass transfer coefficients ε_{ht} and ε_{mt} are tuned to match the dew point effectiveness and water evaporation rates reported by the manufacturer [83].
The cooler is operated in IEC mode, considering the dimensions and air inlet conditions reported in Tables 3.1 and 3.2. The primary air inlet conditions are assumed realistic values after dehumidification in a desiccant wheel and sensible pre-cooling. The selected secondary air inlet conditions are set equal to the primary air dew point conditions (dew point temperature and saturate conditions), meaning that the primary air dew point is the lowest theoretical temperature that the cooler can supply. As the airflow rates are kept constant, the dew point effectiveness directly reflects the primary air temperature drop.

Table 3.1: Reference cooler dimensions.

Parameter	Value
Cooler height H	760 mm
Cooler length L	1380 mm
Secondary inlet length $L_{s,i}$	100 mm
Secondary outlet length $L_{s,o}$	300 mm
Number of plates N_{plates}	158
Primary channel width $W_{p,chan}$	4 mm
Secondary channel width $W_{s,chan}$	3.4 mm
Primary channel height $H_{p,chan}$	4 mm
Wall thickness th_{wall}	0.25 mm
Hygroscopic layer thickness th_{water}	0.1 mm

Table 3.2: Reference airflow inlet conditions.

Airflow	Parameter	Value
Primary	Airflow rate $\dot{V}_{pro}$	5000 m^3/h
	Dry bulb temperature $T_{p,i}$	35°C
	Humidity ratio $x_{p,i}$	7 g/kg
Secondary	Secondary airflow fraction f_{sec}	30%
	Dry bulb temperature T_{ext}	8.7°C
	Humidity ratio x_{ext}	7 g/kg

The comparison with manufacturer data is carried out for varying primary airflow rates, indicated by primary air face velocities, and secondary fractions. The primary air face velocity is defined as the ratio of the total primary airflow rate and the face area occupied by the primary channels, approximately equal to half of the total face area.
Results are reported in Figure 3.8 for the values of heat and mass transfer area effectiveness providing the best fitting with manufacturer data, i.e. both area effectiveness equal to 0.48.
The number of axial control volumes is set to 20, as the air stream outlet conditions do not change for finer grids.

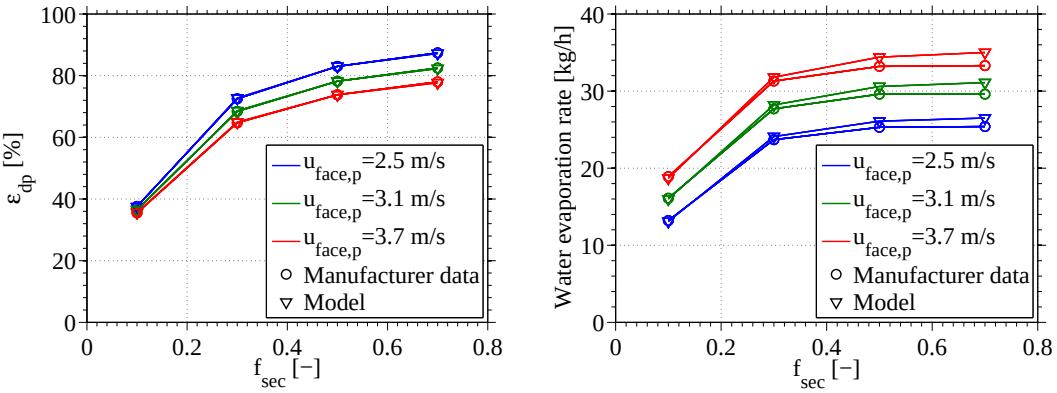

(a) Dew point effectiveness.

(b) Water evaporation rate.

Figure 3.8: Model validation against manufacturer data with ε_{mt}=ε_{ht}=0.48.

Figure 3.8 shows that the dew point effectiveness computed by the tuned model, with heat and mass transfer area effectiveness of 48%, match well the values reported by the manufacturer. Also the computed water evaporation rate is in good agreement with manufacturer data, with differences within 5% at higher secondary fractions.
The secondary fraction has a similar effect on both the dew point effectiveness and the water evaporation rate, while the primary airflow rate affects water consumption the most.
It can also be noticed that, for a fixed secondary fraction, lower primary airflow rates lead to higher cooling performance and lower water evaporation rates, as well as lower pressure drops.

The same values of transfer area effectiveness are found to provide the same level of agreement with manufacturer data also for different cooler geometries, if the ratios of inlet and outlet secondary opening lengths and cooler length are kept constant to $L_{s,i}/L \approx 7\%$ and $L_{s,o}/L \approx 21\%$ (see Figure 3.6). This confirms the idea that the secondary inlet and outlet regions introduce the most important inefficiencies, as no water is sprayed directly from the top and the secondary airflow changes direction from cross-flow to counter-flow arrangement in respect to the primary airflow.

The secondary airflow pressure drop correction factor is found to be dependent on the component height, still considering constant ratios of inlet and outlet secondary opening lengths and cooler length:

$$f_{\Delta P_s,corr} = 0.9087 e^{1.454 H} \tag{3.22}$$

The resulting air pressure drops computed by the model for varying primary and secondary airflow rates are reported in Figure 3.9.

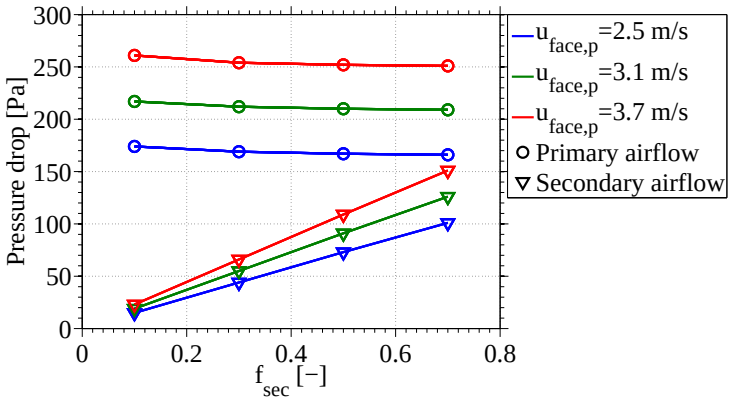

Figure 3.9: Air pressure drops matching manufacturer data.

It can be noticed that both primary and secondary pressure drops vary linearly for varying airflow rates, as the flow regimes are laminar.
As the secondary pressure drop increases at a faster rate than the dew point effectiveness for increasing secondary fractions, an optimum secondary fraction minimizing the Minimum Specific Electricity Consumption ($MSEC$) is expected.

3.3.2 Analysis of cooler operation

The model provides information on the air temperature and humidity variations along the cooler length, which are reported for both IEC and DPC modes, considering the cooler dimensions reported in Table 3.1 and the primary air inlet conditions reported in Table 3.2. In IEC mode, the secondary air inlet temperature and humidity are set equal to the primary air stream conditions. The resulting processes are presented on psychrometric charts in Figure 3.10, and the resulting performance indicators are reported in Table 3.3.

Table 3.3: Comparison of performance indicators for IEC and DPC modes.

Performance indicator	IEC mode	DPC mode
Primary air temperature drop [°C]	12.5	16
Net cooling capacity [kW]	20.1	17.8
Wet bulb effectiveness [%]	77	98
Dew point effectiveness [%]	48	60
MSWC [kg/kWh]	1.62	1.68
MSEC [-]	0.016	0.018

The processes reported in Figure 3.10 show that the primary air stream is cooled at constant humidity ratio, while the secondary air stream is initially cooled and successively heated, and simultaneously humidified. The secondary air stream is cooled until the potential for

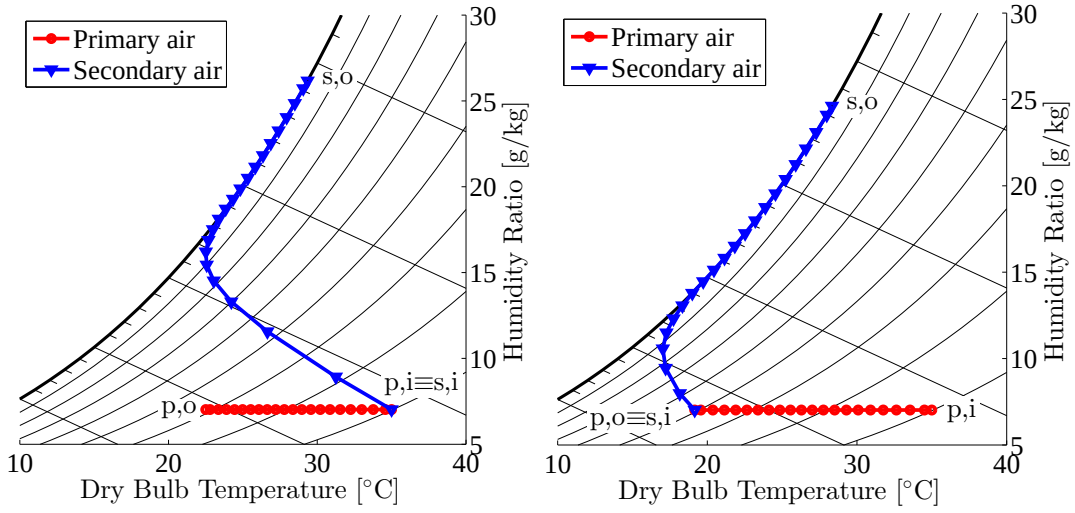

(a) IEC mode.

(b) DPC mode.

Figure 3.10: Example of considered psychrometric processes.

evaporating water is high enough, so that heat required for evaporation is extracted directly from the secondary air stream, starting to be heated as it approaches saturation.
The performance indicators reported in Table 3.3 indicate the IEC mode provides higher supply temperatures but higher useful cooling capacities than the DPC mode, considering equal cooler dimensions, primary air inlet conditions and secondary airflow rates. The IEC mode is also characterized by higher MSWC and MSEC, even though the water evaporation rate is higher than in DPC mode, and the minimum electricity consumption is nearly equal. The wet bulb effectiveness indicates that the DPC provides colder temperatures than conventional DECs (typically approaching 90% [4]), while the dew point effectiveness indicates the cooler is still far from exploiting the whole theoretical potential.

More details on both the IEC and DPC modes of operation are provided in Figure 3.11, which reports the corresponding temperature and humidity profiles along the cooler length, as well as the resulting heat flow rates at the secondary side. The wall temperature is indicated by means of the secondary wall temperature, as the temperature difference across the wall is much smaller than the temperature differences at the air sides, indicating the wall thermal resistance is negligible.

All graphs in Figure 3.11 are divided into two zones by vertical dashed lines, which point out the dimensionless axial positions at which the temperature of the secondary air stream equals the temperature of the wall. At these positions the secondary air stream temperature inverts its trend of variation along the flow direction from an initial decrease to a successive increase. Figures 3.11a, 3.11c and 3.11e provide a comprehensive picture of the processes involved in

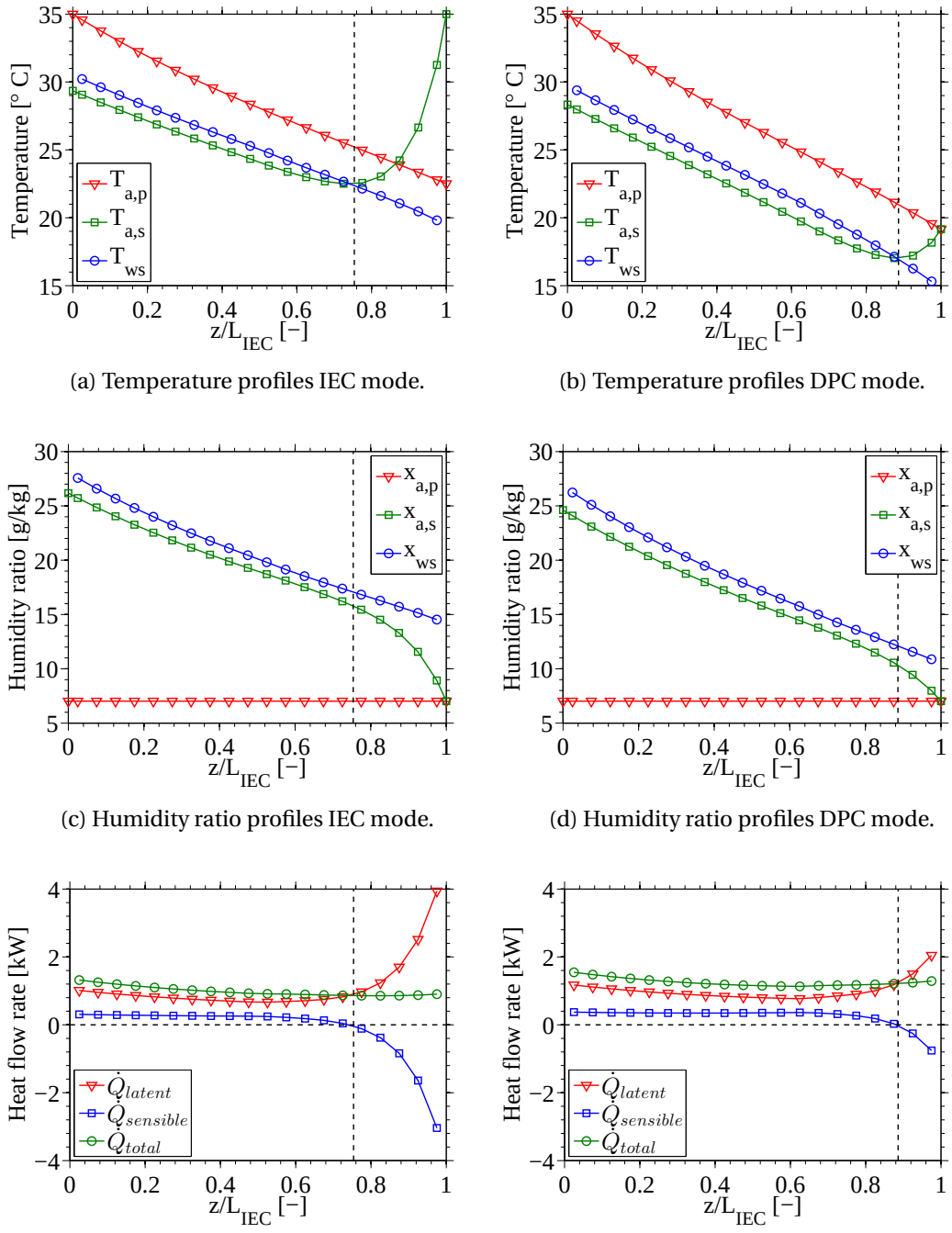

(a) Temperature profiles IEC mode.

(b) Temperature profiles DPC mode.

(c) Humidity ratio profiles IEC mode.

(d) Humidity ratio profiles DPC mode.

(e) Heat transfer rate profiles IEC mode.

(f) Heat transfer rate profiles DPC mode.

Figure 3.11: Internal variations for IEC and DPC modes.

IEC mode. The initial secondary air stream temperature decrease is rapid and associated to a high potential for water evaporation, which is expressed by the humidity ratio difference between the air bulk and the saturated air in thermal equilibrium with the wall. The split of

heat flow rates into latent and sensible components indicates that the high cooling rate, i.e. negative sensible heat flow rate, is associated to a high evaporation rate, i.e. positive latent heat flow rate. The total heat transfer rate at the secondary side, which is opposite to the heat transfer rate at the primary side, does not vary significantly along the cooler length despite of the sensible and latent component variations, resulting into a nearly linear primary air temperature profile.
Similar considerations can be drawn for the DPC mode, which is characterized by smaller potentials for evaporation of water at the inlet of the secondary channels, resulting into smaller latent and sensible heat rates. As a consequence, the position at which the secondary air stream reaches thermal equilibrium with the wall is closer to the secondary channel inlet than in IEC mode.
Figure 3.11a and 3.11b show that, when the secondary air temperature is below the wall temperature, the temperature difference between the air bulk and the wall is higher at the primary side. This indicates that reductions of the heat transfer resistance at the primary side can provide important improvements on the cooler cooling performance, e.g. by employing optimized fin geometries.

3.3.3 Influence of heat and mass transfer area effectiveness

The influence of both transfer area effectiveness on the cooling performance is investigated for the following cases:

1. ε_{mt} is varied for the cooler operating in IEC mode, with ε_{ht}=1.
2. ε_{mt} is varied for the cooler operating in DPC mode, with ε_{ht}=1.
3. ε_{mt} is set equal to ε_{ht} and varied for the cooler operating in DPC mode.
4. ε_{ht} is varied for the cooler operating in HR mode, with ε_{mt}=0.

The cooler dimensions and air stream conditions are the same as reported in Table 3.1 and 3.2. Results are shown in Figure 3.12.

Figure 3.12 shows that, when decreasing only one transfer area effectiveness (cases 1,2 and 4), the dew point effectiveness drops up to 10% for transfer area effectiveness values between 1 and 0.25, while it drops rapidly for lower transfer area effectiveness values. Differently, when decreasing both heat and mass transfer area effectiveness (case 3), the dew point effectiveness drops more gradually.
The highest dew point effectiveness are reached in IEC mode (case 1), as the secondary air inlet conditions are set equal to the primary air dew point. Therefore case 1 represents an upper limit for cases 2 and 3, i.e. for the DPC mode, with maximum dew point effectiveness of 80% related to the specific cooler dimensions. Cases 2 and 3 are coincident for transfer

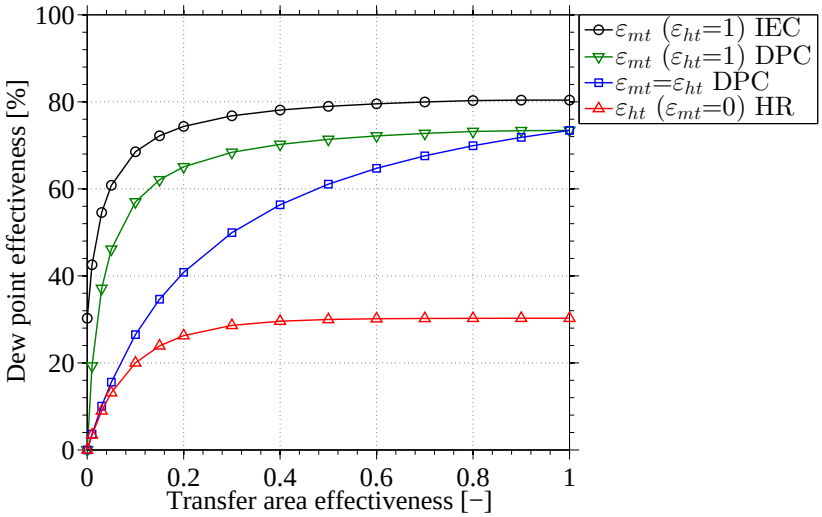

Figure 3.12: Influence of heat and mass transfer area effectiveness on cooling performance.

area effectiveness equal to 1, with dew point effectiveness of 73%, which is quite close to the upper limit given by case 1. For ε_{mt}=0, the cooler does not provide any cooling in DPC mode as primary and secondary inlet conditions become equal, while it still provides cooling in IEC mode as the secondary air inlet temperature is independent of the outlet primary air temperature.
The heat and mass transfer coefficients selected to match manufacturer data are set equal to 0.48, which for case 3 results in 60% dew point effectiveness. The same effectiveness is achieved in case 2 with ε_{mt}=0.12.
The comparison of IEC and HR modes (cases 1 and 4) highlights the contribution of indirect evaporative cooling to the cooling capacity. The dew point effectiveness in case 1 increases more than 150% compared to case 4 because of the additional latent heat transferred for evaporating water in the secondary channels. It can also be noticed that case 1 with ε_{mt}=0 and case 4 with ε_{ht}=1 provide the same cooling capacity, as they represent the same conditions of operation.

More details about the difference between separate and simultaneous variations of the transfer coefficients are provided in Figure 3.13, for the DPC mode with ε_{mt}=0.12 and ε_{ht}=1 (case 2), and with ε_{mt}=ε_{ht}=0.48 (case 3), which provide the same cooling performance and so the same primary air outlet temperature.

Figures 3.13a and 3.13b show that the secondary air stream reaches saturation along the channel in case of equal transfer area effectiveness, while it tends to a lower degree of saturation in case of penalized mass transfer area effectiveness. It can also be observed that the secondary air outlet humidity ratio is higher in case of equal transfer area effectiveness, indicating more water is evaporated for providing the same cooling capacity.

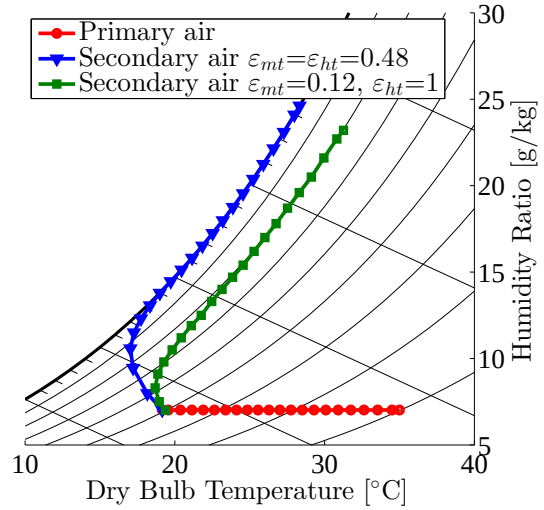

(a) Psychrometric processes.

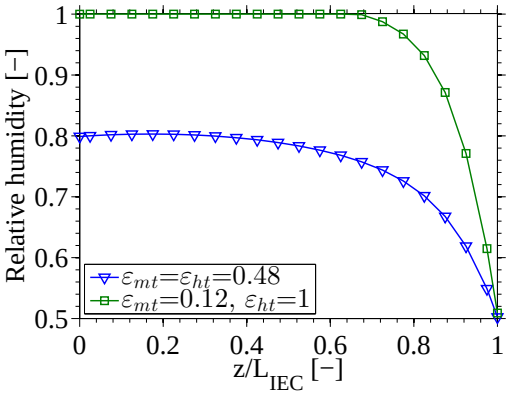

(b) Secondary air relative humidity.

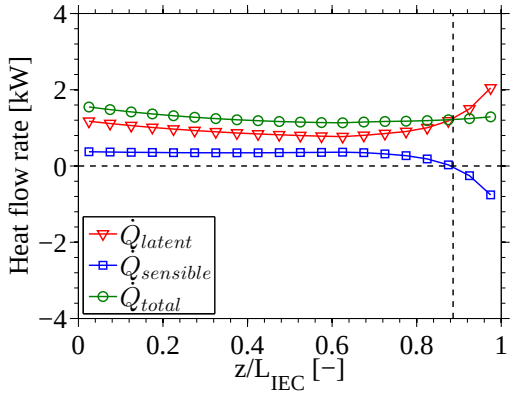

(c) Secondary side heat transfer rates with ε_{mt}=ε_{ht}=0.48.

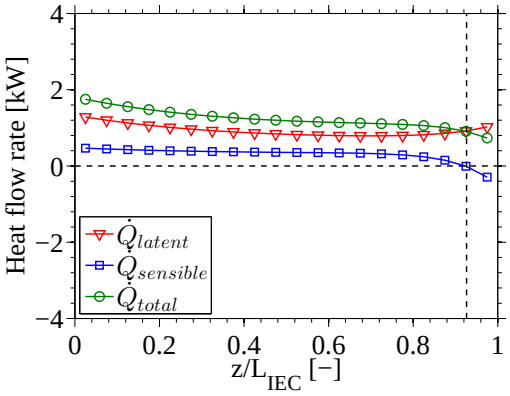

(d) Secondary side heat transfer rates with ε_{mt}=0.12 and ε_{ht}=1.

Figure 3.13: Influence of heat and and mass transfer area effectiveness on DPC mode.

Figures 3.13c presents the same results as Figure 3.11f.
Figure 3.13d shows that the secondary air stream reaches thermal equilibrium with the wall at a closer position to the channel inlet than in Figure 3.13c, and the initial latent heat flow rate is lower, resulting into lower sensible and total heat flow rates.

3.3.4 Influence of operating conditions

The effects of varying air inlet conditions (temperature and humidity at both primary and secondary sides), air flow rates, and secondary air composition are investigated for the cooler geometry specified in Table 3.1.

The external ambient from which part of the secondary air can be taken is considered at the same inlet conditions of the primary air, unless differently stated.

Air inlet conditions

The primary air inlet conditions are varied in the temperature range from 15 to 45°C and humidity ratio range from 7 to 20 g/kg. Both IEC and DPC modes are considered. In IEC mode, the secondary air inlet conditions are set equal to the primary air inlet conditions. The primary airflow rate and secondary fraction are kept constant to 5000 m^3/h, i.e. constant primary air face velocity, and 0.3 respectively, as for the reference scenario in Table 3.2. The effects on the dew point and wet bulb effectiveness, primary air temperature drop, and MSWC are reported in Figure 3.14 for the IEC mode and in Figure 3.15 for the DPC mode. As the mass airflow rates are nearly constant, the total and net cooling capacities are expected to vary in accordance with the primary air temperature drop, so they are not reported in Figures 3.14 and 3.15. For the same reason also the MSEC is not reported. Results are presented on psychrometric charts, such that each point on the chart corresponds to a specific set of primary air inlet conditions, while the resulting performance indicators are reported by means of iso-value curves. Results are shown for primary air inlet relative humidities up to 90%, as the cooling potential drops rapidly for primary air inlet conditions approaching saturation.

Figures 3.14a, 3.15a, 3.14b, and 3.15b show that both the dew point and wet bulb effectiveness increase for increasing primary air inlet temperatures and humidity ratios. The dew point effectiveness ranges approximately from 48% to 78% in DPC mode and from 36% to 66% in IEC mode, while the wet bulb effectiveness ranges approximately from 84% to 104% in DPC mode and from 63% to 87% in IEC mode. The wet bulb effectiveness is more dependent on the temperature than on the humidity ratio of the primary air stream, while the dew point effectiveness is nearly constant along iso-enthalpy lines, particularly at low humidity ratios and relative humidities.
Figures 3.14c and 3.15c show that the primary air temperature drop increases for warmer and drier primary air inlet conditions both in IEC and DPC modes. The cooler operating in DPC mode provides higher temperature drops, with corresponding lower net cooling capacities than in IEC mode.
Figures 3.14d, and 3.15d show that the MSWC increases for warmer and more humid primary air inlet conditions. The MSWC varies less than 10% in the whole range of considered primary air inlet conditions for both IEC and DPC modes. Therefore the amount of water evaporated in the cooler per unit of cooling provided (or unit of primary air temperature drop) can be reasonably considered independent of the primary air inlet conditions.

The effect of varying secondary air inlet conditions is investigated for the cooler operating in IEC mode. The secondary air inlet temperature is varied between 15 and 45°C and its humidity ratio between 7 and 20 g/kg, while the primary air inlet conditions are kept constant to 35°C and 7 g/kg as for the reference scenario in Table 3.2. Results are shown in Figure 3.16 in

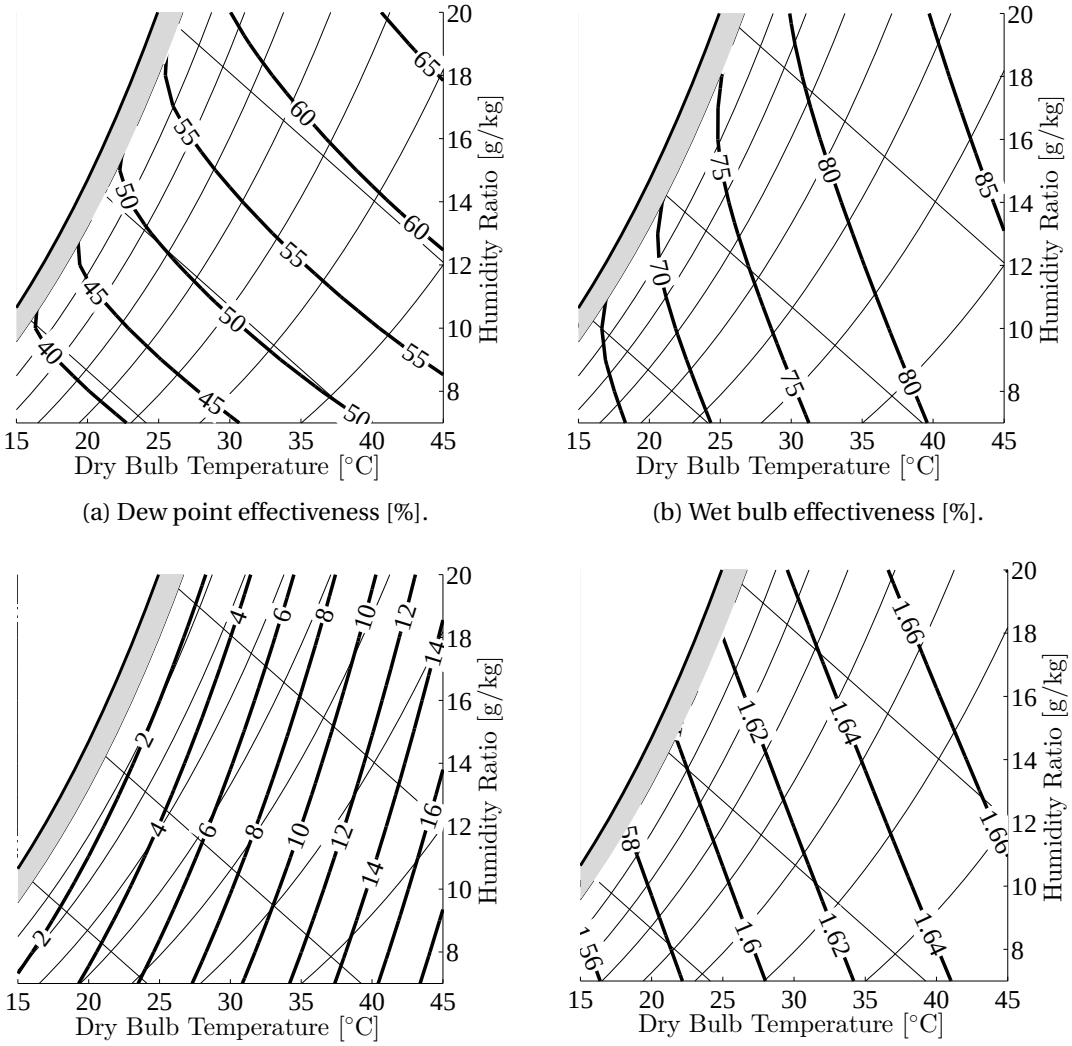

(a) Dew point effectiveness [%].

(b) Wet bulb effectiveness [%].

(c) Primary air temperature drop [°C].

(d) MSWC [kg_w/kWh].

Figure 3.14: Influence of primary and secondary air inlet conditions in IEC mode.

terms of primary air temperature drop and water evaporation rate. The total and net cooling capacities, and the dew point and wet bulb effectiveness are expected to vary in accordance with the primary air temperature drop, as the airflow rates are not varied. For the same reason also the MSEC is not reported.

Figure 3.16a shows that the primary air temperature drop increases for colder and drier secondary air inlet conditions. It can be noticed that the primary air temperature drop is constant for secondary air inlet conditions having the same enthalpy. This result suggests that the air stream with the lowest enthalpy among the available air streams (e.g. outdoor, indoor space, other processes, etc.) should be used as secondary air stream to maximize the cooling performance.

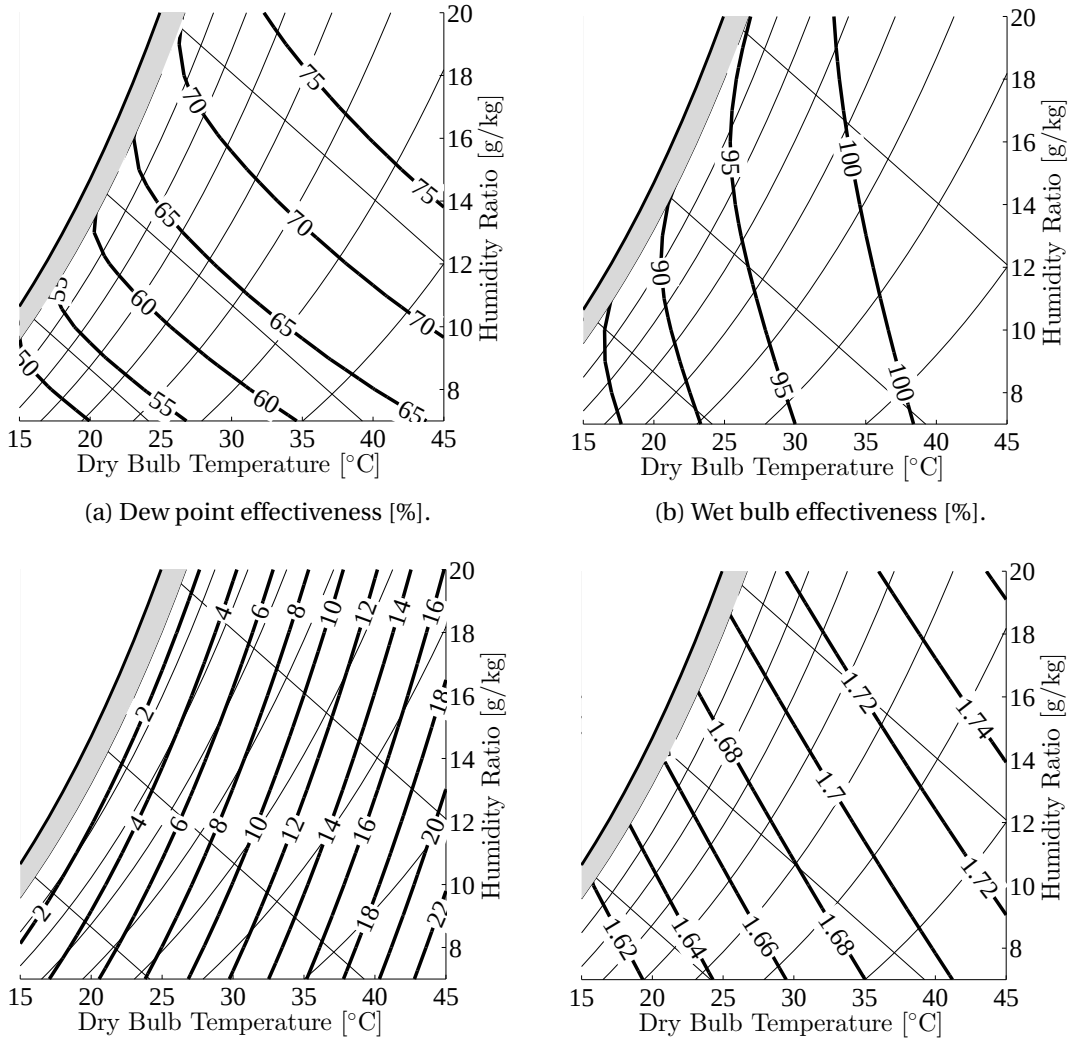

(a) Dew point effectiveness [%].

(b) Wet bulb effectiveness [%].

(c) Primary air temperature drop [°C].

(d) MSWC [kg_w/kWh].

Figure 3.15: Influence of primary air inlet conditions in DPC mode.

Figure 3.16b shows the MSWC increases up to 90% for increasing secondary air inlet temperatures, particularly at high temperatures, with a weak dependence on the secondary air inlet humidity ratio. Therefore the amount of water evaporated in the cooler in IEC mode per unit of cooling provided (or unit of primary air temperature drop) can be considered dependent on the secondary air inlet temperature only.

Air flow rates and secondary air composition

The effects of varying primary airflow rates and secondary air fractions are investigated for the cooler operating in IEC and DPC modes. Primary air inlet conditions are kept constant at

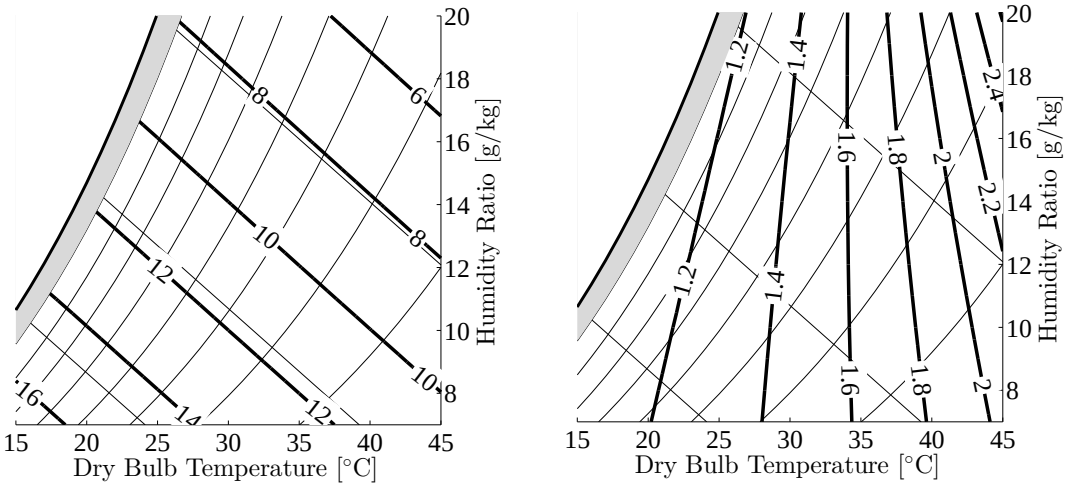

(a) Primary air temperature drop [°C].

(b) MSWC [kg_w/kWh].

Figure 3.16: Influence of secondary air inlet conditions in IEC mode for constant primary air inlet conditions ($T_{p,i}$=35°C and $x_{p,i}$=7 g/kg).

35°C and 7 g/kg, and secondary air inlet conditions in IEC mode are set equal to primary air inlet conditions. The primary airflow rate is expressed in terms of the primary air face velocity, varied from 2 to 5 m/s. The secondary fraction, being either the external or the recirculation fraction depending on the mode of operation, is varied between 0.15 and 0.5. Results are shown in Figure 3.17 in terms of primary air temperature drop and net cooling capacity, and in Figure 3.18 in terms of MSWC and MSEC. The dew point and wet bulb effectiveness vary in accordance to the primary air temperature drop.

Figures 3.17a and 3.17b show that the primary air temperature drop depends weakly on the primary air face velocity at low secondary fractions, and vice versa at high secondary fractions. The cooler in DPC mode provides higher temperature drops with a stronger influence on the secondary fraction.
Figures 3.17c and 3.17d show different variations of the net cooling capacity depending on the cooler operation. In IEC mode, the net cooling capacity (equivalent to the total cooling capacity) increases for increasing primary air face velocities and secondary fractions, with a strong dependence on the primary air face velocity for high secondary fractions. In DPC mode, the net cooling capacity peaks at a specific secondary fraction for each primary air face velocity, indicated by the dotted line in Figure 3.17d, as there is a trade-off between primary air temperature drop and supply air flow rate due to partial recirculation of the cooled primary air stream. In DPC mode, the recirculation fractions providing the maximum net cooling capacities are nearly independent of the primary air face velocity, ranging from approximately 0.3 to 0.28 for increasing primary air face velocities. For both modes of operation, the net cooling capacity increases for increasing primary air velocity, oppositely to the primary air temperature drop. The net cooling capacity in IEC mode is always higher than in DPC mode

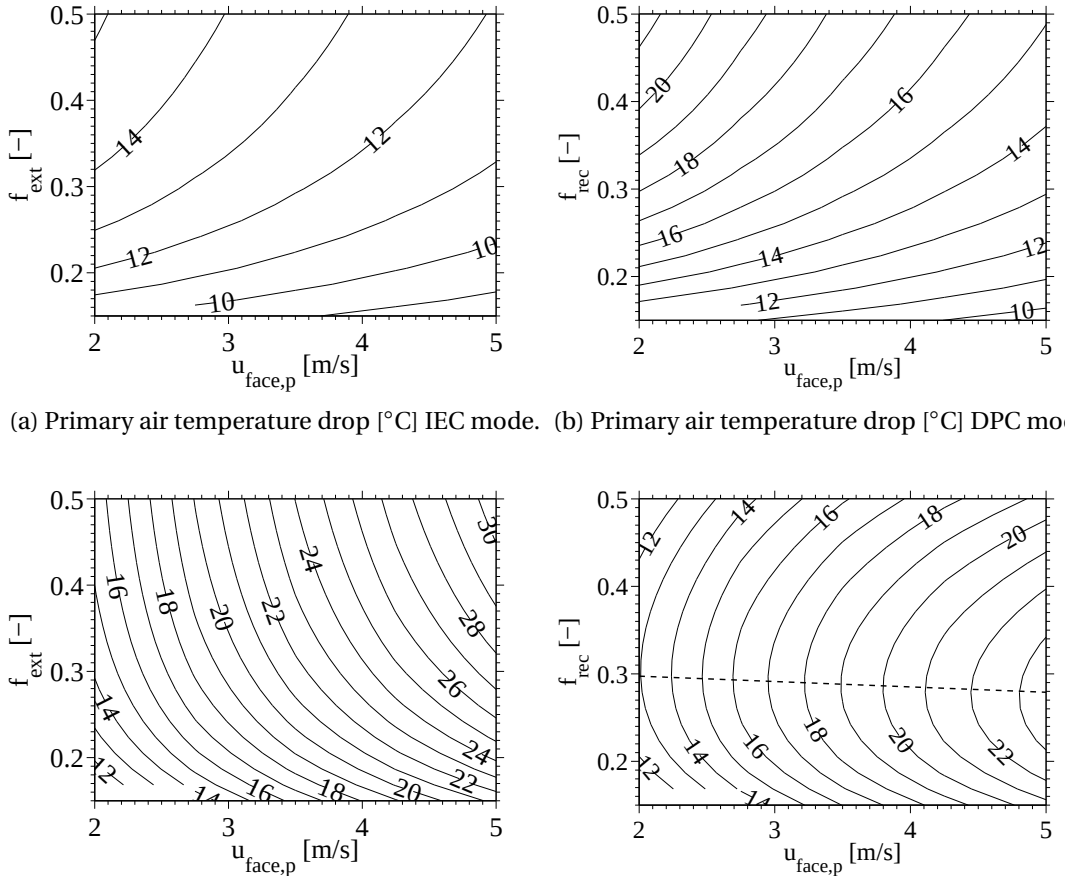

(a) Primary air temperature drop [°C] IEC mode. (b) Primary air temperature drop [°C] DPC mode.

(c) Net cooling capacity [kW] IEC mode. (d) Net cooling capacity [kW] DPC mode.

Figure 3.17: Influence of primary air velocity and secondary air fraction on cooling performance.

for the same primary air face velocity and secondary fraction, tending to similar values for low recirculation fractions.

Figures 3.18a and 3.18b show that the MSWC is mainly influenced by the secondary fraction, varying the most for the cooler operating in DPC mode.
Figures 3.18c and 3.18d show the MSEC is minimized for specific secondary fractions at different primary air face velocities, as indicated by the dashed lines. In IEC mode, the optimal external fraction that minimizes the MSEC is approximately 0.32 for the whole range of primary air face velocities. In DPC mode, the optimal recirculation fraction ranges from 0.26 to 0.24, slightly lower values than the ones maximizing the net cooling capacity.

The effect of different secondary air compositions is investigated varying the external and recirculation fractions in the range 0.15-0.5, i.e. the cooler is operated in IEC mode (f_{rec}=0),

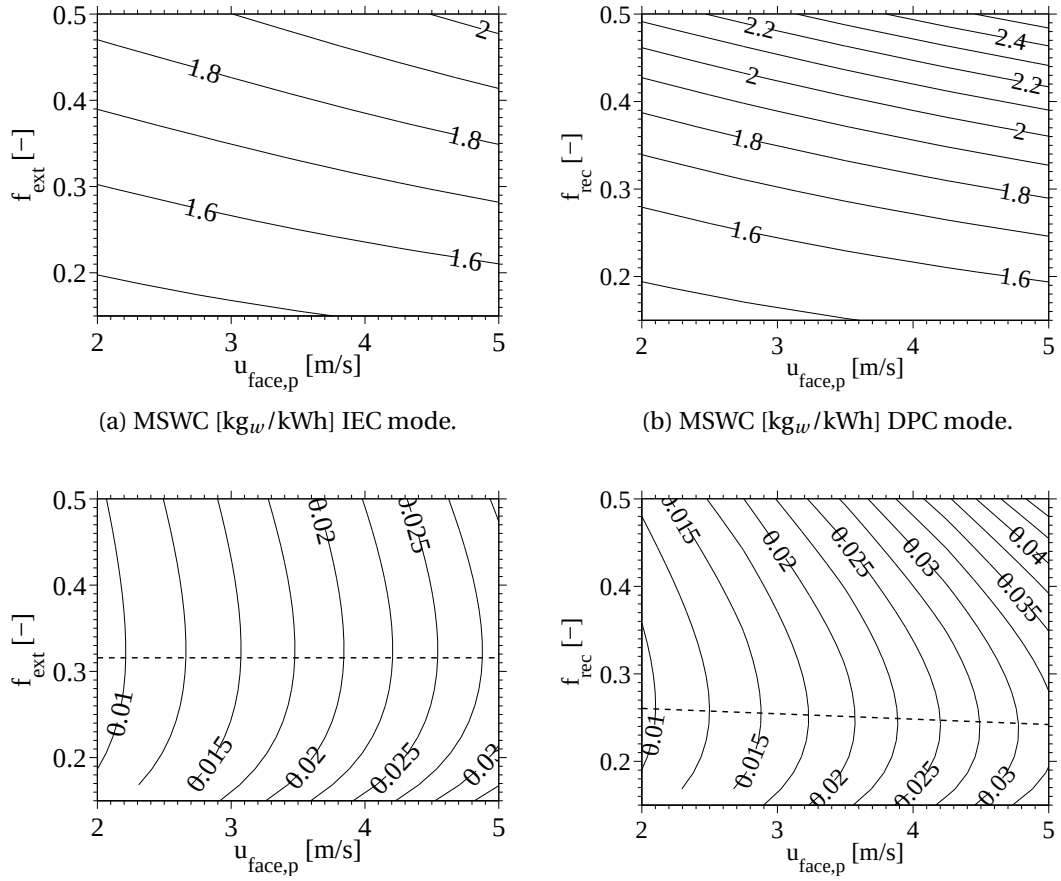

(a) MSWC [kg_w/kWh] IEC mode.

(b) MSWC [kg_w/kWh] DPC mode.

(c) MSEC [-] IEC mode.

(d) MSEC [-] DPC mode.

Figure 3.18: Influence of primary air velocity and secondary air fraction on water and electricity consumptions.

DPC mode (f_{ext}=0), and HIEC mode (f_{rec}>0 and f_{ext}>0). The primary airflow rate is kept constant to 5000 m^3/h. Results are reported in Figure 3.19 in terms of primary air temperature drop, net cooling capacity, MSWC and MSEC. The total cooling capacity and the dew point and wet bulb effectiveness vary in accordance with the primary air temperature drop. Results for secondary fractions below 0.15 are not shown, as the corresponding secondary air velocities are extremely low (below 0.3 m/s).

Figure 3.19a shows that, when operating the cooler in HIEC mode, the primary air temperature drop increases for increasing external fractions if the recirculation fraction is lower than approximately 0.32, and vice versa for higher recirculation fractions.
Figure 3.19b shows that the net cooling capacity always increases for increasing external fractions when there is no recirculation (f_{rec}=0), while it peaks for a recirculation fraction of 0.29 when there is no external air (f_{ext}=0), confirming the results from Figures 3.17c and 3.17d. When operating the cooler in HIEC mode, the net cooling capacity increases for increasing

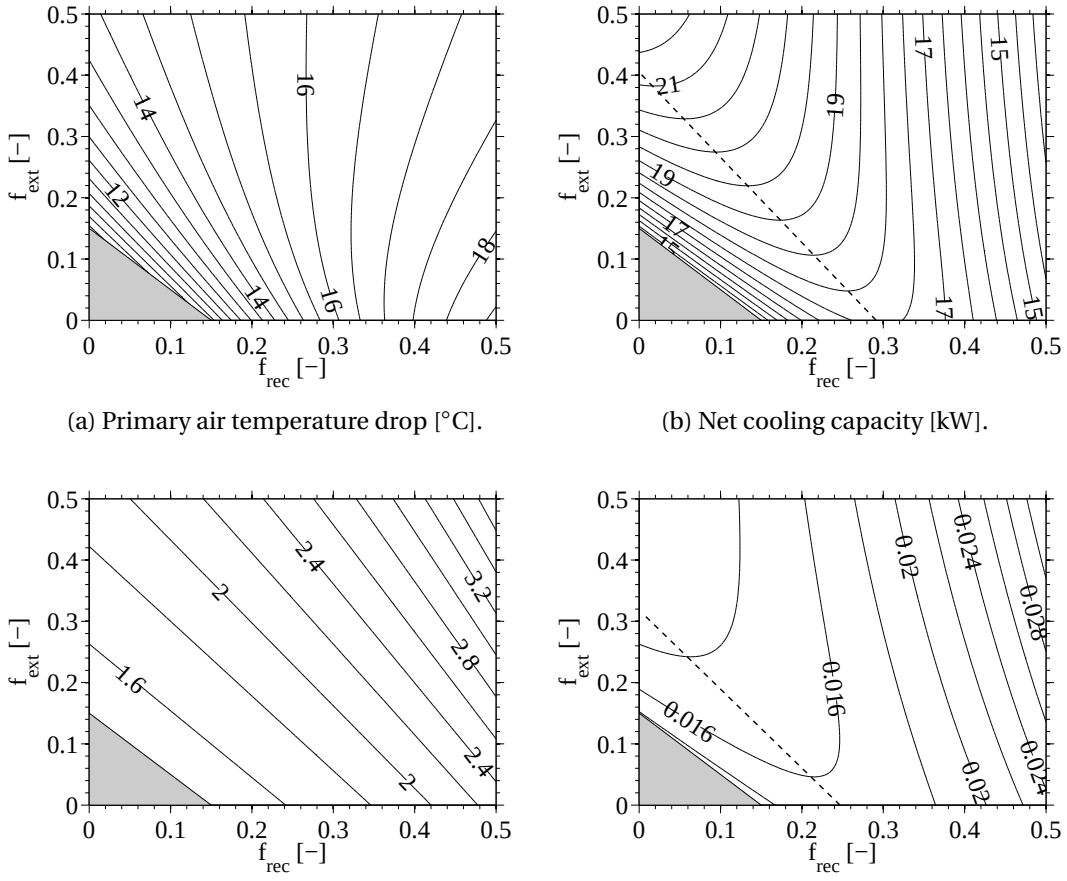

(a) Primary air temperature drop [°C].

(b) Net cooling capacity [kW].

(c) MSWC [kg_w/kWh].

(d) MSEC [-].

Figure 3.19: Influence of airflow fractions on cooler performance.

external fractions up to approximately 0.32, while the recirculation fraction maximizing the net cooling capacity decreases for increasing external fractions, becoming null for external fraction of 0.4, as indicated by the dashed line in Figure 3.19b.
Figure 3.19c shows that the MSWC always increases for increasing secondary air fractions, i.e. increasing external and recirculation fractions, particularly at high recirculation fractions.
Figure 3.19d shows that the MSEC varies analogously to the net cooling capacity, with lower recirculation fractions minimizing the MSEC in HIEC mode, indicated by the dashed line.

3.3.5 Influence of geometrical parameters

The influence of varying geometrical parameters is investigated for the cooler operating in DPC mode. The primary air inlet conditions are kept constant at 35°C and 7 g/kg, with primary airflow rate of 5000 m^3/h and secondary fraction of 0.3.
Results are reported in Figure 3.20 for varying cooler length and face area dimensions (cooler

width and height) in terms of primary air temperature drop, MSWC, MSEC and resulting cooler volume. The dew point and wet bulb effectiveness, and the cooling capacities vary analogously to the primary air temperature drop. The face area dimensions are represented by the primary air face velocity, as the effect of increasing the cooler width, i.e. the number of plates, or the cooler height is to reduce the primary air face velocity for a constant airflow rate. The corresponding cooler volume is computed assuming a constant ratio between the cooler width and height of approximately 1.55, as for the cooler geometry reported in Table 3.1. Different face area proportions are not expected to have a significant influence on the results.

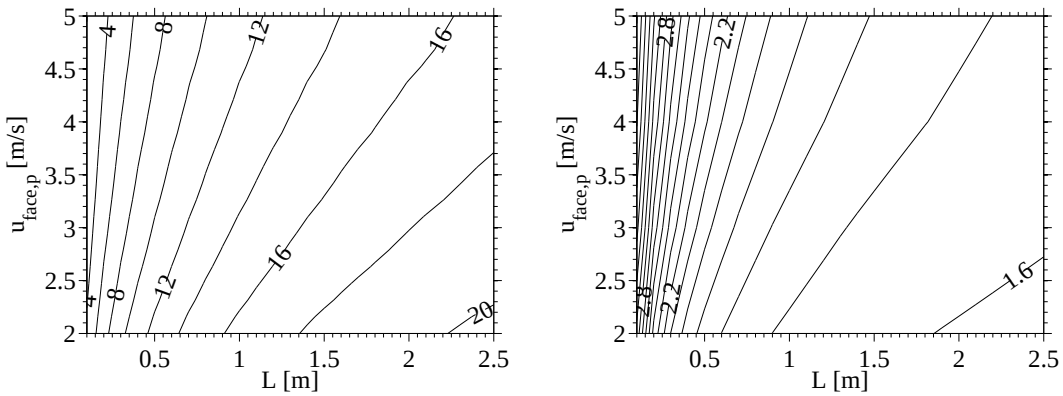

(a) Primary air temperature drop [°C].

(b) MSWC [kg_w/kWh].

(c) MSEC [-].

(d) Cooler volume [m^3].

Figure 3.20: Influence of cooler dimensions.

Figure 3.20a shows that longer coolers provide higher cooling performance. The cooler performance increase rate for increasing cooler lengths decreases as the cooler length increases, particularly at low primary air face velocities, i.e. larger face areas.
Figure 3.20b indicates the MSWC changes similarly to the primary air temperature drop. The MSWC is nearly insensitive to the face area dimensions for short coolers, and it varies little for long coolers.

Figure 3.20c shows the MSEC increases for increasing primary air face velocities and longer coolers, as the air pressure drops increase more than the net cooling capacity.
Figure 3.20d indicates that improved cooling performance and improved utilization of water are achieved at the expense of significantly bulkier coolers. The resulting volumes suggest the cooler is likely to be the bulkier component in complete desiccant cooling systems. The same trends are noticed for the cooler operating in IEC mode.

3.4 Conclusions

A one-dimensional steady state model of counter-flow indirect evaporative coolers has been developed. The model allows to simulate different cooler geometries and operating conditions. From model simulations, it is concluded that:

- The considered cooler design provides good flexibility of operation. Four modes of operation have been identified, namely indirect evaporative cooling, dew point cooling, hybrid indirect evaporative cooling, and heat recovery. Therefore the component can be used for both space cooling and heating.
- There is no direct relationship between the cooling capacity, which is directly proportional to the primary air temperature drop, and the cooler effectiveness, in respect to both dew point and wet bulb. Therefore the dew point and wet bulb effectiveness do not provide a meaningful comparison of coolers operating with different primary and secondary air inlet conditions.
- Dew point cooling supplies the lowest temperatures at the expense of lower supply airflow rates, due to the partial recirculation of the cooled air stream.
- Hybrid indirect evaporative cooling lowers the supply temperature in respect to indirect evaporative cooling, and increases the supply flow rate in respect to dew point cooling.
- The indirect evaporative cooling performance are constant for secondary air streams with the same enthalpy. This suggests the secondary air flow should be selected on an enthalpy basis among available streams.
- Optimal recirculation fractions, maximizing the supply cooling capacity, are identified for dew point cooling around 30%, and for hybrid indirect evaporative cooling depending on the external fraction and external air conditions.
- Optimal secondary fractions, minimizing the electricity consumption per unit of cooling supplied, are identified for all modes of cooling. In case of dew point cooling and hybrid indirect evaporative cooling, the recirculation fractions minimizing the specific electricity consumption are lower than the recirculation fractions maximizing the supply cooling capacity.

4 System design and operation

4.1 System design

The solid desiccant cooling system investigated in this study is characterised by the use of indirect evaporative cooling processes. For this reason the system is termed Desiccant Indirect Evaporative Cooling (DIEC) system in the following.
The DIEC system is composed of a Desiccant Wheel (DW), a Regeneration Heater (RH), an air-to-air Heat Exchanger (HEX), and an Indirect Evaporative Cooler (IEC). The IEC can be operated as conventional IEC, Dew Point Cooler (DPC), or Hybrid Indirect Evaporative Cooler (HIEC), in accordance with the classification provided in Figure 3.1. The IEC's design reported in Figure 3.4 is considered to obtain this flexibility of operation.
A schematic representation of the DIEC system is shown in Figure 4.1, including fans for air circulation and dampers for regulating the IEC secondary air composition and fraction. The corresponding psychrometric processes are also indicated.

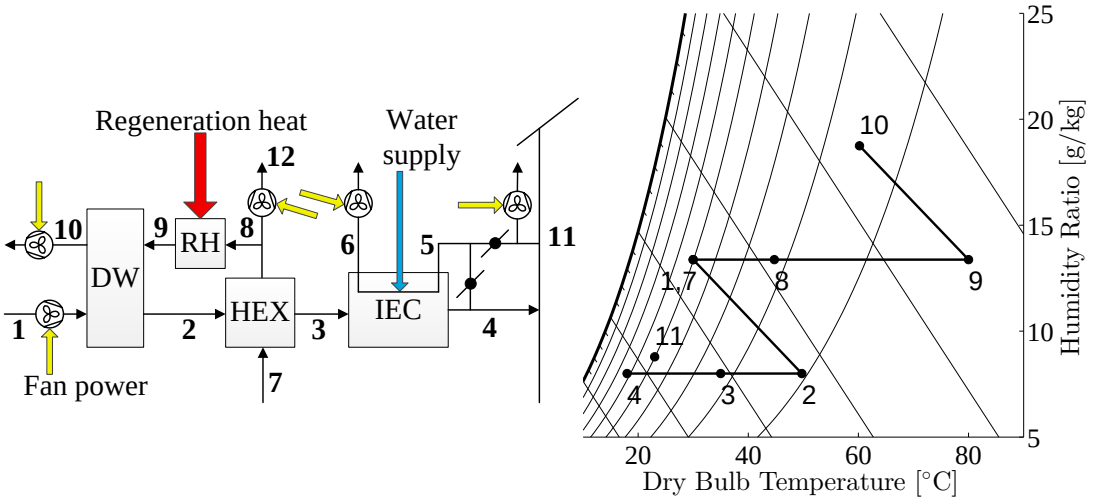

Figure 4.1: DIEC system schematics and psychrometric processes.

Outdoor air is dehumidified and heated in the DW (1)-(2), pre-cooled in the HEX (2)-(3), and ultimately cooled to the supply temperature in the IEC (3)-(4).
The regeneration air stream is initially taken at outdoor conditions, pre-heated in the HEX (7)-(8), successively heated to the required regeneration temperature in the RH (8)-(9), and finally used to regenerate the DW (9)-(10). If the DW does not operate with balanced airflows but the HEX does, the unnecessary fraction of regeneration air is exhausted to the outdoor ambient after the HEX (12).
Water is considered available at suitable conditions for being used in the IEC without additional treatments. Water is evaporated into the secondary air stream, which is heated and humidified (5)-(6). The corresponding process is not indicated in Figure 4.1, as different compositions of the secondary air stream are possible. The secondary air stream can be obtained by recirculating either a fraction of the cooled primary air stream (DPC mode), or a fraction of the exhaust air from the conditioned space (IEC mode), or a mix of these air streams (HIEC mode). The use of exhaust air from the conditioned space instead of outdoor air is preferable due to the fact that indoor conditions are generally characterized by lower enthalpies than outdoor conditions, resulting into higher cooling performance as reported in Figure 3.16a. When recirculating air from the conditioned space, the system performance and indoor conditions become interdependent, while operating in DPC mode makes the system independent of the conditioned space.
The HEX pre-cools the process air stream and pre-heats the regeneration air stream, reducing heat consumption and increasing the system cooling capacity. These benefits are achieved at the expense of higher electricity consumption, space requirements and capital cost. Therefore the use of the HEX should be evaluated depending on the considered application.
The fans are positioned for reducing the amount of dampers to regulate the airflows, which would increase electricity consumption, and for minimizing the risk of air infiltrations from the DW regeneration air inlet (9) to the DW process air outlet (2).
The DIEC system provides 100% fresh air to the conditioned space. Depending on the indoor air quality requirements, a fraction of the exhaust air from the conditioned space could be recirculated to lower the sensible and latent loads on the system. The desiccant air cleaning potential could allow for higher indoor air recirculation fractions than in conventional air conditioners for obtaining the same air quality.

4.2 System model formulation

Two sets of parameters are selected for describing the system dimensions and operation:

- Geometrical parameters. Namely DW diameter (D_{DW}), DW length (L_{DW}), DW face split (S_{DW}), IEC height (H_{IEC}), IEC number of plates ($N_{p,IEC}$) and IEC length (L_{IEC}). More parameters related to component dimensions are included, namely nominal HEX UA value ($UA_{HEX,nom}$) and pressure drop ($\Delta P_{HEX,nom}$) at both HEX sides, and nominal RH pressure drop ($\Delta P_{RH,nom}$).

- Operational parameters. Namely supply air volume flow rate ($\dot{V}_{sup}$), regeneration temperature (T_{reg}), regeneration fraction (f_{reg}), DW rotational speed (N_{DW}), IEC air fractions (f_{sec}, f_{rec}, f_{ext}), and fan efficiency (η_{fan}).

These parameters are indicated in the system scheme in Figure 4.2, distinguishing between geometrical parameters in red and operational parameters in blue. Additionally, outdoor and indoor conditions are also indicated and considered as operational variables.

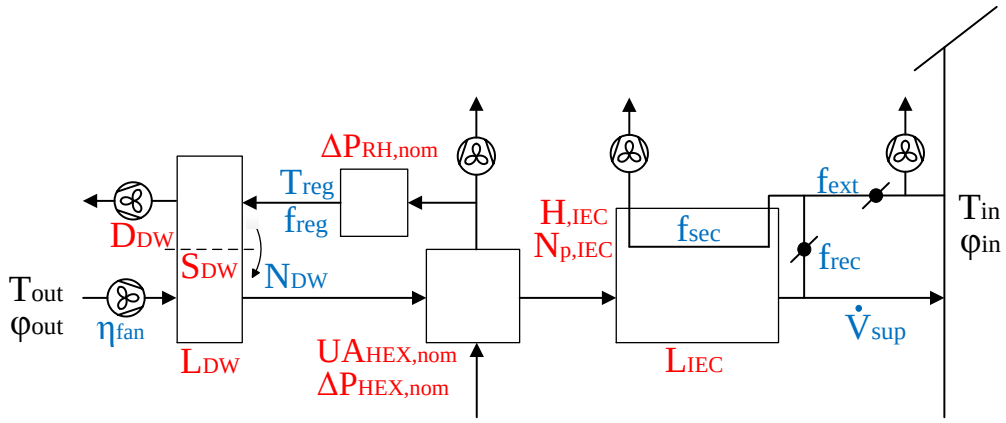

Figure 4.2: Variables and parameters influencing the system performance. Geometrical parameters in red, operational parameters in blue, and operational variables in black.

4.2.1 Governing equations

The steady state system operation is simulated by means of the following component models.

Desiccant wheel

The model described in Chapter 2 is used to compute the DW steady state operation, considering RD silica gel.

Dew point cooler

The model described in Chapter 3 is used to compute the IEC steady state operation.

Heat exchangers

The HEX is regarded as a counter-flow heat exchanger and modelled by the effectiveness-NTU method:

$$\varepsilon_{HEX} = \frac{1 - e^{-NTU_{HEX}(1-R_{HEX})}}{1 - R_{HEX}e^{-NTU_{HEX}(1-R_{HEX})}} \tag{4.1}$$

$$NTU_{HEX} = \frac{UA_{HEX}}{\dot{C}_{min,HEX}} \tag{4.2}$$

$$R_{HEX} = \frac{\dot{C}_{min,HEX}}{\dot{C}_{max,HEX}} \tag{4.3}$$

where $\dot{C}_{min}$ and $\dot{C}_{max}$ are respectively the minimum and maximum air heat capacity rates, U is the overall heat transfer coefficient, and A is the heat transfer area. The UA value specification for nominal conditions allows estimating the component size without a detailed description of its design.
For a fixed heat transfer area, the UA value is assumed to depend only on the airflow rate. Operating with different airflow rates than the nominal value, the UA value is calculated as:

$$UA_{HEX} = \left(\frac{1}{2UA_{HEX,nom}\left(\frac{\dot{m}_{cold,HEX}}{\dot{m}_{cold,HEX,nom}}\right)^{m}} + \frac{1}{2UA_{HEX,nom}\left(\frac{\dot{m}_{hot,HEX}}{\dot{m}_{hot,HEX,nom}}\right)^{m}} \right)^{-1} \tag{4.4}$$

where it is assumed that the heat transfer resistances at the cold and hot HEX sides are equal, and additional heat transfer resistances are negligible. The exponent m corresponds to the exponent of Reynolds number used in the Nusselt number correlation, set to 0.8.
The UA value of the RH is not selected as the heat source is not specified.

The air pressure drops across the HEX and RH are assumed to depend only on the airflow rates:

$$\Delta P = \Delta P_{nom}\left(\frac{\dot{V}_a}{\dot{V}_{a,nom}}\right)^{n} \tag{4.5}$$

where the exponent n depends on the flow regime and the component geometry. For turbulent airflows into the HEX channels n is set to 7/4, while for the RH it is set to 2 [85].

4.2.2 Performance indicators

The following indicators are chosen to describe the system performance referring to the DIEC system scheme in Figure 4.1:

- Thermal COP

$$COP_{th} = \frac{\dot{Q}_{load}}{\dot{Q}_{reg}} = \frac{\dot{m}_{a,4}\left(h_{a,1} - h_{a,4}\right)}{\dot{m}_{a,9}\left(h_{a,9} - h_{a,8}\right)} \tag{4.6}$$

  The thermal COP considers the ratio of the total latent and sensible load on the system and the corresponding regeneration heat consumption.

- Electrical COP

$$COP_{el} = \frac{\dot{Q}_{load}}{\dot{W}_{fan}} = \frac{\dot{m}_{a,4}\left(h_{a,1} - h_{a,4}\right)}{\Sigma_{i=1}^{n_{fan}}\left(\dot{V}_{a,i}\Delta P_{a,i}\right)/\eta_{fan}} \tag{4.7}$$

  The electrical COP considers the fan power required to circulate the air streams across the various components in the system. The power consumption for water pumping and DW rotation is negligible in comparison to the fan power consumption. The air pressure drops due to additional filters and ventilation ductwork is left out of the present definition. In particular the air pressure drops induced by filters can result into high localized pressure drops depending on the type of filter and its level of clogging [86].

- Minimum Specific Water Consumption (MSWC)

$$MSWC = \frac{\dot{m}_{w,evap}}{\dot{Q}_{load}} = \frac{\dot{m}_{a,6}\left(x_{a,6} - x_{a,5}\right)}{\dot{m}_{a,4}\left(h_{a,1} - h_{a,4}\right)} \tag{4.8}$$

  This definition is analogous to Equation 3.20.

- Supply air temperature

$$T_{sup} = T_{a,4} \tag{4.9}$$

- Supply air humidity ratio

$$x_{sup} = x_{a,4} \tag{4.10}$$

The total latent and sensible load on the system is chosen to rate the system performance. When considering a specific conditioned space, i.e. indoor loads and ventilation requirements, it is useful to refer the system performance also to the indoor load.

4.3 Results

The DIEC system is simulated for investigating the influence of the geometrical and operational parameters and operational variables on its performance. The system is simulated both in IEC mode ($f_{sec} = f_{ext}$) and in DPC mode ($f_{sec} = f_{rec}$) to identify the best performing mode of operation.

4.3.1 Reference scenario

Standard summer outdoor conditions, T_{out}=35°C and φ_{out}=40%, are considered as defined by the American Air conditioning, Heating, and Refrigeration Institute [87]. The indoor conditions are set to satisfy the minimum requirements for thermal comfort in category I conditioned spaces in accordance to Standard EN15251 [88], i.e. T_{in}=25.5°C and φ_{in}=50%. These indoor conditions are used to determine the indoor latent and sensible heat loads covered by the system operating under specified conditions, and they also affect the system performance when operating in IEC mode.
The selected reference geometrical and operational parameters are listed in Table 4.1.

Table 4.1: Reference parameters for system simulations.

Geometrical parameters	Operational parameters	Operational variables
D_{DW} = 1.2 m	$\dot{V}_{sup}$ = 5000 m^3/h	T_{out} = 35°C
L_{DW} = 0.2 m	T_{reg} = 80°C	φ_{out} = 40%
S_{DW} = 0.5	f_{reg} = 0.7	T_{in} = 25.5°C
H_{IEC} = 0.76 m	N_{DW} optimal value	φ_{in} = 50%
L_{IEC} = 1.38 m	$f_{sec} = f_{ext}$ = 0.6 (IEC mode)	
$N_{p,IEC}$ = 158	$f_{sec} = f_{rec}$ = 0.3 (DPC mode)	
$UA_{HEX,nom}$ = 5 kW/K (5000 m^3/h)	η_{fan} = 0.6	
$\Delta P_{HEX,nom}$ = 150 Pa (5000 m^3/h)		
$\Delta P_{RH,nom}$ = 150 Pa (5000 m^3/h)		

The DW channel geometry is set as reported in Table 2.1, while the IEC channel geometry is set as reported in Table 3.1.
The system dimensions, i.e. the geometrical parameters, are selected on the basis of the chosen supply air volume flow rate. The resulting process air face velocities on the DW is 2.6 m/s in IEC mode and 3.7 m/s in DPC mode. The IEC dimensions are selected accordingly to the product catalogue from the manufacturer [83], resulting in process air face velocities of 3.2 m/s in IEC mode and 4.6 m/s in DPC mode. Air face velocities are higher in DPC mode, as 30% of the process airflow rate is recirculated into the IEC secondary channels, while maintaining the same supply airflow rate.
The HEX is operated with balanced airflows. The HEX and RH nominal airflow rates are set equal to the supply air volume flow rate. Consequently, the values reported in Table 4.1 directly apply in IEC mode, apart for ΔP_{RH}=120 Pa due to f_{reg}=0.7, while in DPC mode UA_{HEX}=6.7 kW/K, ΔP_{HEX}=280 Pa and ΔP_{RH}=245 Pa.
Therefore the comparison of IEC and DPC modes takes into account fixed component dimensions and the same supply volume flow rate, highlighting the effects of increased airflow rates throughout the system due to partial recirculation of the process air stream in DPC mode.
The optimal DW rotational speeds that maximize the process air dehumidification are used.
The IEC secondary fraction is set to 0.3 in DPC mode, for maximizing the cooler net cooling capacity, and 0.6 in IEC mode, as in this case the cooler net cooling capacity increases for

higher secondary airflow rates.
The resulting system performance are presented in Table 4.2.

Table 4.2: System performance in IEC and DPC modes.

Variable	IEC mode	DPC mode
Supply temperature [°C]	21.2	24.8
Supply humidity ratio [g/kg]	9.9	10.5
Thermal COP [-]	1.13	0.6
Electrical COP [-]	18.1	6.6
MSWC [kg/kWh]	1.05	1.33
Indoor heat load [kW]	8.6	1.1 (with φ_{in}=52%)
SHR [-]	0.84	1

The computed performance indicate that the system operating in IEC mode reaches a lower supply temperature as well as a lower supply humidity ratio with higher thermal (+88%) and electrical (+174%) COPs and lower MSWC (-21%) than in DPC mode.
In respect to the reference indoor conditions, the system operating in IEC mode covers a total indoor heat load of 8.6 kW, with a Sensible Heat Ratio (SHR) of 84%. The system operating in DPC mode does not supply sufficiently dry air, making the indoor relative humidity raise to 52% at the reference indoor temperature, corresponding to no indoor latent heat load and indoor sensible heat load of 1.1 kW.
The optimal DW rotational speeds are 9 rph in IEC mode and 12 rph in DPC mode.
Additional information on the air pressure drops across the components and the corresponding contributions to fan power consumption is given in Figure 4.3.

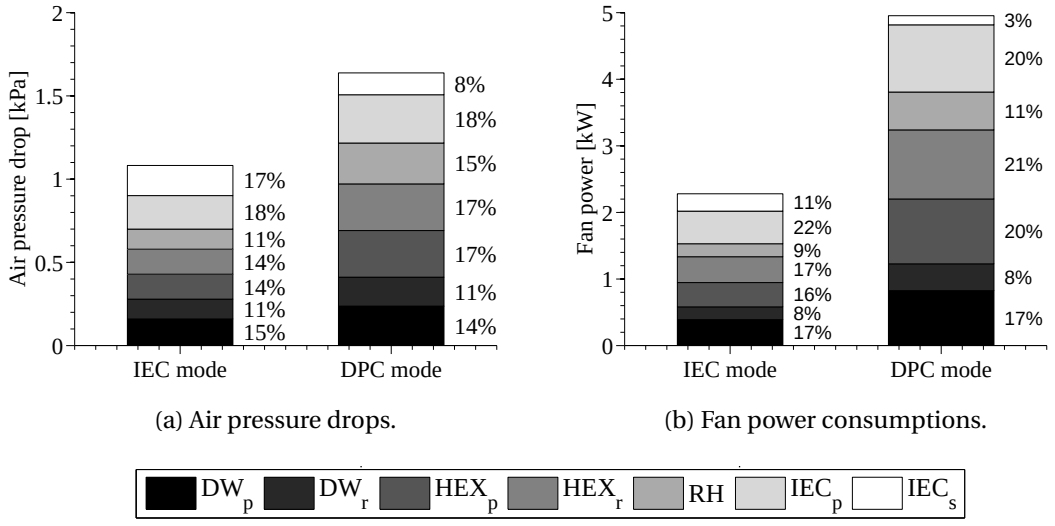

(a) Air pressure drops.

(b) Fan power consumptions.

Figure 4.3: Component air pressure drops and contributions to fan power consumption.

Figure 4.3a shows that the total air pressure drop is nearly 50% higher in DPC mode than in

IEC mode due to the higher airflow rates in the system. The air pressure drops across the HEX and RH have bigger contributions to the total pressure drop in DPC mode, as the flow regime in these components is turbulent, remaining laminar in the other components. The pressure drop across the IEC secondary side is approximately twice as much in IEC mode due to the doubled secondary fraction.
Figure 4.3b shows that the total fan power consumption is approximately twice as much in DPC mode than in IEC mode, due to higher air pressure drops as well as higher airflow rates. Generally, the HEX has the highest contribution to power consumption, with 33% in IEC mode and 41% in DPC mode.

Based on the above mentioned results, the IEC mode clearly outperforms the DPC mode for fixed component geometries and supply airflow rate.

4.3.2 Influence of geometrical parameters

DW and IEC face dimensions

The influence of the DW and IEC dimensions is investigated by varying the DW diameter and the IEC number of plates with fixed IEC height. The DW rotational speed is always set to the optimal values maximizing the process air dehumidification.
The resulting variations of supply conditions are reported in Figure 4.4. Insufficient supply conditions, leading to negative indoor heat loads in respect to the reference indoor conditions, are indicated by means of gray areas. The indoor heat loads covered by the system increase as the supply conditions decrease below the reference indoor conditions. Varying the component face dimensions is expected to give analogous effects to varying the airflow rates, i.e. increasing the face dimensions corresponds to decreasing the airflow rates and vice versa.

Figure 4.4 shows that the system operating in IEC mode reaches better supply conditions than in DPC mode. The IEC number of plates influences the supply temperature the most. In IEC mode, the supply temperature increases for increasing DW diameters, due to higher process air temperature increases across the DW. In DPC mode, the supply temperature decreases for increasing DW diameters, due to drier process air conditions after the DW, which improve the cooler performance. The pre-cooling in the HEX mitigates the process air temperature increase across the DW. The supply temperature does not vary significantly at high DW diameter values. The supply humidity ratio is naturally independent of the IEC number of plates. The system supplies lower humidity ratios in IEC mode due to lower air face velocities on the DW.
The system operating in DPC mode provides the same supply conditions as in IEC mode for the reference scenario with DW diameter of 1.45 m (+20%) and IEC number of plates of 300 (+90%). The system space requirements increase significantly, particularly because of the IEC. The corresponding system performance variations are reported in Figure 4.5. The regions of insufficient supply conditions are indicated by gray areas.

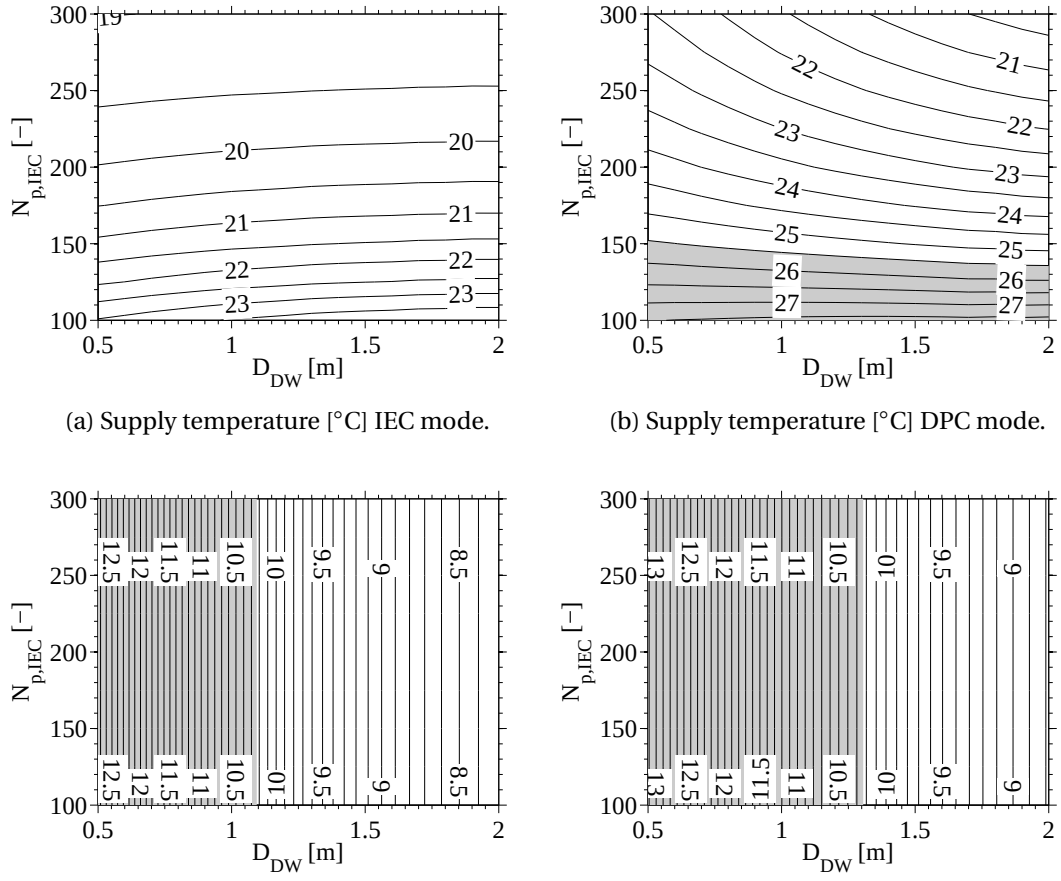

(a) Supply temperature [°C] IEC mode.

(b) Supply temperature [°C] DPC mode.

(c) Supply humidity ratio [g/kg] IEC mode.

(d) Supply humidity ratio [g/kg] DPC mode.

Figure 4.4: Variation of supply conditions in IEC and DPC modes for varying DW diameter and IEC number of plates.

Figures 4.5a and 4.5b show that the thermal COP always increases for increasing component face dimensions, due to lower air face velocities. The system operating in IEC mode is characterized by higher thermal COP than in DPC mode, increasing approximately between 115%, at the smallest component face dimensions, and 65%, at the biggest dimensions.
Figures 4.5c and 4.5d show similar trends for the electrical COP with bigger differences between IEC and DPC modes, as the electrical COP in IEC mode is between 150% and 200% higher. The IEC number of plates has almost no effect for small DW diameters.
Figures 4.5e and 4.5f show that the MSWC is nearly 1 in IEC mode, while it increases more in DPC mode. The MSWC increases for increasing component face dimensions in IEC mode, with little dependence on the DW diameter, while the opposite is observed in DPC mode.
Considering the component face dimensions required to obtain the same supply conditions in DPC mode as for the reference case in IEC mode, the system thermal COP is 0.8, electrical COP is 10.5, and MSWC is 1.25, which are worse than the system performance in IEC mode.

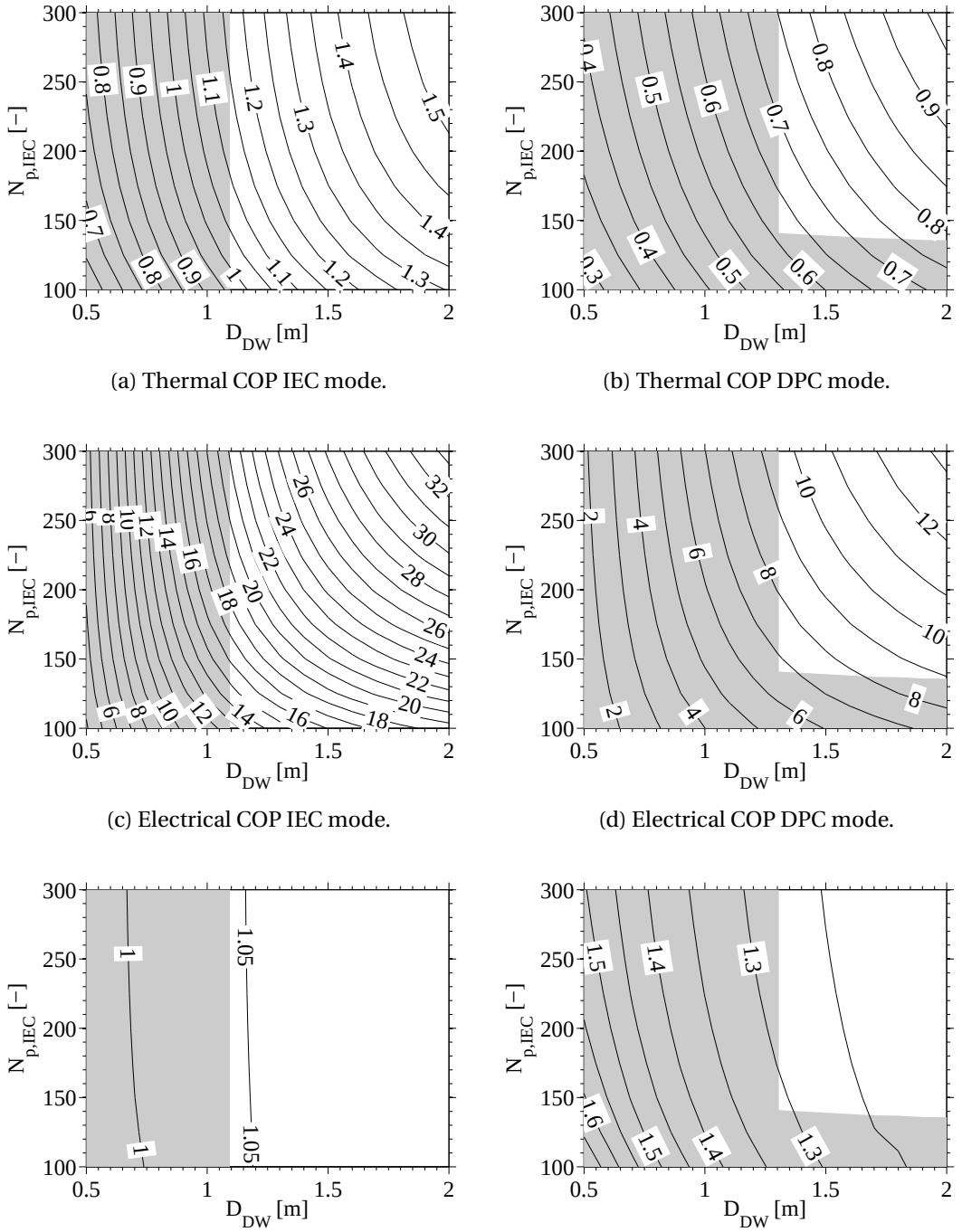

(a) Thermal COP IEC mode.

(b) Thermal COP DPC mode.

(c) Electrical COP IEC mode.

(d) Electrical COP DPC mode.

(e) MSWC [kg/kWh] IEC mode.

(f) MSWC [kg/kWh] DPC mode.

Figure 4.5: Variation of system performance in IEC and DPC modes for varying DW diameter and IEC number of plates.

DW and IEC lengths

The influence of the DW and IEC dimensions is also investigated by varying the DW and IEC lengths. The DW rotational speed is again set to the optimal values maximizing the process air dehumidification.
The resulting variations of supply conditions are reported in Figure 4.6, still indicating infeasible supply conditions for obtaining positive indoor heat loads by means of gray areas.

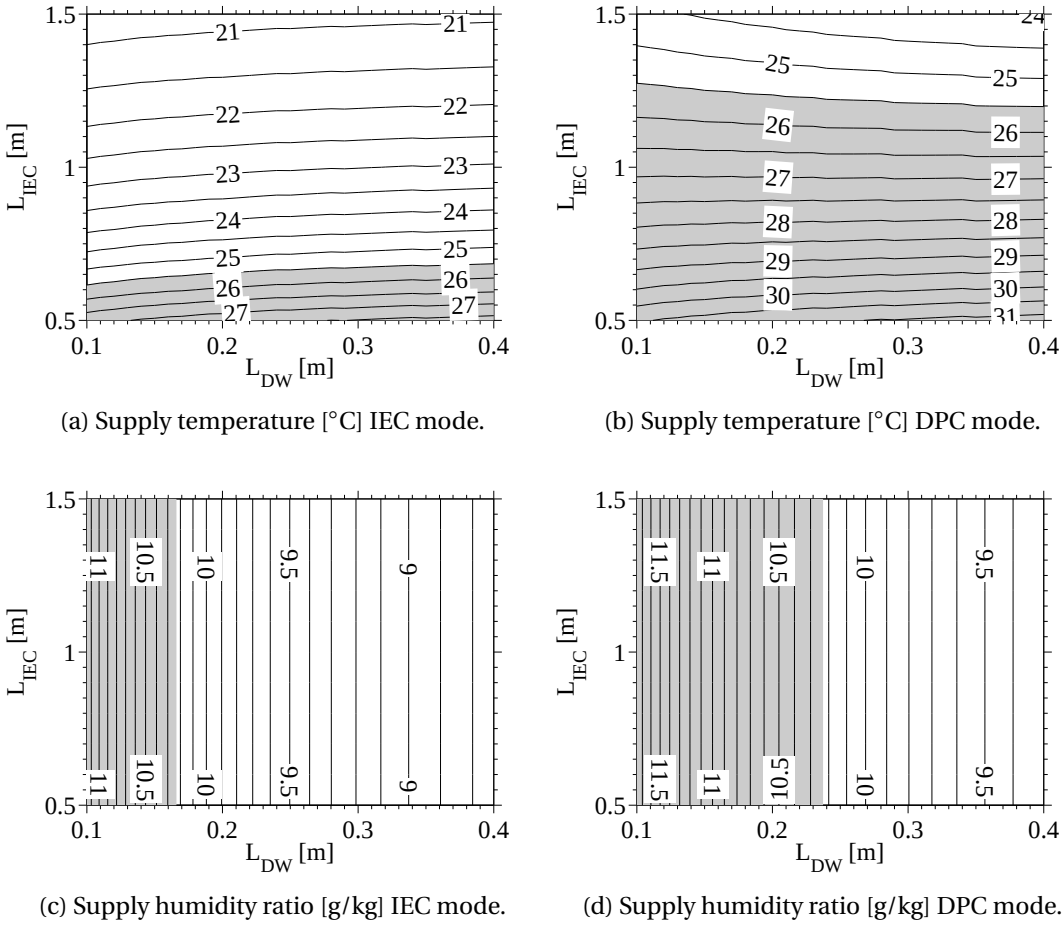

(a) Supply temperature [°C] IEC mode.

(b) Supply temperature [°C] DPC mode.

(c) Supply humidity ratio [g/kg] IEC mode.

(d) Supply humidity ratio [g/kg] DPC mode.

Figure 4.6: Variation of supply conditions in IEC and DPC modes for varying DW and IEC lengths.

Figure 4.6 shows that the system operating in IEC mode always reaches better supply conditions than in DPC mode.
The supply temperature is strongly dependent on the IEC length, and the system operating in DPC mode requires a quite long IEC for reaching feasible supply conditions, still corresponding to small indoor loads. In IEC mode, the supply temperature increases slightly for increasing DW lengths, due to higher process air temperature increases across the DW. In DPC mode, the influence of the DW length on the supply temperature is more complex, as the

supply temperature decreases for increasing DW lengths at high IEC lengths, and vice versa at low IEC lengths. In both modes of operation the supply temperature tends to be constant for DW lengths varying at high values.
The supply humidity ratio is naturally independent of the IEC length. The system still supplies lower humidity ratios in IEC mode due to lower air face velocities on the DW.
The corresponding system performance variations are reported in Figure 4.5, including regions of insufficient supply conditions.

Figures 4.7a and 4.7b show that the thermal COP always increases for increasing DW and IEC lengths, due to increased latent and sensible load capacities. The system operating in IEC mode is characterized by higher thermal COP than in DPC mode, increasing approximately between 115%, at short DW and IEC lengths, and 80%, at long lengths.
Figures 4.7c and 4.7d show that the electrical COP is maximized for specific DW and IEC lengths, with different optimal values between IEC and DPC modes. The system in IEC mode is always characterized by higher electrical COP than in DPC mode, approximately 200% higher. The optimal DW and IEC lengths in IEC mode are approximately 0.14 m and 0.95 m respectively, while in DPC mode they are approximately 0.24 m and more than 1.5 m. The optimal DW length increases of approximately 70% between IEC and DPC modes, while the optimal IEC length increases more than 100%. As the optimal lengths correspond to infeasible supply conditions, longer components should be used, covering higher indoor heat loads with higher thermal COP.
Figures 4.7e and 4.7f show the MSWC is nearly constant around 1 in IEC mode, while it is higher and varying more in DPC mode. The MSWC tends to increase for increasing DW and IEC lengths in IEC mode, while the opposite is observed in DPC mode.

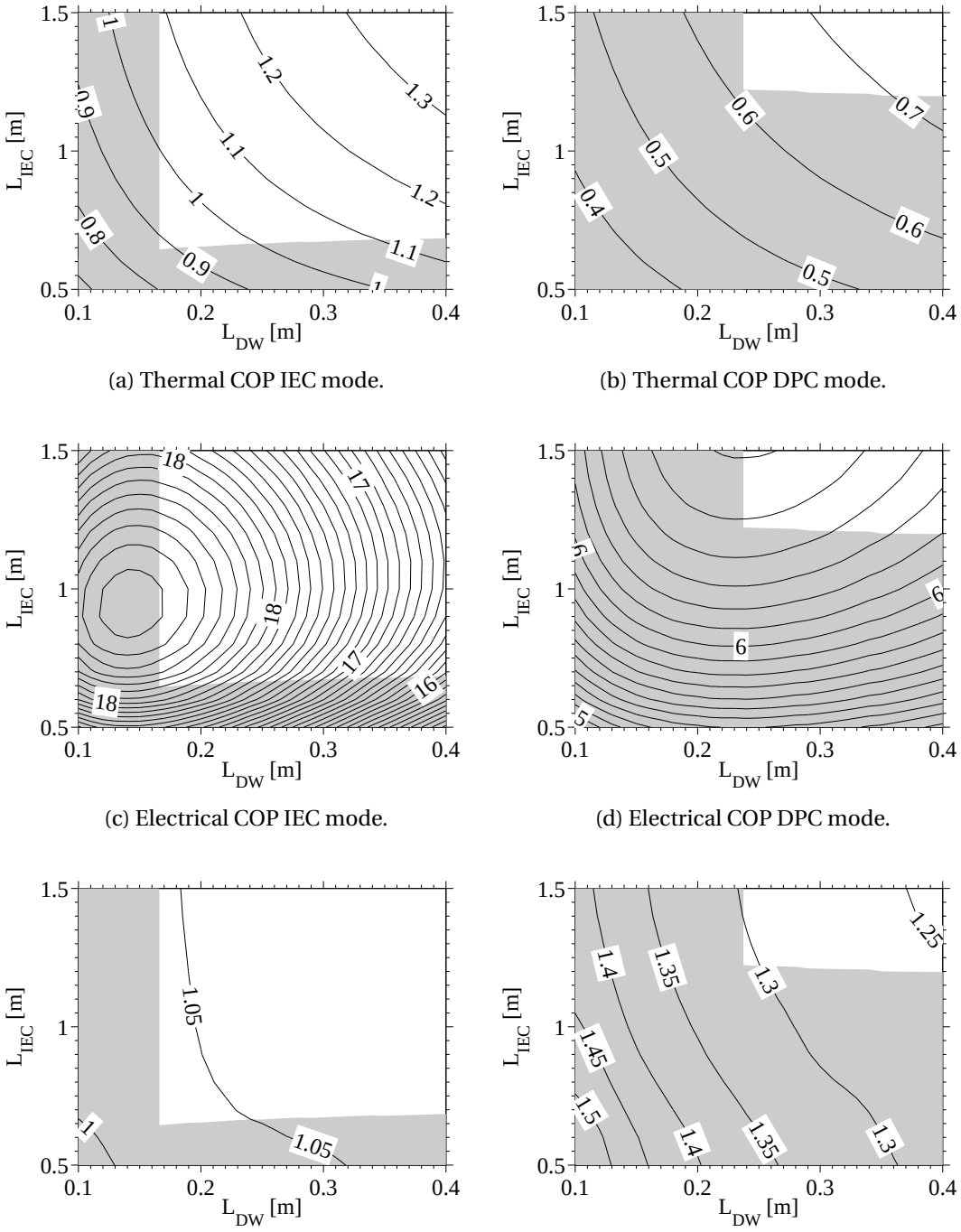

(a) Thermal COP IEC mode.

(b) Thermal COP DPC mode.

(c) Electrical COP IEC mode.

(d) Electrical COP DPC mode.

(e) MSWC [kg/kWh] IEC mode.

(f) MSWC [kg/kWh] DPC mode.

Figure 4.7: Variation of system performance in IEC and DPC modes for varying DW and IEC lengths.

System design with no HEX

The influence of the HEX on the system performance is investigated by considering a system design with no HEX. The cooling and thermal performance are expected to decrease, as the cooling capacity corresponds to the IEC capacity only, and the heat source has to provide all the heat to reach the regeneration temperature, while the electrical performance is expected to increase due to lower air pressure drops.
The resulting supply temperature variations are reported in Figure 4.8 for varying DW length and diameter, and IEC length and number of plates. Infeasible supply conditions are again indicated by means of gray areas. The supply humidity ratio is not reported as it varies analogously to Figures 4.4 and 4.6. The DW rotational speed is still set to optimal values maximizing the process air dehumidification.

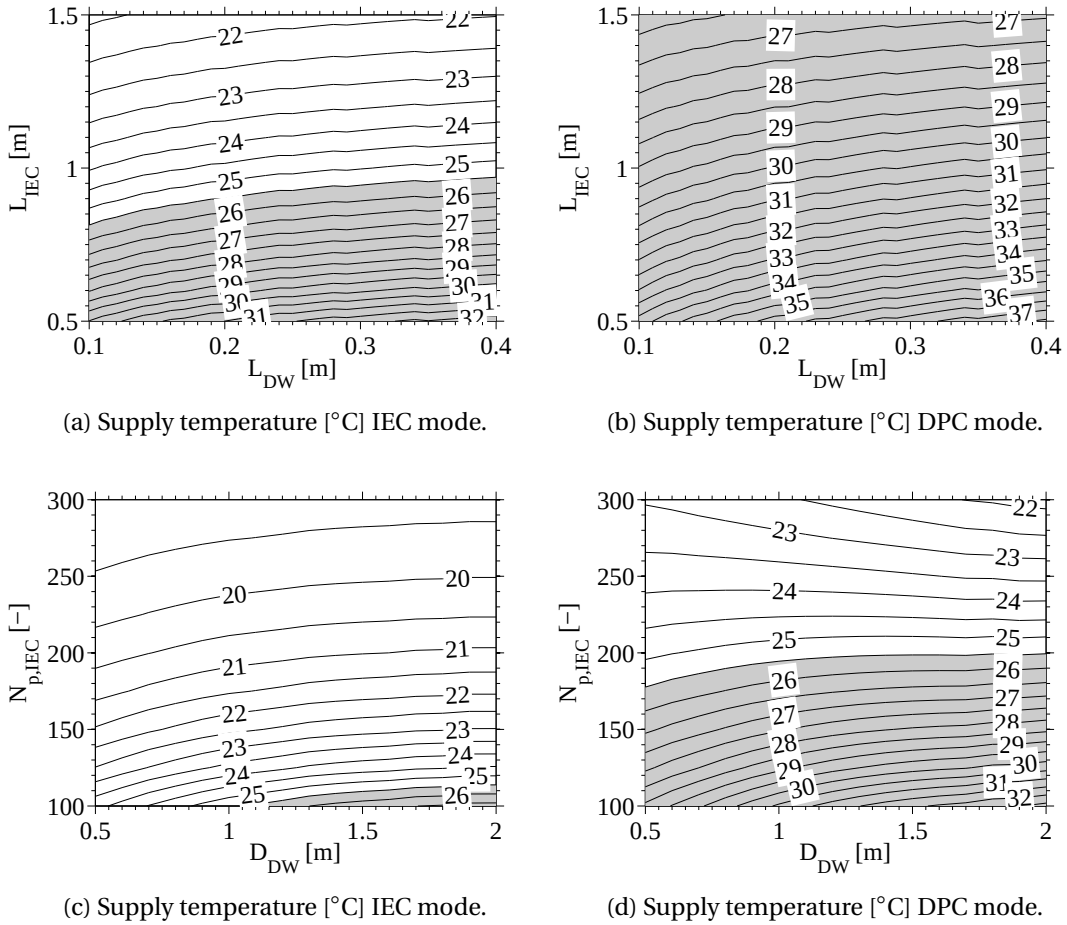

(a) Supply temperature [°C] IEC mode.

(b) Supply temperature [°C] DPC mode.

(c) Supply temperature [°C] IEC mode.

(d) Supply temperature [°C] DPC mode.

Figure 4.8: Variation of supply temperature in IEC and DPC modes for varying DW and IEC geometrical parameters with no HEX.

Figure 4.8 shows that, with no HEX, higher supply temperature are achieved, with strong influences of the IEC length and number of plates. The supply temperature reaches high

values particularly in DPC mode, for which none of the considered IEC lengths allows to reach feasible supply temperatures, but high IEC numbers of plates are necessary, as they result into lower air face velocities. The system operating in IEC mode provides quite lower supply temperatures as the IEC secondary air flow conditions are set to the reference indoor conditions independently of the system performance.
It is noticed that, with no HEX, the influence of the DW length and diameter on the supply temperature in DPC changes, as the absence of pre-cooling makes the supply temperature more sensitive to the process air temperature increase across the DW, decreasing the benefits of drier IEC secondary air stream conditions.
The system operating in DPC mode is found to reach the same supply conditions as in IEC mode for the reference scenario in case of DW diameter of 1.45 m and approximately 300 IEC plates, practically the same dimensions obtained with HEX.
The corresponding system performance variations are reported in Figure 4.9, considering varying DW and IEC lengths only. In case of varying DW diameter and IEC number of plates, the trends are the same as observed in Figure 4.5, with lower thermal COP and higher electrical COP.

Figures 4.9a and 4.9b show that the thermal COP always increases for increasing DW and IEC lengths, analogously to the system configuration with HEX, but the resulting values are lower, with the IEC mode still providing the highest values.
Figures 4.9c and 4.9d show that the electrical COP increases up to 50% in respect to the system configuration with HEX, and also the optimal DW and IEC lengths change considerably, decreasing both in IEC and DPC modes. It seems that, without HEX, the highest electrical COP is reached with no DW. For short IEC and long DW, the electrical COP does not improve significantly in respect to the system configuration with HEX, as the air pressure drops in the DW become dominant while the system load does not increase as much.
Figures 4.9e and 4.9f show that the MSWC increases and varies differently in respect to the system configuration with HEX. The MSWC increases for increasing DW lengths and decreasing IEC lengths both in IEC and DPC modes, with a smaller influence on the DW length in DPC mode for the considered range of values.
Generally, also with no HEX, the IEC mode outperforms the DPC mode.

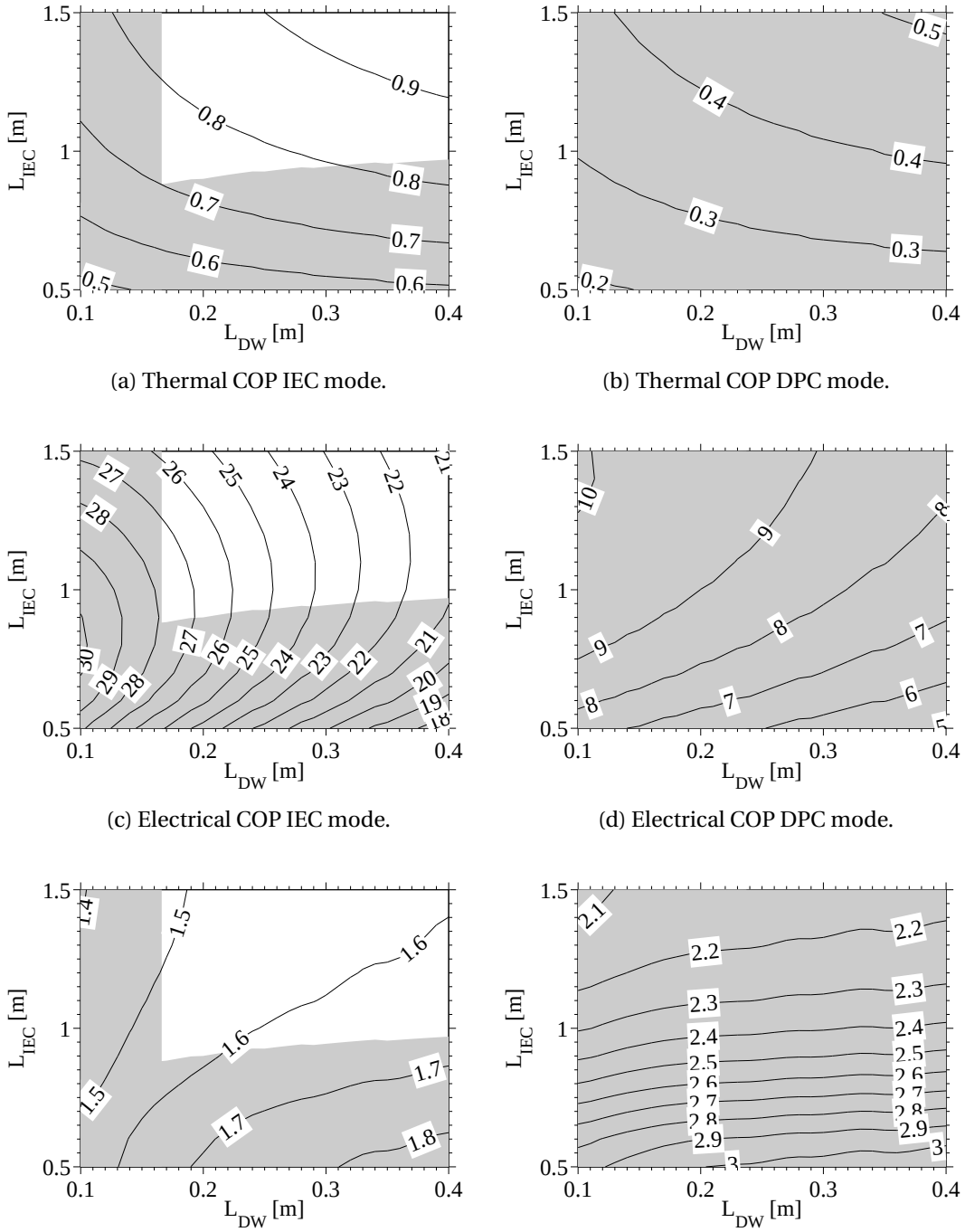

(a) Thermal COP IEC mode.

(b) Thermal COP DPC mode.

(c) Electrical COP IEC mode.

(d) Electrical COP DPC mode.

(e) MSWC [kg/kWh] IEC mode.

(f) MSWC [kg/kWh] DPC mode.

Figure 4.9: Variation of system performance in IEC and DPC modes for varying DW and IEC lengths with no HEX.

Air filtration

Air filtration, required to supply high quality air as well as preserve component performance, is expected to cause considerable pressure drops. Three air filters should be installed in the system, respectively at locations (1), (7) and (11) referring to the scheme in Figure 4.1. The pressure drop across a filter depends on the filter type, as required by the application, and the level of clogging, which increases during operation [86]. Considering fine bag filters F7, often used in HVAC systems, the pressure drop is typically around 100 Pa under unclogged conditions [86]. The effect of the three above mentioned filters on the system electrical COP is investigated, setting their pressure drop equal to 200 Pa. Results are reported in Figure 4.10 for varying DW and IEC face dimensions and lengths.

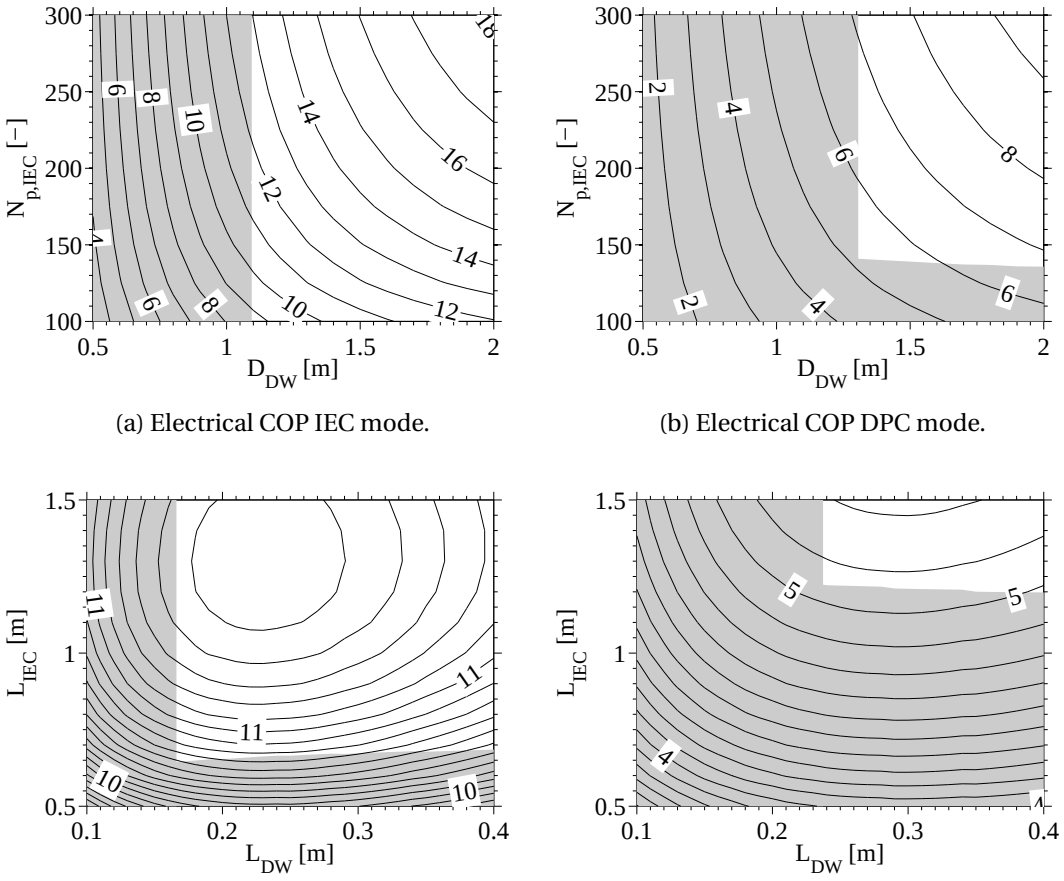

(a) Electrical COP IEC mode.

(b) Electrical COP DPC mode.

(c) Electrical COP IEC mode.

(d) Electrical COP DPC mode.

Figure 4.10: Variation of electrical COP in IEC and DPC modes for varying DW and IEC geometrical parameters including additional pressure drops due to air filtration.

Figure 4.10 shows that the electrical COP drops significantly when considering air filtration. The optimal DW and IEC lengths maximizing the electrical COP increase, resulting in higher pressure drops but also higher cooling and dehumidification capacities.

4.3.3 Influence of operational parameters

Regeneration conditions

The influence of the regeneration temperature and regeneration fraction on the system performance is investigated. The regeneration temperature is varied between 50°C and 90°C, considering the use of low temperature heat sources. The regeneration fraction is kept above 0.4 to avoid reaching too low regeneration air face velocities on the DW. The DW rotational speed is always kept at the optimal values maximizing the process air dehumidification.
The resulting supply conditions are reported in Figure 4.11, identifying infeasible supply conditions with gray areas.

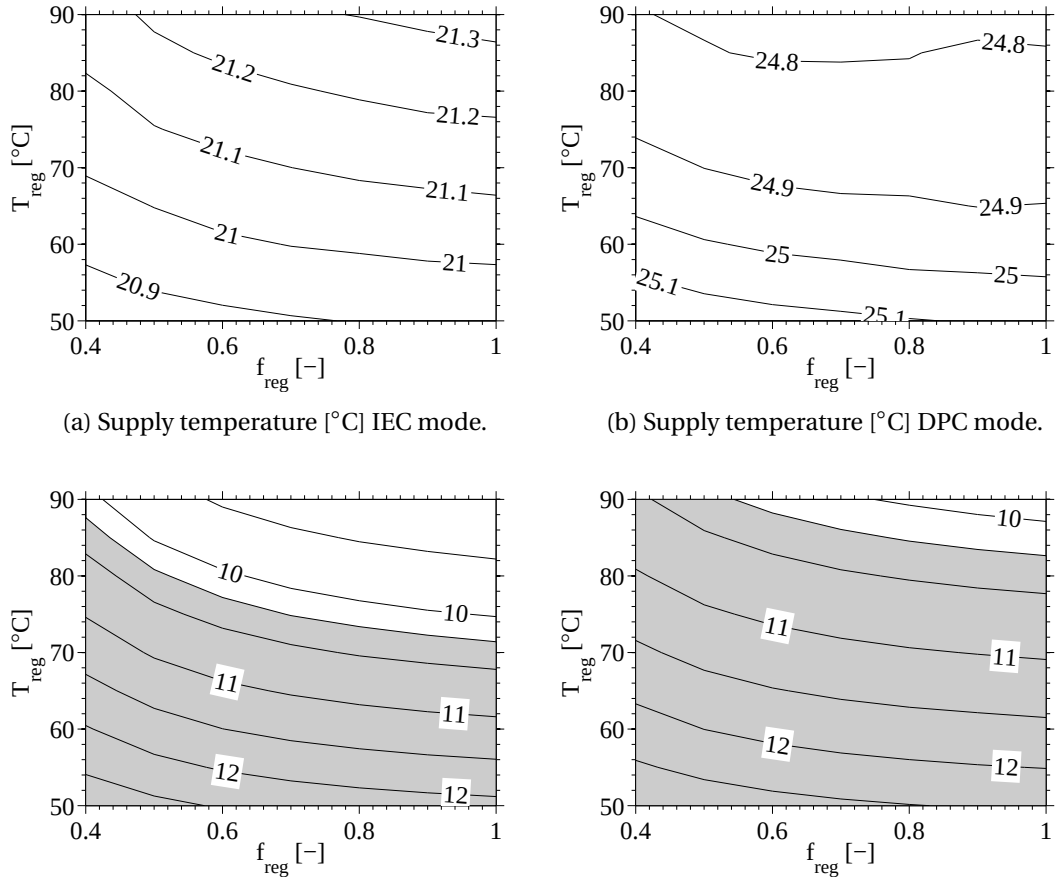

(a) Supply temperature [°C] IEC mode.

(b) Supply temperature [°C] DPC mode.

(c) Supply humidity ratio [g/kg] IEC mode.

(d) Supply humidity ratio [g/kg] DPC mode.

Figure 4.11: Variation of supply conditions in IEC and DPC modes for varying regeneration conditions.

Figures 4.11a and 4.11b show that the supply temperature is nearly independent of the regeneration conditions in both IEC and DPC modes. This is due to the process air pre-cooling in the HEX, which mitigates the process air temperature increase across the DW. It is noticed

that the supply temperature tends to increase for increasing regeneration temperatures and regeneration fractions in IEC mode, while the opposite is observed in DPC mode. This is due to the fact that higher process air dehumidification improves the cooling performance in DPC mode because of drier secondary air inlet conditions, counteracting the higher process air inlet temperature to the cooler.
Figure 4.11c and 4.11d show that the regeneration temperature influences the supply humidity ratio more than the regeneration fraction. Low regeneration temperatures do not provide enough dehumidification to cover positive latent loads for the reference conditions. The supply humidity ratio decreases for increasing regeneration temperatures and increasing regeneration fractions in both IEC and DPC modes. The supply humidity ratio does not decrease substantially for regeneration fractions increasing above approximately 0.7, while the thermal and electrical COP are expected to keep decreasing, which is the reason for choosing this value in the reference scenario.
The corresponding system performance variations are reported in Figure 4.12.

Figures 4.12a and 4.12b show that the thermal COP increases for decreasing regeneration temperatures as well as decreasing regeneration fractions, with very high increase rates at low regeneration temperatures. The thermal COP in IEC mode is nearly doubled than in DPC mode for all the considered conditions.
Figures 4.12c and 4.12d show that the electrical COP tends to be maximized for specific regeneration fractions in both IEC and DPC modes, approximately between 0.4 and 0.5 depending on the regeneration temperatures.
Figures 4.12e and 4.12f show that the MSWC tends to increase for increasing regeneration fractions, increasing also for increasing regeneration temperatures in IEC mode, while decreasing for increasing regeneration temperatures in DPC mode. The MSWC is nearly constant around 1 in IEC mode, while it is higher and varies more in DPC mode, particularly at low regeneration temperatures.

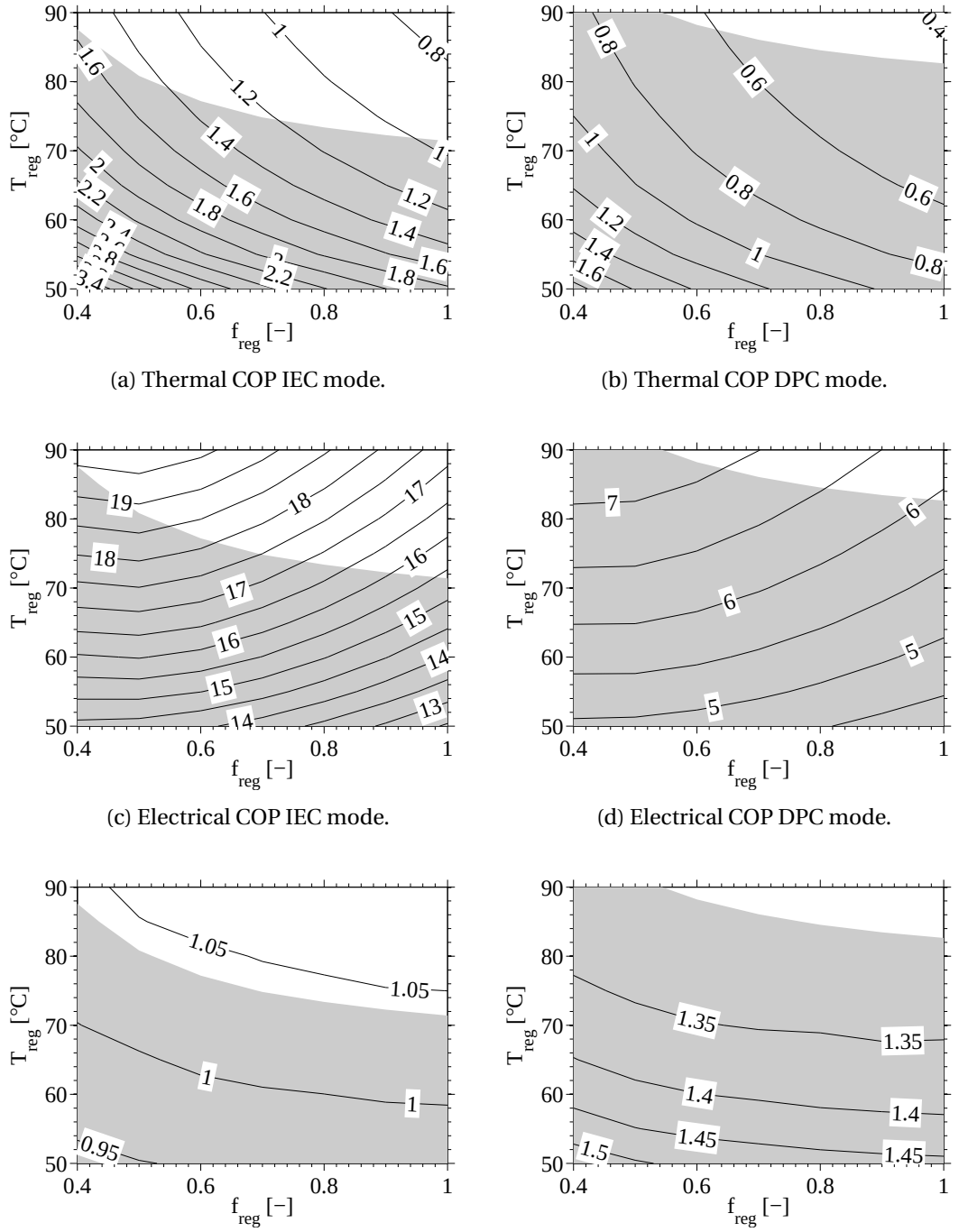

(a) Thermal COP IEC mode.

(b) Thermal COP DPC mode.

(c) Electrical COP IEC mode.

(d) Electrical COP DPC mode.

(e) MSWC [kg/kWh] IEC mode.

(f) MSWC [kg/kWh] DPC mode.

Figure 4.12: Variation of system performance in IEC and DPC modes for varying regeneration conditions.

Air fractions

The influence of the regeneration and secondary fractions on the system performance is investigated. The secondary fraction is varied between 0.1 and 0.9 in both IEC and DPC modes. Consequently, in DPC mode, the airflow rates across the system vary significantly in order to maintain a constant supply airflow rate. The DW rotational speed is always kept at the optimal values maximizing the process air dehumidification.
The resulting supply conditions are reported in Figure 4.13, identifying infeasible supply conditions with gray areas.

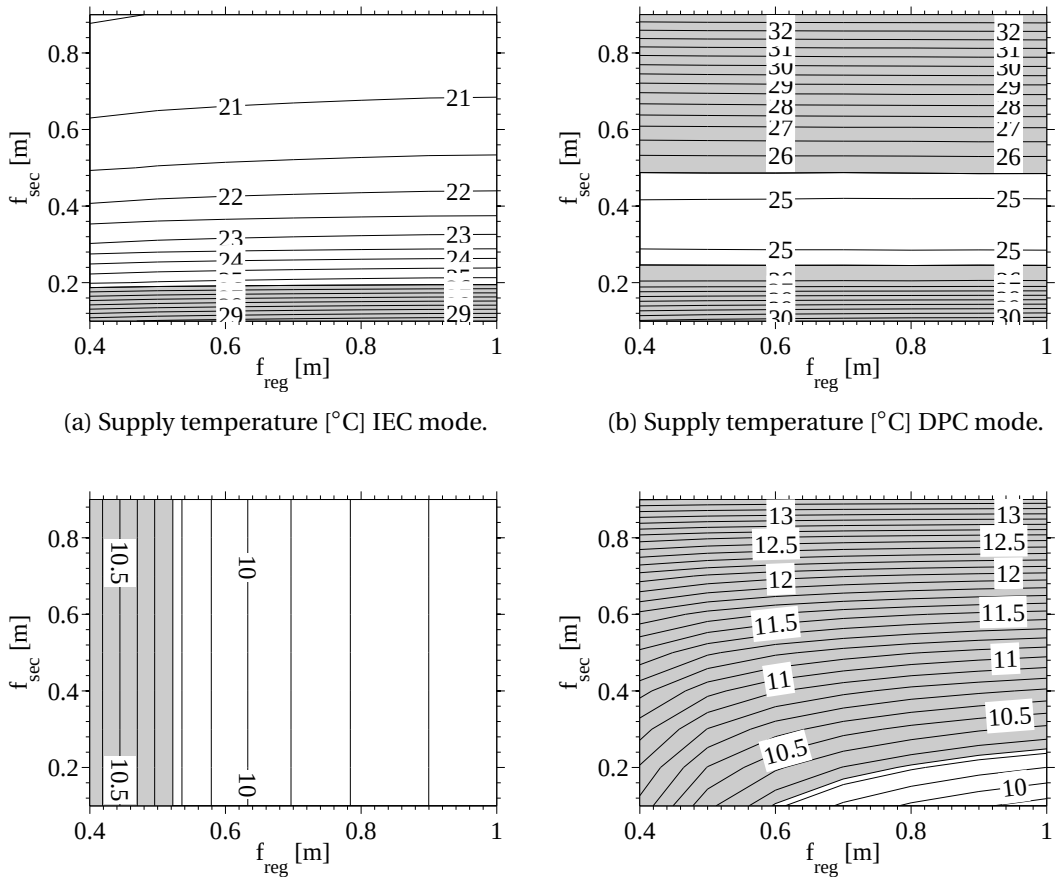

(a) Supply temperature [°C] IEC mode.

(b) Supply temperature [°C] DPC mode.

(c) Supply humidity ratio [g/kg] IEC mode.

(d) Supply humidity ratio [g/kg] DPC mode.

Figure 4.13: Variation of supply temperature in IEC and DPC modes for varying air fractions.

Figures 4.13a and 4.13b show that the supply temperature varies differently between IEC and DPC modes. In IEC mode, the supply temperature always decreases for increasing secondary fractions, with small influence from the regeneration fraction. It is noticed that very small improvements are obtained by increasing the secondary fraction above 0.6, which explains the reason for choosing this value in the reference scenario. In DPC mode, the lowest supply

temperature is reached with a secondary fraction around 0.3, which also maximizes the cooler net cooling capacity, while the regeneration fraction has almost no influence. The system cooling capacity in DPC mode does not benefit from varying the secondary fraction, i.e. the recirculation fraction.
Figures 4.13c and 4.13d show that also the supply humidity ratio varies differently between IEC and DPC modes. In IEC mode, the supply humidity ratio is independent of the secondary fraction, as expected. In DPC mode, the supply humidity ratio increases for increasing secondary fractions and decreasing regeneration fractions, becoming nearly independent of the regeneration fraction at high secondary fractions. This trend is due to the strong increase of airflow rates in the system caused by increasing secondary fractions with constant supply airflow rate.
The corresponding system performance variations are reported in Figure 4.14.

Figure 4.14a shows that the thermal COP in IEC mode increases for increasing secondary fractions and decreasing regeneration fractions. Small improvements are achieved by increasing the secondary fraction above approximately 0.5, with almost no influence from the regeneration fraction.
Figure 4.14b shows that the thermal COP varies differently in DPC mode, always increasing for increasing regeneration fractions, while peaking for secondary fractions of approximately 0.2.
Figure 4.14c shows that the electrical COP in IEC mode is maximized for secondary and regeneration fractions of approximately 0.45. These conditions provide an infeasible supply humidity ratio, requiring the use of higher regeneration fractions.
Figure 4.14d shows that the electrical COP in DPC mode drops dramatically for increasing secondary fractions, due to the increasing airflow rates and pressure drops in the system.
Figures 4.14e and 4.14f show that the MSWC increases for increasing secondary fractions with small influences from the regeneration fraction in both IEC and DPC modes. The MSWC gets very high in DPC mode for increasing secondary fractions as the cooling capacity drops significantly while the water evaporation rate in the cooler increases.

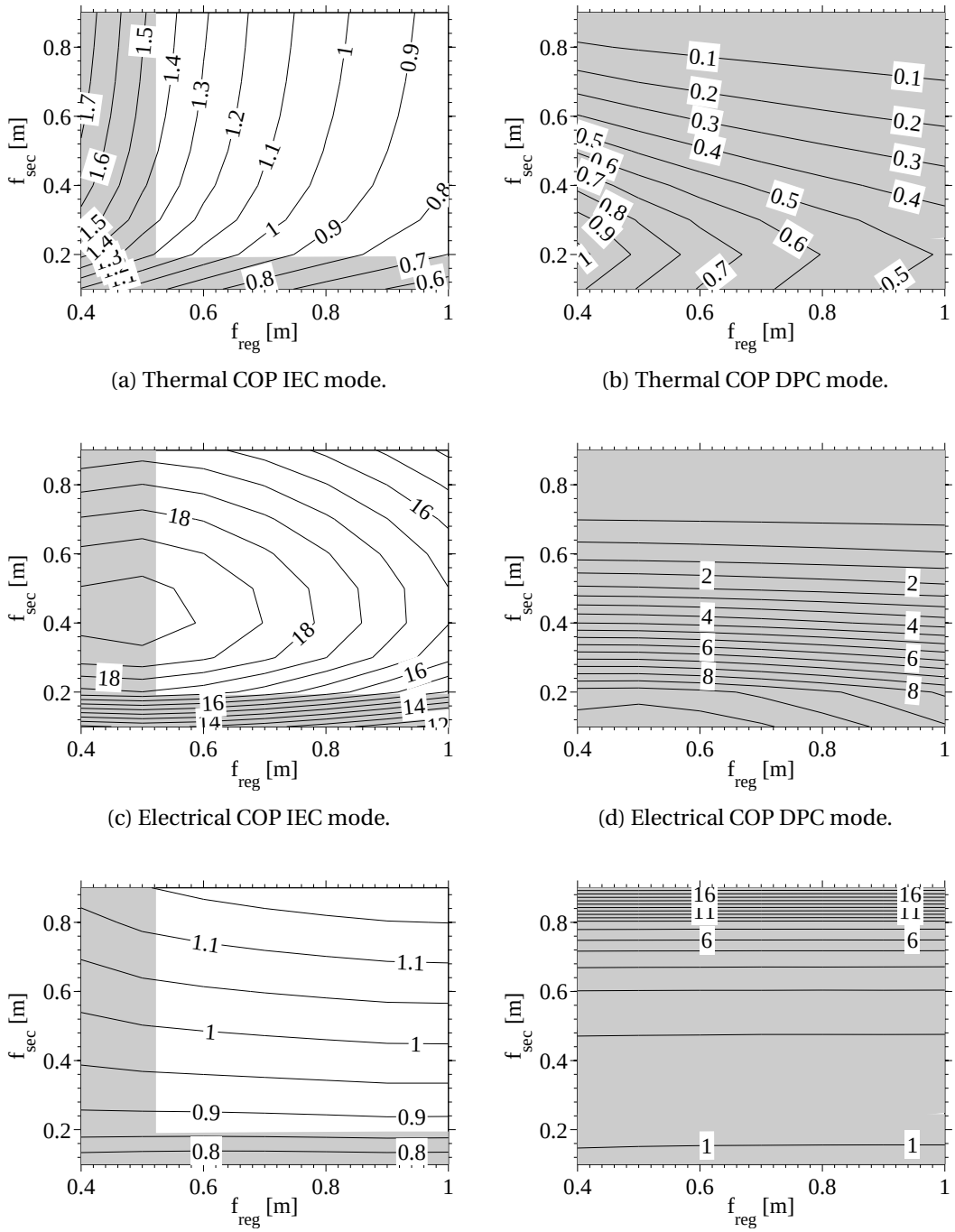

(a) Thermal COP IEC mode.

(b) Thermal COP DPC mode.

(c) Electrical COP IEC mode.

(d) Electrical COP DPC mode.

(e) MSWC [kg/kWh] IEC mode.

(f) MSWC [kg/kWh] DPC mode.

Figure 4.14: Variation of system performance in IEC and DPC modes for varying air fractions.

4.3.4 Influence of outdoor conditions

The system response to varying outdoor conditions is investigated. Outdoor temperature is varied between 25°C and 45°C, while outdoor humidity ratio is varied between 10 and 25 g/kg. The DW rotational speed is kept at the optimal values maximizing the process air dehumidification.
The resulting supply conditions are reported in Figure 4.15 on psychrometric diagrams, on which each point corresponds to different outdoor conditions. Infeasible supply conditions are identified by gray areas.

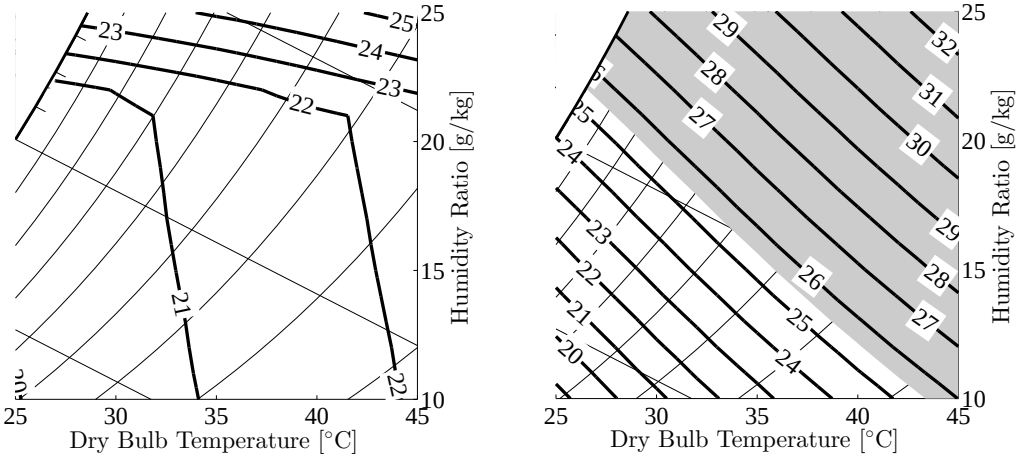

(a) Supply temperature [°C] IEC mode.

(b) Supply temperature [°C] DPC mode.

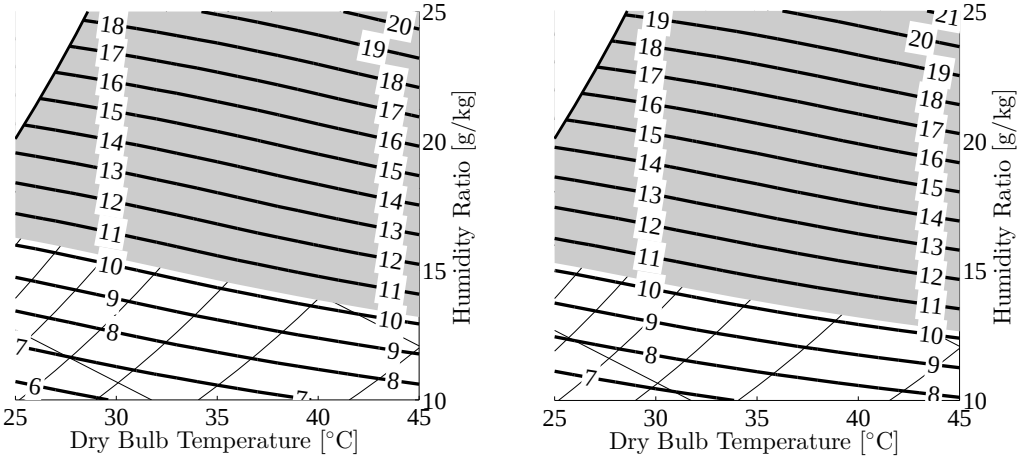

(c) Supply humidity ratio [g/kg] IEC mode.

(d) Supply humidity ratio [g/kg] DPC mode.

Figure 4.15: Variation of supply temperature in IEC and DPC modes for varying outdoor conditions.

Figures 4.15a and 4.15b show that the supply temperature varies following different trends in IEC and DPC modes.

In IEC mode, the system is capable of providing acceptable supply temperatures in the whole range of considered outdoor conditions. The supply temperature varies differently with the outdoor conditions for outdoor humidity ratios below or above approximately 21 g/kg. This is due to the fact that the process air is cooled down to saturated conditions for high outdoor humidity ratios, as its dew point increases while the secondary air inlet conditions are kept constant at the reference indoor conditions. The model does not take into account condensation at the IEC primary side, hence the trends observed at outdoor humidity ratios above 21 g/kg should not be considered exact. At lower outdoor humidity ratios, the supply temperature varies only by about 2°C in the whole range of considered outdoor temperatures, with little dependence on the outdoor humidity ratio.
In DPC mode, the supply temperature exhibits a strong dependence on the outdoor conditions, as in this case the IEC secondary air stream conditions are affected by the outdoor conditions. Differently from all the other parameter variations, the supply temperature in DPC mode reaches lower values than in IEC mode for the coldest and driest considered outdoor conditions.
Figures 4.15a and 4.15b show that the supply humidity ratio varies similarly in IEC and DPC modes. In IEC mode, the supply humidity ratio is slightly lower than in DPC mode for the same outdoor conditions, due to the lower airflow rates across the DW. Generally, the system is able to provide sufficiently low humidity contents only for relatively dry or moderately humid outdoor conditions, under the considered operating conditions.
The corresponding system performance variations are reported in Figure 4.16. In IEC mode, results corresponding to outdoor humidity ratios above approximately 21 g/kg should be disregarded due to the presence of condensation in the IEC primary side, as previously explained.

Figures 4.16a and 4.16b show that the thermal COP increases for increasing outdoor temperatures, as well as for increasing outdoor humidity ratios in IEC mode, which has almost no influence in DPC mode. The thermal COP is always higher in IEC mode, particularly at higher outdoor temperatures.
Figures 4.16c and 4.16d show that also the electrical COP generally increases for increasing outdoor temperatures, while the outdoor humidity ratio provides opposite effects in IEC and DPC modes. The electrical COP varies considerably with the outdoor conditions in IEC mode, due to the small changes in supply temperature.
Figures 4.16e and 4.16f show that the MSWC varies differently in IEC and DPC modes, generally decreasing for increasing outdoor humidity ratios, particularly in IEC mode.

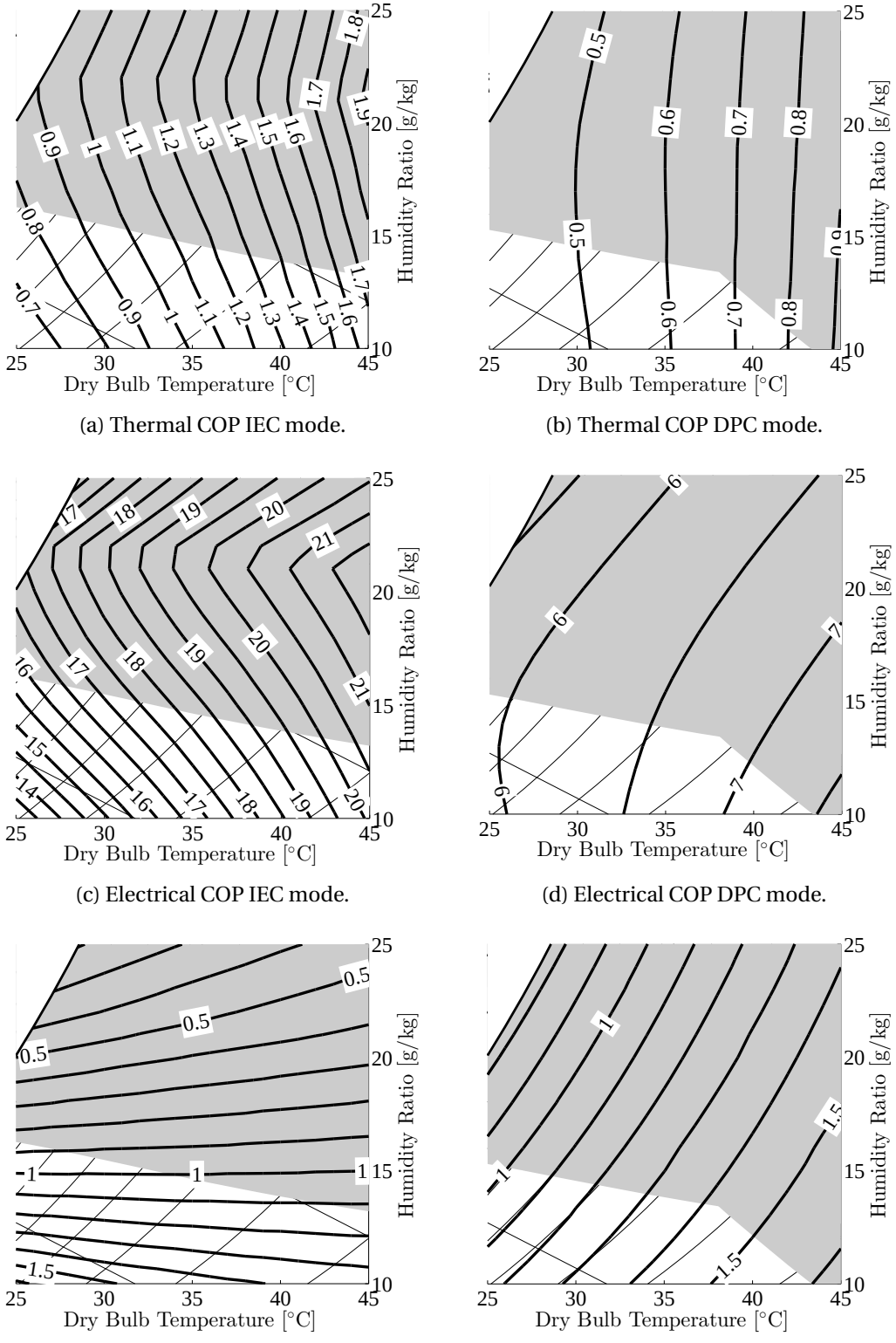

(a) Thermal COP IEC mode.

(b) Thermal COP DPC mode.

(c) Electrical COP IEC mode.

(d) Electrical COP DPC mode.

(e) MSWC [kg/kWh] IEC mode.

(f) MSWC [kg/kWh] DPC mode.

Figure 4.16: Variation of system performance in IEC and DPC modes for varying outdoor conditions.

4.4 Discussion

All results obtained for varying system geometrical and operational parameters and outdoor conditions have shown that the IEC mode outperforms the DPC mode for fixed system dimensions and supply airflow rates, with possibility for tripling the electrical COP and doubling the thermal COP, while providing lower supply temperatures and humidity contents. The electrical COP decreases when considering additional pressure drops, e.g. due to air filtration, particularly in IEC mode, even if the electrical COP is still doubled in comparison to the DPC mode.
The differences between the two modes of operation are expected to increase with more favourable indoor conditions, i.e. lower indoor enthalpies. In all simulations, the indoor conditions have been kept at the maximum indoor temperature and humidity providing acceptable thermal comfort, i.e. the least favourable scenario for the system operating in IEC mode. Lower indoor temperatures and/or humidity contents would increase the cooling capacity in IEC mode, while no effect would be noticeable in DPC mode as the system works independently of the conditioned space.

Even with no HEX, the system operating in IEC mode has been found to be able to maintain indoor thermal comfort with an electrical COP above 20 and a thermal COP above 0.8. The system configuration with no HEX is particularly interesting for desiccant-assisted radiant cooling systems, which cover the majority of the indoor sensible load with chilled water circulating into radiant panels in the ceiling. The DIEC system would then be required to provide fresh and dry air, and, when operating in IEC mode, it would increase its cooling capacity because of lower indoor temperatures provided by the radiative cooling systems, enabling to supply adequately low temperatures also with no HEX. The corresponding high electrical COP can lead to high primary energy savings in respect to conventional air conditioners.

The DIEC system is found to provide satisfactory dehumidification capacity for moderately humid outdoor conditions when driven by regeneration temperatures below 90°C. In humid climates, higher regeneration temperatures are required to increase the system dehumidification capacity, resulting into lower thermal COP and higher electrical COP. The use of two-stage dehumidification, e.g. by means of two desiccant wheels in series with intermediate cooling, would enable to increase the dehumidification capacity and the thermal COP with reduced regeneration temperatures, at the expense of increased fan power consumption. However the high electrical COP obtained in IEC mode suggests that two-stage dehumidification solutions have the potential to extend the applicability of the system in humid regions maintaining competitive electricity consumptions in respect to conventional air conditioners.

The use of both thermal and electrical COP to describe the system performance enables to highlight some important trade-off when varying component dimensions and operational

parameters. Generally, longer components are necessary for maximing the thermal COP but not the electrical COP, while higher regeneration temperatures lead to lower thermal COP but higher electrical COP.
The electrical COP can be considered the economic and environmental justification for preferring desiccant cooling systems over a conventional vapour compression system, usually characterized by an electrical COP of 3-4 [20]. Therefore the DIEC system, both in IEC and DPC modes, has potential for providing primary energy savings in respect to conventional air conditioners.
Data from solar-driven absorption chiller installations with regeneration temperatures up to 90°C [89] indicated thermal COP between 0.5 and 0.7, and electrical COP between 2 and 8, with improvement potential by using efficient fans and pumps and efficient part load control strategies. The comparison of measured absorption chiller performance and computed DIEC system performance indicates that the DIEC system operating in IEC mode has the potential to achieve higher thermal and electrical performance than absorption chillers, whereas the DIEC system in DPC mode seems to have comparable performance.

4.5 Conclusions

In the present chapter a solid desiccant cooling system implementing two types of indirect evaporative cooling process, namely the indirect evaporative cooling process and the dew point cooling process, has been presented and analysed utilizing the detailed component models introduced in the previous chapters.
From the observed effects of varying system geometrical and operational parameters and outdoor conditions, it can be concluded that:

- The system operating with indirect evaporative cooling outperforms the system operating with dew point cooling, with nearly doubled thermal COP and nearly tripled electrical COP. This result is valid for systems with the same component dimensions as well as for systems providing the same supply conditions.
- The use of indirect evaporative cooling provides colder and drier supply air conditions than with dew point cooling for the same component dimensions. This extends the applicability of the system, particularly at high outdoor temperatures. In case of high latent loads, two-stage dehumidification can be implemented.
- The use of indirect evaporative cooling makes the system highly competitive with electric and absorption chiller-based systems in terms of electricity and heat consumptions.
- Component face dimensions should be chosen as big as possibly allowed by space and capital cost limitations for improving the supply conditions and increasing the system thermal and electrical COP.

- Increasing component lengths improves the supply conditions and the system thermal COP. The electrical COP is maximized for specific component lengths, which increase for increasing system electricity consumptions.
- The considered indirect evaporative cooler is by far the biggest component in the system, setting the overall space requirements.
- Regeneration conditions have a small influence on the supply temperature.
- Regeneration temperature has a strong effect on the system thermal and electrical COP.
- The variation of the IEC secondary air fraction enables a simple an effective control of the supply temperature with indirect evaporative cooling, affecting only the IEC operation. When using dew point cooling, the IEC secondary air fraction should be kept at its optimal value as it affects all components.

5 Exergy Analysis

5.1 Introduction

Exergy represents the quality of energy, i.e. the maximum theoretical useful work that can be generated by a system for a given energy input to reach equilibrium with a reference environment. Exergy analysis provides information on how efficiently a certain amount of available energy is used by a system, pointing out the distribution and causes of irreversibility in the processes involved. In this way, systems running on different primary energy sources can be fairly compared among each other, as in the case of desiccant cooling systems and conventional air conditioners.

Exergy analysis has been adopted as an effective method to improve the performance of desiccant cooling systems [90–95]. Previous exergy analyses of different desiccant cooling system configurations [96, 97] have identified that the most important inefficiencies are usually connected to the heat transfer process taking place in the regeneration heater and to the heat and mass transfer processes taking place in the desiccant dehumidifier, not considering power consumption for running the auxiliaires. Analysis of a solar-driven desiccant cooling system [98] has shown that solar collectors are the main contributors to exergy destruction in the whole system, whereas fans are responsible for the highest exergy destruction in the desiccant cooling system.

The present exergy analysis is applied to the Desiccant Indirect Evaporative Cooling (DIEC) system introduced in Chapter 4 and described in Figure 4.1. The scope is to identify the distribution of exergy destruction within the system for different configurations and regeneration temperatures, and compare the efficiency of primary energy consumption with conventional chiller-based systems. The use of solar energy instead of conventional energy sources for producing the regeneration heat is also considered.

5.2 Methods

The exergy flows considered in the analysis, from primary energy sources to final utilization of the produced cool and dry air stream, are indicated in Figure 5.1.

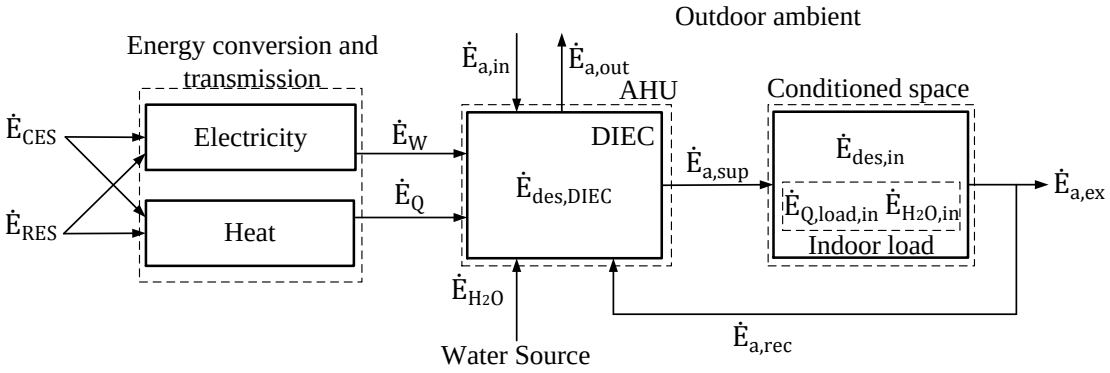

Figure 5.1: Exergy flows from primary energy sources to final utili.

Exergy flows associated to conventional energy sources ($\dot{E}_{CES}$), e.g. coal, oil, natural gas, and to renewable energy sources ($\dot{E}_{RES}$), e.g. wind, solar, biomass, can be used to produce exergy flows of electricity ($\dot{E}_W$) and heat ($\dot{E}_Q$) for running the DIEC system, i.e. the Air Handling Unit (AHU). Electricity and heat can be generated locally, e.g. by means of solar PV and thermal energy systems, boilers, etc., or remotely, e.g. in power plants, wind farms, etc., requiring transmission lines. Additionally, the DIEC system requires an exergy flow of water ($\dot{E}_{H_2O}$) for running the indirect evaporative cooling process. The exergy flows of electricity, heat and water are exergy fuels for the DIEC system.
Exergy flows of outdoor air entering the DIEC system are associated to the process and regeneration air streams ($\dot{E}_{a,in}$), while the air streams exhausted back to the outdoor ambient represent exergy losses ($\dot{E}_{a,out}$).
The AHU supplies an exergy stream of dry and cool air ($\dot{E}_{a,sup}$) to the conditioned space.
The indoor load is identified as the sum of the exergy streams associated to the indoor sensible and latent loads ($\dot{E}_{Q,load,in}$) and the indoor moisture generation ($\dot{E}_{H_2O,in}$). The air exhausted from the conditioned space ($\dot{E}_{a,ex}$) can be partly recirculated ($\dot{E}_{a,rec}$) into the AHU, e.g. when operating the DIEC system in IEC mode.
In the following, the exergy flows inside the conditioned space are not take into consideration, as focus is put on how efficiently the AHU uses the exergy fuels for producing the supply air stream and how efficiently these exergy fuels are obtained from primary energy sources.

The DIEC system is modelled as described in Chapter 4, using the detailed component models developed in Chapters 2 and 3.
The comparison with conventional AHU based on electric chillers, i.e. vapour compression cycles, is carried out by means of simplified models. Electric chiller-based AHU are modelled by means of an overall electrical COP, defined analogously to Equation 4.7, which accounts

for the toal electricity consumption for vapour compression, heat rejection, chilled water distribution, and air circulation. The fans and pumps for heat rejection and chilled water distribution may consume from 10-15% of the total electricity consumption at full load, to 50% or more at part load [99]. The electrical COP is considered between 3 and 5 in the following, covering the range of conventional chiller-based AHU. In case of dehumidification, air is assumed to leave the cooling coil in the AHU at saturated conditions, and a natural gas boiler is considered for reheating the air to the required supply temperature.

5.2.1 Dead state selection

The exergy content of matter and energy is intended as the maximum useful work that can be produced by bringing them into equilibrium with a reference environment, termed dead state, at temperature T_0, pressure P_0 and specified concentrations of substances.
Conditions P_0 and T_0 define the restricted dead state, at which the system is in thermal and mechanical equilibrium with the reference environment. The dead state is reached when also chemical equilibrium is present, so that the system has the same concentrations of substances as in the reference environment.
While the choice of the reference state does not influence energy analysis, exergy analysis is strongly influenced by the reference state selection, as the reference conditions do not level out in the exergy balance. In air conditioning applications, it is meaningful to set the dead state conditions equal to the outdoor ambient air conditions (P_0=P_{atm}, T_0=T_{out} and φ_0=φ_{out}), as the outdoor environment can be considered the ultimate sink and source of all processes occurring in the system, and its conditions can be considered independent of the interactions with the system [100].
When applying exergy analysis to extended periods of time, with varying outdoor conditions, the dead state conditions should be kept constant for obtaining a meaningful evaluation of time-dependent processes, such as heat-storage [101].

5.2.2 Exergy definitions

The exergy of humid air, liquid water and heat flows are defined in the following. The exergy of electricity is simply equivalent to its energy content [102].

Assuming humid air is an ideal mixture of ideal gases, its specific exergy content at a generic thermodynamic state i is defined as [102]:

$$\begin{aligned} e_{ha} = & c_{p,ha} T_0 \left[\frac{T_i}{T_0} - 1 - ln\left(\frac{T_i}{T_0}\right) \right] + (1 + (R_v/R_a) x_i)\, R_a T_0 ln\left(\frac{P_i}{P_0}\right) + ... \\ & ... + R_a T_0 \left[(1 + (R_v/R_a) x_i)\, ln\left(\frac{1 + (R_v/R_a) x_0}{1 + (R_v/R_a) x_i}\right) + (R_v/R_a) x_i ln\left(\frac{x_i}{x_0}\right) \right] \end{aligned} \tag{5.1}$$

The terms on the RHS represent the thermal, mechanical, and chemical exergy components respectively. The sum of the thermal and mechanical exergy of a stream of matter is termed physical exergy.

The specific exergy of liquid water at a generic state i is defined as [102]:

$$e_{w,i} = h_{f,i} - h_{g,0} - T_0 s_{f,i} + T_0 s_{g,0} + (P_i - P_{sat,i}) v_{f,i} - R_v T_0 ln\phi_0 \tag{5.2}$$

The exergy content of heat transferred at constant temperature T_i is defined as [102]:

$$E_{Q_i} = Q_i \left(1 - \frac{T_0}{T_i}\right) \tag{5.3}$$

5.2.3 Exergy destruction rates and exergy losses in the DIEC system

The exergy destruction rates in the DIEC systems are obtained by applying exergy balances around each component. Referring to the numbering introduced in Figure 4.1, the exergy destruction rates are calculated as:

$$\dot{E}_{des,DW} = \dot{E}_1 + \dot{E}_9 - (\dot{E}_2 + \dot{E}_{10}) \tag{5.4}$$
$$\dot{E}_{des,RH} = \dot{E}_8 + \dot{E}_{Q_{reg}} - \dot{E}_9 \tag{5.5}$$
$$\dot{E}_{des,HRU} = \dot{E}_2 + \dot{E}_7 - (\dot{E}_3 + \dot{E}_8 + \dot{E}_{12}) \tag{5.6}$$
$$\dot{E}_{des,fans} = \dot{W} \tag{5.7}$$

Regeneration heat is assumed to be transferred at constant temperature, set equal to the regeneration temperature, as different heat sources can be used. The corresponding exergy stream in Equation 5.5 is calculated by means of Equation 5.3.
The exergy destruction rate of fans is equivalent to the power they consume, as they provide a negligible change of the air stream exergy content.
The exergy destruction rate in the IEC is calculated depending on its mode of operation, considering the inlet secondary air stream in DPC mode to be internally generated:

$$\dot{E}_{des,IEC} = \dot{E}_3 + \dot{E}_5 + \dot{E}_{H_2O} - \dot{E}_6 \quad \text{(IEC mode)} \tag{5.8}$$
$$\dot{E}_{des,IEC} = \dot{E}_3 + \dot{E}_{H_2O} - \dot{E}_6 \quad \text{(DPC mode)} \tag{5.9}$$

The open-cycle nature of the DIEC system leads to exergy losses associated to the air streams exhausted to the outdoor ambient:

$$\dot{E}_{loss} = \dot{E}_{10} + \dot{E}_{12} + \dot{E}_{6} \tag{5.10}$$

5.2.4 Primary energy sources

In the present analysis, conventional energy sources are considered to produce heat and electricity unless differently specified. In particular, natural gas is considered for producing heat with boilers, while a mix of fossil fuels dominated by oil is considered for electricity production in power plants.
The exergy content of a given fuel is related to its Higher Heating Value (HHV). The exergy content associated to the i^{th} stream of primary energy (natural gas or oil-based fuel mix) for heat or electricity production is expressed as [90]:

$$\dot{E}_{PE,i} = \dot{m}_i HHV_i = \dot{PE}_i \left(\frac{HHV_i}{LHV_i} \right) = \dot{PE}_i \psi_i \tag{5.11}$$

where LHV is the fuel Lower Heating Value and PE is the Primary Energy.
The values of the heating value ratio ψ are set to 1.1 for natural gas and 1.06 for the oil-based fuel mix [90]. The boiler thermal efficiency is set to 90%, while the power plant electrical efficiency is set to 37%, also accounting for transmission losses in the electricity grid.

In the following analysis, the use of solar energy for providing part of the regeneration heat to the DIEC system is also considered. Flat-plate solar collectors can be used, as regeneration temperatures do not exceed 90°C.
The exergy content of solar energy reaching the collectors is defined considering its use in a Carnot cycle operating between the dead state temperature (T_0) and the collector plate temperature (T_p) [90]:

$$\dot{E}_{solar} = \dot{PE}_{solar} \left(1 - \frac{T_0}{T_p} \right) = \frac{\dot{Q}_{solar}}{\eta_{th,coll}} \left(1 - \frac{T_0}{T_p} \right) \tag{5.12}$$

Generally, the collector thermal efficiency ($\eta_{th,coll}$) depends on the collector plate temperature, decreasing for increasing plate temperatures due to higher thermal losses from the collector to the surroundings [103].

5.2.5 Exergy performance indicators

The following exergy performance indicators are selected, considering that the useful product provided by the system is the exergy flow associated to the supply air stream:

- Exergy efficiency of the air handling unit

$$\eta_{ex,AHU} = \frac{\dot{E}_{a,sup}}{\dot{E}_{fuels}} = 1 - \frac{\sum_{i=1}^{n_{component}} \left(\dot{E}_{des,i}\right) + \dot{E}_{loss}}{\dot{E}_{fuels}} \tag{5.13}$$

  The fuels for the DIEC system are the regeneration heat, the electricity consumed by the auxiliaries, the water evaporated in the evaporative cooling process. The air streams entering the system are also regarded as fuels, i.e. the process and regeneration air streams and the IEC secondary inlet air stream, if operating in IEC mode.

- Overall exergy efficiency

$$\eta_{ex} = \frac{\dot{E}_{a,sup}}{\dot{E}_{primary\ energy}} \tag{5.14}$$

  The overall exergy efficiency takes into account also the exergy streams of all primary energy sources used to run the system. Conventional and renewable energy sources for producing electricity and heat, water, and the air streams entering the system are considered.

5.3 Results and discussion

The reference scenario for the following exergy analysis is the one reported in Table 4.1. The DIEC system operating in IEC mode is considered in the following, unless differently specified.

Comparison of system configurations

At first, different system configurations are compared, namely the DIEC system operating in IEC mode with and without HEX, and the DIEC system operating in DPC mode with HEX. The configurations are termed IEC, IEC noHEX and DPC respectively.
The comparison is carried out for equal supply conditions, i.e. equal product air stream exergy content. The component dimensions in the IEC configuration are set to the reference dimensions in Table 4.1, resulting in a supply temperature of 21.2°C and a supply humidity ratio of 9.9 g/kg. The same supply conditions are obtained with the IEC noHEX configuration by increasing the IEC number of plates to 188 (+19%). The DPC configuration is instead dimensioned with 278 IEC plates (+76%), UA_{HEX} of 7 kW/K (+40%) with pressure drop of 150 Pa at each side at nominal flow conditions, and DW diameter of 1.45 m (+21%).
A natural gas boiler is considered for providing the regeneration heat, while conventional power plants are considered for electricity generation.
Results are reported in Figure 5.2.

Figure 5.2a shows that the IEC configuration is characterized by the lowest exergy destruction rates, including exergy loss, whereas the DPC configuration is characterized by the highest

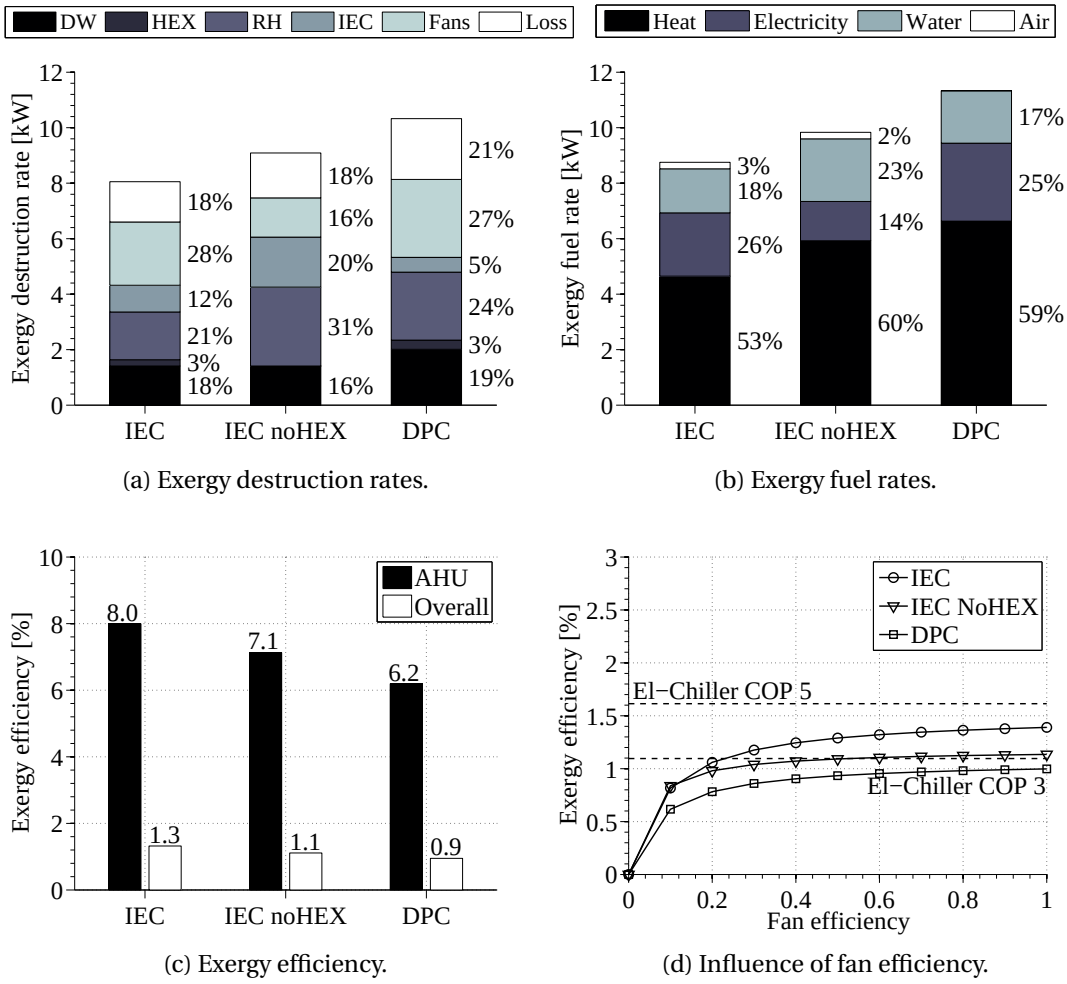

(a) Exergy destruction rates.

(b) Exergy fuel rates.

(c) Exergy efficiency.

(d) Influence of fan efficiency.

Figure 5.2: Comparison of different system configurations.

exergy destruction rates, as it operates with higher air flow rates.

Not considering the fans, the RH is the component with the highest exergy destruction rate, followed by the DW. This is quite evident in the IEC noHEX configuration, as more regeneration heat is transferred with the same airflow rates as in IEC configuration. The exergy destruction rate in the RH is expected to increase when considering the real case of heat transferred across temperature differences, and not at constant temperature. The exergy destruction rate in the fans, necessary for circulating the air streams across the system, is higher in the IEC and DPC configurations, which are characterized by higher air pressure drops than in the IEC noHEX configuration. It is also noticed that the HEX is responsible for the smallest exergy destruction rates, and the IEC is responsible for a quite lower exergy destruction rate when operated in DPC mode.

Figure 5.2b shows that the the exergy fuel consumptions increase accordingly to the exergy destruction rates, with the IEC configuration requiring the least amount of exergy fuel. The

IEC noHEX and DPC configurations have higher exergy fuel consumptions mostly because of the higher amounts of regeneration heat required. In the IEC noHEX configuration, the electricity savings introduced by not using a HEX are counterbalanced by higher heat and water consumptions.
Figure 5.2c shows that the exergy efficiency of the IEC configuration is the highest both at the AHU and overall levels, and the exergy efficiency varies among the configurations following the corresponding variation of regeneration heat consumption. The comparison of the AHU and overall exergy efficiencies indicates that the production of heat and electricity are responsible of consistent exergy destructions.
The influence of the fan efficiency is investigated in Figure 5.2d, comparing the system configurations with conventional electric chiller-based AHU in terms of overall exergy efficiency. Two chiller-based AHU are considered, with electrical COP of 3 and 5 respectively, independent of the fan efficiency. Results show that the IEC configuration approaches the overall exergy efficiency of the chiller-based AHU with electrical COP of 5 for high fan efficiencies. It is noticed that the overall exergy efficiency of all considered DIEC system configurations is nearly constant for fan efficiencies above 0.6, as the exergy content of the consumed natural gas becomes dominant. This result suggests that different heat production technologies should be considered for improving the overall exergy efficiency.
The exergy content of natural gas consumed for air reheating in the chiller-based AHU accounts for approximately 30% (electrical COP 5) and 20% (electrical COP 3) of the respective total exergy input from primary energy sources. This motivates the use of lower supply temperatures with chiller-based AHU for achieving higher exergy as well as energy performance, with possibility for reducing the supply airflow rate if permitted by ventilation and indoor humidity requirements.

Effect of regeneration temperature

Regeneration heat accounts for more than 50% of the exergy fuel input to the DIEC system in the results reported in Figure 5.2. The regeneration temperature at which the heat is available is expected to have a strong impact on its exergy content. Therefore the influence of the regeneration temperature on the exergy performance of the DIEC system operating in IEC mode is investigated.
The system dimensions are set equal to the reference scenario, resulting into different supply conditions as the regeneration temperature is varied. Results are shown in Figure 5.3 for regeneration temperatures of 50°C, 70°C and 90°C. The corresponding supply conditions are characterized by approximately the same supply temperature, while the supply humidity ratio is 12.3, 10.6 and 9.3 g/kg respectively. Low regeneration temperatures do not allow to maintain the indoor humidity content according to the reference scenario, but they are still considered for comparing their impact on the system exergy performance.

Figure 5.3a shows that the total exergy destruction and loss rate is highly affected by the regeneration temperature, increasing of 175% from 50°C to 90°C. At 50°C regeneration temper-

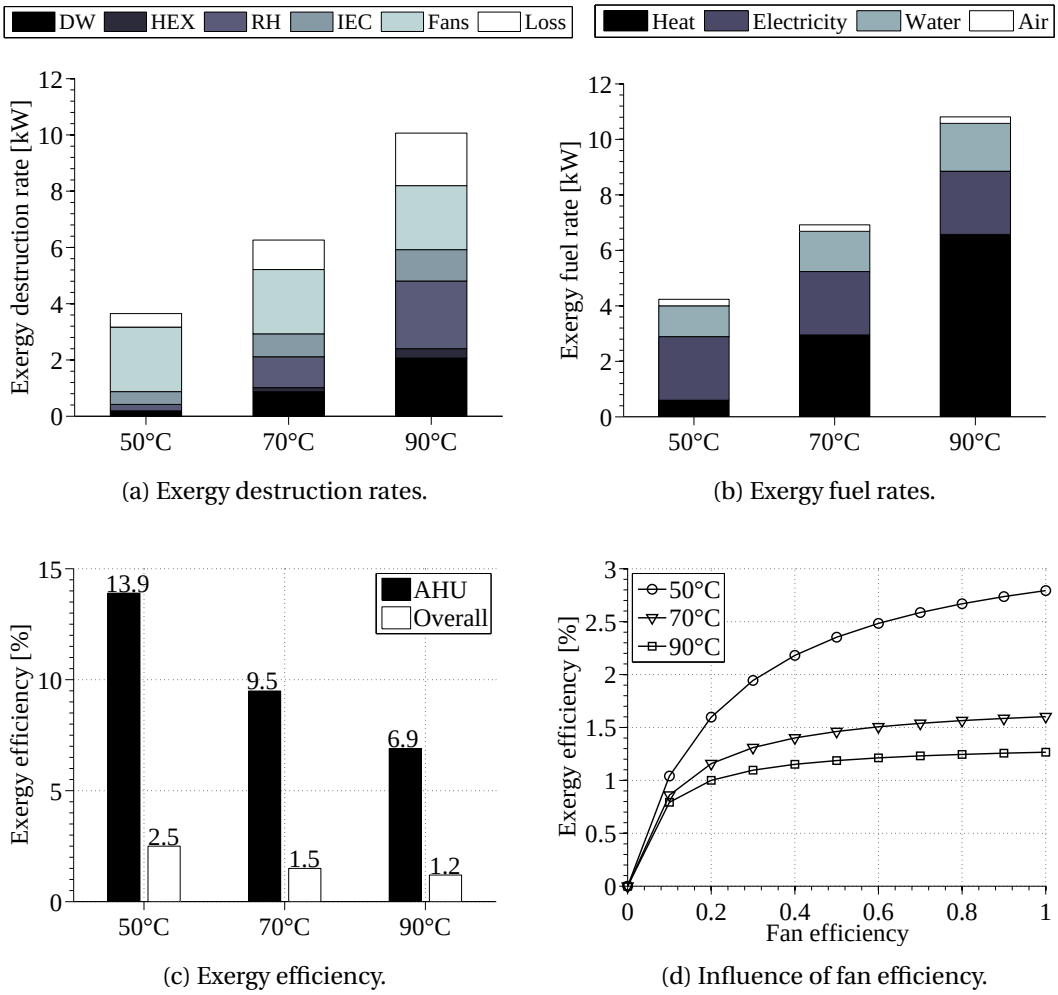

(a) Exergy destruction rates.

(b) Exergy fuel rates.

(c) Exergy efficiency.

(d) Influence of fan efficiency.

Figure 5.3: Effect of varying regeneration temperatures.

ature, the IEC is the component with the highest exergy destruction rate, not considering the fans, whose exergy destruction rate is independent of the regeneration temperature. As the regeneration temperature increases, the exergy destruction rates in the RH and DW become more important, as well as the exergy loss due to warmer and more humid air exhausted by the system after the regeneration process.

Figure 5.3b shows that the total exergy fuel rate varies analogously to the total exergy destruction and loss rate. The variation is connected to varying heat exergy contents, as increasing regeneration temperatures lead to higher regeneration heat consumption as well as higher available heat quality.

Figure 5.3c shows that the both the AHU and overall exergy efficiencies increase more than linearly for decreasing regeneration temperatures. Hence, the DIEC system is also very sensitive to latent loads, as already known for chiller-based AHU.

Figure 5.3d shows that electricity consumption for fans becomes more important at low regen-

eration temperatures, and the use of more efficient fans leads to higher improvements of the exergy efficiency than at higher regeneration temperatures.

Use of solar energy

All previous results considered the use of a conventional natural gas boiler for producing the required regeneration heat, resulting into high exergy destructions during to the high temperature combustion process. The use of solar energy is a promising alternative to burning fuels for producing low temperature heat, suitable for running the DIEC system.
The benefits of using solar energy are shown considering the impact of varying solar fractions, i.e. fractions of the total regeneration heat obtained from solar energy. Results are reported in Figure 5.4 for regeneration temperatures of 80°C and 60°C, indicating also the correspondent overall exergy efficiency of electrical chiller-based AHU powered by conventional energy sources. In case of regeneration temperature of 80°C, flat-plate solar collectors operating at 90°C are considered, with thermal efficiency of 50%. In case of regeneration temperature of 60°C, the collectors are assumed to operate at 70°C, with thermal efficiency increased to 60% due to lower heat losses to the surroundings [103].

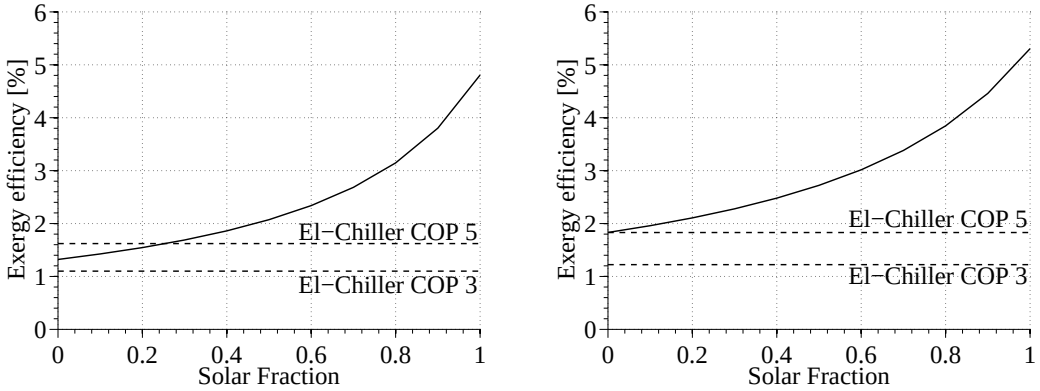

(a) Regeneration temperature 80°C.

(b) Regeneration temperature 60°C.

Figure 5.4: Exergy efficiency for the DIEC system as a function of the solar fraction and comparison with electric chillers.

Figure 5.4 shows that the use solar energy makes the DIEC system outperform electric chiller-based AHU. The DIEC system operating with 80°C regeneration temperature requires a solar fraction of 25% for having the same overall exergy efficiency of the best performing chiller-based AHU. Lower regeneration temperatures, i.e. lower latent loads, make the exergy efficiency of the DIEC system increase more than the exergy efficiency of chiller-based AHU, even by using conventional energy sources, i.e. null solar fraction. Lower regeneration temperatures and higher solar fractions lead to higher exergy efficiencies, due to lower regeneration heat consumption as well as lower exergy content of heat produced from solar energy.

5.4 Conclusions

An exergy analysis of the DIEC system has been carried out for investigating the effects of different system configurations and regeneration temperatures on the exergy destructions taking place in the system. The DIEC system has also been compared to conventional electric chiller-based systems in terms of efficiency of primary energy use, considering conventional primary energy sources as well as solar energy.
From the exergy analysis it can be concluded that:

- The IEC operated in DPC mode is characterized by lower exergy destruction rates than in IEC mode. However, this is not sufficient to achieve better exergy performance on a system level due to the higher airflow rates required by the DPC mode of operation.
- The use of more efficient fans does not improve significantly the system exergy efficiency. Hence, priority should be given to produce regeneration heat more efficiently.
- The system uses primary energy sources more efficiently when operating at lower regeneration temperatures, which also result into lower exergy destruction rates and exergy loss. This represents the conceptual advantage of using two-stage dehumidification processes for covering high latent loads.
- The use of solar energy, which clearly leads to primary energy savings, results also into higher exergy efficiencies, because of lower solar exergy contents in comparison to fossil fuels. Solar energy matches the exergy needs of low temperature heat-driven air conditioning systems better than fossil fuels.

6 Independence of external water sources

6.1 Introduction

Energy and water are to a large extent interdependent resources. Water is necessary for converting energy, extracting, transporting and processing fossil fuels, as well as producing biofuels. On the other hand, energy is necessary for running systems that collect, treat, transport and distribute water. The increasing demands for both energy and water due to economic and population growths and climate change are amplified by their interdependence. Water scarcity and stress of water resources are growing concerns worldwide, already affecting some countries (e.g. China and India), as well as specific regions of countries with apparent high water availability (e.g. USA and Australia) [104]. Limited water availability can affect the reliability of existing energy systems and the viability of new systems. As a result, availability and use of water are gaining importance for assessing the viability of future energy projects [104].

The need for cooling of conditioned spaces is expected to increase concomitantly to decreasing water availability, due to increasing standards of living connected to economic growth, increasing demands connected to population growth, and increasing ambient temperatures connected to climate change.

Conventional vapour-compression air conditioning systems consume water indirectly, i.e. the water needed to generate the electricity, but they can also have a direct water consumption, e.g. if using evaporative cooling processes for the purpose of heat rejection, such as cooling towers.

On the other hand, desiccant cooling systems are always characterized by both direct and indirect water consumptions, as cooling is generated by means of evaporative cooling processes and electricity is consumed for running fans and pumps.

The indirect water consumption of air conditioning systems can be reduced either by increasing their electrical efficiency or by reducing the water consumption per unit of generated electricity. The latter is of particular interest as it provides the highest total savings, and it can be achieved by e.g. improving power plant efficiency and/or increasing the share of production from renewable energy technologies with minimal water requirements, such as

solar PV and wind [104].
The direct water consumption of air conditioning systems depends on the type, dimensions and operating conditions of the employed evaporative cooling technologies.
Water consumption due to evaporation in cooling towers under typical working conditions is rated 1.37 kg/h per kW of heat rejected [105].
The indirect evaporative cooler considered in Chapter 3, is characterized by water consumption rates around 1.7 kg/h per kW of useful cooling produced under typical working conditions, with significant dependence on the operating parameters: the water consumption varies from approximately 1.5 kg/kWh at low primary air flow rates and low recirculation fractions to 2.5 kg/kWh (DPC mode) and 2 kg/kWh (IEC mode) at high primary flow rates and high recirculation fractions (see Figure 3.17), and higher values are obtained for increasing secondary airflow rates (see Figure 3.19).
The use of water demineralization processes to avoid the deterioration of the cooling performance during the system lifetime also influences water consumption. Common types of water demineralization equipment are based on reverse osmosis filter technology or ion exchange bed technology. Reverse osmosis filters produce a permeate demineralized water stream, rejecting a concentrate water stream that typically accounts for 30% of the incoming water stream [106]. Ion exchange beds require a periodic regeneration process, which uses water and chemical reagents to maintain the resin demineralization potential and requires a careful control to avoid unnecessary consumptions [106].
The applicability of desiccant cooling systems could be limited by scarce water availability due to high stresses on water resources, e.g. in densely populated areas, or even absent water availability, e.g. in remote locations.

A novel technical solution for making desiccant cooling systems independent of external water sources is hereby proposed. The solution is based on the idea of recovering the water desorbed from the desiccant dehumidifiers, store it, and use it to run the evaporative coolers. A schematic representation of a desiccant cooling system implementing this solution is shown in Figure 6.1.

Warm and humid air is dehumidified, pre-cooled and at last cooled to the supply conditions in the evaporative cooler. Pre-cooling is used to reduce the cooling capacity required by the evaporative cooler, hence reducing water consumption. The pre-cooling fluid can simply be air, such that the pre-cooling unit is a compact air-to-air heat exchanger. The moisture adsorbed in the desiccant dehumidifier is desorbed by the regeneration air stream, which is circulated in a closed loop constituted by the regeneration section of the desiccant dehumidifier and a so-called desorbed water recovery circuit, where moisture is condensed. The use of a closed loop makes possible to condense the whole amount of desorbed moisture. The coolant used for condensation can conveniently be outdoor air, as it is free and largely available. A water storage tank is used to accumulate the condensed water that is not instantly required by the evaporative cooler, allowing to run the system independently of external water sources also at times with no need for dehumidification.

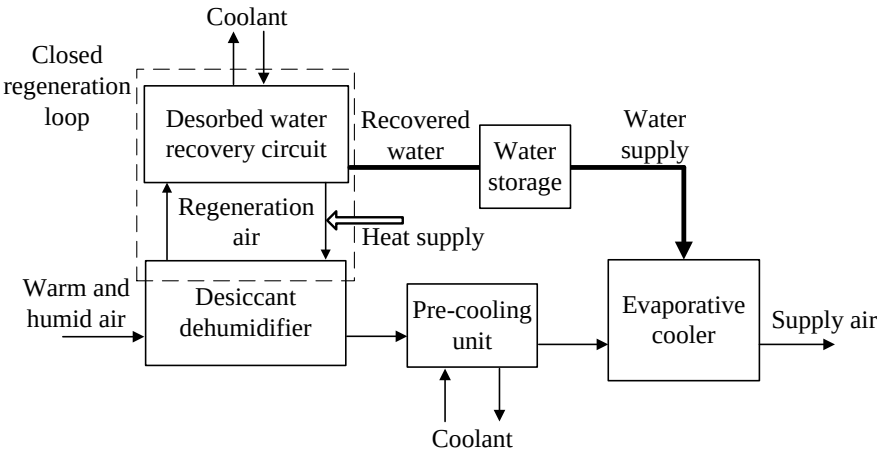

Figure 6.1: Schematics of desiccant cooling system independent of external water sources.

As condensed water is equivalent to distilled water, it can be supplied to the evaporative coolers without further demineralization processes, resulting into lower operational costs, maintenance requirements and waste of water.
The coupling with solar PV and thermal panels, and/or PVT panels can make the system a completely sustainable solution, and in principle it allows to run the system off the grid.
The idea of recovering desorbed water by condensation with an open regeneration loop to run evaporative coolers has been previously patented [107]. However the open regeneration loop does not allow to recover the whole amount of desorbed water. As a result, complete independence of external water sources is difficult to achieve with an open regeneration circuit.

The applicability of the solution presented here is investigated by applying it to the so-called Desiccant Dew-point Cooling (DDC) system shown in Figure 6.2.

The DDC system is constituted by a Desiccant Wheel (DW), a Regeneration Heater (RH), an air-to-air Heat Exchanger (HEX), a Dew Point Cooler (DPC), Water Demineralization Equipment (WDE) and auxiliaries.
The desorbed water recovery solution is implemented by adding an air-to-air Condensation Air Cooler (CAC), an air-to-air Internal Heat Recovery Unit (IHRU), and a water tank to the DDC system, eliminating the WDE. The resulting system, termed DDC Desorbed Water Recovery (DDC-DWR) system, is shown in Figure 6.3.

Outdoor air is dehumidified in the DW (1)-(2) exiting at drier and warmer conditions, pre-cooled in the HEX (2)-(3), and lastly cooled to the supply temperature (3)-(4) in the DPC. Air is used as coolant in the HEX (6)-(7) and it can be taken from different sources, e.g. outdoor ambient, conditioned space exhaust, DPC secondary air exhaust, or a mix from these sources as shown in in Figure 6.3. Differently from the DDC system, the pre-cooling air is not used for

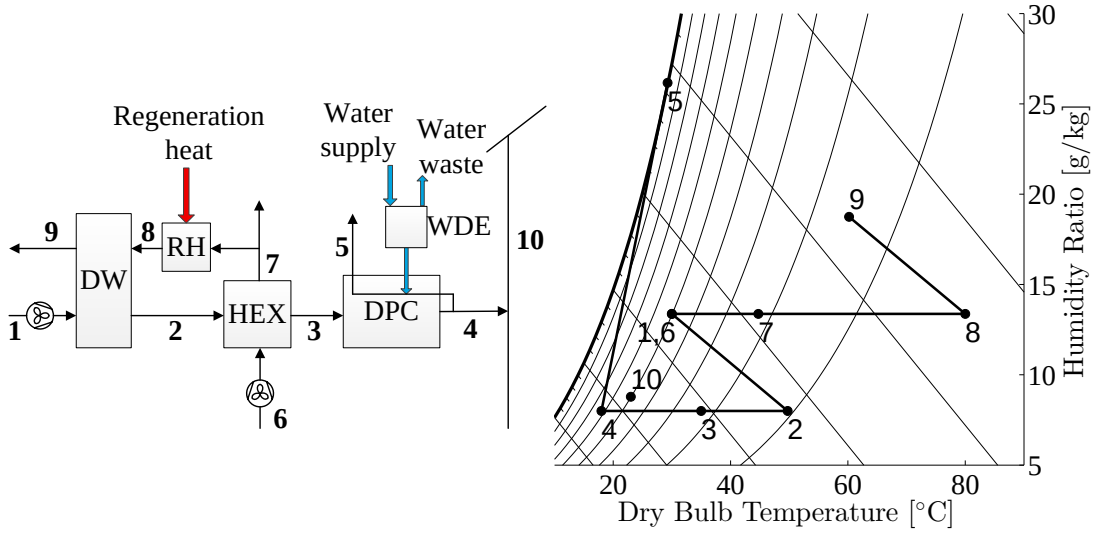

Figure 6.2: DDC system schematics and psychrometric processes.

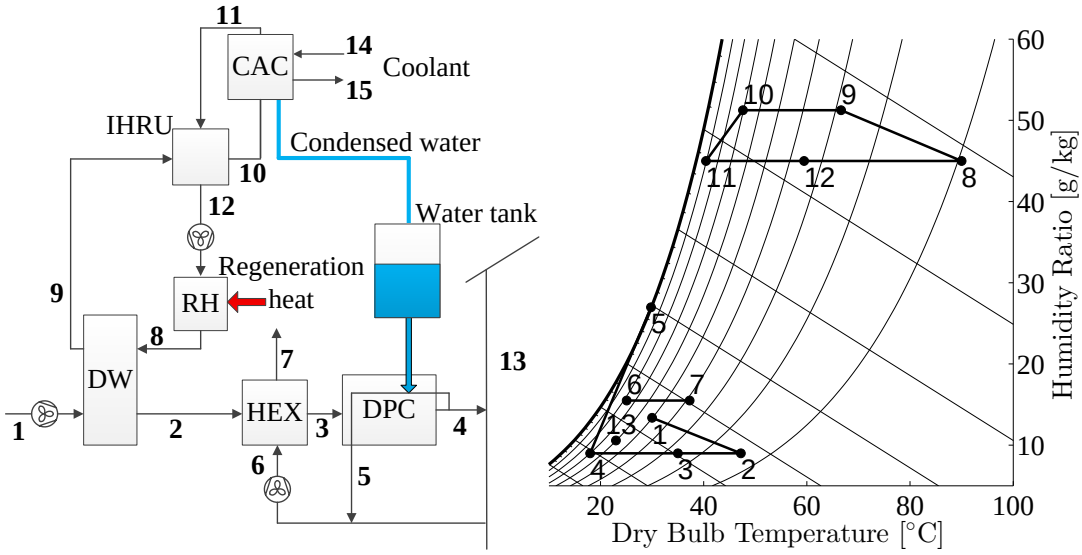

Figure 6.3: DDC-DWR system schematics and psychrometric processes.

regenerating the DW, allowing to select the coldest available air stream, regardless of the air quality. Water is consumed by evaporation into the DPC secondary air stream (4)-(5), which is obtained by recirculating a fraction of the exhaust primary air stream. The regeneration air stream is circulated in a closed circuit, cyclically undergoing moisture desorption from the desiccant (8)-(9), pre-cooling in the IHRU (9)-(10), cooling and dehumidification in the CAC (10)-(11), pre-heating in the IHRU (11)-(12), and heating to the regeneration temperature in the RH (12)-(8). Outdoor air is used as coolant for dehumidifying the regeneration air in the CAC (14)-(15). The condensed water is drained from the CAC and stored into a tank for

running the DPC when required. The IHRU allows to decrease both the CAC cooling capacity, as state (10) gets closer to saturation, and the regeneration heat consumption, as state (12) gets closer to the required regeneration temperature.
Figure 6.3 shows that the regeneration air stream is characterized by considerably higher moisture contents than in the DDC system (see Figure 6.2). This is due to the temperature and type of coolant used in the CAC, outdoor air in the considered case, which affect the CAC apparatus dew point. The result of increasing regeneration air moisture contents is that higher regeneration temperatures are required for achieving the same process air dehumidification.

6.2 DDC-DWR system analysis

The DDC-DWR system is analysed to identify the importance of different components for reaching water independence of external water sources.

6.2.1 Model formulation

All components are modelled by means of zero-dimensional models. The model description reported in the following refers to the air state numbering indicated in Figure 6.3.

Desiccant wheel

Energy and water mass balances around the component are written as:

$$(h_{a,2} - h_{a,1}) + f_{reg}(h_{a,8} - h_{a,9}) = 0 \tag{6.1}$$

$$(x_{a,2} - x_{a,1}) + f_{reg}(x_{a,8} - x_{a,9}) = 0 \tag{6.2}$$

where the regeneration fraction f_{reg} is expressed as:

$$f_{reg} = \frac{\dot{m}_{a,8}}{\dot{m}_{a,1}} \tag{6.3}$$

It is assumed that the process air outlet enthalpy $h_{a,2}$ increases linearly from point (1) to point (2), up to a maximum (2**) set by the process air enthalpy ratio ($f_{h,DW,max}$ defined as in Equation 2.21) at the theoretical lowest achievable relative humidity, i.e. the regeneration air inlet relative humidity $\phi_{a,8}$, as illustrated in Figure 6.4.

The corresponding process air outlet enthalpy is obtained as:

$$h_{a,2} = h_{a,1}\left[1 + (f_{h,DW,max} - 1)\frac{x_{a,1} - x_{a,2}}{x_{a,1} - x_{a,2^{**}}}\right] \tag{6.4}$$

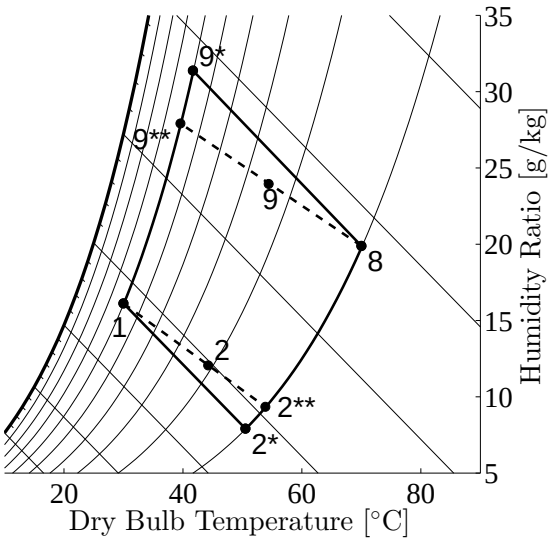

Figure 6.4: Example of operating limits for the considered silica gel desiccant wheel. (1) process air inlet, (2*) theoretical limit process air outlet, (2**) realistic minimum process air outlet, (2) realistic process air outlet, (3) regeneration air inlet, (4*) theoretical limit regeneration air outlet, (4**) realistic limit regeneration air outlet, (4) realistic regeneration air outlet.

The DW effectiveness is defined as:

$$\varepsilon_{DW} = \frac{x_{a,1} - x_{a,2}}{x_{a,1} - x_{a,2^{**}}} \tag{6.5}$$

This definition considers the realistic limit (2**) instead of the theoretical limit (2*) considered in the dehumidification effectiveness definition reported in Equation 2.20. This choice is made to not exceed the limits of operation for a specified process air enthalpy ratio and DW effectiveness close to unity.
In practise the DW effectiveness is a complex function of the DW geometry, desiccant characteristics and operating conditions. In this model, the DW effectiveness is considered independent of the recirculation fraction, while the wheel rotational speed is not specified.
Also $f_{h,DW,max}$ is a complex function of different factors, such as the generated heat of adsorption (due to process air dehumidification and desiccant type) and the carry-over of heat from the DW regeneration to process sections (due to regeneration temperature, DW rotational speed and wheel thermal capacity). Therefore the DW effectiveness and $f_{h,DW,max}$ are interdependent, but considered to not influence each other in this model, as an expression for the variation of $f_{h,DW,max}$ is not known.

Dew point cooler

The energy balance applied around the DPC is written as:

$$(h_{a,4} - h_{a,3}) + f_{rec}(h_{a,4} - h_{a,5}) = 0 \tag{6.6}$$

where the recirculation fraction f_{rec} is defined as:

$$f_{rec} = \frac{\dot{m}_{a,5}}{\dot{m}_{a,3}} \tag{6.7}$$

The amount of water evaporated into the secondary air stream ($\dot{m}_{w,evap}$) is obtained from the water mass balance around the DPC:

$$\dot{m}_{w,evap} + \dot{m}_{a,3} f_{rec}(x_{a,4} - x_{a,5}) = 0 \tag{6.8}$$

The secondary air outlet temperature is obtained assuming saturated conditions, i.e. $\phi_{a,5}$=1. The DPC effectiveness is defined in respect to the primary air dew point accordingly to the dew point effectiveness defined in Equation 3.19:

$$\varepsilon_{DPC} = \frac{T_{a,2} - T_{a,4}}{T_{a,3} - T_{a,3,dewpoint}} \tag{6.9}$$

The amount of water consumed ($\dot{m}_{w,consumed}$) includes the water evaporated in the DPC and eventually the water wasted during the demineralization process. The corresponding water consumption rate is computed as:

$$\dot{m}_{w,consumed} = \frac{\dot{m}_{w,evap}}{(1 - f_{w,waste})} \tag{6.10}$$

where the water waste fraction $f_{w,waste}$ indicates the fraction of water wasted during the demineralization process, null when no water is wasted. The DDC-DWR system does not require any demineralization process, hence the amount of water consumed equals the amount of water evaporated in the DPC.

Condensation air cooler

The CAC is used to condense moisture from the regeneration air stream by means of outdoor air. The regeneration air stream could at best leave the CAC at saturated conditions at the outdoor air temperature, which is not practically possible as the CAC transfer area is limited and the resistance to heat transfer between the two streams is not negligible.
It is assumed that the regeneration air stream approaches an average wall temperature ($\overline{T}_{wall}$)

that is defined considering comparable thermal resistances at the two air sides:

$$\overline{T}_{wall} = \frac{(T_{a,10} + T_{a,11})/2 + (T_{a,14} + T_{a,15})/2}{2} \tag{6.11}$$

The outlet regeneration air state is obtained introducing a By-pass Factor (BF) [5] that considers a fraction of the air stream to by-pass the CAC without changing conditions while the remaining fraction reaches saturation at the average wall temperature:

$$h_{a,11} = (1 - BF)\ h_a|_{\overline{T}_{wall},\phi_a=1} + BF h_{a,10} \tag{6.12}$$

$$x_{a,11} = (1 - BF)\ x_a|_{\overline{T}_{wall},\phi_a=1} + BF x_{a,10} \tag{6.13}$$

$$BF = \frac{\dot{m}_{a,bypass}}{\dot{m}_{a,10}} = \frac{\dot{m}_{a,11}\big|_{T_{a,10},x_{a,10}}}{\dot{m}_{a,10}} \tag{6.14}$$

The amount of water condensed ($\dot{m}_{w,condensed}$) is obtained from the water mass balance around the CAC:

$$\dot{m}_{w,condensed} + \dot{m}_{a,10}(x_{a,11} - x_{a,10}) = 0 \tag{6.15}$$

The conditions of the outdoor air leaving the CAC are obtained from the energy balance around the component:

$$(h_{a,10} - h_{a,11}) + f_{cool,CAC}(h_{a,14} - h_{a,15}) = 0 \tag{6.16}$$

where the coolant fraction ($f_{cool,CAC}$) is defined as:

$$f_{cool,CAC} = \frac{\dot{m}_{a,14}}{\dot{m}_{a,10}} \tag{6.17}$$

The coolant fraction is expected to be always higher than unity as condensation takes place at the regeneration air side while only sensible heat transfer takes place at the coolant side.

Heat exchangers

The HEX, IHRU and RH exchange only sensible heat.
The HEX and IHRU are modelled by means of the conventional effectiveness definition:

$$\varepsilon_{HEX} = \frac{\dot{m}_{a,2} c_{p,a,2}(T_{a,2} - T_{a,3})}{(\dot{m}_a c_{p,a})_{min}(T_{a,2} - T_{a,6})} = \frac{\dot{m}_{a,6} c_{p,a,6}(T_{a,7} - T_{a,6})}{(\dot{m}_a c_{p,a})_{min}(T_{a,2} - T_{a,6})} \tag{6.18}$$

$$\varepsilon_{IHRU} = \frac{\dot{m}_{a,9} c_{p,a,9}(T_{a,9} - T_{a,8})}{(\dot{m}_a c_{p,a})_{min}(T_{a,9} - T_{a,11})} = \frac{\dot{m}_{a,11} c_{p,a,11}(T_{a,12} - T_{a,11})}{(\dot{m}_a c_{p,a})_{min}(T_{a,9} - T_{a,11})} \tag{6.19}$$

The IHRU operates with balanced air mass flow rates ($\dot{m}_{a,9}$=$\dot{m}_{a,11}$) while the HEX can also be operated with unbalanced flows. The coolant fraction in the HEX ($f_{cool,HEX}$) is defined as:

$$f_{cool,HEX} = \frac{\dot{m}_{a,6}}{\dot{m}_{a,2}} \tag{6.20}$$

The RH effectiveness is not defined as no heat source is specified since different options are possible. The regeneration air can be heated directly by the heat source (e.g. circulation through solar air collectors, electric resistances, etc.) or indirectly by means of a secondary fluid circuit (e.g. using hot water from a storage tank heated by solar collectors, boilers, etc.). The regeneration heat flow received by the regeneration air stream is expressed as:

$$\dot{Q}_{reg} = \dot{m}_{a,12}(h_{a,8} - h_{a,12}) \tag{6.21}$$

Performance indicators

The system performances are described considering heat and water consumptions. Electricity consumption for circulating the air streams is not taken into account as component geometries are not described in the models.
The thermal performance is quantified in terms of the system thermal COP:

$$COP_{th} = \frac{\dot{m}_{a,4}(h_{a,1} - h_{a,4})}{\dot{Q}_{reg}} \tag{6.22}$$

The system independence from external water sources is quantified introducing the water recovery fraction:

$$f_{wr} = \frac{\dot{m}_{w,condensed}}{\dot{m}_{w,consumed}} \tag{6.23}$$

which ranges from 0, in case of no water recovery, to infinity, for increasing water recovery rates and/or decreasing water consumption rates.

Analysis of water storage potential

The DDC-DWR system is considered independent from external water sources when $f_{wr} \geq 1$:

$$\dot{m}_{w,condensed} = \dot{m}_{a,1}(x_{a,1} - x_{a,2}) \geq \dot{m}_{w,consumed} = \dot{m}_{w,evap} \tag{6.24}$$

Introducing the DPC Minimum Specific Water Consumption (MSWC) from Equation 3.20:

$$\dot{m}_{a,1}\Delta x_{DW,pro} \geq \frac{\dot{m}_{w,evap}}{\dot{Q}_{DPC,cool,net}}\dot{Q}_{DPC,cool,net} = MSWC \cdot \dot{Q}_{DPC,cool,net} \tag{6.25}$$

The corresponding maximum air temperature drop that the DPC can provide only using recovered water is found by rearranging Equation 6.25 and introducing Equation 3.14:

$$(T_{a,3} - T_{a,4,min}) = \Delta T_{DPC,pro,max} = \frac{\Delta x_{DW,pro}}{c_{p,ha}(1 - f_{rec})MSWC} \tag{6.26}$$

The MSWC can be assumed constant for specified DPC operating conditions (recirculation air fraction and primary air flow velocity) as noticed in Figure 3.15d.
The DPC can provide higher temperature drops as more moisture is removed in the DW. This positive effect is counterbalanced by rising temperatures of the dry air exiting the DW because of higher dehumidification capacities.
An expression for the process air temperature increase in the DW can be derived combining the DW process air enthalpy ratio ($h_{DW,rat,pro}$) definition (Equation 2.21) and the humid air enthalpy definition (Equation 2.4):

$$\Delta T_{DW,pro} = \frac{h_{fg,ref}}{c_{p,ha}} \Delta x_{DW,pro} + (h_{DW,rat,pro} - 1) \left[(T_{a,1} - T_{ref}) + \frac{h_{fg,ref}}{c_{p,ha}} x_{a,1} \right] \tag{6.27}$$

Equations 6.26 and 6.27 provide the rates of change of the respective temperature differences in terms of the DW process air dehumidification.
Considering a reference case ($T_{a,1}$=30°C, $x_{a,1}$=0.015 kg_v/kg_a, $h_{fg,0°C}$=2500 kJ/kg, cp_{ha}=1 kJ/kg) with a silica gel DW characterized by $h_{DW,rat,pro}$=1.1 and a DPC characterized by f_{rec}=0.3 and MSWC=1.7 kg/kWh, Equations 6.26 and 6.27 become:

$$\Delta T_{DPC,pro,max} = 3025 \Delta x_{DW,pro} \tag{6.28}$$

$$\Delta T_{DW,pro} = 2500 \Delta x_{DW,pro} + 6.75 \tag{6.29}$$

indicating that, for increasing DW dehumidification capacities, the maximum temperature drop provided by the DPC increases more than the process air temperature increase in the DW.
Therefore higher DW dehumidification capacities allow to achieve higher system cooling capacities if all the recovered water is consumed (without considering practical limitations to the DPC effectiveness), or alternatively they allow to store more water. This result remains valid for a wide range of process air inlet conditions ($T_{a,1}$, $x_{a,1}$) considering the other parameters do not vary significantly.
The use of an effective pre-cooling unit (HEX) between the DW and DPC increases the system cooling capacity further, or alternatively it lowers the process air dehumidification required for reaching independence from external water sources.

6.2.2 Results and discussion

The models are implemented and simulated in Engineering Equation Solver (EES).

Sensitivity analysis

At first the influence of varying modelling parameters on the DDC-DWR system performance indicators (water recovery fraction and thermal COP) and required regeneration temperature is investigated in respect to a reference scenario.
Referring to Figure 6.3, the reference scenario is characterized by outdoor conditions $T_{a,1}$=30°C and $\phi_{a,1}$=0.5, supply conditions $T_{a,4}$=18°C and $\phi_{a,4}$=0.64, and indoor conditions $T_{a,13}$=23°C and $\phi_{a,13}$=0.5. The corresponding indoor total load is 6.4 kW per unit of supply airflow rate ($\dot{m}_{a,4}$=1 kg/s) with a Sensible Heat Ratio of 0.8. The pre-cooling air stream in the HEX is a mix of the exhaust air streams from the indoor space and the DPC secondary side. The reference values and ranges of variation for the modelling parameters are stated in Table 6.1.

Table 6.1: Reference values and ranges of variation for the modelling parameters.

Parameter	Reference value	Range of variation
ε_{DW}	0.6	0.45-0.9
$f_{h,DW,max}$	1.1	1-1.2
f_{reg}	0.7	0.4-1
ε_{HEX}	0.8	0-1
$f_{cool,HEX}$	1	constant
ε_{IHRU}	0.8	0.5-1
BF	0.1	0.05-0.15
$f_{cool,CAC}$	5	3-7
f_{rec}	0.3	constant
$f_{w,waste}$	0	constant

The selected reference DW effectiveness corresponds to a dehumidification effectiveness of 54% according to the definition given in Equation 2.20, which considers the DW theoretical limits of operation.
In the reference scenario, the water recovery fraction is 1.54, the thermal COP is 0.7, and the regeneration temperature is 122°C. The corresponding air states in the system are reported in Table 6.2, with numbering in accordance to Figure 6.3.
For the same reference values, the DDC system described in Figure 6.2 requires 80°C regeneration temperature, with a thermal COP of 0.66 and water evaporation rate of 25 kg/h per unit of supply mass flow rate ($\dot{m}_{a,4}$=1 kg/s), without considering any waste of water. The required regeneration temperature decreases significantly for the DDC system as the open regeneration circuit operates at lower regeneration air humidity ratios. On the other hand, the DDC-DWR system thermal COP is higher as the IHRU allows to recover a significant amount of heat.

Results of parameter variations are shown in Figure 6.5, considering only the modelling parameters whose variations have an influence on the selected performance indicators.
Some modelling parameters are not varied: the DPC recirculation fraction (f_{rec}) is kept at the optimal value that maximizes the DPC net cooling capacity (see Chapter 3), the HEX coolant fraction ($f_{cool,HEX}$) is not varied so that the HEX is operated with balanced flows, and the

Table 6.2: Air states in the DDC-DWR system for the reference scenario.

Point	Temperature [°C]	Humidity ratio [g/kg]	Relative humidity [%]
1	30	13.3	50
2	46.7	8.2	12.7
3	28.1	8.2	34.8
4	18	8.2	64
5	24.3	19.3	100
6	23.4	11.9	66.1
7	41.9	11.9	23.3
8	121.8	62.5	4.4
9	99.7	69.8	10.2
10	60.5	69.8	50.1
11	49.9	62.5	75.4
12	89.8	62.5	13.3
13	23	8.7	50
14	30	13.3	50
15	36	13.3	35.7

waste water fraction ($f_{w,waste}$) is null as no water demineralization process is utilized.
The variations of the modelling parameters and the corresponding variations of the system performance indicators are reported in respect to the reference values. The relative variation of a generic quantity ξ is defined as $(\xi - \xi_{ref})/\xi_{ref}$. Only the regeneration temperature is indicated with specified units, as its relative variation does not have physical meaning.

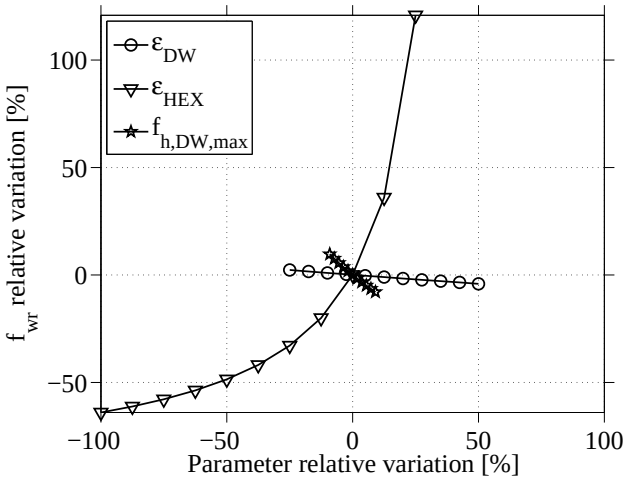

(a) Water recovery fraction.

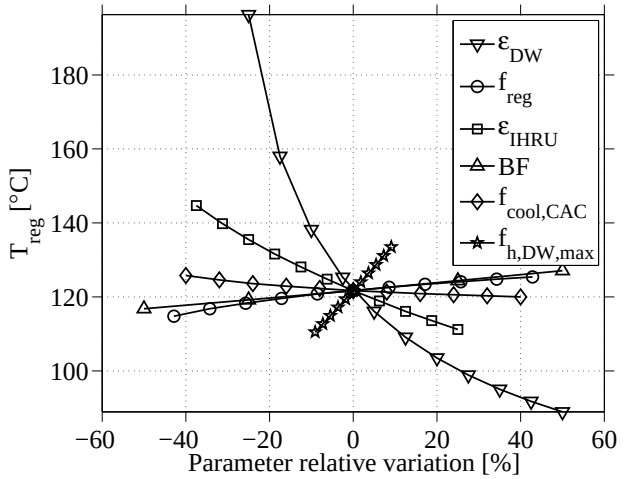

(b) Regeneration temperature.

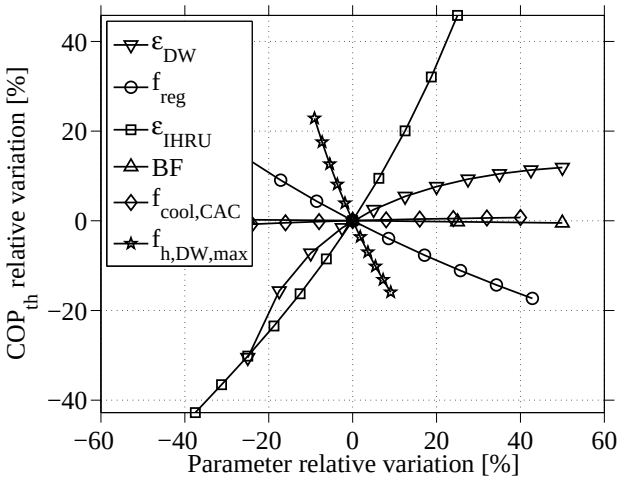

(c) Thermal COP.

Figure 6.5: Influence of modelling parameters on system performance.

Figure 6.5a shows that increasing HEX effectiveness lead to important increments of the water recovery fraction, as less water needs to be evaporated in the DPC. This trend is generally valid, even though its magnitude depends also on the temperature of the pre-cooling air stream ($T_{a,6}$) and on the HEX air flow ratio ($f_{cool,HEX}$). Therefore the HEX is the key component to make the system independent of external water sources.

Figure 6.5a also shows that increasing DW effectiveness cause an almost negligible decrease of the water recovery fraction. This result is influenced by the assumption that the maximum DW process air enthalpy ratio ($f_{h,DW,max}$) is independent of the DW effectiveness. In practise increasing DW effectiveness would lead to lower regeneration temperatures for obtaining the same process air dehumidification as shown in Figure 6.5b, which corresponds to lower carry-overs of heat and consequently lower $f_{h,DW,max}$. Figure 6.5a shows that lower $f_{h,DW,max}$ result into higher water recovery fractions.
Variations of $f_{h,DW,max}$ affect the regeneration temperature and the system thermal COP more, as higher regeneration temperatures are required for keeping the process air dehumidification constant. These influences are in practise expected to be weaker, considering that higher $f_{h,DW,max}$ corresponds to lower DW effectiveness.

Figure 6.5b shows that the DW effectiveness influences the regeneration temperature the most, affecting the thermal COP correspondingly as shown in 6.5c. In the case of $f_{h,DW,max}$ depending on the DW effectiveness, the observed trends would remain the same with increased magnitudes, confirming the criticality of the DW performance to achieve high system thermal COP with limited regeneration temperatures.

The regeneration fraction mostly influences the system thermal COP, which decreases for increasing regeneration fractions as shown in Figure 6.5c, while it marginally influences the regeneration temperature, which increases for increasing regeneration fractions as shown in Figure 6.5b. Considering a fixed DW geometry and desiccant material, the latter trend is expected to reverse, as increasing regeneration fractions would lead to higher DW effectiveness.

The IHRU effectiveness strongly affects the system thermal COP as shown in Figure 6.5c. Increasing the IHRU effectiveness decreases the regeneration air moisture contents in the closed loop (due to reduced sensible loads on the CAC), and it also decreases the required regeneration heat flow (due to reduced regeneration air temperature differences across the RH). The use of highly effective IHRU increases the probability of moisture condensation at the IHRU hot side, which could require the installation of another water drain to recover the whole amount of desorbed water.

The by-pass factor and coolant fraction affect the required regeneration temperature but have

an almost negligible influence on the thermal COP. Lower by-pass factors (corresponding to bigger heat transfer areas) and higher coolant fractions (obtained with variable speed fans) are beneficial as they reduce the regeneration air humidity content in the closed loop, hence the required regeneration temperature. However their influence seems smaller than other modelling parameters, in particular the DW and IHRU effectiveness that also affect the regeneration air humidity content.

Influence of outdoor conditions

The DDC-DWR system is simulated for varying outdoor conditions, considering temperatures in the range 25-40°C and humidity ratios as low as 8.5 g/kg, while keeping the other model inputs as defined in the reference scenario.
The resulting effects on the water recovery fraction, regeneration temperature and system thermal COP are reported in Figure 6.6 on psychrometric diagrams, such that the points indicated on the diagrams correspond to the simulated outdoor conditions. As the modelling parameters are set independently of the outdoor conditions, the results correspond to different system dimensions. For example a different DW geometry is needed to achieve higher dehumidification capacities with the same DW effectiveness.

Some criteria are introduced for considering the DDC-DWR system an applicable solution:

- The regeneration temperature has to be below 90°C, if low temperature heat sources (e.g. solar energy) have to be used, and below 140°C as upper limit for regenerating the desiccant.
- The water recovery fraction has to be above 1 for considering the system independent of external water sources.
- The thermal COP has to be above 0.7 for considering the system competitive with commercial single-stage H_2O-LiBr absorption chillers [103] in terms of thermal energy consumption.

The resulting ranges of outdoor conditions satisfying the above-mentioned conditions are also reported in Figure 6.6.

Figure 6.6a shows that the water recovery fraction increases as the outdoor conditions get colder and more humid. More humid conditions require higher moisture removal in the DW, resulting into higher amounts of condensed water. Colder conditions require lower cooling capacity, i.e. less water is evaporated, and reduce the regeneration air humidity ratio by decreasing the average condensation temperature in the CAC.
For the same reasons the regeneration temperature increases for warmer and more humid outdoor conditions, as shown in Figure 6.6b. Lines of constant regeneration temperature have

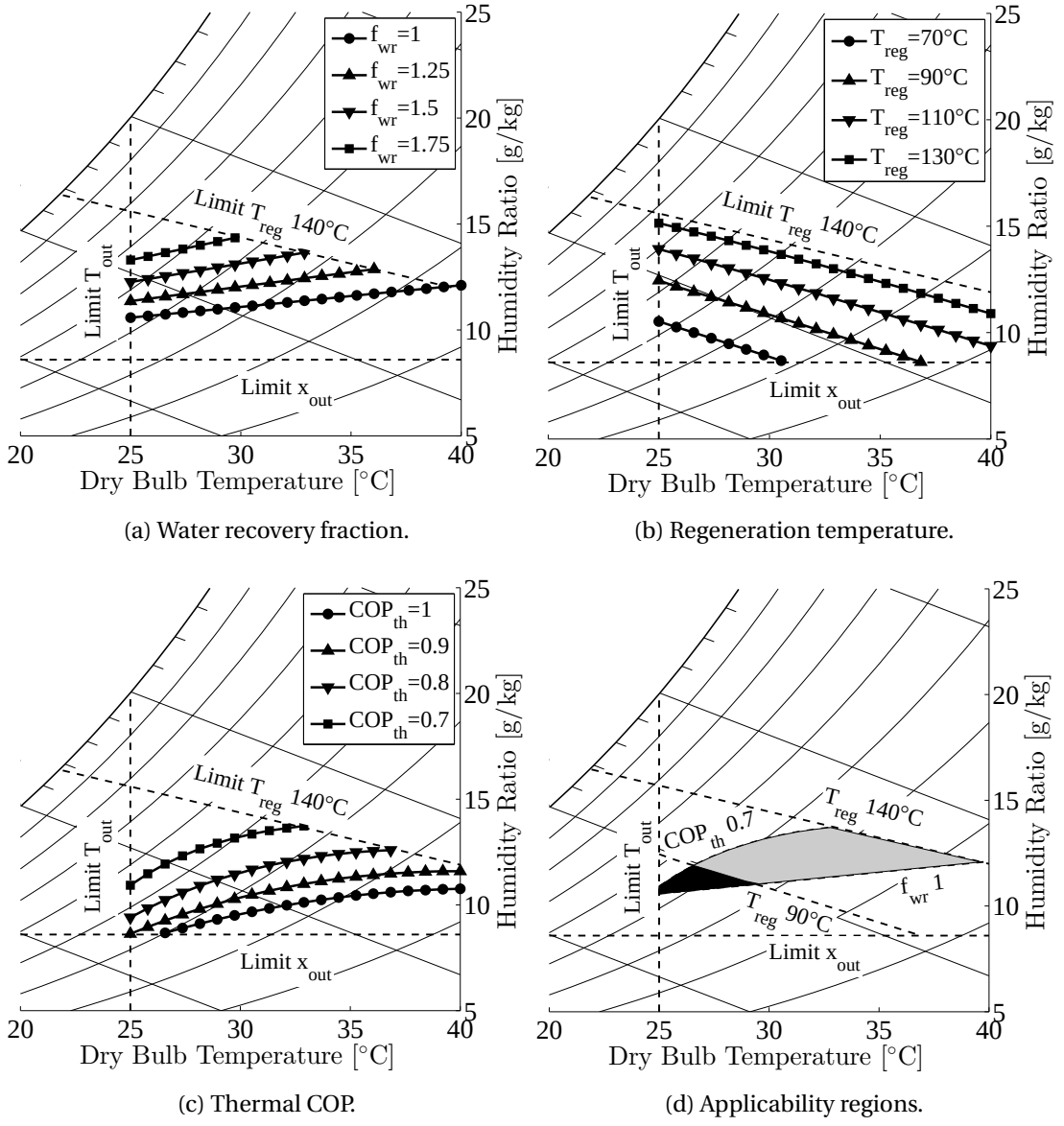

(a) Water recovery fraction.

(b) Regeneration temperature.

(c) Thermal COP.

(d) Applicability regions.

Figure 6.6: Performance of DDC-DWR system for varying outdoor conditions and constant supply conditions.

a higher dependence on the outdoor temperature at lower outdoor humidity contents.
Figure 6.6c shows that the system thermal COP also increases for warmer but drier outdoor conditions. This is due to the fact that regeneration heat is only necessary for covering the latent load on the system, which decreases for drier outdoor conditions, while the sensible load on the system increases for higher outdoor temperatures.
Figure 6.6d highlights two regions of outdoor conditions for which the system is considered applicable in accordance to the above-mentioned criteria, differing because of the regen-

eration temperature limit considered. The black region considers points with regeneration temperature below 90°C, while the grey region considers points with regeneration temperature below 140°C. The former region is small, indicating the use of low temperature heat sources is limited, unless more efficient components are used or higher indoor humidities are acceptable.

Influence of desiccant wheel performance

The DW performance, i.e. the DW effectiveness, was found in Figure 6.5b to be the most critical factor influencing the regeneration temperature required by the system to cover the specified latent load.
The system is again simulated for varying outdoor conditions but DW effectiveness set to 85%, which corresponds to a dehumidification effectiveness of 71% according to Equation 2.20. Results are reported in Figure 6.7.

The comparison of Figures 6.6a and 6.7a shows that the water recovery fraction is approximately constant for the two different DW effectiveness, in accordance with Figure 6.5a.
As expected, Figure 6.7b shows that the regeneration temperature is significantly lower than in Figure 6.6b for the same outdoor conditions, consequently affecting the system thermal COP. The resulting applicability regions shown in Figure 6.7d are bigger than the regions indicated in Figure 6.6d, stressing out the importance of employing high performance DW.

Influence of pre-cooling unit performance

The pre-cooling unit (HEX) is the key component for making the system independent of external water sources as shown in in Figure 6.5a.
The effect of varying HEX effectiveness is investigated by considering the reference scenario, which is characterized by a process air dehumidification of approximately 5 g/kg, and a second scenario with 40% outdoor air relative humidity, which requires half of the reference process air dehumidification. Results are reported in Figure 6.8.

In Figure 6.8, independence from external water sources is provided by an HEX with approximately 60% effectiveness for a process air dehumidification of 5 g/kg, and approximately 85% effectiveness for a process air dehumidification of 2.5 g/kg. This difference would tend to decrease if the DW process air enthalpy ratio is made dependent on the regeneration temperature, as previously discussed for the results reported in Figure 6.5, but the result is generally valid. Therefore the HEX is necessary for obtaining water recovery fractions above 1, and the HEX effectiveness satisfying this condition increases as the process air dehumidification decreases. This result is in agreement with the observations derived from Equations 6.28 and 6.29, i.e. higher dehumidification capacities increase the maximum temperature drop the DPC can provide using only recovered desorbed water, so that a less efficient HEX is needed to reach the same supply temperature.

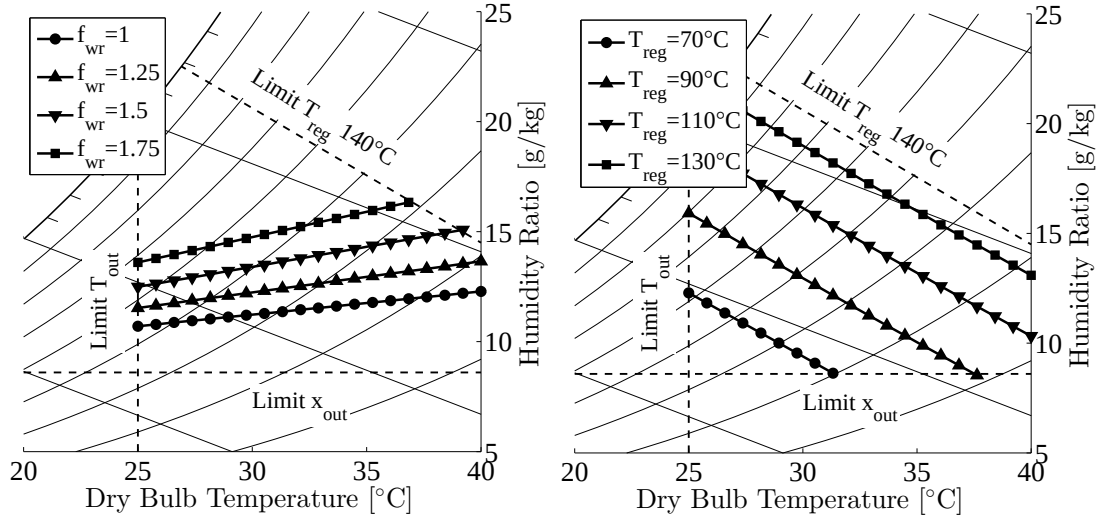

(a) Water recovery fraction.

(b) Regeneration temperature.

(c) Thermal COP.

(d) Applicability regions.

Figure 6.7: Performance of DDC-DWR system for varying outdoor conditions and constant supply conditions setting the DW effectiveness to 85%.

More efficient HEX lower the DPC cooling capacity required to reach the supply temperature, hence water consumption decreases. In Figure 6.8, results characterized by DPC effectiveness above 70%, chosen as a realistic upper limit for commercial DPCs, are indicated by means of dashed curves.

For a given HEX effectiveness, it is observed that higher dehumidification capacities require higher DPC effectiveness, while providing higher water recovery fractions. Therefore, the HEX should be selected to satisfy the most stringent condition between making the system inde-

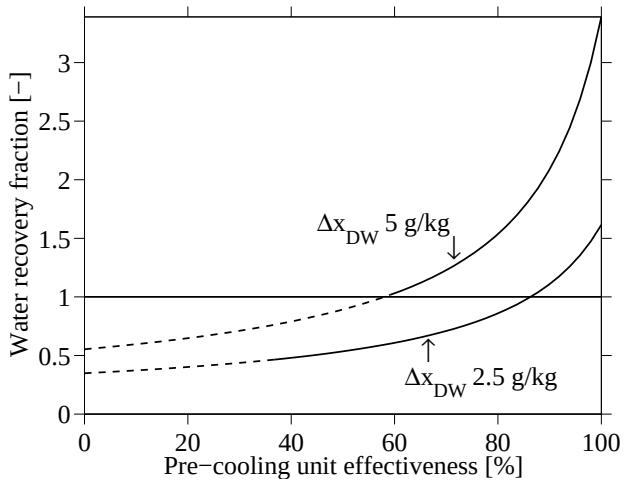

Figure 6.8: Effect of the pre-cooling unit effectiveness on the water recovery water fraction for different dehumidification capacities. Dashed parts of the curves indicate required DPC effectiveness above 70%.

pendent of external water sources and satisfying the sensible load due to practical limitations on the DPC effectiveness.

6.3 Case study - applicability in the Mediterranean climate

6.3.1 Case study definition

The use of the DDC-DWR system for providing dehumidification and cooling is considered in the Mediterranean climate of Rome, aiming to obtain independence of external water sources. The system is required to supply 1500 m^3/h of fresh air constantly. According to European standard EN 15251 [88], the selected supply airflow rate meets category I ventilation requirements for different types of low polluting commercial buildings, e.g. 210 m^2 single offices occupied by 21 people, or 245 m^2 landscape office occupied by 17 people, or 70 m^2 conference room or class room occupied by 35 people.
The supply set point is kept constant at 18°C and 64% relative humidity, corresponding to a dew point of 11°C, which is considered close to the driest conditions deliverable by chiller-based air conditioning systems.
The use of low temperature heat sources (e.g. solar energy) is considered by limiting the regeneration temperature to a maximum of 90°C, which is expected to constrain the system dehumidification and cooling capacities as pointed out in Figures 6.6d and 6.7d. This motivates the choice of the Mediterranean climate, which is typically hot but not very humid.
In order to increase the system dehumidification and cooling capacity, a switch between closed regeneration circuit (DDC-DWR system configuration with water recovery as in Figure 6.3) and open regeneration circuit (DDC system configuration with no water recovery as in Figure

6.2) is considered. Enough water should be stored for running the system independently of external water sources when using the open regeneration circuit. The resulting system, still termed DDC-DWR system, is indicated in Figure 6.9, including dampers for opening and closing the regeneration circuit, as well as dampers and by-pass ducts allowing for different modes of operation, described further in the following.

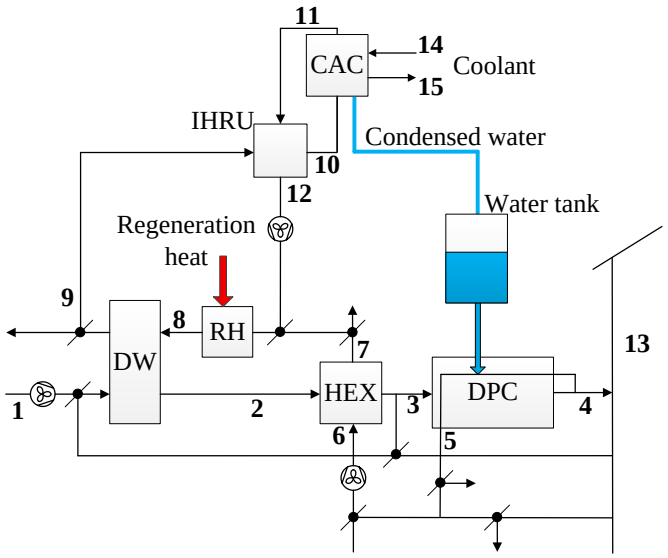

Figure 6.9: DDC-DWR system schematics with possibility for different modes of operation, including switch between open and close regeneration circuit.

6.3.2 Model formulation

The steady state system operation is modelled in more details than in the previous general system analysis in order to predict more accurately the response to varying operating conditions. Component effectiveness are no more fixed, but they are influenced by component dimensions and operating conditions.

Desiccant wheel

The model described in Chapter 2 is used to compute the DW steady state operation. The selected desiccant material is RD silica gel.

Dew point cooler

The model described in Chapter 3 is used to compute the DPC steady state operation.
The DPC cooling capacity is regulated by means of the water spraying rate onto the secondary channels, which is computationally achieved by varying the heat and mass transfer area

effectiveness (see Equations 3.9), which provides the effect shown in Figure 3.12. The transfer area effectiveness are kept equal and varied between 0, i.e. no water is sprayed, and 1, i.e. the whole DPC transfer area works under the assumptions used to build the model.

Heat exchangers

The HEX and IHRU are regarded as counter-flow heat exchangers and modelled by the effectiveness-NTU method:

$$\varepsilon = \frac{1 - e^{-NTU(1-R)}}{1 - Re^{-NTU(1-R)}} \tag{6.30}$$

$$NTU = \frac{UA}{\dot{C}_{min}} \tag{6.31}$$

$$R = \frac{\dot{C}_{min}}{\dot{C}_{max}} \tag{6.32}$$

where $\dot{C}_{min}$ and $\dot{C}_{max}$ are respectively the minimum and maximum air heat capacity rates, U is the overall heat transfer coefficient, and A is the heat transfer area.
The determination of specific UA values allows to estimate the component size without further details on their design.

The effectiveness-NTU method is not directly applicable to the CAC, as both sensible and latent heat are transferred. The method is modified by defining an equivalent thermal capacity for the air stream undergoing dehumidification [108], such that its enthalpy change can be expressed as a function of its temperature change:

$$\Delta h_a = c_{p,eq} \Delta T_a \tag{6.33}$$

The equivalent air thermal capacity is defined as:

$$c_{p,eq} = c_{p,a} + b h_{fg} \tag{6.34}$$

where b is a coefficient derived from assuming the existence of a linear relationship between the air humidity ratio and temperature along the dehumidification process:

$$x_a = b T_a + constant \tag{6.35}$$

Applying Equation 6.35 to the air at the average air stream conditions ($\overline{T}_a$ and $\overline{x}_a$, expressed as arithmetic averages between inlet and outlet) and at the average wall conditions ($\overline{T}_{wall}$ as defined in Equation 6.11, and $\overline{x}_{a,wall}$ at saturated conditions for simplicity), leads to:

$$b = \frac{\overline{x}_a - \overline{x}_{a,wall}}{\overline{T}_a - \overline{T}_{wall}} \tag{6.36}$$

This method allows to simplify the modelling of the dehumidification process. Its accuracy increases by dividing the process into multiple steps that account for variations of the coefficient b with local conditions [108]. In the present model, a single step is used to model the whole CAC, and the consequent approximation is tolerated.

The RH is not modelled in more details as the heat source is not specified.

6.3.3 System modes of operation

The system is operated depending on the outdoor conditions and specified tolerances on the supply set point humidity and temperature.

1. Dehumidification with closed regeneration circuit.
   Dehumidification is required when the outdoor humidity ratio exceeds the supply set point beyond a specified humidity tolerance. The regeneration circuit is kept closed if the dehumidification load on the system can be satisfied within the specified tolerance by regeneration temperatures up to 90°C. Desorbed water is condensed and used to run the DPC, while excess amounts of condensed water are accumulated in the tank. The cold air stream entering the HEX is selected as the coldest between outdoor air and a mix of the exhaust air from the DPC secondary side and the indoor space.

2. Dehumidification with open regeneration circuit.
   If dehumidification is required and the use of the closed regeneration circuit does not provide enough dehumidification, the regeneration circuit is open and the system consumes water accumulated in the tank to run the DPC. The cold air stream entering the HEX is taken directly from the outdoor ambient to avoid contaminations of the desiccant material and keep the supply air quality high, as part of it is further heated in the RH for regenerating the DW.

3. DPC cooling.
   Only cooling is required when the outdoor temperature exceeds the supply set point beyond a specified tolerance, but not the outdoor humidity ratio. The DW and HEX are by-passed, and the DPC runs using water accumulated in the tank.

4. Free cooling.
   If both outdoor temperature and humidity ratio do not exceed the supply set point beyond the specified tolerances, outdoor air is directly used for mechanical ventilation.

A representation of the logic adopted for selecting the mode of operation is reported in Figure 6.10 on the psychrometric diagram. Tolerances on the supply set point (18°C and 64% relative humidity) are set to 4°C and 3 g/kg. The hourly outdoor conditions considered are also plotted on the psychrometric diagram.

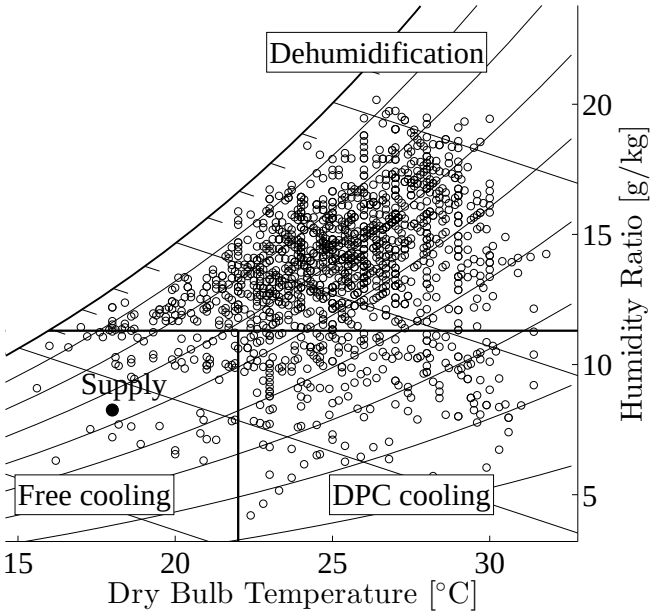

Figure 6.10: System operation mode selection and considered outdoor conditions.

6.3.4 Results and discussion

Selection of component dimensions

The DW dimensions are set to diameter 0.85 m, depth 0.2 m, equal split between process and regeneration sections, and sinusoidal channels with a, b and c set to 3.8, 1.9 and 0.2 mm respectively referring to Figure 2.1. The correspondent DW volume is 0.11 m^3. These dimensions are chosen to obtain a low process air face velocity around 2 m/s at the nominal flow rate, which is desirable to reach high dehumidification capacities, while also limiting the air pressure drop.
The DPC dimensions are set to height 0.75 m, length 1.38 m and width 0.56 m, referring to the design reported in Figure 3.6. The correspondent DW volume is 1.17 m^3. Dimensions are chosen accordingly to the manufacturer catalogue [83] for delivering the required supply airflow rate.
The UA values of the HEX and IHRU are set to 3 and 1.5 kW/K respectively. For air-to-air heat exchangers, a typical U value of 0.025 kW/K and finned area density of 3000 m^2/m^3 are assumed [85]. The correspondent HEX and IHRU volumes are 0.04 m^3 and 0.02 m^3 respectively.
The UA value of the CAC is set to 2 kW/K. The heat transfer resistance is considered equal at both sides, with fins only at the coolant side, and convective heat transfer coefficient of 0.25 kW/K for the condensing air [109]. The correspondent CAC volume is 0.09 m^3.
The comparison of the estimated component volumes indicate the DPC is critical for the system size, as its volume corresponds to approximately 80% of the cumulative component volume.

Example of system operation

The reference scenario used in the previous general system analysis (outdoor conditions 30°C and 50% relative humidity, supply conditions 18°C and 64% relative humidity, indoor conditions 23°C and 50% relative humidity) is considered again for providing an example of the dimensioned DDC-DWR system operation. The system is operated with regeneration fraction of 0.7, DW rotational speed of 8 rph, CAC coolant fraction of 5, and DPC recirculation fraction of 0.3.
In the reference scenario, the system water recovery fraction is 1.47, the thermal COP is 0.74, and the required regeneration temperature is 104°C. The resulting component effectiveness are 81% for the HEX, 78% for the IHRU and 61% for the DPC, which are in good agreement with the reference effectiveness used for the general systems analysis (see Table 6.1). The DW effectiveness is 57% referring to Equation 2.20, which corresponds to 68% using the definition in Equation 6.5.
The most important difference from the general system analysis is the required regeneration temperature, which decreases significantly to 104°C. This is due to lower regeneration air humidity contents and higher DW effectiveness. The corresponding air states for the dimensioned system are reported in Table 6.3, with numbering in accordance to Figure 6.9. The comparison with Table 6.2 shows the difference in regeneration air humidity content.

Table 6.3: Air states in the DDC-DWR system for the reference scenario.

Point	Temperature [°C]	Humidity ratio [g/kg]	Relative humidity [%]
1	30	13.3	50
2	49	8.2	11.2
3	28.7	8.2	33.5
4	18	8.2	64
5	25	20	100
6	23.7	12.2	66.5
7	44.3	12.2	21.1
8	104	38.9	5.1
9	70.2	48.3	23.2
10	43.4	48.3	82.7
11	35.9	38.9	100
12	62.9	38.9	26.2
13	23	8.7	50
14	30	13.3	50
15	36.3	13.3	35.1

Limiting the regeneration temperature to 90°C, the system supplies the same airflow rate at 18°C but 71% relative humidity, with thermal COP increasing to 0.8 and recovery water fraction decreasing to 1.38.

Influence of regeneration air conditions

The regeneration air inlet humidity content varies significantly when using the closed regeneration circuit, with an important impact on the DW dehumidification performance. Therefore, the influence of high regeneration air humidity ratios is investigated for deciding how to best operate the DW.

The influence of regeneration temperature and regeneration air inlet humidity ratio for varying DW rotational speeds are reported in Figure 6.11. Results are obtained by means of the two-dimensional DW model for the above mentioned DW dimensions and the reference outdoor conditions. The regeneration air inlet humidity ratios are selected to represent the cases of open regeneration circuit (x_{reg} 15 g/kg) and closed regeneration circuit (x_{reg} 40 and 65 g/kg). The reported dehumidification effectiveness refer to Equation 2.20, which considers the theoretical limits of operation.

Figure 6.11a shows that the regeneration air humidity ratio has an important influence on the process air dehumidification, mainly because of the different dehumidification potential due to different regeneration air relative humidities. It is noticed that the optimal rotational speed increases for increasing regeneration temperatures and decreasing regeneration air inlet humidity ratios. Higher regeneration air inlet humidity ratios make the process air dehumidification decrease more rapidly at higher rotational speeds. Low rotational speeds should be used to maximize the process air dehumidification, particularly when using low temperature heat sources.
Figure 6.11b shows that the process air enthalpy ratio increases for increasing regeneration temperatures, mainly because of the carry-over of heat from regeneration to process section. The regeneration air inlet humidity ratio has a small influence on the process air enthalpy ratio at low rotational speeds. At higher rotational speeds, increasing humidity ratios result into higher process air enthalpy ratios, as the wheel operates at higher desiccant moisture contents that increase its thermal capacity, resulting into higher carry-overs of heat from regeneration to process section, particularly for low regeneration temperatures.
Figure 6.11c indicates it is reasonable to assume a DW effectiveness of 60% (according to Equation 2.20) at rotational speeds up to approximately 10 rph, unless the regeneration air relative humidity is high, e.g. relative humidity is approximately 30% at 60°C and humidity ratio 40 g/kg. The DW effectiveness exhibits a faster decrease for increasing rotational speeds at higher regeneration air relative humidities, differently from the process air dehumidification whose rate of change appears more sensitive to the regeneration air humidity ratio instead.
Generally, Figure 6.11 suggests the wheel should be operated at low rotational speeds (below 10 rph) for maximizing the process air dehumidification and reducing the process air temperature increase, with high DW effectiveness and low process air enthalpy ratios. Highly effective CAC and IHRU have to be used for reducing the regeneration air humidity contents, hence allowing to run the DDC-DWR system at low regeneration temperatures.

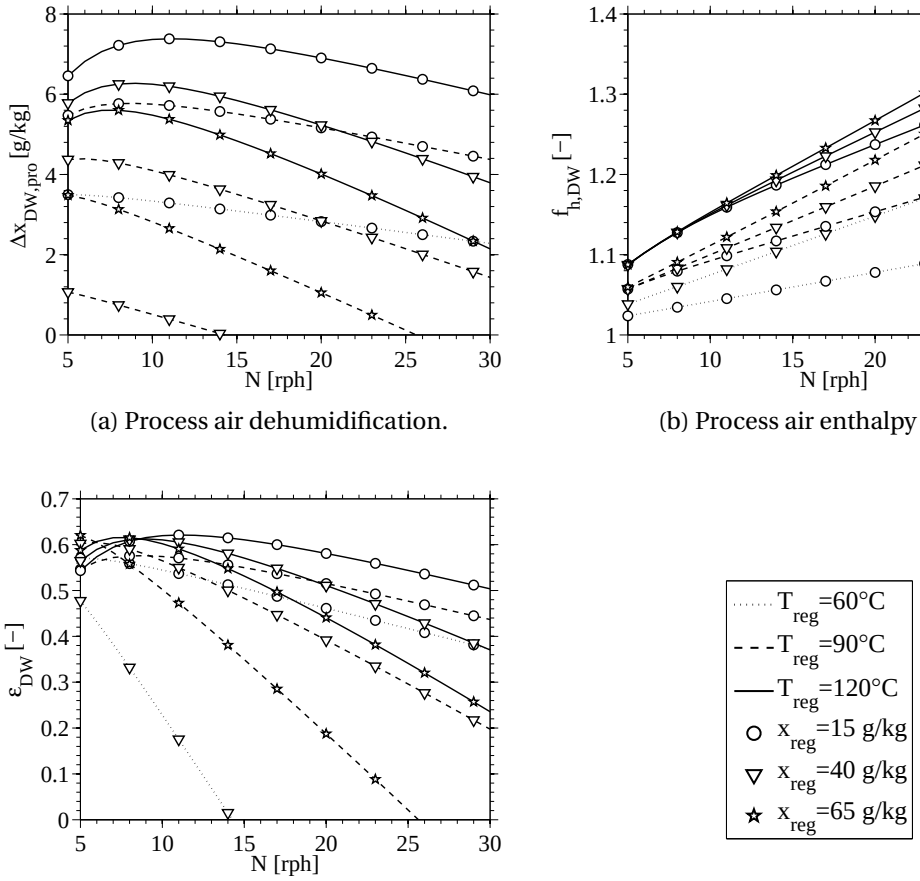

(a) Process air dehumidification.

(b) Process air enthalpy ratio.

(c) Dehumidification effectiveness.

Figure 6.11: Influence of varying regeneration temperature, regeneration air inlet humidity ratios and rotational speed on the DW operation.

The detrimental effect of increasing regeneration air inlet humidity contents is better explained investigating the variations of air conditions across the wheel. Figure 6.12 reports the local variations of the process and regeneration air streams on psychrometric diagrams, in case of 90°C regeneration temperature and regeneration air inlet humidity ratio of 40 g/kg. The physical limits of operation for the average air stream outlet conditions are also reported in Figure 6.12, analogously to Figure 2.12.

Figure 6.12 indicates that the high regeneration air moisture content results into accentuated desorption phenomena in the process section, and adsorption phenomena in the regeneration section. These detrimental phenomena make the process air outlet conditions cross the regeneration air inlet relative humidity at the beginning of the process section. The use of a purge section can be considered to pre-condition the desiccant prior to its entrance in the process section.

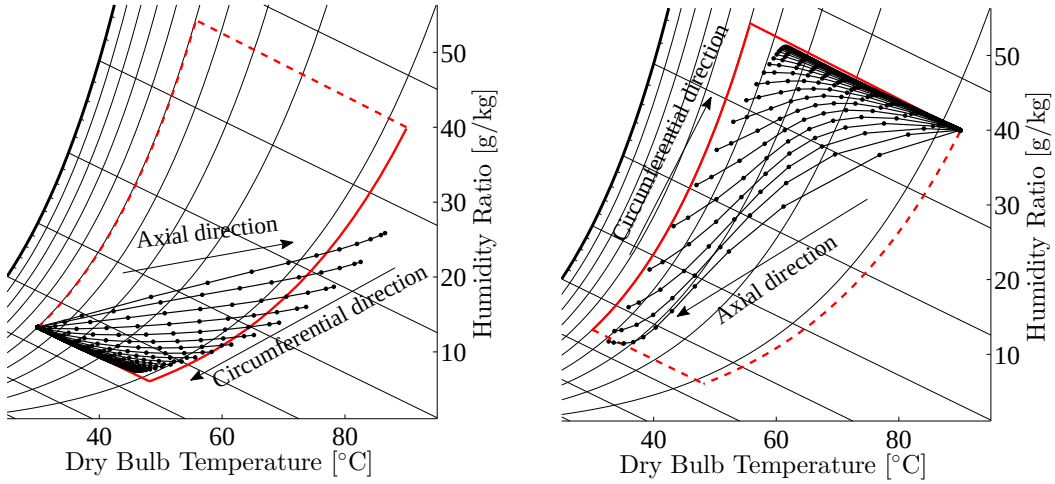

(a) Process air.

(b) Regeneration air.

Figure 6.12: Air conditions across the wheel.

Seasonal simulations

The dimensioned DDC-DWR system is simulated in the Mediterranean climate of Rome on an hourly basis from June to September between 8 am and 7 pm everyday.
The system is operated with a constant regeneration fraction of 0.7, DW rotational speed of 8 rph, CAC coolant fraction of 5, and DPC recirculation fraction of 0.3. The regeneration temperature is varied between 50 and 90°C for regulating the system process air dehumidification, while the DPC surface effectiveness is varied between 0 and 1 (corresponding to varying water spraying rates) for regulating the system cooling capacity.
The DDC-DWR system is compared with the DDC system configured as reported in Figure 6.2, i.e. equivalent to run the DDC-DWR system with open regeneration circuit at all times.
The overall seasonal results for both systems are reported in Table 6.4. The system independence of external water sources is expressed as the ratio of water claimed from external water sources and water evaporated in the DPC. The supply conditions are considered satisfied when matching exactly the supply set point (18°C and 64% relative humidity) and accepted when being within the imposed tolerances (4°C and 3 g/kg) on the supply set point.

The resulting seasonal profile of water stored in the tank by the DDC-DWR system is reported in Figure 6.13.

The DDC-DWR system is considered independent of external water sources as its water independence is 99%. This means that only 1% of the seasonal amount of water evaporated, i.e. approximately 125 liters, should be initially stored in the tank.
The profile of water stored in the tank reported in Figure 6.13 indicates that this small precharge of the water tank is needed to cover the cooling load during the first hours of operation,

Table 6.4: Seasonal results for the DDC-DWR system and DDC system.

	DDC-DWR system	DDC system
Water independence [%]	99	0
Water evaporated [m^3]	10.86	12.05
Seasonal thermal COP	0.64	0.61
Regeneration heat consumption [MWh]	17.62	19.61
Regeneration power peak at 90°C [kW]	20.2	21
Operation mode distribution 1/2/3/4 [%]	71/9/16/4	0/80/16/4
Satisfied supply temperature [%]	97	97
Satisfied/Accepted supply humidity ratio [%]	58/97	73/97

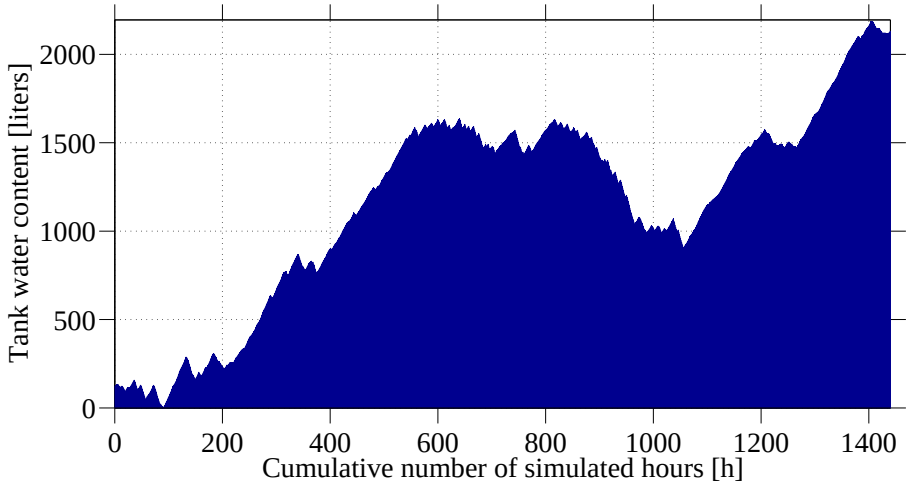

Figure 6.13: Seasonal profile of water content in the tank for the DDC-DWR system.

when outdoor humidity is still not very high and the system cannot recover much water. As the outdoor humidity increases during the season, the DDC-DWR system is able to store a large amount of water. A sudden drop of water content in the tank is noticed around 900 hours of operation, as the required process air dehumidification on the system exceeds the capacity attainable with the closed regeneration circuit, requiring to open the circuit and consuming part of the water stored.

The DDC system evaporates approximately 11% more water than the DDC-DWR system, as outdoor air is used for pre-cooling in the HEX, instead of a mix between air exhausted from the DPC secondary side and the indoor space. Considering the need for water demineralization by means of the reverse osmosis process with waste water fraction of 30%, the DDC system would consume 15.66 m^3 of water.

The DDC-DWR system lowers the regeneration heat consumption by 11% as well as the regeneration power peak by 4% in comparison to the DDC system. These improvements are obtained at the expense of higher supply air humidity contents that, even if generally accept-

able, match the supply set point for 58% of the simulated hours instead of 73% with the DDC system. However, the DDC-DWR system still provides a higher seasonal thermal COP. This result is mainly influenced by the use of highly effective IHRU and CAC, which allow to recover a large fraction of heat in the closed regeneration circuit and limit the increase of regeneration air moisture content.
The thermal performance comparison with absorption chillers should also take into account the additional amount of heat required after the chiller for re-heating the air to the supply temperature. If a heat source is used to re-heat the air, the overall system thermal COP would be lower than the absorption chiller thermal COP. Considering a single-stage H_2O-LiBr with thermal COP of 0.7 [103], the additional heat consumption to provide the same humidity control as the DDC-DWR system (considering 3°C re-heat for acceptable supply humidity contents and 6°C re-heat for satisfied supply humidity contents) makes the thermal COP of the absorption chiller system drop to 0.61. The electricity consumption for auxiliaries as well as the water consumption, as the absorption chiller often needs a cooling tower for heat rejection, should also be considered for determining which system is the most convenient.

The DDC-DWR system operation could be optimized by utilizing the excess amount of water stored in the tank, e.g. cooling the CAC coolant stream by direct water evaporation for lowering the regeneration air humidity content improving both humidity control and thermal performance.
The pressure drop across all components should also be estimated by means of more detailed heat exchanger models, as the electricity consumption increases when operating the system with a closed regeneration circuit.
If the electricity consumption is found to be critical, the excess amount of water stored could also be used to operate the system with an open regeneration circuit for more hours, improving the humidity control and reducing the electricity consumption.
The CAC coolant fraction should also be controlled by means of a variable speed fan for reducing the electricity consumption as much as possible.
Moreover, the use of lower regeneration fractions should be investigated to maximize the thermal COP while limiting the required regeneration temperature and reducing the pressure drop across the components in the closed regeneration circuit.

6.4 Conclusions

A technical solution has been proposed to make desiccant cooling systems independent of external water sources. Decreasing, if not eliminating, water consumption is already relevant in locations with limited or absent water availability, and it is expected to gain importance in future scenarios characterized by high stresses on water resources.
The solution is based on the idea of condensing the water desorbed from the desiccant dehumidifier in a closed regeneration circuit for running evaporative cooling processes. Details on its functioning and applicability are investigated considering a specific desiccant cooling

system that implements the dew point cooling processes.

From a general system analysis, it is concluded that:

- The use of an internal heat recovery unit in the closed regeneration circuit allows increasing the thermal COP of the system in respect to the use of an open regeneration circuit.
- The regeneration air humidity content increases substantially in the closed regeneration circuit, as outdoor air is used for condensing moisture. Consequently, the system requires higher regeneration temperatures for providing the same dehumidification capacities than with an open regeneration circuit.
- The amount of condensed water increases more than the amount of evaporated water for higher dehumidification capacities. This indicates the solution works best for high latent loads, if sufficient dehumidification can be reached.
- Pre-cooling prior to evaporative cooling is essential to make the system independent of external water sources. The pre-cooling unit effectiveness needs to satisfy the most stringent condition between making the system independent of external water sources and satisfying the sensible load due to practical limitations on the evaporative cooler effectiveness.
- The desiccant wheel dehumidification performance should be as high as possible to expand the applicability of the solution. Optimal geometries and optimal operational parameters should be adopted, also considering the use of purge sections and alternative desiccant materials.

From detailed seasonal simulations considering the Mediterranean climate, it is concluded that:

- The system is independent of external water sources, and it is able to provide acceptable supply conditions with low temperature heat sources, e.g. solar energy.
- The thermal COP increases by 5% compared to the system with no water recovery, and the required installed thermal capacity at 90°C also decreases by 4%.
- The system recovers more water than what is consumed throughout the season. The water accumulated can be used to optimize the system operation or for other purposes.
- The use of a purge section in the DW should be considered to reduce the detrimental desorption phenomena in the process section.

Some fundamental aspects have to be investigated in future work:

- The system electricity consumption has to be estimated. The electric COP is expected to decrease in comparison with systems with no water recovery, because of increases fan power consumption and decreased loads covered by the system. The operation of the condensation air cooler is expected to have an important influence on the fan power consumption.
- Eventual problems of bacteria growth, e.g. legionella, in the storage tank and condensation circuit should be also investigated.

7 Concluding remarks

This thesis presents a numerical analysis of the performance of a desiccant cooling system that implements indirect evaporative cooling processes and is driven by low regeneration temperatures. The system includes a silica gel desiccant wheel and a counter-flow indirect evaporative cooler, as well as an air-to-air heat exchanger for enhancing cooling capacity and thermal performance. A clear understanding of the effects of component dimensions and operating conditions on the system performance is necessary for supporting the system development and make it more efficient than cooling-based dehumidification air conditioning systems.

The thesis is divided in two parts. At first, detailed steady state models of the core components are developed, and the characteristics of single component operation are investigated. Successively, the models are combined for analysing the energy and exergy performance of the complete desiccant cooling system in terms of heat, electricity and water consumptions, as well as achievable supply conditions. A novel solution for making desiccant cooling systems independent of external water sources is also presented and investigated.

7.1 Discussion

Desiccant cooling technology has been greatly improved since its first introduction in the 1950s, but it is not mature yet. Improvements of system performance can be achieved by developing more efficient components, as well as by identifying their optimal integration and operation in complete systems. Simple system configurations are preferable to obtain high electricity performance and ease of operation control, given that sufficient thermal performance can be obtained.

The importance of improving the knowledge on component integration and operation in complete systems is highlighted by the comparison of results obtained in Chapters 3 and 4. In

Chapter 3, dew point cooling is found to have potential for reaching lower supply temperatures than conventional indirect evaporative cooling. However, results obtained in Chapter 4 show that indirect evaporative cooling largely outperforms dew point cooling in the complete system for fixed component dimensions, nearly doubling the thermal COP, tripling the electrical COP and reaching lower supply temperatures and humidity ratios, with a more efficient use of the water consumed. These results are mainly caused by the increased airflow rates (approximately +40%) across all components when operating with dew point cooling, as well as by the use of exhaust air from the conditioned space when operating with indirect evaporative cooling. Even by increasing component dimensions for reaching analogous supply conditions, the system operating with dew point cooling consumes more heat, electricity and water than with indirect evaporative cooling. It is also important to consider that indirect evaporative cooling provides an easier regulation of the system cooling capacity by controlling the secondary fraction without affecting other components, differently from dew point cooling. Consequently, dew point cooling is an interesting solution only for applications where exhaust indoor air cannot be reused or indoor conditions lead to poor indirect evaporative cooling performance.

The counter-flow indirect evaporative cooler considered in this study is penalized by the positioning of the secondary air inlet and outlet, which forces the secondary airflow to deviate inside the channels. This is considered the main reason for the fact that approximately 50% of the cooler area does not operate under the counter-flow configuration assumption, as obtained from tuning the cooler model to match manufacturer data. The ineffective use of heat and mass transfer area affects the system space requirements significantly, as the cooler is by far the biggest component in the system. Improved fins at the cooler primary side could increase the cooling performance by reducing the air convective heat transfer resistance, which is estimated to be the highest resistance, but the effects on complexity of construction and pressure drop have to be taken into account. Dew point coolers with different designs and higher cooling performance, e.g. M-cycle dew point coolers, can help reducing space requirements and supply temperatures. Still, the system thermal and electrical performance is expected to suffer from increased airflow rates across all components.

The system dehumidification capacity is found limited to cover moderate latent loads. Improvements can be achieved by using two-stage dehumidification processes, as well as improving the desiccant wheel performance. The use of large wheel face dimensions and optimal rotational speeds is easy to implement and beneficial. Furthermore, the use of thinner desiccant layers can lead to important improvements, as shown by results in Chapter 2 with dehumidification capacity increasing up to 20% by halving the desiccant layer thickness from 0.2 to 0.1 mm. It should be remembered that research on new desiccant materials with high dehumidification capacity, low heat of adsorption, and low regeneration temperature requirements has a central role in the development of high performance desiccant cooling systems, even if outside of the scope of this thesis.

Considering the fundamental question of this thesis, it can be stated that the coupling of desiccant dehumidification and indirect evaporative cooling can lead to high system performance with a relatively simple construction, resulting into an attractive alternative to cooling-based dehumidification technologies. The use of indirect evaporative cooling with recirculation of exhaust air from the conditioned space results in thermal COP above 1 and electrical COP above 20. Air filtration can be critical to the electrical performance, so a careful choice of filters and good maintainable are essential. Based on these results, the system clearly is a more efficient solution than thermally driven absorption and adsorption machines, which are characterized by lower performance. The high electrical COP is at least 5-6 times higher than in conventional air conditioning systems based on vapour compression cycles, indicating the potential for high energy and emission savings when a relatively cheap and clean heat source is available. The comparison of economic savings is also of primary importance for deciding whether a desiccant cooling system should be installed. The high performance suggest the system can lead to operational cost savings, whereas investment costs are expected to be higher. It should be kept in mind that the investment cost of a desiccant cooling system already include components needed by the full HVAC system, such as heat exchangers, fans, filters, and ductwork, which have to be added when considering cooling-based dehumidification machines.

7.2 Conclusions

A summary of the most relevant findings from this thesis is reported in the following.

- The use of indirect evaporative cooling with secondary air from the exhaust of the conditioned space leads to thermal COP above 1 and electrical COP above 20. These results indicate the system is more efficient than thermally driven absorption and adsorption machines, and high energy and emission savings can be achieved in comparison to vapour compression machines by using low temperature clean heat sources.

- The use of indirect evaporative cooling instead of dew point cooling nearly doubles the thermal COP and triples the electrical COP, considering the same component dimensions and supply airflow rate. Supply conditions are also improved, especially in terms of supply temperature. This is mainly due to a 40% increase of the airflow rates in the system with dew point cooling.

- The system cooling capacity can be easily controlled when using indirect evaporative cooling by means of the secondary fraction, without affecting other components. Differently, the secondary fraction should be kept at the optimal value of 30% with dew point cooling, for maximizing the cooler net cooling capacity and providing the lowest supply temperature.

- The impact of air filtration on the system electrical COP is significant. The use of fine bag filters decrease the electrical COP of approximately 40% under typical mid-life clogging conditions.
- Regeneration conditions have almost no influence on the supply temperature, particularly because of the use of pre-cooling. However the supply temperature has a strong impact on the thermal performance, and should be reduced if possible. Regeneration fractions above 0.7 do not improve the thermal performance significantly, while lowering the electrical performance.
- The system is found suitable for both warm and hot climates. However, the system dehumidification capacity is limited to moderate latent loads. Big wheel face dimensions and optimal rotational speeds should be used. The use of thinner desiccant layers can lead to significant increase of the dehumidification capacity. A 20% increase can be obtained reducing the silica gel layer thickness from 0.2 to 0.1 mm, with increased optimal rotational speed. Alternatively, the combination of two-stage dehumidification and indirect evaporative cooling should be considered.
- The system is bulky, and the indirect evaporative cooler is by far the biggest component, accounting for more than 50% of the whole system volume.
- The technical solution proposed for recovering desorbed water enables the system to run independently of external water sources.

7.3 Recommendations for future work

The use of indirect evaporative cooling is an efficient solution for lowering energy consumption and emission levels in comparison to conventional air conditioning systems. However, a complete economic analysis has to be carried out for assessing the desiccant cooling system competitiveness on the market. The economic analysis should point out the differences between investment costs and operational costs, which are strongly affected by the heat source selection.
Desiccant-assisted radiant cooling systems and systems with two-stage dehumidification and indirect evaporative cooling should also be investigated for evaluating the possibility of covering higher loads with increased energy savings.
Validation of results by means of experimental measurements is fundamental. Measurements on a system prototype should be carried out as part of the industrial system development in collaboration with the industrial partners. Experimental data should also be used to further validate the component models.
More detailed studies on the proposed water independent system solution should be carried out, including the estimation of electricity consumption and optimization of system operation in terms of control and use of excess water production.

Bibliography

[1] S. Pezzutto, R. Fazeli, M. De Felice, and W. Sparber. Future development of the air-conditioning market in Europe: an outlook until 2020. *Wiley Interdisciplinary Reviews: Energy and Environment*, 2016.

[2] IEA Solar Heating and Cooling Programme Strategic Plan 2014-2018. Technical report, 2014.

[3] Brandemuehl M. J. Dehumidification Characteristics of Commercial Building Applications. *ASHRAE Transactions*, 110(2), 2004.

[4] Daou K., Wang R. Z., and Xia Z. Z. Desiccant cooling air conditioning: a review. *Renewable & Sustainable Energy Reviews*, 10(2):55–77, 2006.

[5] Nóbrega C. E. L. and N. C. L. Brum. An Introduction to Solid Desiccant Cooling Technology. In *Desiccant-Assisted Cooling*. 2014.

[6] Panaras G., Mathioulakis E., and Belessiotis V. Solid desiccant air-conditioning systems – Design parameters. *Energy*, 36(5):2399–2406, 2011.

[7] Zheng X., Ge T. S., and Wang R. Z. Recent progress on desiccant materials for solid desiccant cooling systems. *Energy*, 74:280–294, 2014.

[8] Fang L. Experimental investigation of the air cleaning effect of a desiccant rotor on indoor air chemical pollutants. *Proceedings of HB 2006 - Healthy Buildings: Creating a Healthy Indoor Environment for People*, 2, 2006.

[9] Mavroudaki P., Beggs C. B., Sleigh P. A., and S. P. Halliday. The potential for solar powered single-stage desiccant cooling in southern Europe. *Applied Thermal Engineering*, 22 (10):1129–1140, 2002.

[10] Bellemo L. *New desiccant cooling system using the regenerative indirect evaporative process*. MSc thesis, Technical University of Denmark, Kongens Lyngby, 2011.

[11] Pennington N. A. Humidity changer for air-conditioning, 1955.

[12] George G. O., Lof, Cler G., and Brisbane T. Performance of a Solar Desiccant Cooling System. *Journal of Solar Energy Engineering*, 110(3), 1988.

[13] Kanoglu M., Bolattürk A., and Altuntop N. Effect of ambient conditions on the first and second law performance of an open desiccant cooling process. *Renewable Energy*, 32 (6):931–946, 2007.

[14] Bourdoukan P., Wurtz E., and Joubert P. Comparison between the conventional and recirculation modes in desiccant cooling cycles and deriving critical efficiencies of components. *Energy*, 35(2):1057–1067, 2010. doi: 10.1016/j.energy.2009.06.021.

[15] Sphaier L. A. and Nóbrega C. E. L. Parametric analysis of components effectiveness on desiccant cooling system performance. *Energy*, 38(1):157–166, 2012.

[16] Waugaman D. G., Kini A., and Kettleborough C. F. A Review of Desiccant Cooling Systems. *Journal of Energy Resources Technology*, 115(1), 1993.

[17] Maclaine-Cross I. L. High-Performance Adiabatic Desiccant Open-Cooling Cycles. *Journal of Solar Energy Engineering*, 107(1):102, 1985.

[18] McLay B. *Analysis and simulation of an advanced open-cycle solid desiccant cooling system*. PhD thesis, Colorado State University, 1989.

[19] Waugaman D. G. Combining direct and indirect evaporative cooling with a rotating desiccant wheel in residential applications. *Solar Engineering*, 2, 1987.

[20] Goldsworthy M. and White S. Optimisation of a desiccant cooling system design with indirect evaporative cooler. *International Journal of Refrigeration*, 34(1):148–158, 2011.

[21] Maisotsenko V. The Maisotsenko Cycle for air desiccant cooling. *Proceedings of the 4th International Symposium on Heating, Ventilating and Air Conditioning*, pages 1011–1020, 2003.

[22] Worek W. M., Khinkis M., Kalensky D., and Maisotsenko V. Integrated desiccant-indirect evaporative cooling system utilizing the Maisotsenko cycle. In *Proceedings of the Asme Summer Heat Transfer Conference*, pages 21–28, 2012.

[23] Meckler G. Two-stage desiccant dehumidification in commercial building HVAC systems. *ASHRAE Transactions*, 95(2):1116–1123, 1989.

[24] Ge T. S., Dai Y. J., Wang R. Z., and Li Y. Experimental investigation on a one-rotor two-stage rotary desiccant cooling system. *Energy*, 33(12):1807–1815, 2008.

[25] Ge T. S., Li Y., R. Z. Wang, and Dai Y. J. Experimental study on a two-stage rotary desiccant cooling system. *International Journal of Refrigeration*, 32(3):498–508, 2009.

[26] Schinner E. and Radermacher R. Performance Analysis Of a Combined Desiccant/Absorption Air-Conditioning System. *HVAC&R Research*, 5(1):77–84, 1999.

[27] Dhar P. L. and S. K. Singh. Studies on solid desiccant based hybrid air-conditioning systems. *Applied Thermal Engineering*, 21(2):119–134, 2001.

[28] Worek W. M. and Moon C. J. Desiccant integrated hybrid vapor-compression cooling: Performance sensitivity to outdoor conditions. *Heat Recovery Systems and CHP*, 8(6): 489–501, 1988.

[29] Sand J. R. and Fischer J. C. Active desiccant integration with packaged rooftop HVAC equipment. *Applied Thermal Engineering*, 25(17):3138–3148, 2005.

[30] Jia C. X., C. Kung, Je W., and H. P. Li. Performance analysis of a hybrid desiccant air conditioning system. *Journal of Engineering Thermophysics*, 26(6), 2005.

[31] Kamel K. Ghali. Energy savings potential of a hybrid desiccant dehumidification air conditioning system in Beirut. *Energy Conversion and Management*, 49(11):3387–3390, 2008.

[32] Niu J. L., Zhang L. Z., and Zuo H. G. Energy savings potential of chilled-ceiling combined with desiccant cooling in hot and humid climates. *Energy and Buildings*, 34(5):487–495, 2002.

[33] Goldsworthy M. and White S. The Performance of Desiccant Wheels for Desiccant Air-Conditioning. In *Desiccant-Assisted Cooling*, pages 109–141. 2014.

[34] Jurinak J. J. *Open cycle solid desiccant cooling : component models and system simulations*. PhD thesis, 1982.

[35] Collier R., Cale T. S., and Lavan Z. Advanced desiccant materials assessment. Technical report, Gas Research Institute, Chicago, 1986.

[36] Collier R. Desiccant Properties and Their Effects on the Performance of Desiccant Cooling Systems. *ASHRAE Trans*, (1):823–827, 1989.

[37] Collier R. and Cohen B. M. An Analytical Examination of Methods for Improving the Performance of Desiccant Cooling Systems. *Journal of Solar Energy Engineering*, 113(3): 157, 1991.

[38] Jia C. X., Dai Y. J., Wu J. Y., and Wang R. Z. Experimental comparison of two honeycombed desiccant wheels fabricated with silica gel and composite desiccant material. *Energy Conversion and Management*, 47(15-16):2523–2534, 2006.

[39] Aristov Y. I., Tokarev M. M., Cacciola G., and Restuccia G. Selective water sorbents for multiple applications, 1. CaCl2 confined in mesopores of silica gel: Sorption properties. *Reaction Kinetics & Catalysis Letters*, 59(2):325–333, 1996.

[40] Czanderna A.W. and Neidlinger H. H. Polymers as Advanced Materials for Desiccant Applications. Technical report, Solar Energy Research Institute Colorado, 1988.

[41] Lee J. and Lee D. Y. Sorption characteristics of a novel polymeric desiccant. *International Journal of Refrigeration*, 35(7):1940–1949, 2012.

[42] White S., Goldsworthy M., Reece R., Spillmann T., Gorur A., and Lee D. Y. Characterization of desiccant wheels with alternative materials at low regeneration temperatures. *International Journal of Refrigeration*, 34(8):1786–1791, 2011.

[43] Goldsworthy M. and White S. Limiting performance mechanisms in desiccant wheel dehumidification. *Applied Thermal Engineering*, 44:21–28, 2012.

[44] Pesaran A. A. and Mills A. F. Moisture transport in silica gel packed beds - I Theoretical study. *International Journal of Heat and Mass Transfer*, 30(6):1037–1049, 1987.

[45] Pesaran A. A. and Mills A. F. Moisture transport in silica gel packed beds - II Experimental study. *International Journal of Heat and Mass Transfer*, 30(6):1051–1060, 1987.

[46] Ge T. S., Y. Li, Wang R. Z., and Dai Y. J. A review of the mathematical models for predicting rotary desiccant wheel. *Renewable & Sustainable Energy Reviews*, 12(6):1485–1528, 2008.

[47] Do D. D. and Rice R. G. Validity of the parabolic profile assumption in adsorption studies. *AIChE Journal*, 32(1):149–154, 1986.

[48] Chant E. E. On the use of the parabolic concentration profile assumption for a rotary desiccant dehumidifier. *Journal of Solar Energy Engineering*, 117(1):45–50, 1995.

[49] Bellemo L., B. Elmegaard, Kærn M. R., Markussen W. B., and Reinholdt L. O. Formulation and validation of a two-dimensional steady-state model of desiccant wheels. *Science and Technology for the Built Environment*, 21(3):300–311, 2015.

[50] Tsutsui K. Effect of design and operating conditions on performance of desiccant wheels. In *IIR HVAC energy efficiency best practice conference*, Melbourne, 2008.

[51] Mills A. F. *Mass Transfer*. Prentice Hall, 2001.

[52] Lide D. R. *Handbook of Chemistry and Physics*. CRC Press, 1996.

[53] Close D. J. and Banks P. J. Coupled equilibrium heat and single adsorbate transfer in fluid flow through a porous medium — II Predictions for a silica-gel air-drier using characteristic charts. *Chemical Engineering Science*, 27(5):1157–1169, 1972.

[54] U. Eicker, Schürger U., Köhler M., Ge T., Dai Y., Li H., and Wang R. Experimental investigations on desiccant wheels. *Applied Thermal Engineering*, 42:71–80, 2012.

[55] ANSI/ASHRAE Standard 139 - Method of Testing for Rating Desiccant Dehumidifiers Utilizing Heat for the Regeneration Process. Technical report, 2007.

[56] Chung J. D. and Lee D. Y. Effect of desiccant isotherm on the performance of desiccant wheel. *International Journal of Refrigeration*, 32(4):720–726, 2009.

[57] Duan Z., C. Zhan, X. Zhang, M. Mustafa, X. Zhao, B. Alimohammadisagvand, and A. Hasan. Indirect evaporative cooling: Past, present and future potentials. *Renewable and Sustainable Energy Reviews*, 16(9):6823–6850, 2012.

[58] Porumb B., Ungureşan P., Tutunaru L. F., Şerban A., and Bălan M. A Review of Indirect Evaporative Cooling Technology. *Energy*, 85:461–471, 2016.

[59] Maisotsenko V., Gillan L. E., Heaton T. L., and Gillan A. D. Method and plate apparatus for dew point evaporative cooler, 2003.

[60] Gillan L. Maisotsenko cycle for cooling processes. *International Journal of Energy for a Clean Environment*, 9(1-3):47–64, 2008.

[61] P. Glanville, Kozlov A., and Maisotsenko V. Dew point evaporative cooling: technology review and fundamentals. 2011.

[62] Hsu S. T., Lavan Z., and Worek W. M. Optimization of wet-surface heat exchangers. *Energy*, 14(11):757–770, 1989.

[63] Riangvilaikul B. and Kumar S. Numerical study of a novel dew point evaporative cooling system. *Energy and Buildings*, 42(11):2241–2250, 2010.

[64] Riangvilaikul B. and Kumar S. An experimental study of a novel dew point evaporative cooling system. *Energy and Buildings*, 42(5):637–644, 2010.

[65] M. Janssen, and P., Uges. Parameters affecting the performance of a dewpoint cooler consisting of a counter flow heat exchanger using water as refrigerant. In *Proceedings of the Gustav Lorentzen Conference*, Sydney, Australia, 2010.

[66] Bellemo L., B. Elmegaard, Kærn M. R., Markussen W. B., and Reinholdt L. O. Modeling of a regenerative indirect evaporative cooler for a desiccant cooling system. 2013.

[67] Zhao X., Li J. M., and Riffat S. B. Numerical study of a novel counter-flow heat and mass exchanger for dew point evaporative cooling. *Applied Thermal Engineering*, 28(14): 1942–1951, 2008.

[68] Zhan C., Duan Z., Zhao X., Smith S., Jin H., and Riffat S. Comparative study of the performance of the M-cycle counter-flow and cross-flow heat exchangers for indirect evaporative cooling – Paving the path toward sustainable cooling of buildings. *Energy*, 36(12):6790–6805, 2011.

[69] Zhan C., Zhao X., Smith S., and Riffat S. B. Numerical study of a M-cycle cross-flow heat exchanger for indirect evaporative cooling. *Building and Environment*, 46(3):657–668, 2011.

[70] A. Hasan. Indirect evaporative cooling of air to a sub-wet bulb temperature. *Applied Thermal Engineering*, 30(16):2460–2468, 2010.

[71] A. Hasan. Going below the wet-bulb temperature by indirect evaporative cooling: Analysis using a modified ϵ-NTU method. *Applied Energy*, 89(1):237–245, 2012.

[72] Anisimov S., Pandelidis D., and Danielewicz J. Numerical analysis of selected evaporative exchangers with the Maisotsenko cycle. *Energy Conversion and Management*, 88:426–441, 2014.

[73] Anisimov S. and Pandelidis D. Numerical study of the Maisotsenko cycle heat and mass exchanger. *International Journal of Heat and Mass Transfer*, 75:75–96, 2014.

[74] Anisimov S., Pandelidis D., Jedlikowski A., and V. Polushkin. Performance investigation of a M (Maisotsenko)-cycle cross-flow heat exchanger used for indirect evaporative cooling. *Energy*, 76:593–606, nov 2014.

[75] Anisimov S. and Pandelidis D. Theoretical study of the basic cycles for indirect evaporative air cooling. *International Journal of Heat and Mass Transfer*, 84:974–989, 2015. doi: 10.1016/j.ijheatmasstransfer.2015.01.087.

[76] Anisimov S., Pandelidis D., and Danielewicz J. Numerical study and optimization of the combined indirect evaporative air cooler for air-conditioning systems. *Energy*, 80: 452–464, 2015.

[77] Pandelidis D. and Anisimov S. Numerical analysis of the selected operational and geometrical aspects of the M-cycle heat and mass exchanger. *Energy and Buildings*, 87: 413–424, 2015.

[78] Pandelidis D. and S. Anisimov. Numerical analysis of the heat and mass transfer processes in selected M-Cycle heat exchangers for the dew point evaporative cooling. *Energy Conversion and Management*, 90:62–83, 2015.

[79] Pandelidis D., Anisimov S., and Worek W. M. Performance study of the Maisotsenko Cycle heat exchangers in different air-conditioning applications. *International Journal of Heat and Mass Transfer*, 81:207–221, 2015.

[80] Pandelidis D., Anisimov S., and Worek W. M. Comparison study of the counter-flow regenerative evaporative heat exchangers with numerical methods. *Applied Thermal Engineering*, 84:211–224, 2015.

[81] Lin J., Thu K., Bui T. D., Wang R. Z., K. C. Ng, and Chua K. J. Study on dew point evaporative cooling system with counter-flow configuration. *Energy Conversion and Management*, 109:153–165, 2016.

[82] Pandelidis D., Anisimov S., and Worek W. M. Performance study of counter-flow indirect evaporative air coolers. *Energy and Buildings*, 109:53–64, 2015.

[83] StatiqCooling. URL http://statiqcooling.com/.

[84] Mills A. F. *Heat transfer*. Prentice Hall, 1999.

[85] Verein Deutscher Ingenieure. *VDI Heat Atlas*. Springer, 2010.

[86] Gustavsson J., editor. *REHVA Guidebook 11 - Air Filtration in HVAC Systems*. REHVA Federation of European Heating, Ventilation and Air–Conditioning Associations, 2nd edition, 2011.

[87] Eicker U., Schneider D., Schumacher J., Ge T., and Y. Dai. Operational experiences with solar air collector driven desiccant cooling systems. *Applied Energy*, 87(12):3735–3747, 2010.

[88] EN Standard 15251 - Indoor environmental input parameters for design and assessment of energy performance of buildings addressing indoor air quality, thermal environment, lighting and acoustics. Technical report, 2007.

[89] IEA Solar Heating and Cooling Program Task 38 - Solar Air Conditioning and Refrigeration - Subtask A: Pre engineered Systems for Residential and Small Commercial Applications - Monitoring Results. Technical report, 2011.

[90] IEA Solar Heating and Cooling Program Task 38 - Solar Air Conditioning and Refrigeration - Subtask C3: Exergy Analysis of Solar Cooling Systems. Technical report, 2011.

[91] Lavan Z., Monnier J. B., and Worek W. M. Second Law Analysis of Desiccant Cooling Systems. *Journal of Solar Energy Engineering*, 104(3):229, 1982.

[92] Pons M. and Kodama A. Entropic analysis of adsorption open cycles for air conditioning. Part 1: first and second law analyses. *International Journal of Energy Research*, 24(3): 251–262, 2000.

[93] A. Kodama, Jin W., M. Goto, Hirose T., and Pons M. Entropic analysis of adsorption open cycles for air conditioning. Part 2: interpretation of experimental data. *International Journal of Energy Research*, 24(3):263–278, 2000.

[94] Kanoğlu M., M. Özdinç Çarpınlıoğlu, and Yıldırım M. Energy and exergy analyses of an experimental open-cycle desiccant cooling system. *Applied Thermal Engineering*, 24(5): 919–932, 2004.

[95] Kanoğlu M., Bolattürk A., and Altuntop N. Effect of ambient conditions on the first and second law performance of an open desiccant cooling process. *Renewable Energy*, 32 (6):931–946, 2007.

[96] D. La, Y. Li, Dai Y. J., Ge T. S., and Wang R. Z. Development of a novel rotary desiccant cooling cycle with isothermal dehumidification and regenerative evaporative cooling using thermodynamic analysis method. *Energy*, 44(1):778–791, 2012.

[97] La D., Y. Li, Dai Y., Ge T., and Wang R. Effect of irreversible processes on the thermodynamic performance of open-cycle desiccant cooling cycles. *Energy Conversion and Management*, 67:44–56, 2013.

[98] Enteria N., H. Yoshino, Takaki R., Yonekura H., Satake A., and Mochida A. First and second law analyses of the developed solar-desiccant air-conditioning system (SDACS) operation during the summer day. *Energy and Buildings*, 60:239–251, 2013.

[99] Doty S. Part-load HVAC efficiency. *Energy Engineering: Journal of the Association of Energy Engineering*, 107(3), 2010.

[100] ECBCS Annex 49 Low Exergy Systems for High-Performance Buildings and Communities. Technical report, 2011.

[101] Pons M. *International Journal of Thermodynamics*, 12(12):113–121, 2009.

[102] Bejan A. *Advanced engineering thermodynamics*. John Wiley & Sons, 2006.

[103] Duffie J. A. and W. A. Beckman. *Solar engineering of thermal processes*. Wiley, 2013.

[104] IEA. Water for Energy: Is energy becoming a thirstier resource? Technical report, IEA, 2012.

[105] IEA Solar Heating and Cooling Program Task 38 - Solar Air Conditioning and Refrigeration - Subtask C5 - Heat Rejection. Technical report, 2010.

[106] WRAP. Reducing water use in cooling towers and evaporative condensers. Technical report, 2010.

[107] Calsonic Corp. Patent JPH11182969A, 1999.

[108] Jiang H. *Development of a Simulation and Optimization Tool for Heat Exchanger Design*. PhD thesis, 2003.

[109] F. Bozzoli, S. Rainieri, and Pagliarini G. Estimation of the local heat transfer coefficient in forced convection of moist air in presence of water vapour surface condensation. In *5th European Thermal-Sciences Conference*, The Netherlands, 2008.

A Desiccant wheel model numerical implementation

In the following, the desiccant wheel model implementation is presented for a desiccant wheel divided into 1 process section and 1 regeneration section. The same approach is applicable when considering additional sections, e.g. purge sections, staged regeneration sections, staged dehumidification sections.
The two-dimensional computational grid reported in Figure 2.4 is considered.

Air inlet boundary conditions

For the process air stream at the process section inlet:

$$z = 0, \quad \left.\begin{array}{l} T_a = T_{a,p,in} \\ x_a = x_{a,p,in} \end{array}\right\} \text{for } 0 < \theta < N_{chan,tot} P_{wet} \frac{\gamma_p}{2\pi}$$

For the regeneration air stream at the regeneration section inlet:

$$z = L, \quad \left.\begin{array}{l} T_a = T_{a,r,in} \\ x_a = x_{a,r,in} \end{array}\right\} \text{for } N_{chan,tot} P_{wet} \frac{\gamma_p}{2\pi} < \theta < N_{chan,tot} P_{wet}$$

Where the length of the heat and mass transfer area along the θ axis is expressed as a function of the total number of channels in the wheel ($N_{chan,tot}$), the wet perimeter of a single channel (P_{wet}), and the process section face angle (γ_p) expressed in radians.

Solution strategy

The governing equations are solved separately for the process and regeneration sections, starting from the process section and proceeding accordingly to the direction of wheel rotation, i.e. solid stream direction.
Initially, desiccant temperature and moisture content are guessed at all locations in the wheel. For each section, the air governing equations (Equations 2.6 and 2.7) and the desiccant gov-

erning equations (Equations 2.8, 2.10 and 2.11) are discretized by means of finite difference methods. The discretized air system of equations is solved first, for constant desiccant conditions, while the discretized desiccant system of equations is solved subsequently considering the newly computed air conditions. After both air and desiccant systems of equations are solved once for a wheel section, the desiccant conditions at the boundary with the next section are updated. These procedure is iterated until the desiccant conditions at all locations in the wheel are converged, i.e. conditions change below a specified tolerance.

- *Initial guess on desiccant conditions*
  The desiccant conditions temperature and surface water content (T_d and W_surf) are initially guessed, choosing the following values:

$$\left.\begin{array}{c} T_{d,i,j} = (T_{a,p,in} + T_{a,r,in})/2 \\ W_{d,i,j} = (W_{d,eq,p} + W_{d,eq,r})/2 \\ W_{s,i,j} = W_{d,i,j} \end{array}\right\} \text{for } i = 1 : N_z \text{ and } j = 1 : N_\theta$$

  The values $W_{d,eq,p}$ and $W_{d,eq,r}$ are the desiccant moisture contents at equilibrium with the process and regeneration inlet air streams respectively.

- *Air system of equations*
  Equations 2.7 and 2.6 are discretized using the Central Difference Scheme (CDS). Considering Equation 2.7, the term $c_{p,ha}T_a$ is differentiated altogether to account for variations in the air specific heat capacity. The LHS of Eq. 2.7 is discretized for the generic (i, j) CV:

$$\left.\frac{\partial c_{p,ha}T_a}{\partial z}\right|_{i,j} \approx \frac{(c_{p,ha}T_a)_{i,j+1} - (c_{p,ha}T_a)_{i,j-1}}{2\Delta z} \tag{A.1}$$

  Hence, Equation 2.7 is rewritten as:

$$\frac{(c_{p,ha}T_a)_{i,j+1}}{2} - \frac{(c_{p,ha}T_a)_{i,j-1}}{2} + \frac{\alpha A_{i,j}}{\dot{m}_{a,i,j}} T_{a,i,j} = \frac{\alpha A_{i,j}}{\dot{m}_{a,i,j}} T_{d,i,j} \tag{A.2}$$

  that is rewritten by introducing the term $C_{ht} = \dfrac{\alpha A_{i,j}}{\dot{m}_{a,i,j}}$:

$$\frac{(c_{p,ha}T_a)_{i,j+1}}{2} - \frac{(c_{p,ha}T_a)_{i,j-1}}{2} + \frac{C_{ht}}{c_{p,a,i,j}}(c_{p,ha}T_a)_{i,j} = C_{ht}T_{d,i,j} \tag{A.3}$$

  note that C_{ht} is a constant for for all CVs in the same wheel section, as α, $A_{i,j}$ and $\dot{m}_{a,i,j}$ are constant values.

Boundary conditions are applied to the first and last CVs along the airflow direction inside a channel:

$$\left.\frac{\partial c_{p,ha}T_a}{\partial z}\right|_{1,j} \approx \frac{(c_{p,ha}T_a)_{1,j} + (1/3)(c_{p,ha}T_a)_{2,j} - (4/3)(c_{p,ha}T_a)_{in,j}}{\Delta z} \tag{A.4}$$

$$\left.\frac{\partial c_{p,ha}T_a}{\partial z}\right|_{N_z,j} \approx \frac{(1/2)(c_{p,ha}T_a)_{N_z-2,j} + 2(c_{p,ha}T_a)_{N_z-1,j} - (3/2)(c_{p,ha}T_a)_{N_z,j}}{\Delta z} \tag{A.5}$$

where $(c_{p,ha}T_a)_{in,j}$ is evaluated at the air free stream conditions.

The discretized form of Equation 2.6 is derived analogously, resulting into:

$$\frac{x_{a,i+1,j}}{2} - \frac{x_{a,i-1,j}}{2} + C_{mt}x_{a,i,j} = C_{mt}x_{d,i,j} \tag{A.6}$$

where $C_{mt} = \dfrac{\sigma A_{i,j}}{\dot{m}_{a,i,j}}$ is a constant value.

For a row of CVs in the air flow direction, Equations A.3 and A.6 constitute linear systems of equations, if the desiccant conditions T_d and W_d are constant values. Therefore the Gaussian elimination method can be applied. The air humidity ratio x_a is computed first, and used for computing the corresponding air specific heat capacity $c_{p,ha}$, and so the air temperature T_a.

The linear system of equations described by Eq. A.6 is solved in a matrix form for each circumferential position j of the considered wheel section:

$$\left[A\right]\begin{Bmatrix} x_{a,1,j} \\ x_{a,2,j} \\ x_{a,3,j} \\ \vdots \\ x_{a,N_z-2,j} \\ x_{a,N_z-1,j} \\ x_{a,N_z,j} \end{Bmatrix} = \begin{Bmatrix} C_{mt}x_{d,1,j} + (4/3)x_{a,in,j} \\ C_{mt}x_{d,2,j} \\ C_{mt}x_{d,3,j} \\ \vdots \\ C_{mt}x_{d,N_z-2,j} \\ C_{mt}x_{d,N_z-1,j} \\ C_{mt}x_{d,N_z,j} \end{Bmatrix}$$

$$\left[A\right] = \begin{bmatrix} 1+C_{mt} & 1/3 & 0 & 0 & \cdots & \cdots & 0 \\ -1/2 & C_{mt} & 1/2 & 0 & & & \vdots \\ 0 & -1/2 & C_{mt} & 1/2 & & & \\ \vdots & & \ddots & \ddots & \ddots & & \vdots \\ & & & -1/2 & C_{mt} & 1/2 & 0 \\ \vdots & & & 0 & -1/2 & C_{mt} & 1/2 \\ 0 & \cdots & \cdots & 0 & 1/2 & -2 & 3/2+C_{mt} \end{bmatrix}$$

The linear system of equations described by Equation A.3 is solved analogously in the matrix form:

$$\left[B\right] \begin{Bmatrix} (c_{p,ha}T_a)_{1,j} \\ (c_{p,ha}T_a)_{2,j} \\ (c_{p,ha}T_a)_{3,j} \\ \vdots \\ (c_{p,ha}T_a)_{N_z-2,j} \\ (c_{p,ha}T_a)_{N_z-1,j} \\ (c_{p,ha}T_a)_{N_z,j} \end{Bmatrix} = \begin{Bmatrix} C_{ht}T_{d,1,j} + (4/3)(c_{p,ha}T_a)_{i,in} \\ C_{ht}T_{d,2,j} \\ C_{ht}T_{d,3,j} \\ \vdots \\ C_{ht}T_{d,N_z-2,j} \\ C_{ht}T_{d,N_z-1,j} \\ C_{ht}T_{d,N_z,j} \end{Bmatrix}$$

$$\left[B\right] = \begin{bmatrix} 1+B_{i,1} & 1/3 & 0 & 0 & \cdots & \cdots & 0 \\ -1/2 & B_{i,2} & 1/2 & 0 & & & \vdots \\ 0 & -1/2 & B_{i,3} & 1/2 & & & \\ \vdots & & \ddots & \ddots & \ddots & & \vdots \\ & & & -1/2 & B_{i,M-2} & 1/2 & 0 \\ \vdots & & & 0 & -1/2 & B_{i,M-1} & 1/2 \\ 0 & \cdots & \cdots & 0 & 1/2 & -2 & 3/2+B_{i,M} \end{bmatrix}$$

where $B_{i,j} = \dfrac{C_{ht}}{c_{p,a,i,j}}$

Therefore the air conditions T_a and x_a are updated.

- *Desiccant system of equations*
  The desiccant governing Equations 2.8 and 2.10 are discretized applying the CDS, while Equation 2.11 is directly computed:

$$\left.\frac{\partial W_d}{\partial \theta}\right|_{i,j} \approx \frac{W_{d,i,j+1}}{2} - \frac{W_{d,i,j-1}}{2} = -\frac{\sigma A_{i,j}}{f_{des}\dot{m}_{d,i,j}}\left(x_{d,i,j} - x_{a,i,j}\right) = -C_{W_d}\left(x_{d,i,j} - x_{a,i,j}\right) \tag{A.7}$$

$$\left.\frac{\partial h_d}{\partial \theta}\right|_{i,j} \approx \frac{h_{d,i,j+1}}{2} - \frac{h_{d,i,j-1}}{2} = -\frac{\alpha A_{i,j}}{\dot{m}_{d,i,j}}\left(T_{d,i,j} - T_{a,i,j}\right) - h_{ads}\frac{\sigma A_{i,j}}{\dot{m}_{d,i,j}}\left(x_{d,i,j} - x_{a,i,j}\right)$$
$$= -C_{T_d}\left(T_{d,i,j} - T_{a,i,j}\right) - h_{ads} f_{des} C_{W_d}\left(x_{d,i,j} - x_{a,i,j}\right) \tag{A.8}$$

The resulting system of equations is non-linear, hence the Newton-Raphson method is applied. The residual function is computed as:

$$Res = \left[C\right]\begin{Bmatrix} W_{d,i,1} \\ W_{d,i,2} \\ \vdots \\ W_{d,i,N_\theta-1} \\ W_{d,i,N_\theta} \\ h_{d,i,1} \\ h_{d,i,2} \\ \vdots \\ h_{d,i,N_\theta-1} \\ h_{d,i,N_\theta} \\ W_{surf,i,1} \\ W_{surf,i,2} \\ \vdots \\ W_{surf,i,N_\theta-1} \\ W_{surf,i,N_\theta} \end{Bmatrix} - \begin{Bmatrix} b_{W_d,i,1} + (4/3)W_{d,i,in} \\ b_{W_d,i,2} \\ \vdots \\ b_{W_d,i,N_\theta-1} \\ b_{W_d,i,N_\theta} \\ b_{h_d,i,1} + (4/3)h_{d,i,in} \\ b_{h_d,i,2} \\ \vdots \\ b_{h_d,i,N_\theta-1} \\ b_{h_d,i,N_\theta} \\ b_{W_{surf},i,1} \\ b_{W_{surf},i,2} \\ \vdots \\ b_{W_{surf},i,N_\theta-1} \\ b_{W_{surf},i,N_\theta} \end{Bmatrix}$$

$$\left[C\right] = \begin{bmatrix} [D]_{N_\theta x N_\theta} & [0]_{N_\theta x N_\theta} & [0]_{N_\theta x N_\theta} \\ [0]_{N_\theta x N_\theta} & [D]_{N_\theta x N_\theta} & [0]_{N_\theta x N_\theta} \\ [0]_{N_\theta x N_\theta} & [0]_{N_\theta x N_\theta} & I_{N_\theta} \end{bmatrix}$$

$$\left[D\right] = \begin{bmatrix} 1 & 1/3 & 0 & \cdots & 0 \\ -1/2 & 0 & 1/2 & & \vdots \\ \vdots & \ddots & \ddots & \ddots & \vdots \\ \vdots & & -1/2 & 0 & 1/2 \\ 0 & \cdots & 1/2 & -2 & 3/2 \end{bmatrix}$$

where the same boundary conditions as for the air streams are used, and the following terms are introduced:

$$b_{W_d,i,j} = -C_{W_d}\left(x_{d,i,j} - x_{a,i,j}\right)$$
$$b_{T_d,i,j} = -C_{T_d}\left(T_{d,i,j} - T_{a,i,j}\right) - h_{ads} f_{des} C_{W_d}\left(x_{d,i,j} - x_{a,i,j}\right)$$
$$b_{W_{surf},i,j} = -\frac{\sigma c}{3 f_{des}\rho_d D_{eff}}\left(x_{d,i,j} - x_{a,i,j}\right) T_{d,i,j} + W_{d,i,j}$$

The updated desiccant conditions are calculated as:

$$\left[W_{d,new}; h_{d,new}; W_{surf,new}\right] = \left[W_{d,old}; h_{d,old}; W_{surf,old}\right] - \frac{Res}{J}$$

where the Jacobian J is obtained by computing the numerical derivatives of the source terms b_{W_d}, b_{h_d} and $b_{W_{surf}}$ for very small increments (1E-8) of the variables W_d, h_d and W_{surf}. The Jacobian is written as:

$$J = \left[C\right] - \begin{bmatrix} I_{N_\theta}\frac{\partial b_{W_d}}{\partial W_d} & I_{N_\theta}\frac{\partial b_{W_d}}{\partial h_d} & I_{N_\theta}\frac{\partial b_{W_d}}{\partial W_{surf}} \\ I_{N_\theta}\frac{\partial b_{h_d}}{\partial W_d} & I_{N_\theta}\frac{\partial b_{h_d}}{\partial h_d} & I_{N_\theta}\frac{\partial b_{h_d}}{\partial W_{surf}} \\ I_{N_\theta}\frac{\partial b_{W_{surf}}}{\partial W_d} & I_{N_\theta}\frac{\partial b_{W_{surf}}}{\partial h_d} & I_{N_\theta}\frac{\partial b_{W_{surf}}}{\partial W_{surf}} \end{bmatrix}$$

The Newton-Raphson method is applied only once, i.e. the new desiccant conditions are calculated only once.

- *Convergence test*
  After a complete iteration (air and desiccant equations are solved in both process and regeneration sections), the change of desiccant conditions (W_d and h_d) at all locations relatively to the previous iteration is computed. If the biggest of the relative changes is smaller than a specified tolerance (1E-6), the solution is considered converged. Otherwise new iterations are carried out until convergence is reached.

B Silica gel properties

Regular Density (RD) silica gel is considered. A list of the properties implemented in the desiccant wheel model is reported in the following:

- Bulk density ρ= 720 kg/m^3 [33]
- Specific heat capacity c_p=921 J/(kgK) including support structure with desiccant mass ratio f_{des}=0.7 [33]
- Adsorption heat $h_{ads} = h_{fg}\left(1 + 0.2843e^{-10.28W_d}\right)$ [46]
- Adsorption isotherm $\varphi_{eq} = 0.0078 - 0.0576W_d + 24.17W_d^2 - 124.48W_d^3 + 204.23W_d^4$ independent of temperature [46]
- Effective Surface diffusivity $D_s = D_0 e^{-0.947 h_{ads}/T_d}$ with T_d in K, D_0=1.6E-6 m^2/s and pore tortuosity factor ζ = 2.8 [44]

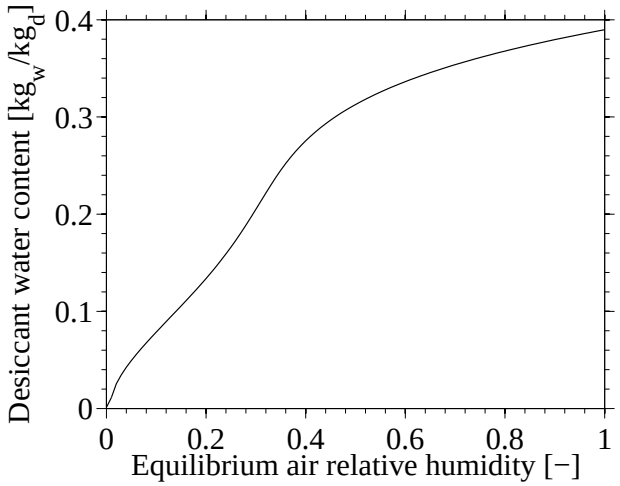

Figure B.1: Equilibrium adsorption curve.

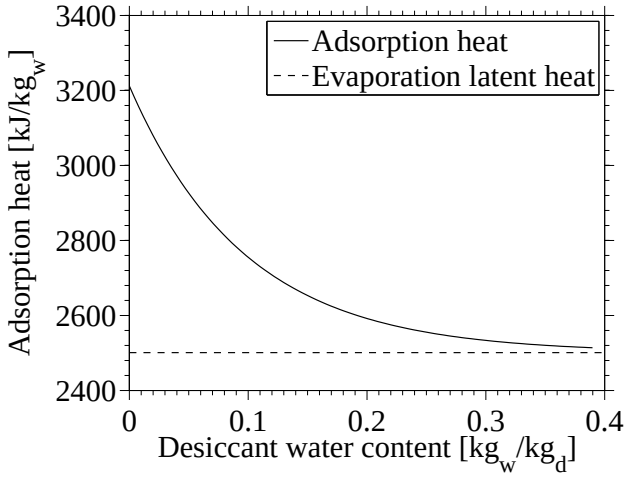

Figure B.2: Adsorption heat.

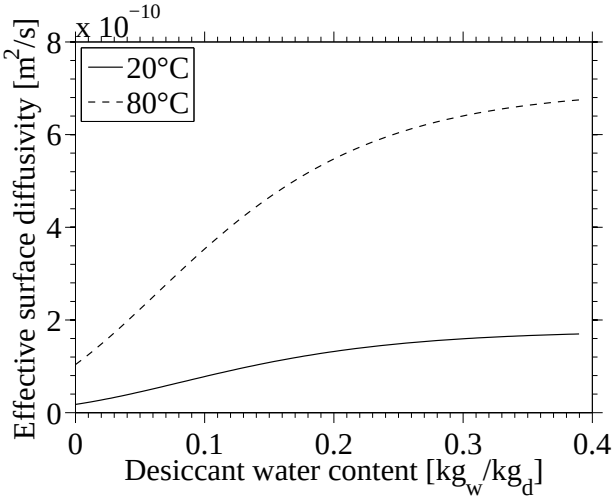

Figure B.3: Effective surface diffusivity in the pores.

C Indirect evaporative cooler model numerical implementation

The governing equations of the indirect evaporative cooler cooler model are at first discretized by means of the Central Difference Scheme, analogously to what report for the desiccant wheel model governing equations in Appendix A. The resulting systems of equations at the primary and secondary sides are linear, so Gaussian elimination is applied by assuming constant wall temperature, analogously to what reported for the air governing equations in Appendix A. The wall temperature is successively updated by means of the Newton-Raphson method.

The evaporative cooler model is solved by means of the following solution strategy:

1. The secondary wall temperature is initially guessed equal to the primary air inlet temperature.

2. The primary air system equations describing heat transfer are solved along the whole channel length by means of Gaussian elimination for fixed secondary wall temperature.

3. The secondary air equations describing heat and mass transfer are solved along the whole channel length by means of Gaussian elimination for the same secondary wall temperature.

4. The secondary wall temperature is updated along the channel length by means of the Newton-Raphson method.

5. The procedure is repeated until the relative change of secondary wall temperature is lower than a specified tolerance.

The procedure for updating the secondary wall temperature is reported in the following.

The thermal resistance at the primary side including convection in the air and conduction

across the wall is:

$$R_{th,p} = \frac{1}{\alpha_p A_p} + \frac{th_{wall}}{k_m A_s} \tag{C.1}$$

The heat transfer rate from primary to secondary side is expressed as:

$$\dot{Q}_p = \frac{T_{a,p} - T_{w,s}}{R_{th,p}} = \dot{Q}_s = \alpha_s A_s \left(T_{w,s} - T_{a,s}\right) + \dot{m}_w h_{fg} \tag{C.2}$$

An expression for the secondary wall temperature is obtained by rearranging Equation C.2:

$$T_{w,s} = \frac{1}{1 + \alpha_s A_s R_{th,p}} T_{a,p} + \frac{\alpha_s A_s R_{th,p}}{1 + \alpha_s A_s R_{th,p}} T_{a,p} - \frac{R_{th,p}}{1 + \alpha_s A_s R_{th,p}} \dot{m}_w h_{fg} \tag{C.3}$$

The residual function is defined as:

$$Res = T_{w,s,old} - T_{w,s} \tag{C.4}$$

$$= T_{w,s,old} - \frac{1}{1 + \alpha_s A_s R_{th,p}} T_{a,p} + \frac{\alpha_s A_s R_{th,p}}{1 + \alpha_s A_s R_{th,p}} T_{a,p} - \frac{R_{th,p}}{1 + \alpha_s A_s R_{th,p}} \dot{m}_w h_{fg} \tag{C.5}$$

Hence, the new secondary wall temperature is computed as:

$$T_{w,s,new} = T_{w,s,old} - Res \Big/ \frac{dRes}{dT_{w,s}} \tag{C.6}$$

where the derivative of the residual in respect to the secondary wall temperature is:

$$\frac{dRes}{dT_{w,s}} = 1 + \frac{1}{1 + \alpha_s A_s R_{th,p}} \left(R_{th,p} \sigma A_s \frac{dh_{fg}}{dT_{w,s}} (x_{w,s} - x_{a,s}) + h_{fg} \frac{dx_{w,s}}{dT_{w,s}} \right) \tag{C.7}$$

The latent heat of evaporation of water is expresses as:

$$h_{fg} = -2.4263 T_{w,s} + 2502.544 \tag{C.8}$$

The derivative of air humidity ratio at saturated conditions in respect to the secondary temperature wall temperature is approximated (R^2=0.9986) as:

$$\frac{dx_{w,s}}{dT_{w,s}} = 0.0002901866750590 * e^{0.0572540741519774 T_{w,s,old}} \tag{C.9}$$

DTU Mechanical Engineering
Section of Thermal Energy
Technical University of Denmark

Nils Koppels Allé, Bld. 403
DK-2800 Kgs. Lyngby
Denmark
Phone (+45) 4525 4131
Fax (+45) 4588 4325
www.mek.dtu.dk
ISBN: 978-87-7475-509-8

DCAMM
Danish Center for Applied Mathematics and Mechanics

Nils Koppels Allé, Bld. 404
DK-2800 Kgs. Lyngby
Denmark
Phone (+45) 4525 4250
Fax (+45) 4593 1475
www.dcamm.dk
ISSN: 0903-1685